A theoretical evaluation of transmission dosimetry in 3D conformal radiotherapy

Paul D Reich

Thesis submitted for the degree of

Doctor of Philosophy

in

The School of Chemistry and Physics,

University of Adelaide

September 2008

Contents

List of Tables

List of Figures

Abstract

Two-dimensional transmission dosimetry in radiotherapy has been discussed in the literature for some time as being a potential method for *in vivo* dosimetry. However, it still remains to become a wide spread practice in radiotherapy clinics. This is most likely due to the variety in radiotherapy treatment sites and the challenges they would present in terms of detection and interpretation at the transmitted dose level. Thus, the full potential and limitations of applying transmission dosimetry in the presence of dosimetry errors still need to be demonstrated.

This thesis is a theoretical evaluation of transmission dosimetry using the Pinnacle^3 treatment planning system. The accuracy of predicting reliable and accurate absolute transmitted dose maps using the planning system dose algorithm for comparison with measured transmitted dose maps was initially investigated. The resolution in the dose calculations at the transmitted level was then evaluated for rectilinear and curved homogeneous phantoms and rectilinear inhomogeneous phantoms, followed by studies combining both surface curvature and heterogeneities using anthropomorphic phantoms. In order to perform transmitted dose calculations at clinically relevant beam focus-to-transmitted dose plane distances using clinical patient CT data it was first necessary to extend the CT volume. Finally, the thesis explored the efficacy of applying transmission dosimetry in the clinic by simulating realistic dosimetry errors in the planning system using patient treatment plans for a prostate, head and neck, and breast CRT (Conformal Radiotherapy) treatment. Any differences at the transmitted dose level were interpreted and quantified using the gamma formalism. To determine whether the transmitted dose alone was a sufficient indicator

of the dosimetry errors, the magnitude in transmission dose differences were compared with those predicted at the midplane of the patient. Dose-Volume Histograms (DVHs) were also used to evaluate the clinical significance of the dose delivery errors on the target volume and surrounding healthy tissue structures.

Signed Statement

This work contains no material which has been accepted for the award of any other degree or diploma in any university or other tertiary institution and, to the best of my knowledge and belief, contains no material previously published or written by another person, except where due reference has been made in the text.

I consent to this copy of my thesis, when deposited in the University Library, being available for loan and photocopying.

SIGNED: ..... DATE: .....

Acknowledgements

Firstly I owe my gratitude to Tim van Doorn who planted the first seed for this project in 2003. It seems like only yesterday that I first step foot in your office and asked to do a PhD. I would also like to thank you for your supervision throughout the first half of my candidature and for sharing your expertise with me.

Although it is slightly unorthodox to thank a building, however I must thank the RAH Medical Physics department itself! It has been a pleasure to share the same office space once occupied by previous PhD students (the likes of Paul Keall, Wayne Beckham, Peter Hoban, Jeremy Booth and Peter Greer, who's door name placards are enshrined on one of the office walls) whom some of which have become house-hold names in the Medical Physics community. I have fond memories of this place and I am proud to have been a member of a highly regarded and well established Medical Physics department.

A warm thank you to Loredana Marcu, whom I had the pleasure of sharing an office with during the first years. Thanks for your patience, honesty, approachability and words of encouragement.

Mohammad Mohammadi ("Momo"). What can I say? I have never met such a dedicated and hard-working individual in my life. It was a pleasure having you as a close colleague and friend whom I bonded so well with. Thank you for sharing many laughs with me and for burning the midnight oil with me towards the end of our candidatures. Your Xmas party antics shall live on ...

There are so many other people to thank along the way. I would like to start with Christine Robinson for just being her - a happy and cheerful individual to have around. Thanks also for organising all the social events and lunches for the department. In particular, I would also like to thank Kurt Byas, Kym Quach, Madhava Bhat, Ralph Nicholls, Lotte Fog, Judith Pollard, Neil Piller, and all the students in the department whom I got to know. Please forgive me if I have left anybody out!

Last but not least, I would like to express my warmest and sincere thanks to Eva Bezak, who'm I am grateful for accepting to take over the reins from Tim as my supervisor in the second half of my candidature. She is a true professional and great leader whom I have tremendous respect for as a physicist and individual. Thank you for your patience, mentorship and diligence towards my project throughout the years.

On a personal note, I would like to thank my family, particularly my parents for their patience and support throughout this large undertaking. Above all, thank you for having faith in me. Now its time to celebrate!

Publications in refereed journals

1. **P. Reich** and E. Bezak, "The use of a treatment planning system to investigate the potential for transmission dosimetry in detecting patient breathing during breast 3D CRT," *Australas. Phys. Eng. Sci. Med.* 31(2), 110-21 (2008).

2. M. Mohammadi, E. Bezak, and **P. Reich**, "Verification of dose delivery for a prostate sIMRT treatment using a SLIC-EPID", *Applied Radiation and Isotopes*. In press.

3. M. Mohammadi, E. Bezak, and **P. Reich**, "The use of extended dose range film for dosimetric calibration of a scanning liquid-filled ionization chamber electronic portal imaging device", *J Appl Clin Med Phys.* 8, 69-84 (2007).

4. **P. Reich**, E. Bezak, M. Mohammadi, and L. Fog, "The prediction of transmitted dose distributions using a 3D treatment planning system," *Australas. Phys. Eng. Sci. Med.* 29, 18-29 (2006).

5. M. Mohammadi, E. Bezak, and **P. Reich**, "Comparison of two-dimensional transmitted dose maps: evaluation of existing algorithms," *Australas. Phys. Eng. Sci. Med.* 29, 179-187 (2006).

Papers submitted in refereed journals

P. Reich, E. Bezak, and M. Mohammadi, "A theoretical evaluation of transmission dosimetry for a 3D conformal four-field box prostate treatment." *Submitted to Physics in Medicine and Biology.*

Conference presentations

International

1. Mohammadi, E. Bezak, and **P. Reich**. "Using a Scanning Liquid Ionization Chamber EPID for Prostate and Head and Neck Treatments". *World Congress on Medical Physics and Biomedical Engineering*. 2006. Seoul, South Korea.

2. **P. Reich**, E. Bezak, and M. Mohammadi. "Using a TPS to model the impact of 3D CRT patient treatment set up errors on predicted transmitted dose". *9th International Workshop on Electronic Portal Imaging*. 2006. Melbourne, Australia.

3. M. Mohammadi, E. Bezak, and **P. Reich**. "Verification of sIMRT for prostate dose delivery using a SLIC-EPID". *9th International Workshop on Electronic Portal Imaging*. 2006. Melbourne, Australia.

4. **P. Reich**, E. Bezak, L. Fog, and M. Mohammadi. "Predicting 2D transmitted dose maps using a 3D treatment planning system". *8th Biennial ESTRO Meeting on Physics and Radiation Technology for Clinical Radiotherapy*. 2005. Lisboa, Portugal.

National

5. **P. Reich**, E. Bezak, and M. Mohammadi. "What accuracy is required of predicted transmitted dose maps for EPID dosimetry in breast CRT ?". *Engineering and the Physical Sciences in Medicine 31st Annual Conference*. 2007. Fremantle, Australia.

6. **P. Reich**, E. Bezak, and M. Mohammadi. "The effects of simulated patient set-up errors on transmitted dose in 3D prostate CRT". *Engineering and the Physical Sciences in Medicine 29th Annual Conference*. 2005. Adelaide, Australia.

7. M. Mohammadi, E. Bezak, and **P. Reich**. "Investigation of two-dimensional dose

distribution evaluation tools". *Engineering and the Physical Sciences in Medicine 29th Annual Conference*. 2005. Adelaide, Australia.

- Awarded IOP Publishing Student Poster Prize.

8. M. Mohammadi, E. Bezak, and **P. Reich**. "Verification of two-dimensional transmitted dose measurements in the presence of homogeneous/inhomogeneous phantoms". *Engineering and the Physical Sciences in Medicine 29th Annual Conference*. 2005. Adelaide, Australia.

9. **P. Reich**, E. Bezak, and L. Fog. "Transmission dosimetry in Pinnacle 3D treatment planning system". *Engineering and the Physical Sciences in Medicine 28th Annual Conference*. 2004. Geelong, Australia.

Other presentations

1. **P. Reich**, E. Bezak, and M. Mohammadi. "The effect of simulated patient set-up errors on transmitted dose in 3D prostate CRT". *Postgraduate Student Papers Night*. Adelaide, Australia. 2005. Sponsored by ACPSEM, SAMBE and EACBE (SA branches).

2. **P. Reich**, E. Bezak, and L. Fog. "Transmission dosimetry using Pinnacle 3D treatment planning system: towards an online in vivo dosimetry verification system". *Postgraduate Student Papers Night*. Adelaide, Australia. 2004. Sponsored by ACPSEM, SAMBE and EACBE (SA branches).

To my parents

Chapter 1

Introduction

1.1 Patient dose verification: A major challenge in modern radiotherapy

One of the major and ongoing challenges in radiotherapy is determining whether the dose *prescribed* to the patient was correctly *delivered* during treatment. It is well known that ionising radiation is harmful to both cancerous and healthy tissue cells, which underlies the need to minimise the risk of serious accidental mistreatments and ensure that the dose was delivered as planned. *In vivo* dosimetry literally means measuring the dose inside the patient during treatment. However, in most cases (with the exception of naturally occurring cavities inside the body) this would resort to invasive measures such as surgically implanting dose detectors inside the patient. Fortunately, less invasive approaches to *in vivo* dosimetry have emerged over the years.

One of the first approaches was the placement of small detectors (diodes, thermoluminescent detectors and more recently Metal-Oxide Semiconductor Field-Effect Transistors (MOSFETs)) on the surface of the patient at the beam entrance. An advantage of such an approach is the simplicity of the setup on the patient, although there is still some degree of invasiveness involved due to the direct contact of the devices with the patient

skin. Apart from the ability to check the dose at the surface and to an extent verify patient setup, entrance dosimetry is limited to verifying the dose in a single dimension. Furthermore, it does not provide doses of interest inside the patient.

Similarly, point exit dosimetry can potentially be used to detect patient positioning errors relative to the radiation field as well as changes in patient thickness, which could negatively impact on the intended dose delivery. However, like entrance dosimetry, exit dosimetry suffers the draw back of being one-dimensional in nature which is not ideal, especially for verifying segmented intensity modulated fields.

Combining entrance with exit dose measurements has the advantage of being able to estimate the dose inside the patient, usually in the geometric midplane. One of the simplest methods (originally proposed by Rizzotti *et al*) for midplane dose estimation involves measuring depth dose data in water to determine a midplane dose and then combining this data with entrance and exit dose measurements to formulate an empirical correlation between midplane and the entrance and exit doses. Variations of this approach have been proposed by Leunens *et al*. Alternatively, Huyskens *et al* and Terrón *et al* approximated the attenuation of dose with depth inside a medium as exponential, in order to derive an expression for the midplane dose in terms of the geometric mean of the entrance and exit doses. Unfortunately, the above approaches do not appropriately model the scatter and are known to be unreliable in scenarios involving the asymmetric location of inhomogeneities about the midplane.

The importance of accounting for scatter behind the patient led to more sophisticated 2D models for calculating the dose inside the midplane. Boellaard *et al* developed a convolution algorithm for converting the 2D transmitted dose behind the patient to the exit dose and later the midplane dose. Other back-projection techniques have also been proposed and more recently have evolved into reconstructing 3D dose distributions inside the patient. However, overcoming problems of calculating the dose in regions of electronic

disequilibrium and regions consisting of asymmetric heterogeneities are yet to be resolved.

An alternative approach to back-projection techniques is the "forward" prediction of the transmitted dose based on patient treatment planning data, which when directly compared with a measured transmitted dose distribution during treatment can reveal potential dosimetry errors occurring at the patient level. Accurate predictions of transmitted doses have become possible with the advent of 3D treatment planning systems and more recently Monte Carlo models that explicitly simulate particle transport.

Despite efforts in the literature for investigating transmission dosimetry as a potential method of dose verification, there is still a lack of widespread implementation in the clinic. However, understandably this is most likely attributed to the complexity and variety of available radiotherapy treatments, which most likely require investigation on a case-by-case basis. For example, certain combinations of patient geometry and delivery errors may affect the sensitivity of error detection at the transmitted dose level. In addition, the confounding effects of random variations in linear accelerator output or noise and calibration uncertainty associated with dose detectors could mask certain unknown dosimetry errors. Hence a proper evaluation of transmission dosimetry as a plausible technique requires a simulation of dosimetry errors in a controlled environment and in the absence of measurement uncertainties.

1.2 Aims of the current thesis

The principle aim of this work is to evaluate transmission dosimetry as an *in vivo* dosimetry technique from a theoretical standpoint for the purposes of simulating specific dosimetry errors in a controlled environment and in the absence of any experimental error. The investigation begins with the evaluation of a commercial treatment planning system used clinically in the radiotherapy department of the Royal Adelaide Hospital for its accuracy in modelling the transmitted dose (in a flat, homogeneous medium) relative to correspond-

ing measurements using a calibrated two-dimensional liquid-filled EPID. Although this is not the major focus of this work, it is important to establish the accuracy of the dose calculations before further evaluating the sensitivity of the dose calculations for a variety of simulated dosimetry errors. The resolution of the the transmitted dose calculations to dosimetric errors is evaluated in a systematic fashion beginning with flat homogeneous phantoms and progressing to more complex phantom geometries. The efficacy of transmitted dose in detecting dosimetry errors for three specific conformal radiotherapy treatment plans is finally investigated.

1.3 Thesis outline

Chapter 1 introduces the challenge of patient dose verification, the role of *in vivo* dosimetry in radiotherapy and the various techniques that have been developed.

Chapter 2 addresses the need for dosimetric verification in radiotherapy and discusses the strengths and weaknesses of the various techniques developed for *in vivo* dosimetry.

Chapter 3 evaluates the accuracy of a treatment planning system in modelling the transmitted dose relative to dose measurements with a calibrated liquid-filled EPID (under flat, homogeneous conditions) using isocentric and fixed SSD treatment setups. The noise characteristics in the dose calculations as a function of phantom thickness and the minimum detectable change in phantom thickness as detected by the dose calculations (within the determined noise level) at the transmitted plane, is also evaluated.

Chapter 4 investigates the resolution of the transmitted dose calculations in detecting the presence of small inhomogeneities on the central beam axis in a flat, homogeneous phantom, as well as the displacement of inhomogeneities perpendicular and parallel to the central beam axis. Relative shifts in phantom position and radiation field are simulated using cylinders (uniform density) of varying diameters to assess the sensitivity of the

calculations in differentiating between varying degrees of surface curvature. Studies are further extended using more realistic phantom studies by combining patient-like surface contours with heterogeneities.

In **Chapter 5** the sensitivity in the transmitted dose for detecting dosimetry errors for a 3D conformal four-field box prostate treatment is evaluated in the planning system using clinical patient CT data. Due to limitations of the planning system in calculating the transmitted dose for the EPID at distances used in our clinic, an in-house solution is provided by extending the volume of air surrounding the original CT data. Dosimetry errors caused by a difference in planned and delivered treatment geometries are simulated by displacing the position of the isocentre in the original plan. Discrepancies between transmitted dose distribution before and after introducing the shifts are evaluated in two-dimensions using the gamma formalism. A possible correlation between the calculated transmitted dose maps and midplane dose maps at the centre of the PTV is investigated. The impact of the dosimetry errors in terms of dose-volume histograms in the PTV and at critical structures is also investigated.

In **chapter 6** the sensitivity in the transmitted dose for detecting dosimetry errors in a 3D conformal head and neck treatment is evaluated in the planning system using clinical patient CT data. Random positioning errors varying in magnitude for single, multiple entire leaf banks were simulated. The accuracy of the planning system in modelling the transmitted dose on a rectilinear dose grid for the oblique beams is assessed.

Chapter 7 investigates the potential of transmission dosimetry for detecting patient breathing in breast 3D conformal radiotherapy. A conformal radiotherapy plan is used to simulate possible delivery errors related to respiratory motion in combination with certain setup errors. Shallow and deep breathing excursions between the breast and the beam tangents are simulated by displacing the isocentre along a medial-lateral axis perpendicular to the central beam axis. Gamma analysis at the transmitted dose plane and midplane

are performed to investigate a possible correlation in the observed dose differences. Dose-volume histograms are also evaluated to determine the potential magnitude of errors on the PTV, heart and lungs caused by breathing.

The thesis is concluded in **Chapter 8** with the discussion of possible avenues of further research.

Chapter 2

In vivo dosimetry in radiotherapy: A review

2.1 The need for dosimetric verification in radiotherapy

External beam radiotherapy destroys both unhealthy and normal tissue cells and therefore, ideally requires the sparing of normal tissue to prevent unnecessary harm to the patient, while destroying unhealthy tissue to prevent recurrence of the disease. In reality however, there are a variety of uncertainties in the radiotherapy chain which compromise this ideal. Uncertainties include (but are not limited to) outline of patient structures, patient positioning errors, accuracy of the planning system dose algorithm, absolute dose calibration of machine, random variations in linear accelerator output, mechanical accuracy of linear accelerator, variations in patient geometry from time of planning to time of treatment, and organ motion (internal and external). Due to such uncertainties national and international organisations [8–11] recommend *in vivo* dosimetry (verification of dose delivered to the patient) to be performed on a regular basis.

2.2 Techniques for *in vivo* dosimetry in external beam radiotherapy

The development of techniques for *in vivo* dosimetry in radiotherapy is an evolving process which aims to verify the dose delivered to the patient as efficiently and accurately as possible. In order to build upon previous and current techniques it is important to understand their strengths and weaknesses, which are described in the following sections.

2.2.1 Entrance and exit dosimetry

Although the most direct form of *in vivo* dosimetry is to physically place detectors inside the patient [12], this is only practical for naturally occurring cavities inside the body such as the mouth, vagina and rectum. The next closest approach is to measure the dose directly on the surface of the patient. Entrance dose measurements at the surface of patients are performed routinely in some centres during radiotherapy due to their simple preparation and setup on the surface of the patient [13–15]. However, they are effectively only useful for identifying some setup errors (such as incorrect patient Source-to-Surface Distance (SSD)) and variability in machine output. Furthermore, entrance dosimetry is usually performed with point detectors such as semiconductor diodes or Thermoluminescent Detectors (TLDs) which do not cover the entire radiation field, and can lead to possible dosimetry errors going undetected. Point dose detectors are especially unsuitable for Intensity Modulated Radiotherapy (IMRT) treatments to the large number of steep dose gradients occurring in the combined beam segments.

The exit dose, defined as the dose detected on the patient at the exit side of the beam, can potentially be used to identify changes in tissue thicknesses and detect inhomogeneities via changes in dose transmitted through the patient, in addition to the errors mentioned above [2].

2.2.2 Midplane dosimetry using the entrance and exit dose

Entrance and exit point dose measurements have been combined to determine a midplane dose inside the patient [1, 16–18]. Combined entrance and exit dose measurements have shown to be valuable for immediately identifying errors related to the inaccuracy of planning system dose algorithms (especially at inhomogeneities for 2D planning systems), fluctuations in linear accelerator (linac) output, setup errors and human error. However, a major drawback of the approach has been in the simplicity of the algorithms used to determine the midplane dose. In the various algorithms assumptions are made about the midplane dose which only yield reliable results under certain geometric and symmetrical (phantom) conditions [17]. These algorithms will be discussed in the following sections.

Method of Rizzotti *et al*

For a ^{60}Co beam, entrance and exit doses for a flat, homogeneous water phantom were measured for a range of phantom thicknesses and field sizes [16]. Midline dose from depth dose data in water was derived [19]. Plotting D_{mid}/D_{ent} and D_{ext}/D_{ent} together against phantom thickness for each field size, a one-to-one correspondence between the quantities was observed. An empirical curve of D_{mid}/D_{ent} versus D_{ext}/D_{ent} could then be used to derive the midplane dose from a phantom of a given thickness. The empirical relationship was found to be nearly independent of field size, SSD and either with or without the presence a wedge [20–22]. Leunens *et al* later adopted the method but instead used Tissue Phantom Ratio (TPR) data instead of depth dose data to derive midplane doses [17]. The accuracy of the method proposed by Rizzotti *et al* is known to be unreliable where the change in patient (or phantom) thickness is asymmetric about the midplane. For example, using an anterior-posterior (AP) and posterior-anterior (PA) field arrangement on a 20 cm thick phantom, thickness variations of $\pm$ 5 cm either side of the midplane were estimated to cause an error of 7 % in midplane dose [16].

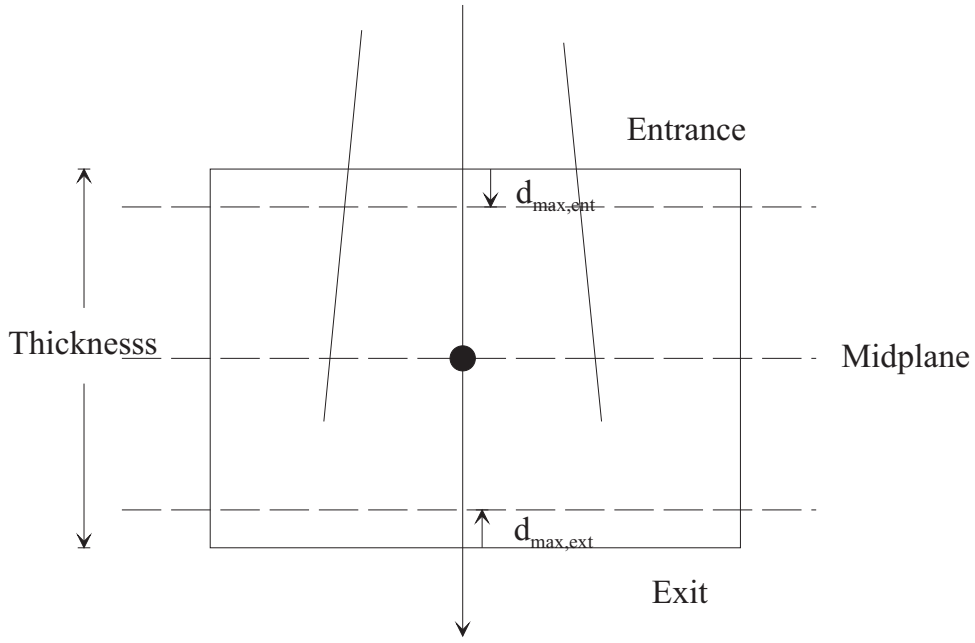

Figure 2.2.1: *The homogeneous water phantom geometry used by Rizzotti et al to determine the midplane dose from measurements of entrance and exit doses.*

Geometric mean method

Several authors have estimated the midplane dose from the geometric mean of the entrance and exit dose [1,18]. The geometric mean method assumes exponential attenuation of absorbed dose with depth (ignoring scattering effects), under homogeneous phantom conditions. Furthermore, in the presence of inhomogeneities, the total physical thickness can be converted into an effective water-equivalent thickness and the midplane dose determined, assuming that the inhomogeneities are symmetrically located above and below the midplane. However, the accuracy of the algorithm depends on the position of the inhomogeneities relative to the entrance and exit doses and their density relative to water due to differences in scatter contributions relative to a water-equivalent phantom. To account for the latter effect, Terrón *et al* implemented scatter corrections into the geometric mean method by fitting an empirical polynomial function to the ratio of measured and calculated midplane doses under homogeneous conditions [18]. The basic formula applied

in the geometric method is given by:

$$D_{mid} = \sqrt{D_{ent} D_{ext}}, \tag{2.2.1}$$

where D_{mid}, D_{ent} and D_{ext} are the midplane, entrance and exit doses, respectively. A more comprehensive formula for the geometric mean, derived by Huyskens *et al* [1] includes the inverse square law factor due to the difference in distances of the entrance and exit dose points relative to the beam focus, and is defined as follows:

$$D_{mid} = \sqrt{D_{ent} D_{ext}} \frac{F(+d/2)F(-d/2)}{(SAD)^2} \tag{2.2.2}$$

The inverse square correction is given by the variables $F(+d/2)$, $F(-d/2)$ and SAD where:

$$F(+d/2) = SAD + d/2 + d_{max},$$

$$F(-d/2) = SAD - d/2 + d_{max},$$

d is the total physical thickness, SAD is the source-to-axis (isocentre) distance and d_{max} is the depth of dose maximum.

In addition, Huyskens *et al* combined the entrance and exit point doses with 2D film dose measurements 20 cm behind the phantom to be able to calculate the dose throughout the entire 2D midplane of the phantom. The midplane dose on the central axis was corrected by off-axis correction factors, with the assumption that the off-axis ratios at the exit side of the phantom correlate well with off-axis ratios at the plane of the film [23]. Hence the midplane dose off axis, $D_{mid,y}$ at a distance y from the central axis is given by:

$$D_{mid,y} = \sqrt{D_{ent,y} D_{ext,y}} \frac{F(+d_y/2)F(-d_y/2)}{(SAD)^2}, \tag{2.2.3}$$

where

$$F(+d_y/2) = SAD + d_y/2 + d_{max},$$

$$F(-d_y/2) = SAD - d_y/2 + d_{max},$$

d_y is the total thickness of the phantom at a distance y, off-axis along the diverging ray line, and $D_{ent,y}$ and $D_{ext,y}$ are the respective entrance and exit point doses measured off-axis (figure 2.2.4).

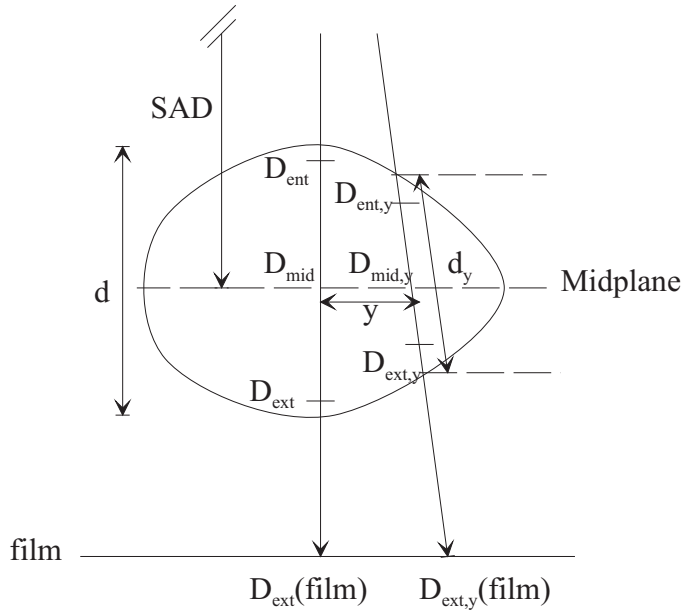

Figure 2.2.2: *A schematic representation of the phantom and variables used in the geometric mean method (figure courtesy of Huyskens et al [1]).*

The accuracy of geometric mean method proposed by Huyskens *et al* in determining the midplane dose for phantoms containing symmetric inhomogeneities has been reported to be within 5 %. The advantage in this method is that it can be used as a quick rule of thumb for estimating the midplane dose, however a clear disadvantage is the inaccuracy of the method when applied to phantoms (patients) containing asymmetrically positioned inhomogeneities with respect to the midplane.

2.2.3 Two-dimensional midplane dosimetry

Algorithms for determining the midplane dose at a single point were later extended to two-dimensions by correlating the 2D transmitted dose measured with film at a certain distance behind the phantom (patient) with a 2D dose at the exit surface of the pa-

tient. This in turn could then be used to determine a two-dimensional midplane dose distribution [1, 23, 24]. For measurements performed under various phantom geometries several authors have reported an agreement between exit dose derived from transmitted film dose measurements and measurements with diodes to be within 5-8 %. Inaccuracies were mainly attributed to approximations in scatter contributions for large phantom-to-detector distances and/or curvature in phantom geometry at the exit beam side. Under such conditions the correlation in off-axis ratios at the midplane and transmitted dose planes deteriorates due to the decrease in contribution of scattered dose relative to the primary dose contribution. This was shown to overestimate the dose near the edges of the field calculated at the midplane relative to measurements or TPS calculations at the midplane [23–25]. Alternatively, Broggi *et al* performed similar measurements of transmitted dose at smaller phantom-to-detector air gaps and also proposed a method that avoided applying inverse square law corrections used by previous authors for curved phantom surfaces at the exit plane [2, 26]. The patient contour was replaced by a flat, rectilinear phantom with a uniform thickness equal to that of the patient's on the central beam axis and a density that varied off-axis (figure 2.2.3).

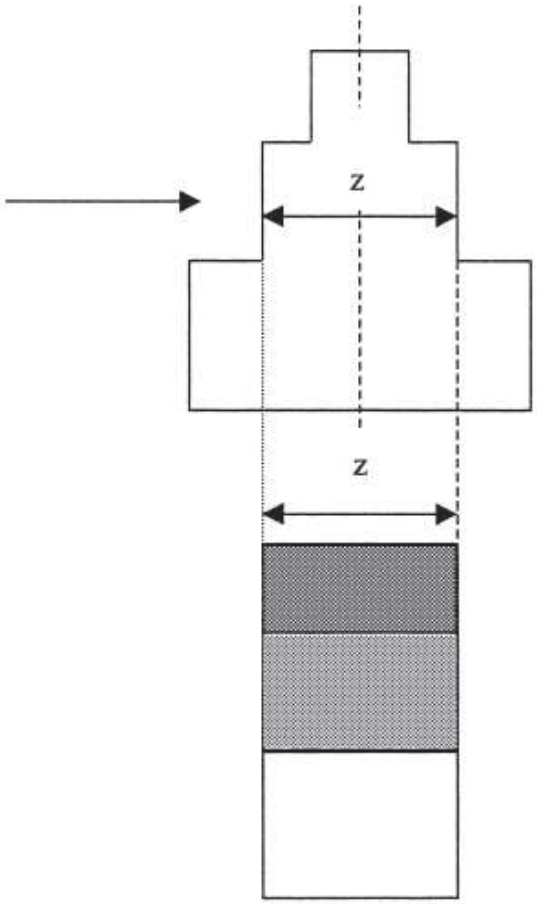

Figure 2.2.3: *A schematic of an equivalent rectilinear phantom (with varying off-axis density) used to represent a curved phantom geometry as proposed by Broggi et al. The beam entrance is indicated by the arrow located to the left of the figure (figure courtesy of Broggi et al [2]).*

For 6 MV photon beams incident on homogeneous phantoms (symmetric and non-symmetric) the agreement between estimated and measured midplane doses agreed within 3-6 % [2]. A later study by the same group of authors tested the accuracy of the algorithm on head and neck patient treatments. The dose measured at the midplane (as derived by the algorithm) was compared with corresponding planning system dose calculations and were found to be in agreement of within 5 % [26]. Limitations in the accuracy of the 'equivalent' phantom model become apparent in the presence of inhomogeneities. For example, midplane doses were shown to underestimate the dose for bony anatomy (or any high density medium) and overestimate the dose for air cavities (or other low density regions). A

further disadvantage of this approach is that its assumptions are valid at relatively small phantom-to-detector distances (< 15 cm) which can not always be measured by transmitted dose detectors such as Electronic Portal Imaging Devices (EPIDs) (see later). Some authors have taken advantage of this scenario by determining the midplane dose at large phantom-to-detector air gaps which tends to overestimate the true midplane dose, thus counterbalancing errors in the presence of bony anatomical structures [27, 28].

2.2.4 The transition from film to EPID

EPIDs were developed with the same intentions of film (for 2D portal imaging of patient treatment geometry) but with the advantage of real-time image acquisition, easy electronic storage and image enhancement capabilities. The natural progression of experimenting with EPIDs for exit dosimetry [29, 30] and later midplane dosimetry soon followed (as discussed in the following sections). Since their inception, various types of EPIDs have been designed [31–35] which has led to widespread investigations as potential 2D dosimeters [31, 36–42]. For a good review of the history and technology of portal imaging devices the interested reader is referred to the following references: [43–47].

Kirby and Williams [30, 48] were one of the first authors to use an EPID for determining exit doses of phantom and patients. The authors initially configured a fluoroscopic EPID as an integrated dosimeter [30] using 6 MV photons and determined an empirical relationship between exit dose measured with diodes and transmitted dose measured with the EPID based on homogeneous phantom measurements performed for a variety of thicknesses and patient-to-EPID air gap distances. Precise patient-to-EPID air gap distances were determined by attaching a brass ring of known dimensions to the exit surface of the phantom and measuring the dimensions of the ring in the EPID images to determine the air gap distance. In a following paper [48], more elaborate measurements were performed using 20 MV photon beam and determining an empirical relationship between exit and EPID dose for a variety of homogeneous phantom thicknesses, air gap distances and field

sizes. The empirical data was tested on a variety of irradiation geometries using an anthropomorphic phantom as well as on patients undergoing radiotherapy. The measured and estimated exit doses agreed to within 8 % under the heterogeneous phantom conditions and ± 7 % for the patient studies (which are both unacceptable according to the ± 5 % recommendation of the International Commission on Radiation Units and measurements (ICRU) [8]). The main shortcoming of the exit dose model was its failure to accurately predict the exit dose under asymmetric scatter conditions.

2.2.5 Midplane dosimetry: 2D back-projection techniques

Previous approaches of calculating 2D midplane doses were only accurate for small air gap distances (eg 10 cm) between the exit surface of the patient and the transmitted dose plane and did not take into account the decrease in scatter contributions for larger sized air gaps. Furthermore, if EPIDs are to be used for exit and midplane dosimetry, such models need to be adjusted for the extended distances from the beam focus and patient for which EPIDs are installed. As a consequence, Boellaard *et al* developed a convolution model for converting transmitted doses to exit doses more accurately at larger phantom-detector air gaps ($\sim$ 50 cm) [3]. The central idea behind the convolution model is to explicitly separate the exit dose into the primary and scattered components:

$$E_{calc}(i,j) = P(i,j) + S_{calc}(i,j), \tag{2.2.4}$$

where $E_{calc}(i,j)$ is the total dose calculated at the exit surface of the phantom/patient, corresponding to the EPID pixel position i,j, $P(i,j)$ is the (measured) primary dose at the exit surface at pixel position i,j, and $S_{calc}(i,j)$ is scattered dose calculated at the exit surface at pixel position i,j. The primary dose at the exit surface of the phantom, $P(i,j)$ was obtained by subtracting the small constant scatter contribution from the total transmitted dose measured at an air gap of 90 cm [1]. The primary dose at the exit

[1]This is possible since at sufficiently large air gaps (> 50 cm) the scattered dose distribution is nearly constant across the EPID and can be subtracted from the total transmission signal.

surface is then obtained by applying a simple inverse-square law factor and taking beam divergence into account. The scattered dose, $S_{calc}(i,j)$ at the exit surface was calculated by convolving the primary exit dose with an exponential function termed, the Exit Dose Spread Function[2] (EDSF). Namely,

$$S_{calc}(i,j) = P(i,j) \otimes EDSF(r), \tag{2.2.5}$$

where

$$EDSF(r) = \begin{cases} N \ \frac{e^{-\mu x r}}{r^q}, & \text{for } r \geq 0.127 \text{ cm} \\ N, & \text{for } r < 0.127 \text{ cm} \end{cases}, \tag{2.2.6}$$

where r is the radial distance from the central ray path, at the exit surface, μ is the total linear mass attenuation coefficient of water, q is a dimensionless constant, and N is a normalisation constant. Finally equation 2.2.5 is multiplied by a scaling factor, $NSPR(T(i,j))$ to account for the variation of scatter with phantom thicknesses:

$$NSPR(T(i,j)) = \frac{SPR(T(i,j))}{SPR(T_{20}(i,j)}, \tag{2.2.7}$$

where $SPR(T(i,j))$ is the Scatter-to-Primary Ratio of transmissions, $T(i,j)$ at the exit surface (for pixel position i,j), through the total thickness of the phantom, and $SPR(T_{20}(i,j)$ is the corresponding Scatter-to-Primary Ratio for a reference phantom thickness of 20 cm. The parameters q, N and $NSPR(T(i,j))$ are determined by fitting $EDSF(r)$ to measured data.

The agreement between exit dose calculated with the convolution model compared with the exit dose measured with an ionisation chamber for an 8 MV photon beam, under homogeneous and inhomogeneous phantom geometries was found to be within 2.5 % [3]. However, for low beam energies (eg 4 M V) the model was found to be unreliable in the presence of large inhomogeneities with errors of up to 7.5 % [49]. As a result an additional

[2]Defined for a given phantom thickness.

geometric factor, G was introduced to improve the accuracy of the convolution model:

$$G = \frac{SPR(Th(i,j))}{SPR(Z(i,j))}, \tag{2.2.8}$$

where $Th(i,j)$ is the actual thickness of an inhomogeneous phantom at each pixel position i,j and $Z(i,j)$ is the thickness of an equivalent homogeneous phantom at each pixel position i,j, with the same radiological thickness (figure 2.2.4). The geometric factor accounts for the difference in the nature of scatter between a real inhomogeneous phantom and a homogeneous phantom with the same radiological path length used in the model. For various heterogeneous phantom and patient studies using 4 MV photons, inclusion of the geometric factor was found to improve the accuracy of the results from 7.5 % to within 1.7 %.

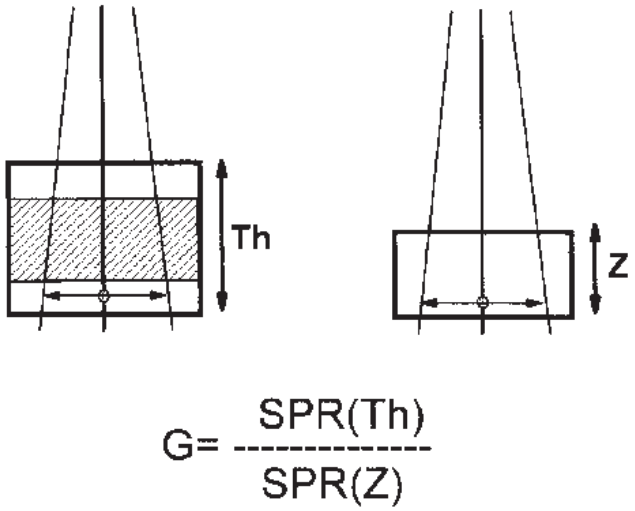

Figure 2.2.4: *A schematic of the phantoms used to determine the geometric factor, G. SPRs are measured at the exit surface of an inhomogeneous phantom with a symmetrically placed inhomogeneity, and an equivalent homogeneous phantom with the same radiological thickness (figure courtesy of Boellaard et al [3]).*

Despite the improved accuracy in the model systematic errors were expected to remain as the model does not take into account the different scatter conditions between scenarios for which inhomogeneities are located at different locations along the beam axis [3].

The convolution model used to determine the 2D exit dose from the 2D transmission measured by the EPID was naturally extended by the authors for calculating the 2D dose at the midplane [22]. The midplane dose was derived from the exit dose by applying three corrections. Firstly, an inverse-square law term is applied to account for beam divergence between the midplane and exit plane:

$$ISL = \frac{(SSD + Th(i,j) - d_{max})^2}{(SSD + Th(i,j)/2)^2}, \tag{2.2.9}$$

where $Th(i,j)$ is defined previously, and d_{max} is the depth of maximum dose. Secondly, attenuation in the primary beam between the two planes is corrected for:

$$e^{\mu(Z(i,j)/2 - d_{max})} = \frac{e^{-\mu d_{max}}}{\sqrt{T}(i,j)}, \tag{2.2.10}$$

where the variables μ, $Z(i,j)$ and $T(i,j)$ are as defined previously. The third and final correction accounts for the difference in scatter contribution between the midplane and exit planes:

$$\frac{1 + SPR_{mid}(i,j)}{1 + SPR_{exit}(i,j)}, \tag{2.2.11}$$

where $SPR_{mid}(i,j)$ and $SPR_{exit}(i,j)$ are the scatter-to-primary ratios at the midplane and exit plane (at each pixel position i,j), respectively. Combining all three corrections with the exit dose calculated using equation 2.2.4 (along with the geometric correction in equation 2.2.8) yields the following equation for calculating the midplane dose:

$$D_{mid}(i,j) = E_{calc}(i,j)\,(ISL)\left(\frac{e^{-\mu d_{max}}}{\sqrt{T}(i,j)}\right)\left(\frac{1 + SPR_{mid}(i,j)}{1 + SPR_{exit}(i,j)}\right). \tag{2.2.12}$$

The midplane model proposed by Boellaard *et al* was assessed against the geometric mean method (of Huyskens *et al* and of Terrón *et al*) and the method of Rizzotti *et al* using 4, 8 and 18 MV beams for a variety of test phantoms [22]. It was found that the the method of Boellaard *et al* was at least as accurate as the other methods for predicting the midplane dose in each of the phantoms. In particular, the former method was superior in

accuracy than the other methods for phantoms in the presence of large inhomogeneities. The applicability of the midplane dose model in the clinic was further assessed for various treatment sites including the larynx, breast, lung and prostate [50]. In such cases the predicted midplane doses were compared with corresponding 2D midplane doses calculated by a 3D treatment planning system. Across all treatment sites, on average the agreement was generally within 2.5 % with larger dose differences of up to 10 % due to identified differences between planning and treatment anatomy. Discrepancies between measured and calculated midplane doses of up to 5 % were observed in regions containing asymmetric inhomogeneities (eg near the pelvic bone) or in regions of electronic disequilibrium (eg along the edge between the lung and mediastinum), neither of which are taken into account by the model.

More recently, the original convolution model of Boellaard *et al* was extended for other EPID types such as the a-Si based EPIDs. In particular, additional kernels were applied to account for the unique response of the a-Si EPID as well as lateral scatter effects occurring within the EPID itself. Corrections were also made for improving the accuracy of the model in the beam penumbra regions. For a detailed mathematical discourse, the interested reader is referred to the work by Wendling *et al* [51]. Other recent related work involved extending the convolution model (effectively a 2D dose reconstruction model) into a 3D dose reconstruction model applied to more complex scenarios such as breast irradiations [52] as well as dose reconstruction at critical organs such as the heart [53]. Modifications such as the inclusion of patient contour information were included and were found to significantly improve the results. Furthermore, the model was modified to account for scenarios in which the radiological midplane does not coincide with the isocentre plane (such as in breast treatments) as was implicitly assumed in the original model.

Finally, an alternative approach to all *in vivo* dosimetry techniques discussed above was proposed by Bogaerts *et al*. Rather than determining the exit or midplane dose from the transmitted dose measured in a plane behind a phantom/patient, the authors calculated the dose at the transmitted dose (termed *transit* dose) plane from the exit dose at the

surface of the phantom. This was achieved by extracting the primary component of the exit dose calculated by the planning system and deriving an empirical based function to independently model the scattered dose component [54]. The motivation behind the approach was to derive a more simpler algorithm than used in previous approaches by using an analytical scatter function that was independent of phantom thickness and a single line of best fit parameter that described scatter under multiple combinations of field sizes and phantom thicknesses. The predicted transit dose behind a given phantom were compared with corresponding film dose measurements. The model was tested on a breast phantom geometry using opposing 6 MV beams and showed agreement with measured transit doses of within 4.5 %. Discrepancies of 4–8 % were observed for clinical breast patient studies. Deviations of 5 % or more were believed to be caused by changes in patient breast thickness between planning and treatment phases.

The same authors also sought to investigate under what circumstances (in particular, for 6 MV photons irradiating an irregular phantom geometry) do transit dose beam profiles sufficiently correlate with exit dose profiles to eliminate the need for sophisticated scatter models. In order to investigate this further, various phantom geometries were considered; A flat inhomogeneous phantom and a homogeneous phantom with oblique edges were firstly used to separate the influence of inhomogeneities and varying thickness on the relative change in dose profiles, followed by a phantom with the above combined features. The exit dose profiles (measured with a scanning ionisation chamber) and transit dose profiles (measured with film) were superimposed, normalised on the central axis and corrected for beam divergence to achieve a relative comparison. Measurements were also tested on a clinical head and neck patient treated with 6 MV photons. The authors concluded that for a patient presenting a variable thickness across the radiation field, simply correcting the transit dose profile using the classical inverse-square law (ISL) provides a good estimate of the dose profile at the exit surface of the patient, provided that the transit dose plane is located close to the exit surface of the patient. Furthermore, the transit dose profile can also be used to estimate the exit dose profile (ie no ISL applied) provided that the transit dose is measured at a large distance (20–30 cm) behind the

patient. The authors claimed that the combined influences of scatter and the effect of the ISL on the dose profiles tend to cancel each other out. That is, for certain treatment geometries (eg head and neck irradiations with 6 MV photons), the Gaussian shaped distribution of scattered dose at large distances compensates for the ISL effect between the midplane and exit planes, thus requiring no additional correction factors. The accuracy of the assumptions were found to be within 3-5 %.

2.2.6 Alternative back-projection techniques

Hansen *et al* proposed a similar method for reconstructing 3D dose inside the patient based on primary fluence (as opposed to dose) extracted from measured EPID images. Furthermore, since the dose calculations were based on planning CT data the authors applied rigid body transformations to the planning CT data to correct for possible translations or rotations introduced at treatment time. This was achieved by registering EPID images acquired during treatment with Digitally Reconstructed Radiographs (DRRs) calculated from the CT data. The model does not account for non-rigid transformations such as tissue deformations, tumour growth or shrinkage, bladder and/or rectal filling and weight loss or gain, for example. The radiological thickness of the phantom/patient was derived from the EPID images using a quadratic calibration method relating EPID image intensity to radiological thickness [33]. Monte Carlo simulations of SPRs were performed and were used to derive a simple relationship between SPR, field size and radiological thickness for a 6 MV beam beam [55]. This allowed the primary fluence at the EPID to be derived by separating the total image intensity into the primary and scatter components. The primary fluence is then back-projected at each point inside the CT data taking beam divergence into account. The total dose is obtained through a convolution of the Total Energy Released per unit Mass (TERMA) with energy deposition kernels. The accuracy of the dose calculations inside a humanoid phantom were found to be within 2 % relative to TLD and film measurements. Following Hansen *et al's* original paper improvements and modifications were made to the procedure for extracting the primary fluence and

simulating the SPRs, for example [55, 56].

In a following paper Hansen *et al* proposed an alternative method to previous back-projection methods by using an interative forward process of evaluating the primary signal with the initial condition that the total transit signal at the transit plane is equal to the primary signal. The original MC code used to calculate SPRs [55] was also modified to be valid in the presence of inhomogeneities. For simplicity and time-efficiency, a circularly symmetric convolution pencil-beam scatter kernel was chosen in determining the scattered signal component. However, in reality this would not precisely describe the spread of scatter near an inhomogeneity, which would most likely be asymmetric in nature. A similar iterative procedure for reconstructing the incident signal at the transit level was also proposed [57]. Another iterative dose reconstruction method which incorporated the convolution/superposition algorithm was developed [58] and tested in the presence of simulated noise and using multi-field treatment plans and patient CT data [59]. Elaborate back-projection techniques incorporating Monte Carlo dose deposition kernels and convolution/superposition (C/S) algorithms for reconstructing 3D doses inside CT data sets were also independently developed by McNutt *et al* [58, 59]. Based on an iterative C/S algorithm developed by the authors an accuracy of 3 % was obtained between the reconstructed dose and forward planned dose (calculated by the planning system) for homogeneous and anthropomorphic phantoms irradiated by 6 MV beams.

Modelling the scatter itself has become a dedicated field of investigation [55, 60–63]. This has also branched out to the field of modelling of specific detector response of EPIDs [64] which is intrinsically linked to modelling the scatter at the transmit plane [55]. This is especially important with the current variety of EPID detector types.

2.2.7 Transmitted dose prediction

A more simple, direct approach to *in vivo* dosimetry is to compare the 2D transmitted dose measured during treatment with a corresponding predicted transmitted dose based

on the planned treatment. Any discrepancy found between the measured and predicted transmitted doses would imply a dosimetry error. The efficacy of this approach requires both an accurate dose calibration of a two-dimensional detector (preferably an EPID) and an accurate dose algorithm to model the transmitted dose. Furthermore, there is still contention on limitations of 2D transmission dosimetry in being able to account for 3D dose errors inside the patient. Transmission dosimetry can in principle be performed with any detector type (EPID, film or a 2D diode array, eg) provided that it is appropriately calibrated under clinical conditions relative to a gold standard (such as ionisation chamber dose measurements performed in water).

The 3D Delta Volume algorithm

The fact that treatment verification using portal images was limited to only geometric aspects of verification (namely patient setup) motivated Wong *et al* to extend the concept of a *portal image* to a *portal dose image* (PDI) [65]. The need for portal dose imaging was apparent as treatment errors such as an incorrect wedge orientation in the linac head or wrong compensating filter are not detected in port films or in EPID images in which software automatically corrects for optimal image quality resulting in a loss in dosimetric information. As a result the authors implemented a 3D Delta Volume (DV) algorithm, originally developed for computing 3D photon doses for ^{60}Co beams [66], to be able predict PDIs for comparison with PDI measurements. The feasibility of predicting PDIs using the DV algorithm was tested under a variety of scenarios including a rectilinear "modular" phantom, an anthropomorphic phantom, and a lung patient. The predicted PDIs were compared against PDI measurements consisting of TLDs, scanned ionisation chamber dose profiles and 2D film measurements. For the two phantom studies a general agreement of 3 % was achieved, provided the alignment between measurement and calculation were reproduced. For the lung phantom discrepancies of 5–10 % were encountered and may have been due to patient positioning errors or changes in patient anatomy. In a companion paper by Ying *et al* an iterative CT correction model was proposed for cal-

culating the 3D dose based on the patient geometry at the time of treatment [67]. As previously, PDIs predicted with the Delta Volume algorithm were compared with measured PDIs, but if differences above a certain tolerance were exceeded then the original CT data was modified and the predicted PDIs were recalculated using the updated CT data set. The process was repeated in an iterative fashion until a reasonable agreement (within 3 %) between the predicted and measured PDIs was attained. The 3D Delta Volume algorithm was then applied to provide a dose distribution (based on the updated CT data) that would have been received by the patient at the time of treatment. Although the concept of adaptive CT correction is a very interesting and potentially useful one, the procedure can become very complex when applied to clinical patient CT data. In the above study, CT corrections were specifically designed for a simple, in-house lung phantom geometry with specific corrections and assumptions made. Currently, the work has not been extended to other treatment sites nor tested on patient CT data.

In summary, the Delta Volume algorithm itself is based on applying corrections to dose measurements performed in a water phantom. In the presence of inhomogeneities, the change in absorbed dose relative to water is accounted for by using an average density scaling method [66,68]. This approach is only valid for small inhomogeneities where contributions of first order scatter dominate any higher-order scatter components. For larger inhomogeneities, and hence at large distances away from the primary interaction site, secondary scatter contributions become comparable to first order scatter and hence become more important. The path lengths of the secondary scatter are substantially different from those of the primary scatter and hence the average density scaling greatly overestimates or underestimates the local densities. This can effectively overestimate or underestimate the absorbed dose immediately below the inhomogeneities inside the phantom by up to 50 % [69]. Hence, the Delta Volume algorithm is not recommended for performing dose calculations involving phantoms with large air gap separations and in particular for predicting the transmitted dose at extended distances [5, 64, 70].

The convolution/superposition algorithm

The convolution/superposition (C/S) algorithm was originally developed as a dose engine for 3D treatment planning systems and is currently employed by several planning systems such as Pinnacle^3. Like Wong *et al* with the DV dose algorithm, McNutt *et al* investigated the accuracy of the C/S algorithm for predicting 2D transmitted dose distributions [70]. The algorithm was tested for homogeneous and heterogeneous phantoms and compared against relative film and liquid-filled EPID dose measurements. The agreement between the measured and predicted dose distributions was generally within 4 % for all phantoms, however larger differences of 6–10 % were observed with 6 % differences occurring in the homogeneous water phantom and 10 % differences for a Rando Thorax phantom. Unlike the Delta Volume method, the C/S method can be applied to scenarios involving large inhomogeneities by adopting kernel scaling techniques (see below). This also allows transmitted dose to be calculated at a given distance behind the phantom, which is incorporated as a large (air) "inhomogeneity" correction in the model [71]. Although not explicitly quantified, the accuracy of the model is claimed to improve with increasing air gap as the dose contribution from first scatter photons relative to higher-order scatter increases at larger air gaps [70, 72].

Due to the wide application of convolution integrals in radiotherapy and other related fields, a brief account of the theory involved in the convolution/superposition algorithm will be given.

The convolution of two functions $f(x)$ and $g(x)$ is defined as [73]:

$$f \otimes g = \int_{-\infty}^{\infty} f(x')g(x - x')dx' \tag{2.2.13}$$

Similarly, the dose, $D(\mathbf{r})$ at a point, $\mathbf{r}$ inside a homogeneous medium (figure 2.2.5) may be expressed as the convolution of the TERMA, $T(\mathbf{r}')$ with an energy deposition kernel, $K(\mathbf{r} - \mathbf{r}')$ [4]:

$$D(\mathbf{r}) = \int_{\mathbf{r}'} T(\mathbf{r}')K(\mathbf{r} - \mathbf{r}')d^3\mathbf{r}', \tag{2.2.14}$$

where

$$T(\mathbf{r}') = \frac{\mu}{\rho}(\mathbf{r}')\Psi(\mathbf{r}'),$$

and $\frac{\mu}{\rho}(\mathbf{r}')$ is the mass attenuation coefficient defined at each position $\mathbf{r}'$, and $\Psi(\mathbf{r}')$ is the energy fluence of primary photons. To combine the primary and scattered doses, the kernel is usually further separated into primary and scatter kernels. Energy deposition kernels are usually derived from Monte Simulations of photons forced to interact at the centre of a spherical water phantom [72]. It is important to note that the kernel in equation 2.2.14 is a function of displacement only and is therefore spatially *invariant* [3]. In an inhomogeneous medium, the dose deposition will also depend on the position of the interaction site, hence convolution based calculations are more suitable for homogeneous media. However, an advantage of such convolution calculations in homogeneous media is that they can be performed in Fourier space with a significant reduction in computation time [74].

A calculation of the dose in an inhomogeneous medium would in principle require Monte Carlo simulations of dose deposition kernels for each heterogeneity encountered. To avoid such rigour, Mackie *et al* adopted a technique known as *kernel scaling* [75]. Kernel scaling is based on the assumption that the energy loss by electrons in a medium scales inversely with the electron density in the medium [76]. That is to say, the number and energy of electrons in traversing any combination of heterogeneities will be the same if the total effective path length across the heterogeneities is the same [4]. Although this assumption is invalid for higher order electron scatter (since the fluence and energy of multiply scattered electrons change significantly), the errors are small due to the small contribution of multiply scattered electrons to the overall dose. The convolution in an inhomogeneous medium can be expressed as [4]:

$$D(\mathbf{r}) = \frac{1}{\rho(\mathbf{r})}\int_{\mathbf{r}'} T(\mathbf{r}')\rho_e^w(\mathbf{r}')K(\rho_{avg}, \mathbf{r}-\mathbf{r}')\left(\frac{\rho_e^w(\mathbf{r}')}{\rho_{avg}}\right)d^3\mathbf{r}', \tag{2.2.15}$$

[3] A convolution with a *non-invariant* kernel is called a superposition.

NOTE: This figure is included on page 28 of the print copy of the thesis held in the University of Adelaide Library.

Figure 2.2.5: *Geometry used in the convolution/superposition algorithm. The primary interaction site and dose deposition site are represented by vectors* **r**' *and* **r** *(relative to the surface), respectively (figure adapted from Metcalfe et al [4]).*

where $\rho(\mathbf{r})$ is the electron density at r, ρ_e^w (**r**') is the electron density relative to water at **r**' and ρ_{avg} is the average density given by:

$$\rho_{avg} = \frac{1}{|\,\mathbf{r} - \mathbf{r}'\,|} \int_{\mathbf{r}'}^{\mathbf{r}} \rho(\mathbf{r}'')d\mathbf{r}''$$

Hence in convolution/superposition based planning systems calculations may be performed quickly using a convolution (homogeneous correction) or more rigorously using a superposition (heterogeneous correction).

In-house models for transmitted dose prediction

Not all treatment planning systems are capable of accurately computing the transmitted dose at large air gaps between the patient and transmitted dose plane. This was the main motivation of Pasma et al to develop an in-house algorithm for predicting the transmitted dose for a fluoroscopic type EPID positioned at a fixed beam focus-to-detector distance of 160 cm, [5, 77] which translate to patient-to-detector air gaps of 30-50 cm. Such an approach provides additional versatility in the distance of the predicted transmitted dose

plane, compared with that of McNutt *et al*, which is restricted to the CT volume. Pasma *et al* adapted a pencil beam algorithm [78, 79] for predicting the transmitted dose:

$$D_{EPID}(x,y) = T(x,y)D_{EPID,0}(x,y), \tag{2.2.16}$$

where $D_{EPID}(x,y)$ is the dose predicted dose at (x,y) in the plane of the EPID, $T(x,y)$ is a transmission function based on measured data (open beam) in a water phantom, and $D_{EPID,0}(x,y)$ is the predicted dose in the absence of a patient at the corresponding position (x,y). Note that transmission data for $T(x,y)$ are measured separately for primary and scattered components:

$$T(x,y) = T^P(x,y) + T^S(x,y), \tag{2.2.17}$$

where

$$T^P(x,y) = C_{open}(r_{x,y}, t_{x,y})P(t_{x,y}),$$

and $C_{open}(r_{x,y}, t_{x,y}) = P(r_{x,y}, t_{x,y})/P(t_{x,y})$ is a correction factor to account for the change in primary transmission off-axis (due to change in beam quality away from the central axis), and $P(t_{x,y})$is a primary transmission function obtained from measured total transmissions on the central axis for a variety of fields sizes, extrapolated back to zero field size. The transmission scatter function, $T^S(x,y)$ is calculated as follows:

$$T^S(x,y) = \int_{(x,y)\varepsilon field} \frac{f(r_{x',y'})}{f(r_{x,y})} s(r_{(x'-x,y'-y)}, t_{x',y'}, L_{x',y'})dx'dy', \tag{2.2.18}$$

where $s(r_{(x'-x.y'-y)}, t_{x',y'}, L_{x',y'})$ is a scatter kernel defined at a distance, $r_{(x'-x,y'-y)}$ away from the central beam axis that contribute to the scatter at (x,y), $f(r_{x',y'})$ and $f(r_{x,y})$ are derived functions of fluence beam profiles at (x',y') and (x',y'), respectively, and $t_{x',y'}$ and $L_{x',y'}$ are defined below. In particular, the functions $f(r_{x',y'})$ and $f(r_{x,y})$ were obtained from a measured, large field diagonal profile that was modified at the penumbras to obtain fluence. For derivation of the scatter kernels the reader is referred to [5]. All transmission

dose measurements were performed on a flat, homogeneous polystyrene phantom using an ionisation chamber. Transmitted dose predictions for anthropomorphic phantoms were carried out by converting the CT data into a virtual Equivalent Homogeneous Phantom (EHP) with a density equivalent to that of polystyrene but varying in thickness such that the thickness along each ray line (as projected onto the central axis) was equivalent to the radiological thickness of the phantom (figure 2.2.6).

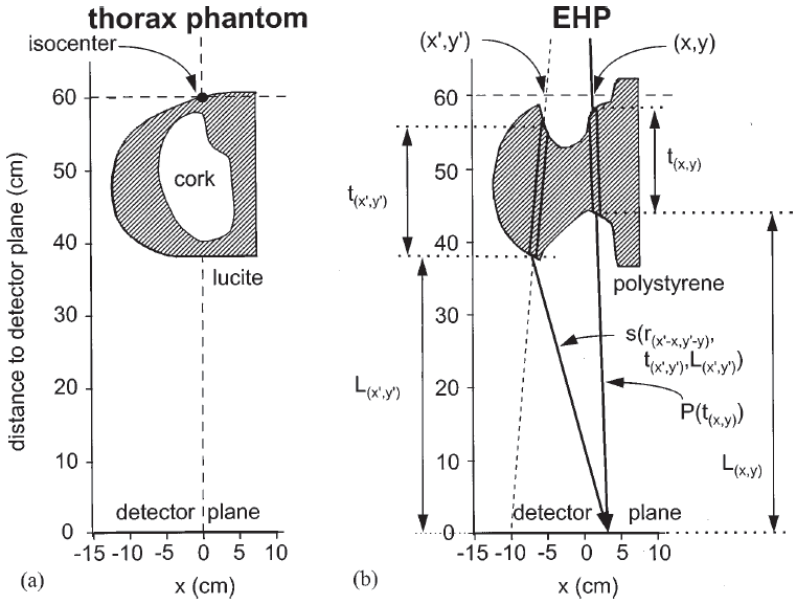

Figure 2.2.6: *Schematic of the anthropomorphic phantom ("thorax" phantom) and the corresponding virtual EHP used to predict the transmitted dose. The variables $t_{x,y}$ and $L_{x,y}$ correspond to the polystyrene thickness of the EHP along a beam ray-line at (x, y) and the distance from the exit surface of the EHP to the transmitted dose plane, respectively (figure courtesy of Pasma et al [5]).*

The accuracy of the predicted transmitted dose compared with corresponding fluoroscopic EPID dose measurements for the thorax phantom was found to be of the order of 1 % [5]. The algorithm was later extended for performing calculations in the presence of wedges and reported a similar accuracy of about 1 % [77]. The original algorithm of Pasma *et al* was further modified by Van Esch *et al* for predicting the transmitted dose for an a-Si EPID (for pre-treatment verification of dynamic IMRT fields) [80] and has since

been made available for commercial use in the Cadplan and Eclipse treatment planning systems.

More recently, van Elmpt *et al* adapted the PDI prediction model of Pasma *et al* to be able to extract the radiological thickness of the patient/phantom for the purposes of 3D dose reconstruction or even reconstruction of incident fluence infront of the patient as developed by previous authors [81]. In addition, the set of measurements required to derive analytical scatter kernels were reduced compared with those of Pasma *et al* by using a single midplane-to-detector distance and applying a scaling factor to account for other distances. Measurements were also performed under full-scatter conditions with an EPID rather than with ion chamber measurements as used by Pasma *et al*. However, the accuracy of the model adapted by van Elmpt *et al* depends on inhomogeneities inside phantom being symmetric about the midplane. This assumption along with additional simplifications of the original model yield a slightly lower accuracy in PDI prediction compared with that of Pasma *et al*. For various flat, inhomogeneous phantom geometries differences in measured and predicted transmitted doses differed by about 3 %.

McCurdy and Pistorius developed an algorithm for predicting transmitted dose distributions in EPIDs of arbitrary atomic (Z) composition, applicable over a wide range of air gaps and beam energies [64]. Their approach was essentially a Monte Carlo (MC) analogue of the empirical approach taken by Pasma *et al*. Primary and scattered photon fluence were modeled separately [63]. Incident energy spectra were first generated generated from Monte Carlo simulations of the linac head [82,83]. The primary fluence was ray traced through EHPs (converted from the original CT data) from which the radiological path length for each ray line was derived [84]. Using the radiological path length, exponential attenuation in the primary photon fluence was calculated to obtain the primary photon fluence at the detector plane. Radially symmetric scatter kernels were generated from MC simulations [85] for a variety of slab thicknesses (1–50 cm) and air gaps (0–100 cm) [62]. Absorbed dose at the detector was obtained by convolving the photon fluence with detector specific dose deposition kernels for each energy bin of the incident energy

spectrum [85, 86]. In particular, due to the relative increase in response of scattered low photon energies to high Z materials inside the detector, polyenergetic scatter kernels were incorporated rather than monoenergetic kernels. Off-axis spectrum softening was also included in the model by calculating radiological path lengths through the flattening filter and appropriately re-weighting the central axis incident primary photon fluence spectrum. Factors affecting the accuracy of the scattered photon fluence as predicted by the pencil beam algorithm were discussed in depth by the authors [63]. Firstly, the pencil beam algorithm over-estimated the multiple scatter fluence component (especially for larger field sizes) since the library of scattered photon fluence was generated (using MC) for semi-infinite phantom geometries. For the same reason this also reduced the mean photon energy of multiply-scattered photons. However, this effect is somewhat balanced out by the low relative response of low Z EPID detectors to low energy photons. For half-slab phantom geometries, the pencil beam algorithm underestimated single scattered photon fluence due to MC simulations in a semi-infinite phantom geometry in which the single scattered photon kernels are radially symmetric about the incident pencil beam. This caused the single scattered photon fluence to be over-attenuated compared with those exiting the face of a half-slab phantom geometry. However, a follow-up study addressed these issues by re-calculating the scattered fluence kernels using cylindrical water slabs of a finite radius [87]. A disadvantage of the EHP concept used by McCurdy and Pistorius for converting phantom CT data into water-equivalent homogeneous phantoms, is that it shifts the position of the mean scatter source which causes either an overestimate or underestimate of the scattered photon fluence and is analogous to the effect caused by average density scaling in CT data [69]. Under a variety of phantom geometries (homogeneous and inhomogeneous) the maximum discrepancy between the predicted and MC simulated scatter fluences were 6.9 % for a mediastinum phantom irradiated by a 6 MV photon beam. However, by reducing the air gap distance between phantom and EPID the majority of errors were found to be within 3% for all phantom geometries.

Dahlgren *et al* adapted the collapsed-cone superposition algorithm [88] used in the Helax-TMS and Oncentra treatment planning systems (Nucletron Scandinavia AB, Uppsala,

sweden) for performing transmitted dose calculations in a water-equivalent detector phantom [89]. The calculated dose at the detector phantom was normalised to the measured dose per monitor unit inside a phantom under standard dose calibration conditions. This was achieved using the dose-to-energy fluence formalism [90]. Calculations were performed for both 6 MV and 15 MV photon beams and compared with MC simulations and ion chamber dose measurements. For both the collapsed-cone and MC calculations, the transmitted dose was calculated separately as a "Patient Energy Released" (PER) dose and a "Detector Energy Released" (DER) dose. For the 6 MV beam, the C-C calculations tended to over-estimate the dose (relative to measurements) for small field sizes (5 $\times$ 5 cm) by up to 3 % and under-estimate the dose by 1–1.5 % for the larger field sizes (25 $\times$ 25 cm). A similar trend was observed for the 15 MV beam, with slightly larger differences within $\pm$ 3–4 % for the smaller and large field sizes. A comparison of C-C and MC simulations for 6 MV photons showed an underestimation in C-C transmitted dose of up to 3 % for the combination of a large field size of 20 $\times$ 20 cm and small air gap (10 cm). For the 15 MV beam, C-C calculations were generally lower (by up to 2.5 %) than predicted by MC, particularly for the larger field sizes. The discrepancy is partly attributed to the average density scaling used in the collapsed-cone calculations [69, 91] which showed a clear underestimate (up to $\sim$ 50 %) in C-C dose calculations (relative to MC) for nearly all depths in PER primary depth dose curves, for both 6 and 15 MV energies. The formalism was then tested for two different EPIDs (liquid-filled and fluoroscopic types) for 6 MV and 15 MV photon beams [92]. C-C calculations agreed with corresponding liquid-filled EPID dose measurements to within 4 % (for both 6 and 15 MV beams) and were partly attributed to the under-estimation in PER described above. Systematic differences were observed for the fluoroscopic EPID measurements (using the 6 MV beam) which were underestimated (up to 3 %) by the collapsed-cone calculations, especially for the larger field sizes. The predicted underestimation was most likely due to the unaccounted response of the fluoroscopic EPID dose to low energy photons. Large deviations (above 3 %) between measurement and prediction also occurred with the combination of the high energy photon beam (15 MV) and thin phantoms ($<$ 10 cm).

2.2.8 Transmitted dose prediction using Monte Carlo

The prediction of transmitted dose as measured by an EPID have been investigated by performing full Monte Carlo simulations of particle transport from inside the linac head to the detailed structure of the EPID itself [93–97]. The accuracy of such MC simulations are found to generally be within 2 %. Other branches of Monte Carlo simulations of the EPID include modelling of the EPID calibration itself and of the dosimetric response of the EPID [98, 99].

2.3 Summary and conclusions

The above review demonstrates the evolution of *in vivo* dosimetry techniques in radiotherapy beginning with simple, one-dimensional entrance and exit dose measurements on the surface of patients, to combining entrance and exit doses in determining the dose at a mid-point in the patient, to estimating the two-dimensional midplane doses from 2D exit and transmitted dose distributions (measured by film or EPID) using back-projection techniques. More recently, with the advent of EPID technologies two mainstream approaches have emerged from the literature; 3D patient dose reconstruction techniques (using back-projection) from planar EPID dose distributions and the "forward" approach of 2D transmitted dose prediction. Despite the publicised efforts and recognised potential toward the latter approach there still remain important research into exploring the full potential and possible limitations of transmission dosimetry under a variety of clinical treatment scenarios. In particular, if transmission dosimetry is to be successfully implemented in the clinic it should be able to detect a range of clinical errors associated with different treatment sites such as: changes in delivered and planned treatment geometries (for example, patient positioning errors or tumour and/or organ motion in prostate treatments), dosimetry errors caused by individual MLC leaf positioning errors and/or leaf bank calibration errors in MLC based treatments which are critical in sparing normal tissue structures while tightly conforming to the target volumes (for example, head and neck conformal radiotherapy treatments). Finally, the issue of dynamic patient motion

during treatments such as respiratory motion in conformal breast radiotherapy. There are a limited number of studies on investigating and quantifying the impact of breathing on the dose distribution in the target volume and surrounding organs such as lung and heart. The objectives of this thesis are to investigate the efficacy of transmission dosimetry by simulating specific dosimetry errors encountered in conformal radiotherapy treatments with case studies of a prostate four-field box treatment technique, a patient head and neck treatment and an opposing tangential breast treatment technique. In particular, the nature of the investigation is theoretical in nature with the aim of eliminating a range of possible confounding effects introduced by experiment.

Chapter 3

Evaluation of a treatment planning system for modelling transmitted dose

3.1 Introduction

In order for transmission dosimetry to be a useful concept for patient *in vivo* dosimetry it should be proficient in detecting and quantifying differences in dose transmitted behind the patient resulting from treatment related dosimetry errors. Prerequisites for modelling transmitted dose accurately in the clinic include evidence of acceptable agreement between predicted and measured two-dimensional dose as well as sufficient sensitivity to a range of dosimetry errors. This chapter investigates the possibility of using a commercially available treatment planning system for accurately calculating absolute transmitted dose distributions as well as evaluating the minimum resolution in the transmitted dose calculations to subtle changes in transmission thickness. The accuracy of the transmitted dose calculations was performed for a range of rectilinear, homogeneous phantom thicknesses set up to both isocentric and fixed Source-to-Surface Distance (SSD) beam configurations. The impact of varying the air gap between the phantom and transmit-

ted dose plane on the accuracy of the calculations was also investigated. The accuracy of the transmitted dose calculations were benchmarked against two-dimensional absolute dose measurements performed using a calibrated liquid-filled Electronic Portal Imaging Device (EPID). In order to overcome the spatial limitations of performing transmitted dose calculations at extended clinical distances, a CT scan of a phantom, air gap and a water-equivalent slab representing an EPID, was acquired.

3.2 Materials and methods

3.2.1 Pinnacle^3 treatment planning system

Pinnacle^3 treatment planning system (version 6.2b, Philips Medical System, Milpitas, CA) is based on the convolution/superposition algorithm which was previously used by McNutt *et al* [70] for predicting transmitted dose distributions relative to film and EPID dose measurements. However, the dose calculation models currently used in modern versions of Pinnacle^3 have since evolved significantly. New features include the collapsed-cone convolution dose engine and the inclusion of multiple polyenergetic kernels which account for off-axis beam spectrum variations, and beam hardening which is known to increase the accuracy of the convolution/superposition calculations. In addition, beam divergence via kernel tilting which was not included in the original study by McNutt *et al* is modelled in Pinnacle^3.

3.2.2 Dosimetric calibration of the SLIC-EPID

EPIDs were originally designed for imaging in the MV energy range to ensure correct patient set up on the treatment couch. This requires a uniform signal response to the radiation across the detector plane. To achieve this, the raw signal is manipulated in EPID software by subtracting off a background signal (measured in the absence of radiation), electrometer offsets, and applying a flood-field correction to account for the variation in detector sensitivity across the EPID [37, 38, 44, 100, 101]. However, such corrections

remove the characteristic "horns" in the radiation beam profile which are essential for dosimetry. Consequently, prior to using the EPID as a two-dimensional dosimeter the original response of the EPID to clinical beams needs to be restored. In this study, EPID measurements were performed using a Scanning Liquid Ionisation Chamber EPID (SLIC-EPID) (Portal Vision LC250, Release 6.1, Varian Medical Systems, Inc.) and a 6 MV beam from a Varian 600CD accelerator (Varian Medical Systems, Palo Alto, CA, USA). Since the calibration of the SLIC-EPID was the objective of other work [37, 102] it will not be discussed here in detail but will be briefly outlined in the following sections.

Pixel value to dose conversion

The results presented in the following subsections are borrowed with permission from a colleague [6] and are included in the methodology section as supporting material for this chapter. The signal acquired by an EPID due to incident radiation is not a measure of absorbed dose but rather an ionisation current produced at the sensitive layer (liquid) of the EPID, that is proportional to the absorbed dose. The ionisation current is recorded as a 16 bit (0–65535) grey-scale Pixel Value (PV). The theoretical relationship between absorbed dose and PV for SLIC-EPIDs can be derived using ionisation chamber theory in the presence of pulsed polarizing voltage [103, 104]. The pixel values are found to be proportional to the square root of the dose rate (at low dose rates) which is in good agreement with measurement [37,38]. An important characteristic of the EPID to be used as a 2D dosimeter is to be able to integrate the signal over the total delivered Monitor Units (MUs). However, the integrating option is not available in our department. Instead, images are acquired within a known *acquisition time*, which is a fraction of the total MU delivery time. Since EPID pixel values vary in proportion to the incident dose rate, for calibration measurements the effective dose rate at the EPID was varied by acquiring images at different beam focus-to-EPID distances (110–160 cm). The dose rate at the corresponding EPID positions were measured using a calibrated ionisation chamber and were used to directly relate pixel values to dose rate and consequently to dose using the known acquisition time (figure 3.2.1). Figure 3.2.1 are plots of calibration curves using

different nominal linac repetition rates in which the EPID software acquires images using a given acquisition time. All measurements were performed using a Varian 600CD linear accelerator set to a repetition rate of 300 MU/min using 6 MV photons with a 10 × 10 cm^2 open field.

Figure 3.2.1: *Calibration curves for the SLIC-EPID at different nominal linac repetition settings (MU/min). The curve corresponding to 300 MU/min was used in this study. Error bars may not be visible due to their similar size to corresponding data points. (Figure courtesy of M. Mohammadi [6])*

The following calibration equation (line of best fit) was thus used:

$$D_{i,j} = a(PV_{i,j})^b, \tag{3.2.1}$$

where $D_{i,j}$ is the dose (cGy) at position (i, j) in the liquid chamber array, $PV_{i,j}$ is the corresponding EPID pixel value, $a = 5.27 \times 10^{-7}$, and $b = 1.79$. The values for parameters

a and b were derived from a second-order polynomial line of best fit and are highly dependent on the acquisition mode of the EPID, EPID construction, beam energy, specific linac settings and several other factors [100,105,106].The relationship between pixel value and repetition rate also depends on radiation field size. For large field sizes there is a small over response in EPID signal compared with ionisation chamber measurements, however, this effect is negligible for the field size used here [102]. Finally, the EPID signal response was found to strongly depend on the nominal linac repetition rate (MU/min) (as reported in the literature [100]) which will yield different characteristic curves. Thus, for dosimetry purposes it is critical to use the correct PV-to-dose calibration relationship with the corresponding linac repetition rate setting.

Correction Factor Matrix (CFM)

The flat response of the EPID in imaging mode, as discussed earlier, was corrected by multiplying the images with a 2D Correction Factor Matrix (CFM) in order to re-introduce the characteristic beam profile of the radiation field into the EPID images as removed in software. The CFM was derived from measurements with Extended Dose Range (EDR2) film [102] which was found to be suitable for two-dimensional calibration of the EPID due to its extended dose range characteristics as well its near independent response of photon energies used in radiotherapy. The CFM is defined as the pixel-by-pixel ratio of EDR2 film relative dose values ($D_{i,j}(film)$) to corresponding EPID relative dose values ($D_{i,j}(EPID)$) [107]:

$$CFM_{i,j} = \frac{D_{i,j}(film)}{D_{i,j}(EPID)} \tag{3.2.2}$$

Equation 3.2.1 is then multiplied by equation 3.2.2 to yield a 2D calibrated EPID dose image. A typical CFM for a 15.8 $\times$ 19.5 cm^2 open field acquired with EDR2 film and the EPID is shown in figure 3.2.2. The blue end of the coloured spectrum in the centre of the image represent values close to or equal to unity, whereas the red end of the spectrum represent values greater than unity, which are required to restore the beam profiles in the

NOTE: This figure is included on page 42 of the print copy of the thesis held in the University of Adelaide Library.

Figure 3.2.2: *A Correction Factor matrix defined for a 6MV photon beam in an open field (15.8 × 19.5 cm² at isocenter) at an SED of 140 cm. (Figure courtesy of M. Mohammadi [6])*

raw EPID images. Details of the CFM and its dependance on field size and SED can be found elsewhere [107] and were not the objective of this thesis. To minimise statistical noise in the current measurement, two consecutive EPID images were acquired in full resolution, fast-readout mode. All EPID measurements were performed with additional 5 mm of water equivalent build up material to achieve electronic equilibrium at the sensitive layer of the EPID [106].

3.2.3 Simulation of phantom and EPID

Square 30 cm × 30 cm slabs of RW3 (PTW, Freiburg, Germany) material (ρ = 1.045 g/cm^3) were arranged on a CT couch top to simulate a homogeneous phantom and EPID as shown in figure 3.2.3.

An air gap of approximately 35 cm separating the phantom and EPID representation was chosen to investigate the accuracy of the convolution/superposition calculations at clinically applied air gaps (larger than previously used by McNutt *et al* [70]). This was also within the range used in previous portal dosimetry studies [3,5,46,64,108]. The EPID

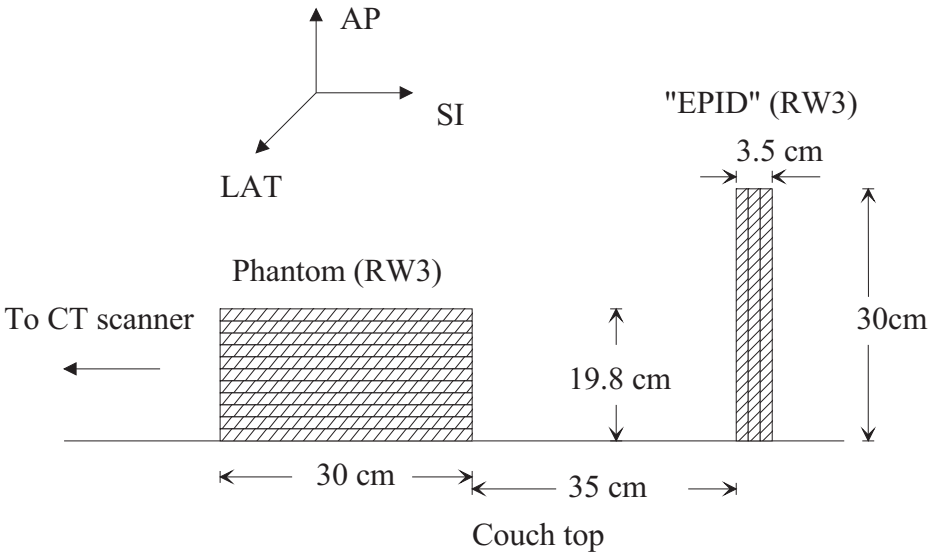

Figure 3.2.3: *CT arrangement of RW3 used to simulate a phantom and EPID separated by an air gap. (Not to scale).*

was modelled as 3.5 cm thick water-equivalent medium. This was chosen in order to be able to simulate the electronic equilibrium depth of the SLIC-EPID with the additional 0.5 cm build up of water-equivalent material. In addition, for the beam energy to be used, 3.5 cm also provides sufficient back-scatter to simulate full electronic equilibrium conditions. The RW3 configuration was scanned using a Philips AcQSim CT scanner (Philips Medical Systems, Cleveland, Inc.) and all CT images were exported via the hospital network in DICOM format. The single CT file was then imported into a Pinnacle^3 planning workstation.

Acquiring and exporting the above CT scan configuration to the TPS rather than simulating it directly using Pinnacle^3 was a necessary step due to spatial limitations in the planning system. Although a water phantom option consisting of a 50 $\times$ 50 $\times$ 50 cm^3 planning volume is available (in the version of the planning system used here), it is insufficient to simulate the desired 35 cm air gap using the 30 cm thick solid water and an isocentric beam configuration. Such limitations were reported in the work of McNutt *et al.*

3.2.4 Simulation of transmitted dose using treatment planning system

Once the CT images were imported into the planning system, a single 6 MV beam with a 10 × 10 cm^2 field size was created. However, the default beam and couch angles were such that they required a 90^0 (clockwise) rotation so that the actual relationship between beam, phantom and EPID was correctly simulated. In addition, due to the presence of CT artifacts caused by air gaps in between the slabs of solid water (see figure 3.2.3) the electron density values in the CT planning volume were changed to $\rho = 1.00$ g/cm^3 for the whole volume of slabs.

In order to investigate the accuracy of the transmitted dose predicted by Pinnacle[3] under a variety of clinical scenarios, the phantom was varied in thickness from 4–30 cm (as measured along the central axis of the beam). Furthermore, beam delivery was simulated using isocentric and fixed Source-to-Surface Distance (SSD) techniques (figure 3.2.4).

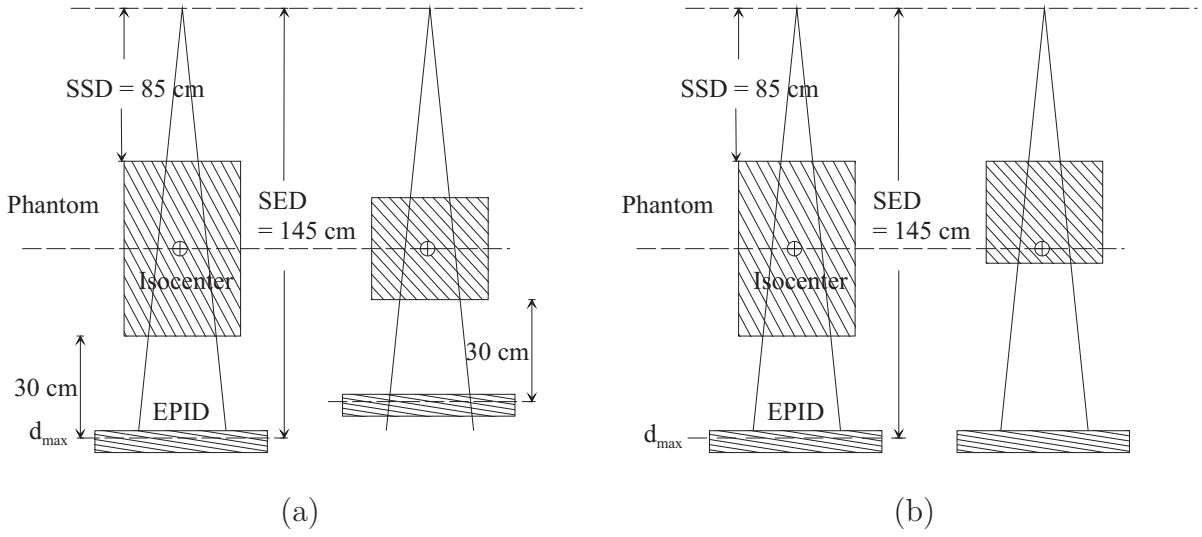

Figure 3.2.4: *Isocentric (a) and SSD (b) treatment setups simulated by the planning system for the RW3 phantom geometry.*

In the isocentric set up, the isocentre was placed at the geometric center for each phantom thickness and in the fixed SSD set up, the SSD was set to 85 cm for phantom thicknesses of 16–30 cm (16 cm being the thinnest phantom with the closest possible isocenter to the

exit surface of the phantom). Finally, in addition the Source-to-EPID surface Distance (SED) of the virtual EPID in the TPS was shifted such that the air gap separating the phantom and EPID was fixed for each phantom thickness. This allows the accuracy of the convolution/superposition algorithm to be tested under both variable air gap scatter conditions (figure 3.2.4(b)) and fixed air gap scatter conditions (figure 3.2.4(a)). The second option may also provide dosimetric validation for the SLIC-EPID calibrated at SEDs of 110–160 cm. However, for brevity the position of the EPID was only shifted for the the isocentric set up. This was believed to be sufficient for the purposes of investigating the accuracy of the predicted EPID dose distribution under different scatter conditions. Hence, including all possible scenarios would not necessarily add any new knowledge to the current investigation. All dose calculations were performed using the collapsed-cone convolution/superposition dose engine with a $0.25 \times 0.25 \times 0.25$ cm^3 grid resolution. A prescription dose of 300 MU was used in both scenarios.

3.2.5 Extraction of the transmitted dose plane from Pinnacle^3

At the completion of all Pinnacle^3 dose calculations, the 3D dose matrix file for each plan was identified on the planning system workstation and transferred to another work station for further processing. A Matlab (version 7.0, The MathWorks, Inc.) script was written to read in the dose matrix file which was a string of binary values. The script reconstructed a 3D array from the string and converted the file format from binary to decimal. A linear scaling factor defined by the ratio of the absolute dose display window in Pinnacle^3 to the corresponding value in the 3D array was used to convert the array values into absolute dose (Gy). The 2D dose plane corresponding to the depth at maximum dose, d_{max} inside the EPID (modelled by the TPS) was identified by translating the x, y and z co-ordinates of d_{max} in Pinnacle to corresponding rows, columns and array slice in Matlab. As shown in Figure 3.2.5, plane # 246 corresponds to $d_{max} = 1.5$ cm inside the water-equivalent EPID.

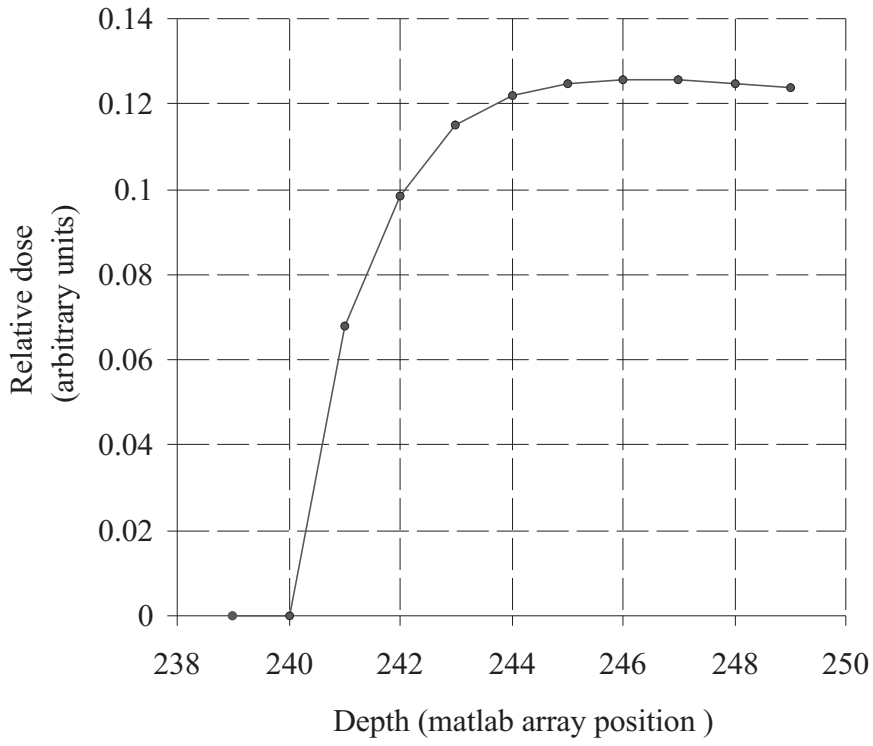

Figure 3.2.5: *Relative depth dose values (on the central axis) obtained from Matlab, to confirm the position of d_{max} (plane # 246) inside the water-equivalent EPID. Plane separation = 0.25 cm.*

3.2.6 Orientation, scaling and alignment of measured and computed images

Before the measured and calculated transmitted dose images can be compared pixel-by-pixel, it is essential that the two images have the same Beam's Eye View (BEV) orientation. This is especially critical for more complex shaped fields used in conformal and IMRT modalities. Since a single open field was used here that has numerous axes of symmetry it is impossible to determine whether the two images have the same orientation. Thus, the orientation of the measured EPID images was determined by acquiring an open field with radiopaque markers placed on the EPID panel to indicate "left" and "right" on the image (see figure3.2.6).

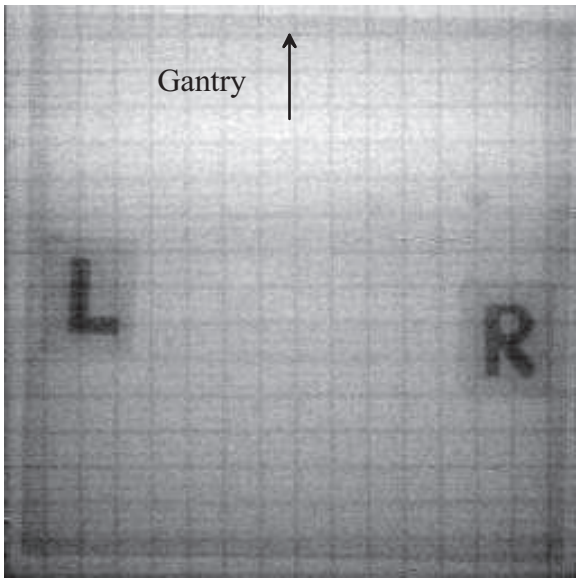

Figure 3.2.6: *A reference alignment image for determining "left" and "right" orientations in the EPID images.*

Simple rotation and flip matrix operations using Matlab were applied to the computed EPID dose images so they had identical orientations as the measured EPID images. The second step of image processing involved applying an image scaling factor to the computed EPID dose image, defined as the ratio of the pixel size in the measured EPID image (0.127 cm) to the pixel size of the computed EPID image (0.25 cm). Finally, the images were co-registered by cropping both images at the 50 % isodose lines, relative to the absolute dose at the center of each image.

3.2.7 Noise analysis of images

All EPID images in this study were acquired in "standard" acquisition and"fast" read-out modes using single frame averaging. In order to minimise noise in the acquired SLIC-EPID images, two images were acquired consecutively and averaged. The standard deviation in dose on the central beam axis was calculated as a function of phantom thickness for both

measured and computed EPID dose images using:

$$\sigma = \left(\sum_{i=1}^{m} \sum_{j=1}^{n} \frac{(D_{i,j} - \overline{D}_{CAX})^2}{m \times n} \right)^{\frac{1}{2}}, \tag{3.2.3}$$

where $\overline{D}_{CAX}$ is the dose averaged over an $m \times n$ (9×9 pixels) array of dose values, $D_{i,j}$ centered about CAX. The Signal-to-Noise Ratio (SNR) defined as, $SNR = (\overline{D}_{CAX}/\sigma)$ was then calculated on the central axis as a function of phantom thickness. In addition, the *relative error* in dose on the central axis was defined as, $\varepsilon = (\sigma/\overline{D}_{CAX}) \times 100$ %.

3.2.8 Comparison of measured and predicted images

A known limitation of comparing two-dimensional dose distributions by image subtraction is that slight misalignment can result in very large dose differences at the edges of the radiation field due to the sharp fall off in dose. In addition, with the advent of new intensity modulation techniques, steep dose gradients can occur anywhere within the radiation field. Such dose differences due to imperfect image alignment can be erroneously inferred to as clinically significant. As a result, recommendations have been proposed on giving separate criteria of acceptability for low dose gradient and high dose gradient regions within the radiation field [109–113]. Criteria of acceptability were defined in terms of a percentage dose differences (%) and spatial tolerance (maximum allowable separation of isodose lines (mm) between two given dose distributions). The concept of a spatial tolerance or *Distance-To-Agreement* (DTA) was previously introduced by several authors [110,114,115]. However the concept of a DTA alone, when applied to dose distributions would be overly sensitive in regions of low dose gradients, analogous to a dose difference metric being oversensitive in regions of high-dose gradients. As a consequence several authors [116, 117] combined the two metrics to form a binary, "gamma" function that yields values of "1" whenever both DD and DTA criteria are fulfilled or "0", when either DD or DTA (or both) are not fulfilled, at individual points in the evaluated dose distribution. The gamma function was later modified by Low *et al* [118] to have continuous

values, where gamma values between "0" and "1" (inclusive) are considered a "pass" and values exceeding "1" are considered a "fail". Furthermore, the magnitude of the gamma value indicates the degree to which dose values are in agreement or disagreement and thus provides a more quantitative analysis than the former binary gamma function. Expressed mathematically:

$$\gamma(\mathbf{r}_r) = \min\{\Gamma(\mathbf{r}_r, \mathbf{r}_e)\}\forall\{\mathbf{r}_e\}, \tag{3.2.4}$$

where:

$$\Gamma(\mathbf{r}_r, \mathbf{r}_e) = \sqrt{\frac{r^2(\mathbf{r}_r, \mathbf{r}_e)}{\Delta d^2_{max}} + \frac{\delta^2(\mathbf{r}_r, \mathbf{r}_e)}{\Delta D^2_{max}}}, \tag{3.2.5}$$

$r(\mathbf{r}_r, \mathbf{r}_e) =\mid \mathbf{r}_e - \mathbf{r}_r \mid$, and $\delta(\mathbf{r}_r, \mathbf{r}_e) = D_e(\mathbf{r}_e) - D_r(\mathbf{r}_r)$.

The result is a two-dimensional gamma map consisting of gamma indices indicating regions of agreement and/or disagreement:

$$\gamma(\mathbf{r}_r) = \begin{cases} \text{"pass"}, & \text{for } 0 \leq \gamma(\mathbf{r}_r) \leq 1 \\ \text{"fail"}, & \text{for } \gamma(\mathbf{r}_r) > 1 \end{cases}$$

By setting $\Gamma(\mathbf{r}_r, \mathbf{r}_e) = 1$, equation 3.2.5 can be interpreted as an ellipsoid with a surface defining the limits of acceptable criteria (figure 3.2.7).

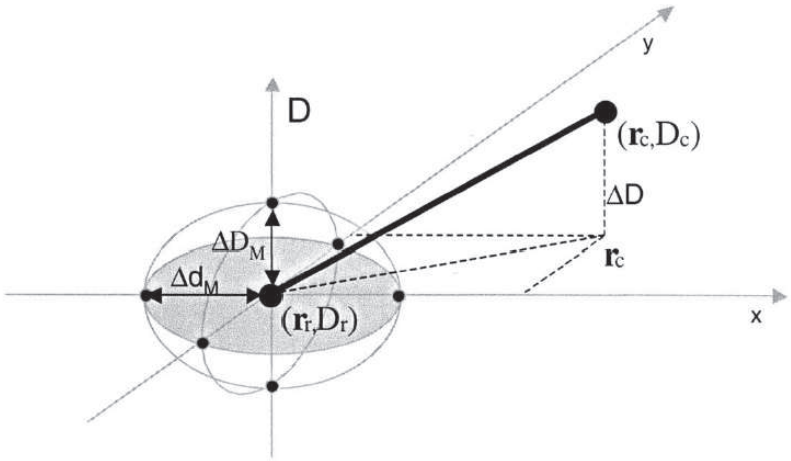

Figure 3.2.7: *A geometric interpretation of the gamma concept used in this study. (Figure courtesy of Depuydt et al [7]).*

It is well documented that when the gamma function is applied to discrete data sets (eg pixels), it can report incorrect points of disagreement in regions of high dose gradients. The effect becomes more noticeable for lower resolution data sets [7,119] Although interpolation between data points can to some extent overcome this issue, the processing time can become substantially longer. As a result, several authors have refined the gamma algorithm for application to discrete data sets that filter out such false negative data points without the need for interpolation [7]. Gamma criteria typically used for gamma map analysis are 3 %/3 mm [80, 118, 120, 121]. However, other combinations have been reported to be used in the clinic. For example, some authors have used 4 %/3 mm for comparing planned and measured head and neck IMRT dose distributions [122], while other authors that compared predicted and measured portal dose distributions for conformal breast fields, analysed gamma maps using 3 %/5 mm criteria [81]. In some instances, more relaxed DD criteria (5 %) combined with tighter DTA criteria (2-3 mm) have also been reported to be used [119, 123].

More recently, Bakai *et al* [124] proposed an alternative method of applying Low *et al's* original concept from a different perspective. A function, χ, analogous to γ was derived and can be interpreted in terms of the laws of error propagation used in statistics. The χ function gives similar results to that of the gamma function but does not involve a search algorithm, hence reducing processing time. Furthermore, it can be successfully implemented on discrete or continuous data sets. Several authors have introduced additional tools to aid the interpretation and analysis of 2D gamma maps. For example, *gamma area histograms* have been used to statistically categorise gamma values. This is especially useful for volumetric dose distributions where the gamma concept is extended to 3D. A *gamma angle* distribution has also been introduced for aiding the interpretation of the gamma map. The gamma angle determines the influence of DTA and dose difference on gamma values. For example, assuming a gamma angle of 0 is defined on the dose difference axis, a gamma angle between 0^0 and 45^0 (ie closer to the dose difference axis) is dominated by the dose difference parameter, whereas a gamma angle greater between 45^0 and 90^0 is more strongly influenced by DTA.

In this study, the original gamma function developed by Low *et al* was used to compare the calculated transmitted dose distributions against the measured EPID dose distributions.[1] Here the measured EPID dose image was chosen as the *reference* map and the calculated transmitted dose distribution was chosen to be the *evaluated* dose map since it is the planning system that is being evaluated for predicting the transmitted dose. This specific labeling of the dose maps is important since the calculated gamma results will not necessarily be identical if the definitions are reversed [119].

3.3 Results

3.3.1 Noise analysis of images

The SNR on the central axis of the measured EPID dose images decreased on average with increasing phantom thickness (figure 3.3.1), which corresponds to an increasing relative error from 0.1 – 0.8 % (not shown).

The increase in noise is most likely a result of the reduced radiation signal at the EPID layer, the increase in scatter contribution with depth inside the phantom, and consequently the smaller SNR at the detector. Figure 3.3.1 also shows that the SNRs for the Pinnacle^3 calculations are significantly higher (< 10000) than corresponding SNRs for the EPID dose measurements (<1000). This is to be expected since the dose calculations are based on an analytical model that does not incorporate measured data, where as the EPID dose measurements inherently include a certain degree of noise. Consequently, the higher SNR in the dose calculations corresponded to a relative error on the central beam axis of less than 0.1 %. In summary, a noise level between 0.1 –0.8 % is relatively small and thus is an acceptable level of uncertainty for 2D transmission dosimetry.

[1] An in-house Matlab routine for the gamma function was used, courtesy of M. Mohammadi [125].

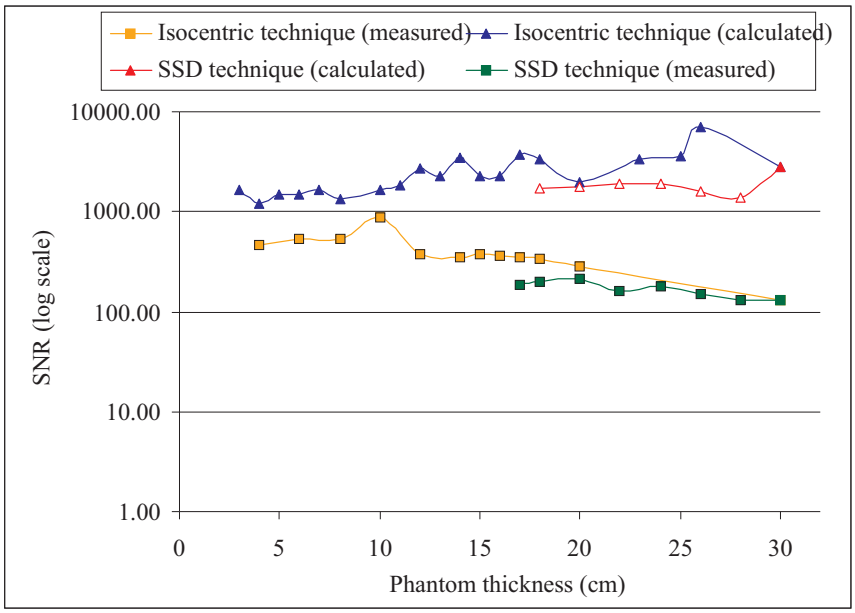

Figure 3.3.1: *SNRs in measured and predicted EPID doses on CAX as a function of phantom thickness.*

3.3.2 Comparison of measured and predicted EPID doses for varying phantom thicknesses

The calculated mean doses on the central axis as a function of phantom thickness were compared with corresponding SLIC-EPID dose measurements. In the isocentric phantom set up, the calculated mean doses were within +5 % of all phantom thickness measurements and on average the dose difference was less than +2 % . In the fixed SSD set up, the calculated doses were within + 3% for any given phantom thickness and less than +2 % averaged over all phantom thicknesses. The results are displayed in Figures 3.3.2 (a) and (b).

In the isocentric set up, typical beam profiles for measured and predicted EPID doses through the central axis (for phantom thicknesses of 10, 20 and 30 cm), with superimposed gamma profiles are shown in figure 3.3.3). Similarly, in the fixed SSD set up, beam profiles and gamma profiles were for phantom thicknesses of 28, 22 and 18 cm are displayed in

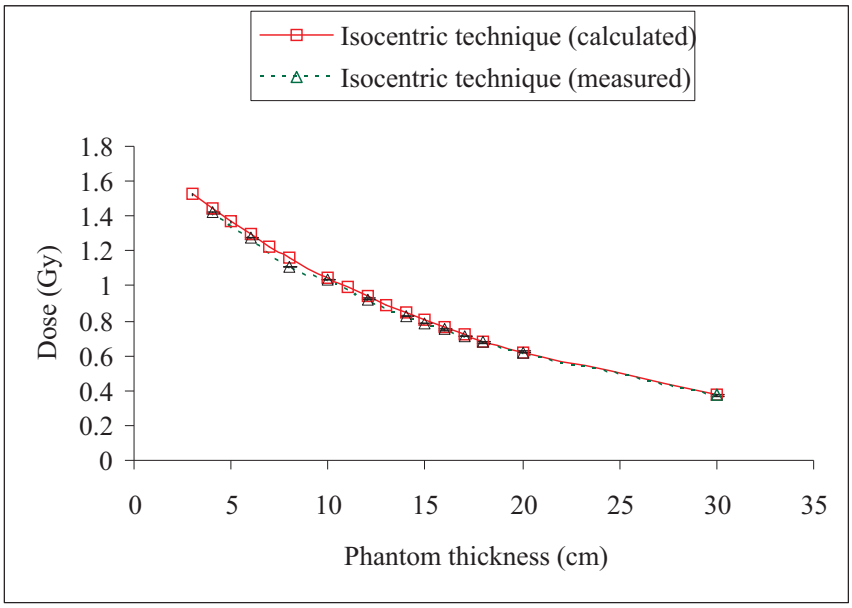

(a)

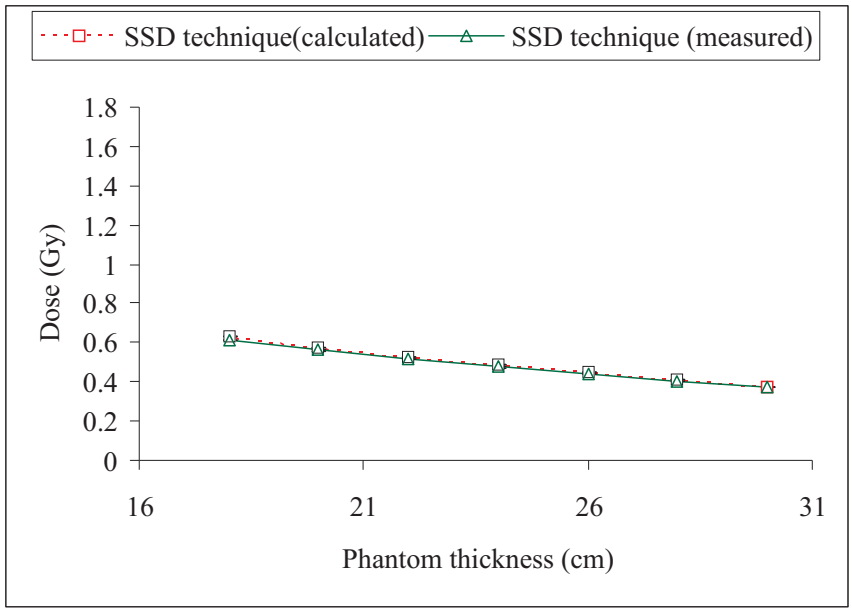

(b)

Figure 3.3.2: *Comparison of calculated and measured mean doses on CAX for different phantom thicknesses. (a) Isocentric set up. (b) Fixed SSD set up. All points contain error bars, but are too small to appear in the vertical scale.*

figure 3.3.4).

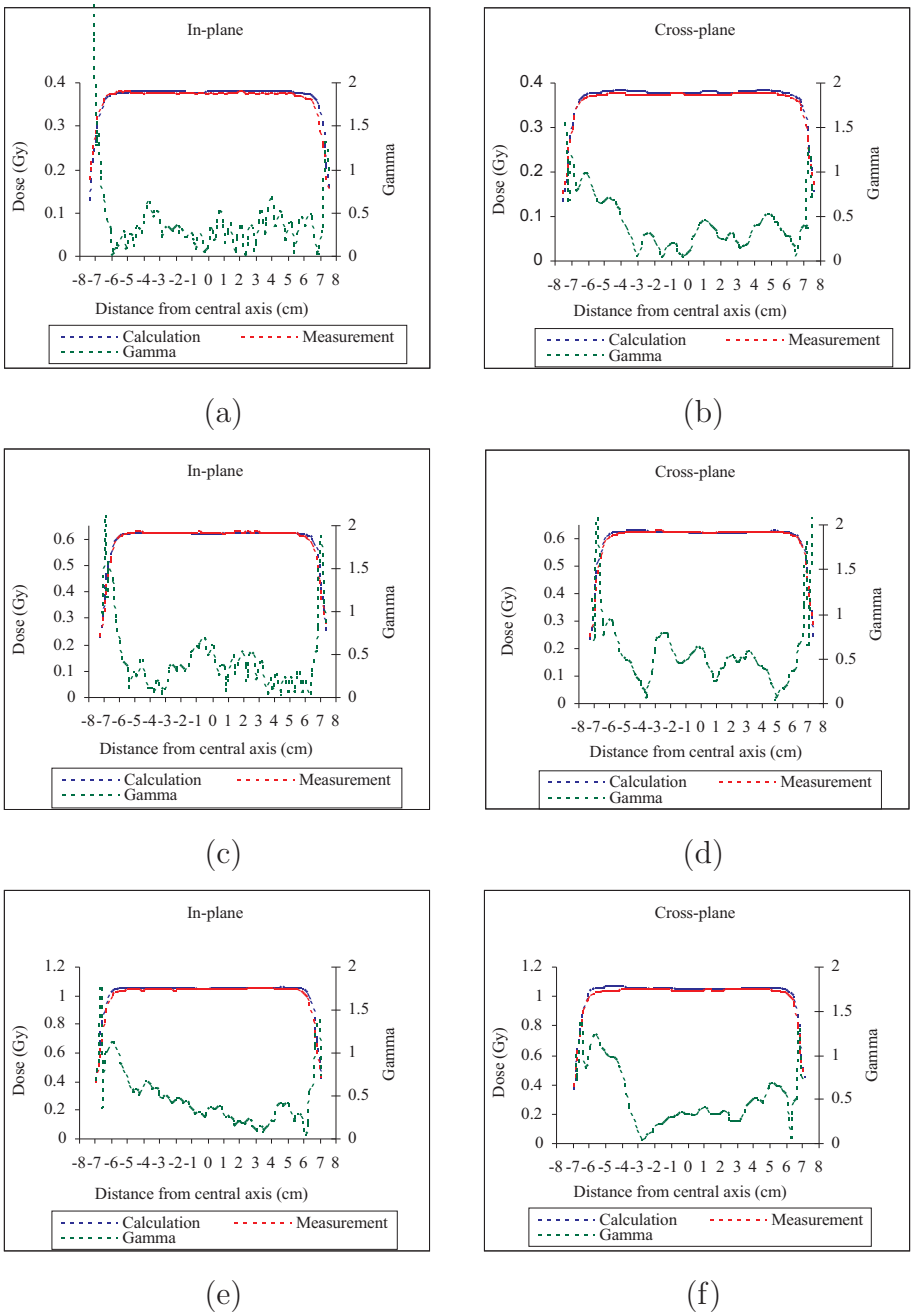

Figure 3.3.3: *Isocentric set up: comparison of calculated and measured EPID dose beam profiles with gamma profiles also shown. (a)–(b) Phantom thickness of 30 cm. (c)–(d) Phantom thickness of 20 cm. (e)–(f) Phantom thickness of 10 cm.*

Ideally the accuracy of the EPID dose calculations should not change under varying conditions such as phantom thickness, treatment set up, or EPID position, otherwise this

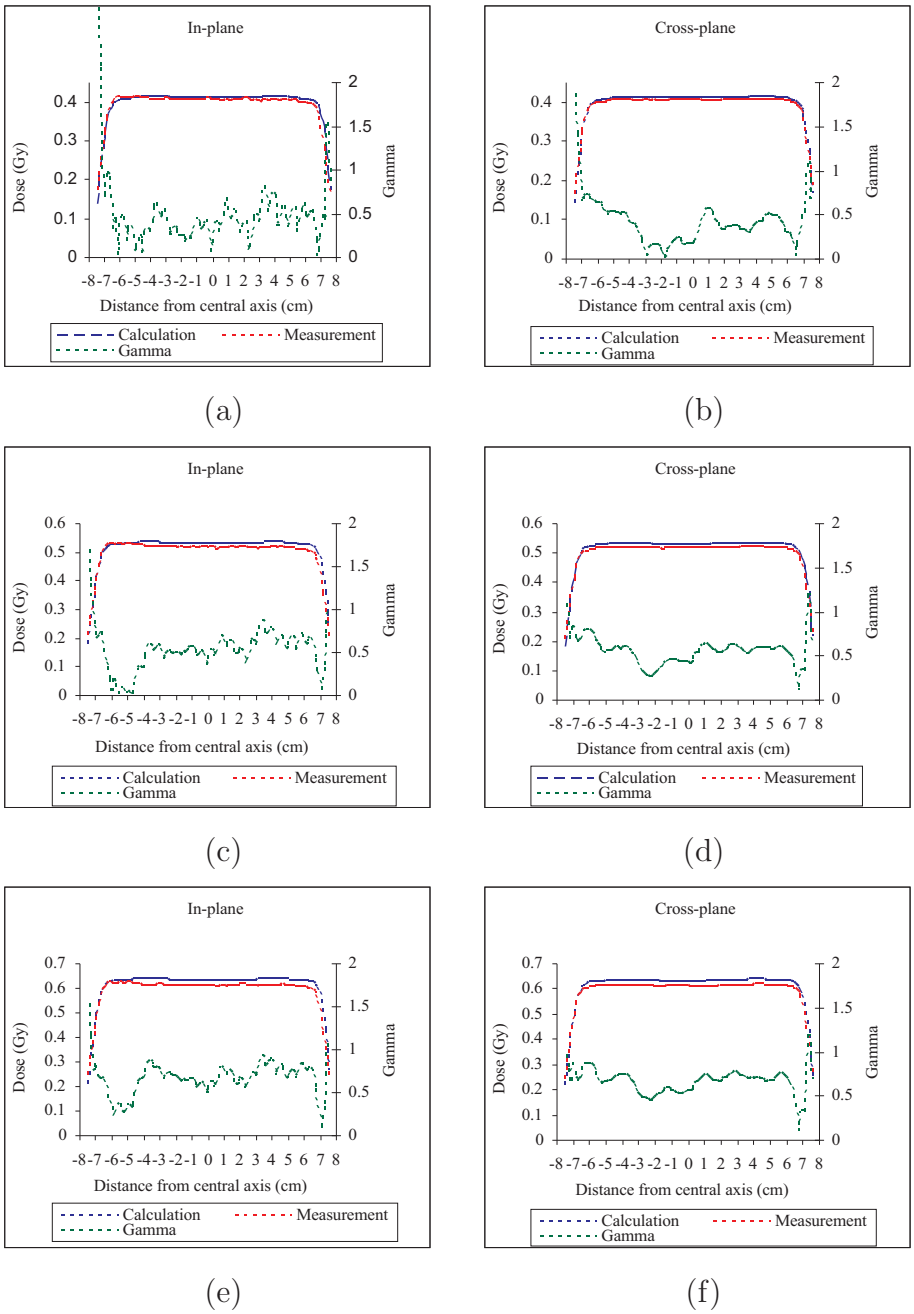

Figure 3.3.4: *Fixed SSD set up: comparison of calculated and measured EPID dose beam profiles with gamma profiles also shown. (a)–(b) Phantom thickness of 28 cm. (c)–(d) Phantom thickness of 22 cm. (e)–(f) Phantom thickness of 18 cm.*

would be impractical when applied in clinical situations which contain many variables including the above. Results in the first and last columns of tables 3.3.1 and 3.3.2 show

that there is no strong correlation in dose differences observed on CAX as a function of phantom thickness. This suggests that the accuracy of the calculations (on the central axis) does not strongly depend on the thickness of the phantom, treatment set up or position of the EPID. To determine how well the calculated and measured dose maps agreed, gamma analysis was implemented in an inverse manner; that is, what combination of Dose Difference (DD) and Distance-To-Agreement (DTA) criteria would be required to obtain acceptable agreement between the two dose maps? Hence DTA and DD gamma criteria were adjusted systematically until gamma scores, were on average $\geq$ 90 % for all phantom thicknesses. Although gamma analysis is becoming more widely used in clinical departments for quality assurance, there is currently no "official" consensus on a lower limit for gamma scores (for a given DD%/DTA combination) that would constitute an acceptable level of agreement (for example, a gamma score of 99 or 100 % is ideal but clinically unrealistic). Furthermore, the gamma score alone may not be a sufficient indicator of agreement as it does not provide spatial information of the errors (for example, whether errors are highly localised or randomly distributed) and should thus be used in combination with a 2D gamma map. Here, a gamma score of 90 % or greater was considered to be a reasonable lower limit for acceptable agreement between measured and calculated dose distributions as suggested by some authors [126, 127]. It was found that increasing DTA from 1.27 –5.08 mm improved gamma scores by accounting for imperfect co-registration of the images but only up to a point, at DTA = 3.8 mm, beyond which did not further improve the gamma scores. This implies that the uncertainty in co-registration of the dose maps is about 3 pixels. Thus, DTA = 3.8 mm was chosen as an optimum value for all phantom thicknesses. The DD parameter was then varied with DTA = 3.8 mm, until gamma scores were on average 90 % or greater for all phantom thicknesses. It was found that for the isocentric set up, on average 91 % of measured and calculated dose values agreed within an average of 3.7% /3.8 mm. In fact, for the fixed SSD set up, on average 91 % of measured and calculated dose values also agreed within an average of 3.7% /3.8 mm. This confirms that the accuracy of the dose calculations does not depend on phantom thickness, treatment set up or position of the EPID. The results are

Phantom thickness (cm)	DD (%)	DTA (mm)	Total gamma score (%)	Total gamma score (excl 1.5 cm edges) (%)	Dose difference on CAX (%)
30	3.0	3.8	85	92	−1.2
20	2.0	3.8	81	94	+0.33
18	3.0	3.8	83	92	−1.1
17	3.5	3.8	82	91	−1.6
16	3.5	3.8	80	92	−1.4
15	4.0	3.8	78	92	−1.9
14	4.0	3.8	80	91	−2.2
12	4.0	3.8	80	89	−1.6
10	3.0	3.8	81	90	−0.85
8	7.5	3.8	85	90	−4.8
6	4.0	3.8	80	93	−1.5
4	3.5	3.8	76	87	−1.4

Table 3.3.1: *Isocentric set up: Gamma evaluation study to determine which (ideal) combination of DD and DTA yield gamma scores of 90 % or more averaged over all phantom thicknesses.*

Phantom thickness (cm)	DD (%)	DTA (mm)	Total gamma score (%)	Total gamma score (excl 1.5 cm edges) (%)	Dose difference on CAX (%)
30	3.0	3.8	85	92	−1.2
28	3.0	3.8	84	87	−1.4
26	3.5	3.8	87	90	−1.6
24	4.0	3.8	90	93	−2.0
22	4.5	3.8	93	96	−2.4
20	3.5	3.8	88	92	−1.8
18	4.5	3.8	88	89	−2.9

Table 3.3.2: *Fixed SSD set up: Gamma evaluation study to determine which (ideal) combination of DD and DTA yield gamma scores of 90 % or more averaged over all phantom thicknesses.*

summarised in tables 3.3.1 and 3.3.2.

Typical two-dimensional gamma maps (cropped at the 50 % isodose lines relative to the measured EPID dose images) are displayed for both the isocentric and fixed SSD techniques, for a variety of phantom thicknesses (figure 3.3.5).

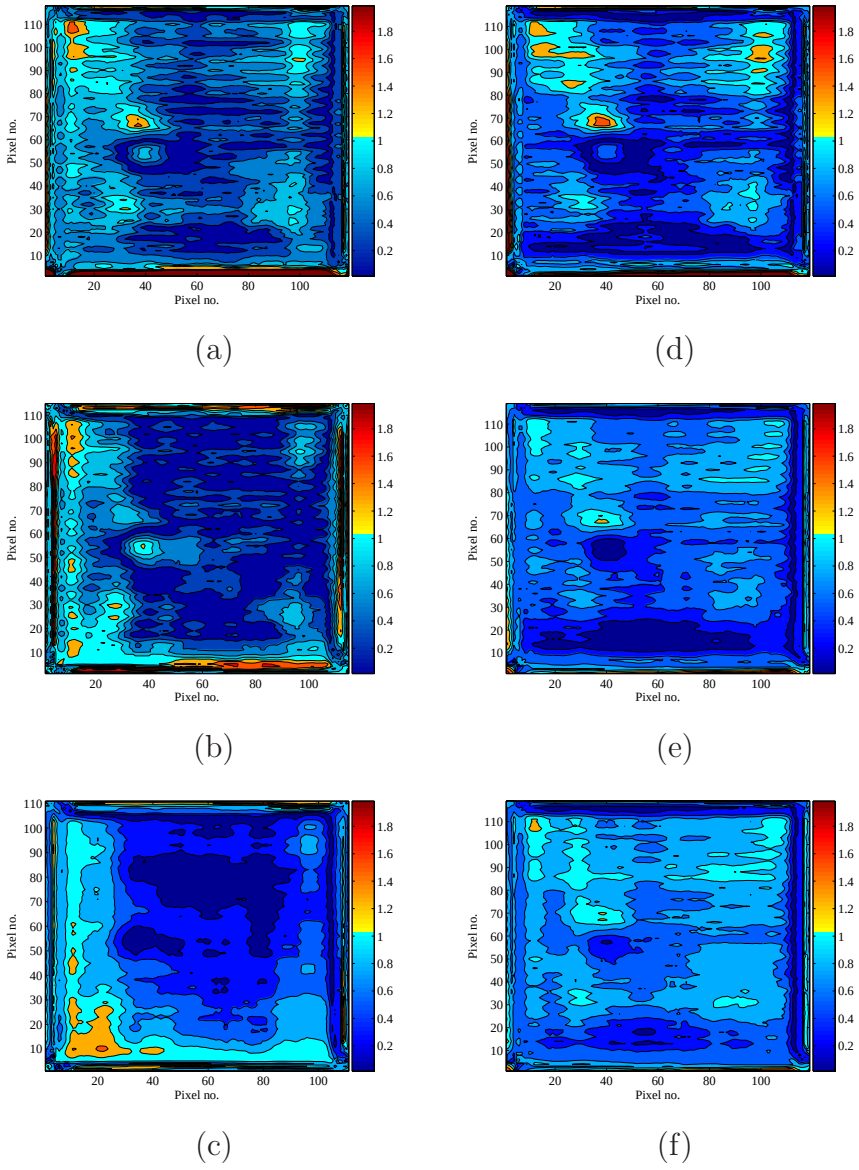

Figure 3.3.5: *Gamma maps. (a)–(c) Isocentric set up. (a) Phantom thickness 30 cm (3%/3.8 mm), (b) Phantom thickness 20 cm (2%/3.8 mm), (c) Phantom thickness 10 cm, (3%/3.8 mm). (d)–(f) Fixed SSD set up. (a) Phantom thickness 28 cm (3%/3.8 mm), (b) Phantom thickness 22 cm (4.5%/3.8 mm), (C) Phantom thickness 18 cm (4.5%/3.8 mm). Corresponding gamma scores are shown in tables 3.3.1 and 3.3.2.*

3.3.3 Evaluation of minimum detectable phantom thickness changes using transmitted dose

The minimum detectable change in phantom thickness can be derived from figures 3.3.2 (a) and (b) by linear interpolation at selected points of the reference phantom thicknesses. In the isocentric phantom set up a change in transmitted dose of + 0.6 ± 0.1 % (1σ) and −0.5 % ± 0.1 % (1σ) on the central axis, corresponded to phantom thickness changes along CAX of −1 mm and + 1 mm, respectively (Figures 3.3.6 (a)–(c)). Similarly, in the fixed SSD phantom set up, dose changes of + 0.5 ± 0.1 % (1σ) and −0.4 % ± 0.1 % (1σ), corresponded to phantom thickness changes of −1 mm and + 1 mm, respectively (figures 3.3.6 (d)–(e)).

However, in practice such small changes may not be detectable using actual EPID dose measurements due to the much smaller SNRs already observed as well as the additional uncertainties associated with dosimetric calibration. However, such small differences predicted and identified by the dose calculations confirms the reliability of the planning system to minute changes and that Pinnacle[3] is a promising tool for the evaluation and prediction of transmitted dose.

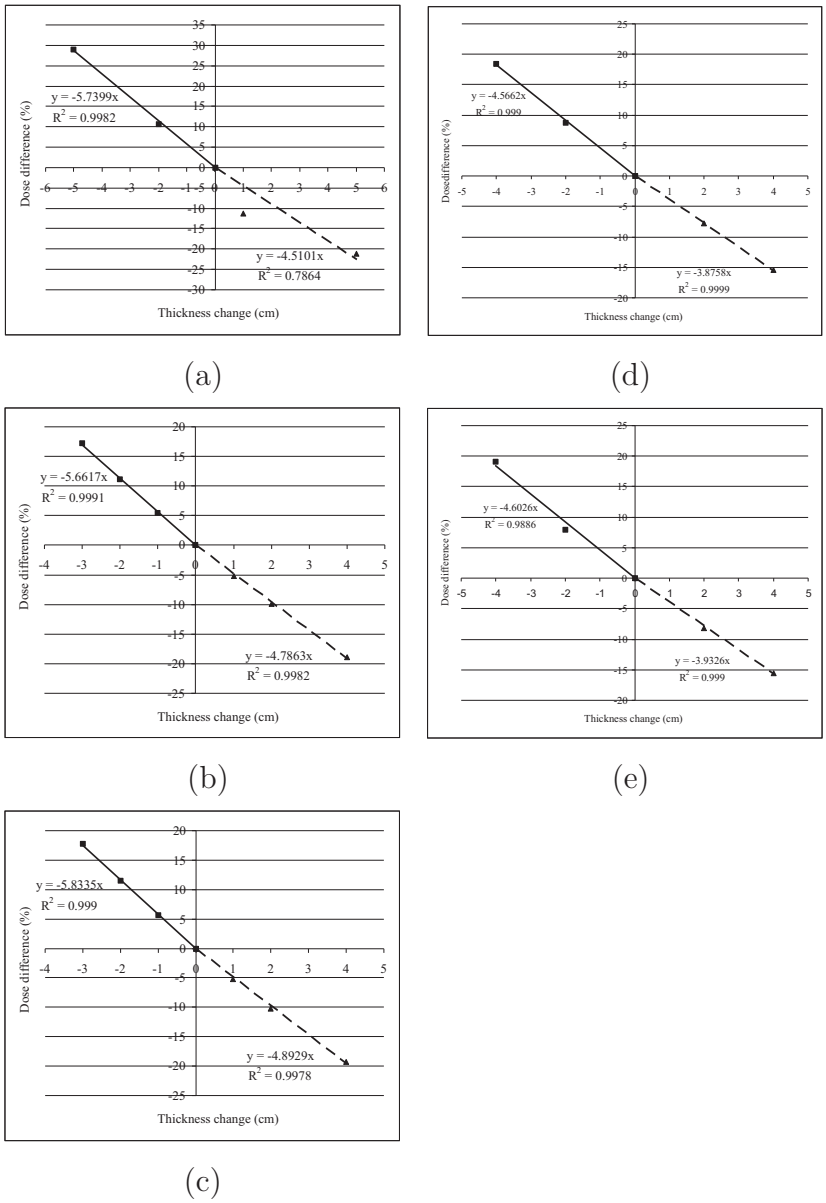

Figure 3.3.6: *Minimum detectable resolution in collapsed-cone superposition dose calculations at the transmitted dose plane (d_{max}) as a function of phantom thickness. (a)–(c) Isocentric set up. (a) reference phantom thickness 25 cm, (b) reference phantom thickness 15 cm, (c) reference phantom thickness 6 cm. (d)–(e) Fixed SSD set up. (d) reference phantom thickness 26 cm, (e) reference phantom thickness 22 cm.*

3.4 Discussion

3.4.1 Overestimation of transmitted dose calculations relative to measurement

Tables 3.3.1 and 3.3.2 show that the transmitted dose predicted by the planning system is consistently greater than the measured EPID dose for all phantom thicknesses in the fixed

SSD technique, and all but one phantom thickness (20 cm) in the isocentric technique. This is especially apparent in figures 3.3.4(c)–(f). A contributing factor for this was the absence of the couch top in the direct path of the beam due to the necessary rotation of the beam axis in the planning system, as discussed in the Methods section. A comparison with other studies that have also compared SLIC-EPID dose measurements with predicted EPID doses using the collapsed-cone superposition or convolution/superposition methods under homogeneous phantom geometries is desirable. However, there are only a few known studies that have been performed. Unfortunately, the study by McNutt *et al* [70] performed calculations and measurements with a flat, homogeneous phantom using 10 MV photons rather than 6 MV photons used in the current study. Nevertheless, a more recent paper by Dahlgren *et al* [92] compared SLIC-EPID doses with corresponding collapsed-cone superposition calculations based on a water-equivalent EPID model for both 6 and 15 MV photon beam energies for a range of field sizes, phantom thicknesses (homogeneous). An isocentric phantom set up with a SED of 140 cm was used throughout the study. For the 6 MV beam and 10× 10 cm^2 field size, the magnitude in errors were comparable with the current study. For the different phantom thicknesses incorporated by Dahlgren *et al* there appeared to be no systematic differences between calculation and measurement. For example, for a 5 cm and 13.5 cm thick phantom, the collapsed-cone superposition calculation slightly overestimated the dose relative to the SLIC-EPID measurements, whereas the calculations underestimated the dose for a 7 cm thick phantom. However, varying the field size appeared to impact on the direction of the dose differences. For example, for small field sizes (ie 5 cm × 5 cm^2), calculations tended to underestimate the dose relative to EPID dose measurements while larger field sizes (ie 15 × 15 cm^2) overestimated the dose. Monte Carlo simulations have also been utilised for comparing the dose response of a water-equivalent detector with that predicted using the collapsed-cone superposition algorithm [89]. For a 6 MV photon beam, 10 × 10 cm^2, at a depth of 1.7 cm below the water-equivalent detector, the CCS calculations slightly overestimated the dose for a 5 cm and 10 cm thick water phantom (30 cm air gap). However, for a 20 cm and 30 cm thick water phantom, same air gap the CCS algorithm underestimated the

dose relative to the MC simulations. For a smaller air gap (10 cm), the underestimation in dose appeared to be largest ($\sim$ 1 %). Finally, a Monte Carlo study comparing the dose response of a SLIC-EPID relative to a water-equivalent medium has been published [94]. The paper concluded that for a 6 MV photon beam, the dose at d_{max} in a water-equivalent medium is predicted to be 3.8 % greater than the dose measured using a SLIC-EPID. Such a prediction appears to be in close agreement (both magnitude and direction) with the results of the current study.

A further possible cause for the apparent overestimation of the dose calculations may be accounted for, by fundamental assumptions used in the planning system dose algorithm, namely that of *average density scaling*. It is well known that average density scaling is accurate for primary and first-order scattered photons but not for higher-order scattered photons [4, 69]. The contribution of dose (in a plane downstream from the source) from multiply scattered photons highly depends on the position of the inhomogeneity relative to the beam source. In the current planning system set up, a water-equivalent medium precedes a large air gap, which in turn is preceded by the water-equivalent EPID layer. Hence, average density scaling in the convolution/superposition calculations predicts a greater number of multiple-scattering events due to the scattering source being closer to the transmitted dose at d_{max} inside the EPID layer compared with reality in which the scattering source is further upstream, namely at the exit surface of the water phantom. The discrepancy increases for larger air gap distances and smaller field sizes [69]. Although the effect has been reported for small air gap distances (up to 10 cm) only it is reasonably consistent with the current study. For the fixed SSD technique in which the air gap increased with decreasing phantom thickness, a steady increase in discrepancy with increasing air gap was observed.

However, a more likely cause of the systematic differences observed between the measured and predicted transmitted dose distributions would be the density override performed on the CT density values in the planning system, which was intended to remove air gaps present in the CT data. In hindsight, the density change from 1.045 g/cm^3 to 1.00 g/cm^3

would be expected to cause an overall increase in the Pinnacle^3 dose calculation at the virtual EPID, of the order of 3 %. This would explain the lower dose that was measured by the SLIC-EPID using the higher density RW3 material (1.045 g/cm^3).

3.4.2 Dosimetric uncertainties in the SLIC-EPID measurements

The procedure necessary for calibrating the EPID involve several uncertainties. In particular, uncertainties in equation 3.2.1 (corrected with CFM) can be quantified by estimating the individual standard deviations in each of the parameters and combining them in quadrature to determine the overall uncertainty:

$$\sigma_{\dot{D}} = \sqrt{\left(\frac{\partial \dot{D}}{\partial (CFM)}\right)^2 \sigma_{CFM}^2 + \left(\frac{\partial \dot{D}}{\partial a}\right)^2 \sigma_a^2 + \left(\frac{\partial \dot{D}}{\partial b}\right)^2 \sigma_b^2 + \left(\frac{\partial \dot{D}}{\partial (PV)}\right)^2 \sigma_{PV}^2}, \qquad (3.4.1)$$

where σ_{CFM}, σ_a, σ_b and σ_{PV} are the standard deviations in CFM, a, b and PV, respectively.

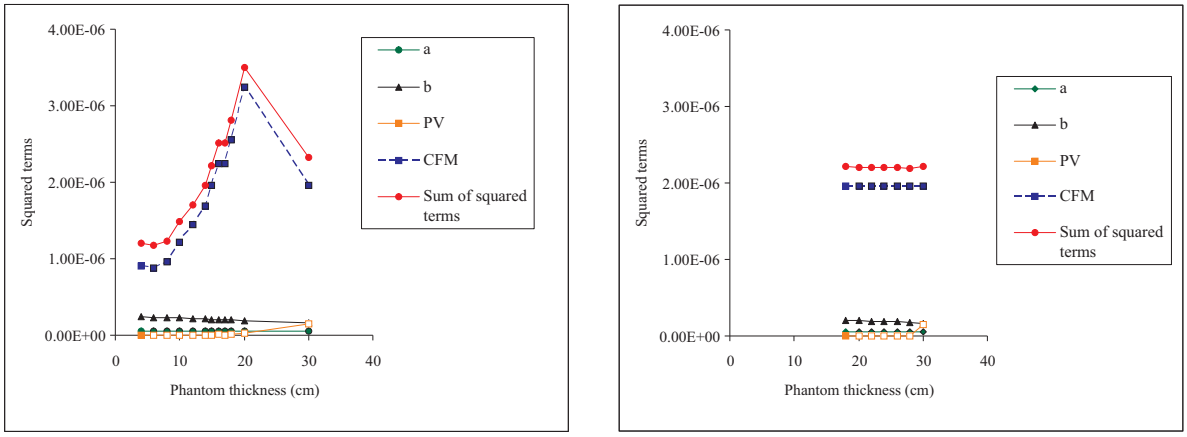

Figure 3.4.1: *The total error (variance) in the dose calibration curve and the sum of its parts, as a function of phantom thickness. (a) Isocentric set up. (b) Fixed SSD set up.*

The standard deviations in a and b were estimated by fixing one parameter at a time while varying the remaining parameters from 0.5–10 %. The resulting line fits were then used as an indicator of the uncertainty in a and b (refer to appendix 1). The standard error

in $\dot{D}$ is then $\varepsilon_{\dot{D}} = \frac{\sigma_{\dot{D}}}{\dot{D}} \times 100\%$. The total relative error was calculated separately for each phantom thickness using both phantom set ups. The total variance plus the individual error terms in equation 3.4.1 as a function of phantom thickness are shown in Figures 3.4.1 (a) and (b). Although, the CFM had the greatest contribution to the uncertainty (see figure 3.4.1), the combined uncertainty in equation 3.4.1 was only ± 0.15 %. Finally, we estimated the error in ionisation chamber measurements in water, ε_{IC} to be of the order of ± 0.5 %. Combining these two uncertainties the square of the total error, ε^2_{tot} is:

$$\varepsilon^2_{tot} = \varepsilon^2_{\sigma_{\dot{D}}} + \varepsilon^2_{IC} \tag{3.4.2}$$

Expressed as a percentage error the errors combine to form an uncertainty in the measured dose of ± 0.52 % . Furthermore, taking into account the accepted uncertainties in treatment planning dose calculations (photons) of 3 % /4 mm under homogeneous/inhomogeneous conditions, [112] the above agreement with measurement is close to acceptable limits. One outlier in the data which can not be accounted for was the EPID dose measurement in the isocentric set up for the 8 cm phantom. The discrepancy compared with calculation was 5 % . Figure 3.3.2(a) shows that the outlier was a result of measurement not calculation. As a result the measurement was repeated a second time under identical conditions but a similar result was obtained. The reason for this discrepancy was not identified. However, if one discards this data point the average discrepancy between measurement and calculation for the isocentric set up becomes 3 % .

3.4.3 Image alignment

Gamma scores shown in tables 3.3.1 and 3.3.2 suggests a possible alignment error between the measured and calculated EPID dose imgages. In the fourth column gamma scores were calculated within the 50 % isodose line region and were on average 81 %. However, in the fifth column gamma scores were calculated with images cropped 1.5 cm inside the 50 % isodose line region, significantly improving (on average) gamma scores by 10 % . This possible alignment error was most likely systematic in nature and may have been due to an experimental set up error or incorrect co-ordinates defined in the image processing software. It has also been reported in the literature that the gamma evaluation tool developed by Low *et al* has some limitations when applied to discrete pixelated data sets [7] such as, the current study. The definition of the distance-to-agreement parameter defined by Low *et al* is not ideal for pixelated data sets as it is based on the radial distance of a circle. Such a definition for a rectangular array of data points would incorrectly assign larger distances for diagonally positioned pixels, compared with other adjacent pixels, if the distance is measured from the centre of the pixels.

3.5 Summary and conclusions

The Pinnacle^3 treatment planning system has been evaluated for its ability to predict the transmitted dose under homogeneous phantom conditions in a water equivalent medium. The predicted dose distributions were compared with the transmitted dose measured by a calibrated SLIC-EPID. The dosimetric uncertainty in the calibration of the EPID was estimated to be $\pm$ 0.52 %. The performance of the planning system dose calculations under varying conditions was evaluated by comparing predicted doses for a range of phantom thicknesses (4–30 cm) with corresponding EPID measurements and by simulating isocentric and fixed SSD set ups using 6 MV photon beam with a 10 $\times$ 10 cm^2 field size at zero gantry angle. The gamma evaluation tool was used to quantify any differences between the measured and predicted 2D dose distributions. A gamma score of 90 % or more was used as a benchmark for an acceptable agreement between measurement and

calculation. In addition, since the accuracy of the dose calculations should not change under varying geometrical conditions, gamma scores at or near 90 % were deliberately set for all phantom thicknesses by varying dose-difference and distance-to-agreement criteria, in which 3.7 %/3.8 mm (on average) criteria produced an average gamma score of 91 % for all phantom thicknesses, for both isocentric and fixed SSD set ups. The pixel-to-pixel variations (standard deviation) on the central beam axis of measured and predicted dose distributions were evaluated as a function of phantom thickness. The standard deviation in measured EPID dose generally increased with increasing phantom thickness from 0.2 % for the thinnest phantom up to 0.8 % for the thickest phantom. In contrast, the standard deviation in calculated dose was generally constant with phantom thickness and did not exceed 0.1 %. Based on this, the minimum change in phantom thickness that could be evaluated from the predicted transmitted dose on the central axis was ± 1 mm. Given the accuracy of the treatment planning system dose calculations (3%/4 mm) under these conditions and the uncertainties in measured EPID doses (± 0.52 %), the transmitted dose predicted by Pinnacle^3 is an accurate representation of the transmitted dose as measured in the clinic. Once this sensitivity and accuracy of the Pinnacle^3 calculations have been confirmed the planning system can be used for the assessment of more complex and clinical scenarios as reported in subsequent chapters.

Chapter 4

Resolution of Pinnacle^3 dose calculations for predicting changes in transmitted dose

4.1 Introduction

In order for Pinnacle^3 to be a useful tool for evaluating the efficacy of transmission dosimetry for patient dose verification, the resolution in the transmitted dose calculations should be able to identify clinically relevant dose delivery errors, simulated in the planning system. In this chapter, transmitted dose distributions were modelled by the Pinnacle^3 treatment planning system for a variety of geometrically simple but realistic phantoms. The resolution of the transmitted dose calculations were evaluated by deliberately introducing small inhomogeneities into homogeneous phantoms to simulate, for example, the presence and movement of gas pockets inside the patient. Homogeneous cylindrical phantoms of two different sizes were used to determine the impact of patient contours on transmitted dose resulting from relative shifts between the radiation field and patient anatomy. Anthropomorphic phantoms of the pelvis, head and neck and chest regions were used to assess the impact of geometrical shifts on the predicted transmitted dose calcu-

lations in the combined presence of surface contours and heterogeneities. The predicted dose changes were quantified in two-dimensions and on the central axis to demonstrate the limitations of assessing transmitted dose at single point in the radiation field.

4.2 Materials and methods

4.2.1 Predicting the presence of small inhomogeneities

In the following subsections CT scans of the homogeneous phantom, air gap and and EPID (water-equivalent) configuration used in Chapter 3 were imported into a new Pinnacle^3 plan. A 6 MV photon beam defined with a 10 $\times$ 10 cm^2 field size was used to simulate an isocentric delivery with the isocenter located at the geometric center of the phantom. The resolution of the transmitted dose calculations was tested by creating the smallest possible Region Of Interest (ROI) on the central beam axis and assigning it a density of 0 g/cm^3. The dimensions of the ROI were 0.1 $\times$ 0.1 $\times$ 0.5 cm^3. Transmitted dose calculations obtained before and after the inhomogeneity was introduced in the homogeneous phantom, were compared. In case no changes occurred in the calculated dose distributions, the size of the inhomogeneity was gradually increased, separately along the width and height of the ROI from 0.1 – 5.0 cm (figure 4.2.1 (a)) and 0.1 – 1.5 cm (figure4.2.1 (b)), respectively.

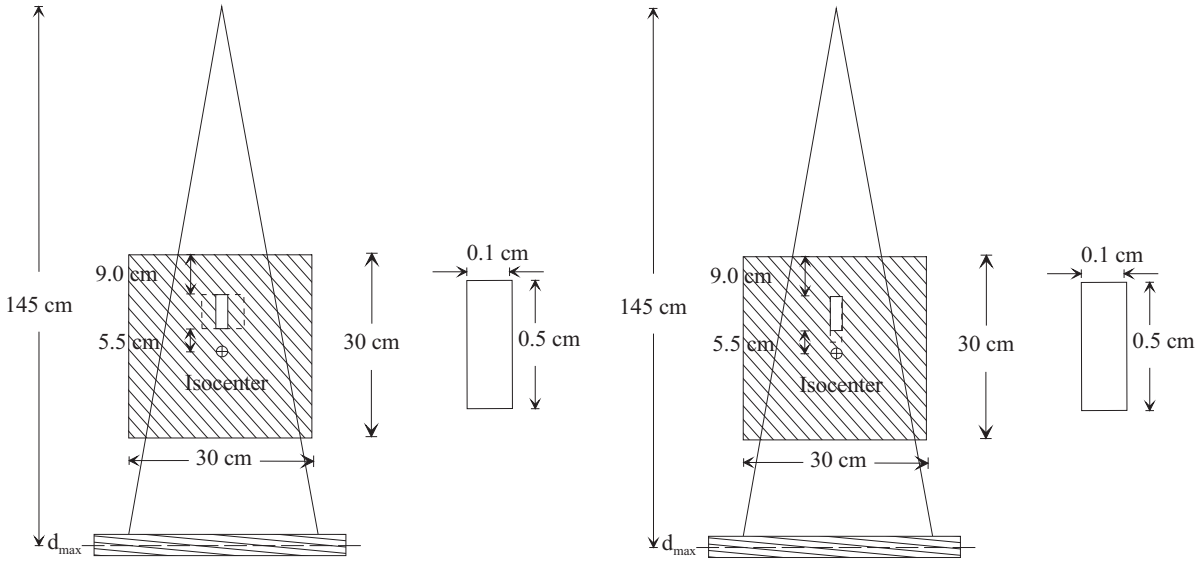

Figure 4.2.1: *Model of an inhomogeneity inside a homogeneous phantom using Pinnacle^3. (a) Set up for increasing the width of the inhomogeneity from 0.1 – 5 cm. (b) Set up for increasing the height of the inhomogeneity from 0.5 –1.5 cm.*

4.2.2 Predicting shifts in inhomogeneity position

Of clinical concern are the possible dosimetric errors pertaining to the displacement of target volume, internal organs and bowel motion (eg air pockets) over the course of treatment. The purpose of this study was to simulate the progressive displacement of an inhomogeneity in order to evaluate how these shifts are reflected in the transmitted dose and how sensitive the transmitted dose is to the progressive shifts. The inhomogeneity was modelled as a $5 \times 5 \times 5$ cm^3 ROI with the same density used above. The center of the inhomogeneity was initially aligned on the central beam axis, 4 cm below the surface of the larger phantom (figure 4.2.2). The inhomogeneity was displaced laterally from 0–8 cm of the central axis. Separate dose calculations were performed at each incremental shift to evaluate any changes in transmitted dose.

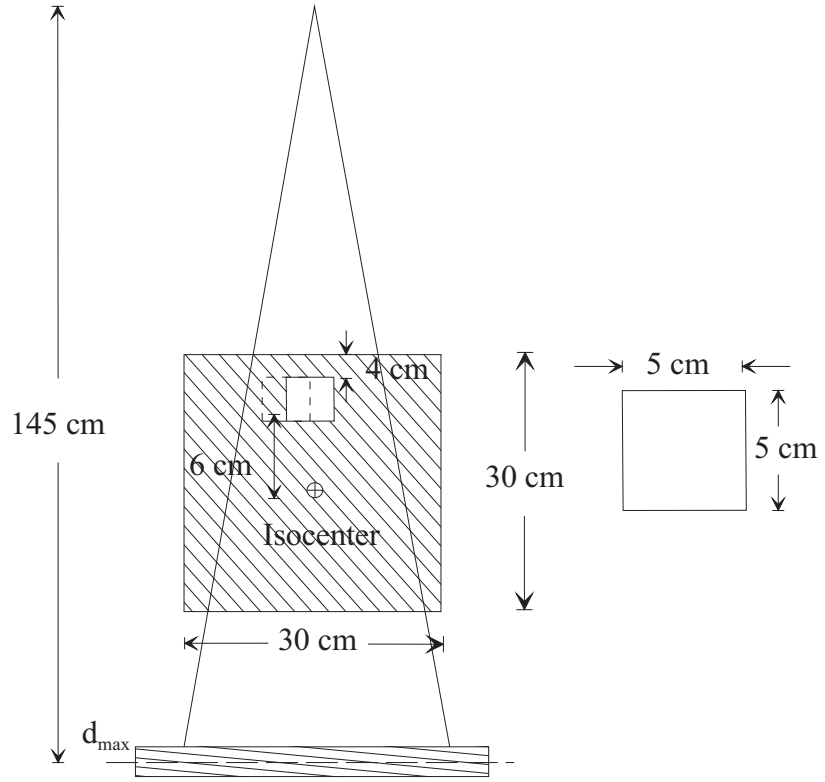

Figure 4.2.2: *The 5 × 5 × 5 cm^3 inhomogeneity used for simulating inhomogeneity displacements off-axis from 0 – 8.0 cm.*

As a complementary study, a 2 cm by 30 cm wide inhomogeneity (ρ = 0 g/cm^3) inside a 20 cm thick phantom (modified from the original CT phantom scans from Chapter 3) was displaced along the central beam axis. The inhomogeneity was chosen to be the same width of the phantom (30 cm) in order to avoid geometric magnification as the inhomogeneity is shifted towards and away from the beam focus. The ROI was positioned at three different positions as shown in figure 4.2.3. The first position was 4 cm above the isocenter, then at the isocenter, followed by 5 cm below the isocenter. The predicted transmitted dose distribution corresponding to the three positions were then compared. The purpose of this exercise was to determine whether the transmitted dose calculations performed in the "virtual" EPID model correctly predict little or no change in the transmitted dose distribution for each of the three scenarios, as to be expected by performing EPID measurements. An empirical investigation, previously performed

by a colleague confirmed this [6]. A calibrated SLIC-EPID was used to measure the 2D transmitted dose resulting from 6 MV photons incident on homogeneous layers of RW3 material, containing a rectangular slab of foam (with a density close to air) sandwiched between the RW3 layers. The transmitted dose distributions were compared for different placements of the foam layer along the central beam axis. Insignificant differences (< 0.5 % on the central axis) in the in-plane and cross-plane beam profiles of the virtual EPID were observed.

In all the above sections, 300 MU were prescribed to the phantoms and dose calculations were performed using the collapsed-cone superposition dose engine on a $0.25 \times 0.25 \times 0.25$ cm^3 calculation grid.

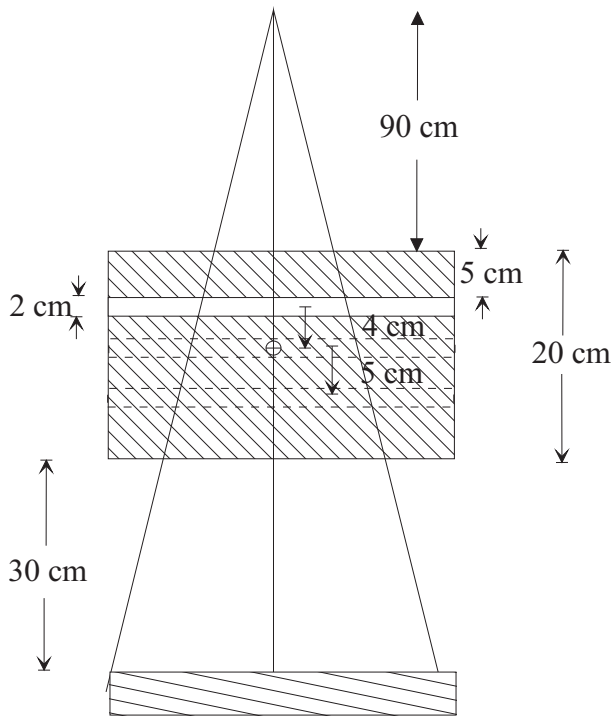

Figure 4.2.3: *The semi-infinite inhomogeneity contained inside a 20 cm thick phantom for simulating displacements at three different depths.*

4.2.3 Predicting changes in transmission in presence of surface contour

Since patient geometry is usually not rectilinear especially at treatment sites such as the head and neck and breast, it is important to simulate transmission dosimetry under these conditions. Furthermore, curved patient contours present a potentially greater risk for dosimetry errors compared with flatter geometries due to the change in tissue thickness across the beam. Furthermore, wedges used to compensate for missing tissue (due to patient curvature) in breast and head and neck, for example, are prone to patient positioning errors as well as possible wedge positioning errors (or incorrect wedge/wedge orientation), which can lead to undetected dosimetry errors. The curved surfaces of two different size cylinders were used to simulate the surface of a patient. Relative shifts between phantom geometry and beam path were introduced to simulate a delivery error influenced solely by a patient's surface contour and to determine whether the changes are sensitive at the transmitted dose level. The first cylinder consisting of perspex material of a 19.5 cm diameter, was used to represent the surface of a patient's abdomen or chest. The second cylinder consisted of paraffin wax with a smaller diameter of 10.5 cm which has a similar contour of a patient's head or body extremity. The cylinders were each scanned using a Philips AcQSim CT scanner (Philips Medical Systems, Cleveland, Inc.) with RW3 material to simulate the presence of an EPID (figures 4.2.4 (a) and (b)). Due to the extra long scan length, the optimum CT pitch and fan separation was 2 mm and 3 mm, respectively.

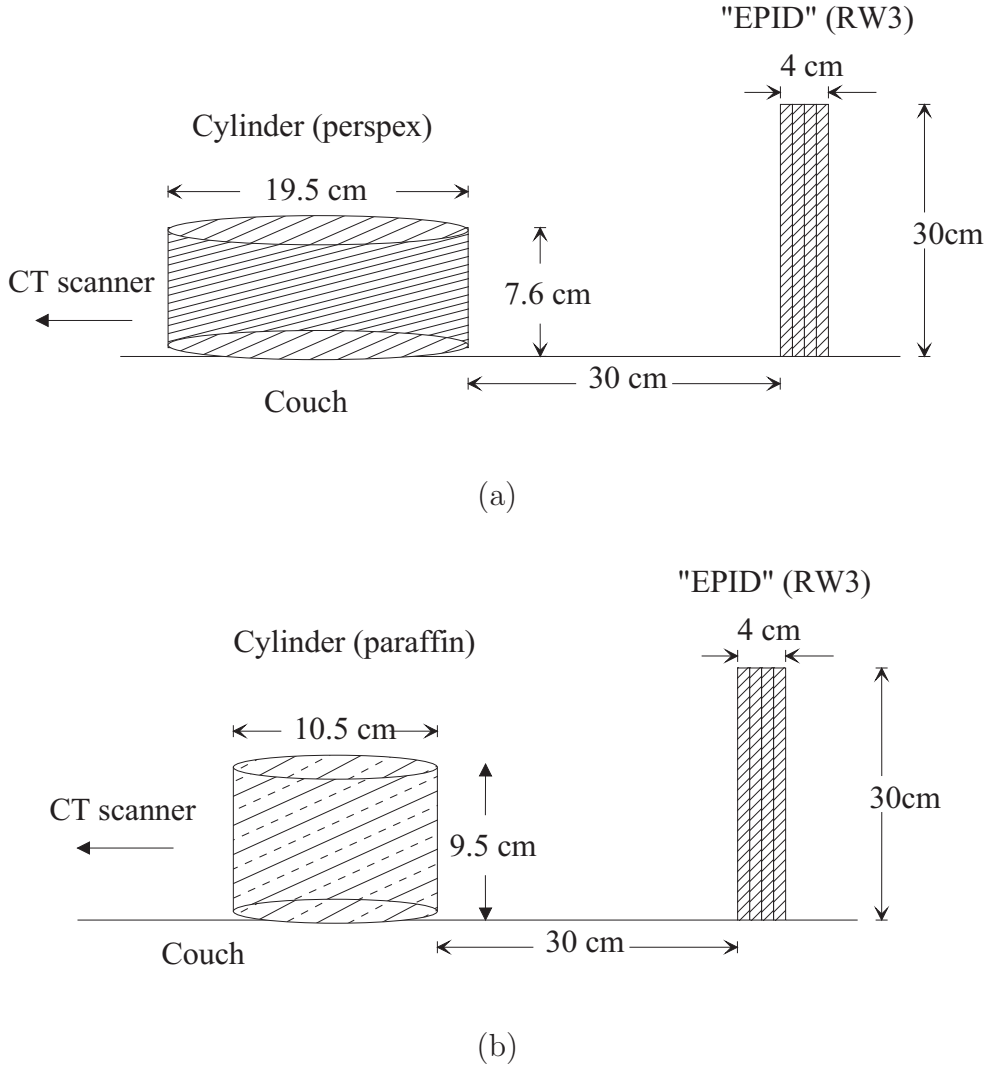

Figure 4.2.4: *Set up for CT scanning the two cylindrical phantoms and EPID representation. (a) Large cylinder. (b) Small cylinder.*

The CT images were then imported as DICOM files into a Pinnacle^3 workstation under separate patient plans. In order to eliminate other variables contributing to the transmitted dose (other than surface curvature) CT density values caused by imperfections or drilled holes in the cylinders) were overridden. A 6 MV beam was created for each plan. Due to the configuration of the cylinders and EPID phantom on the CT couch, the couch and beam had to be rotated 90^0 to ensure the central axis of the beam passed through the common axes of the cylinder and EPID phantom (refer back to Chapter 3). For the

large cylinder, a field size of 4 × 10 cm^2 (*width* × *length along cylinder axis*) was defined with the isocenter placed at the geometric center of the cylinder. Similarly, for the small cylinder, a field size of 6 × 4 cm^2 (*width* × *length along cylinder axis*) with the isocenter placed at the geometric center of the cylinder. The field sizes for each cylinder were chosen so that they did not overshoot the edges of the phantom to avoid dose differences occurring outside the phantom. That is, the purpose was to investigate the magnitude of dosimetry errors restricted to within the phantom itself, as caused by the effects of surface curvature only. For each cylinder, dosimetry errors were simulated by introducing relative shifts between the phantom and beam path of 0.5–3.0 cm, perpendicular to the central beam axis (figure 4.2.5).

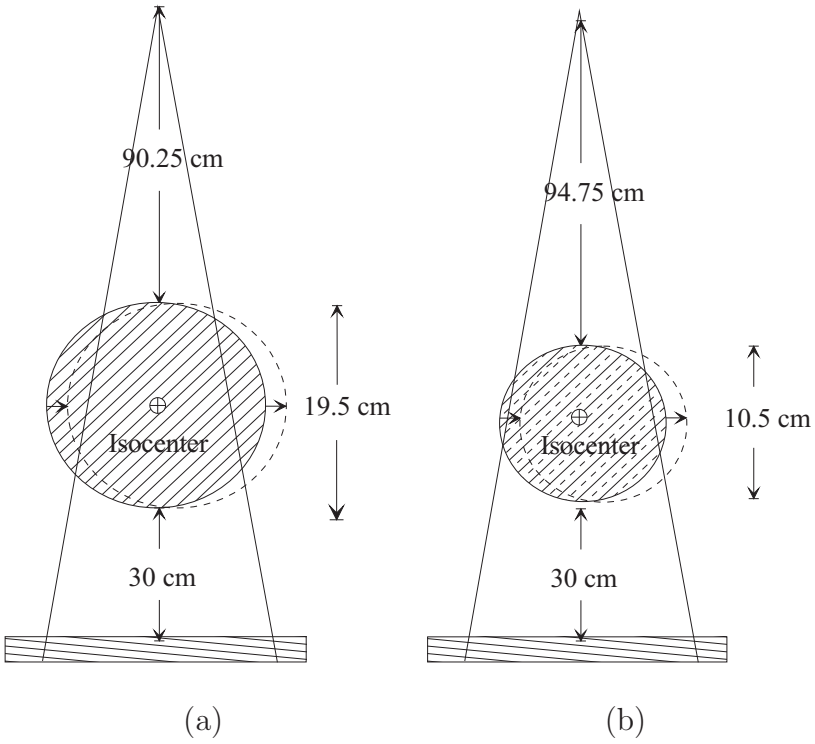

Figure 4.2.5: *Pinnacle^3 plans of the cylindrical phantoms for simulating relative beam displacements (0.5 - 3.0 cm).(a) Large cylinder and (b) Small cylinder.*

A homogeneous phantom containing a more realistic patient contour was also used in relation to the current study. The phantom consisted of a pelvic section (middle 9 physical slices) from an Alderson Rando phantom (Phantom Laboratory, Salem, NY) as pictured in figure 4.2.6. A CT scan of the phantom was acquired using the same approach outlined above. The CT images were imported into the planning system and modified to have a uniform density of 1.00 g/cm^3. This eliminates the heterogeneities inside the phantom so that any changes in transmitted dose due to relative shifts may be compared with those resulting from the cylindrical phantoms. For the pelvic phantom relative shifts in the radiation field of 0.5 – 2.0 cm were introduced to keep the shifts within a clinically relevant range.

Figure 4.2.6: *A pelvic section from Rando used for the surface contour study.*

4.2.4 Predicting changes in transmission in presence of surface contour and heterogeneities

Finally, the combined effects of patient contour and heterogeneities on the transmitted dose distribution were investigated using two anthropomorphic phantoms. From a radia-

tion interaction point-of-view anthropomorphic phantoms are anatomically accurate and tissue equivalent models of a human. Rando, the first phantom was disassembled into a head and neck phantom (first 11 physical slices) as shown in figure 4.2.7(a). The second class of phantom (not part of Rando) comprised of a left breast and internal lungs (figure 4.2.7(b)). Both phantoms provided potentially different treatment sites for evaluating transmitted dose.

(a)

(b)

Figure 4.2.7: *Anthropomorphic phantoms. (a) Rando head and neck phantom and (b) breast and lung phantom.*

The phantoms were each scanned using the AcQSim CT scanner which included a 30

cm air gap followed by rectangular blocks of RW3 material (5 cm) for calculating the transmitted dose. Due to the curved surface of the phantoms, the 30 cm air gap was measured from the most protruding edge of the phantom to the surface of the rectangular blocks. The CT images were exported in DICOM format across the hospital network and imported into 3 separate Pinnacle^3 patient plans. For each phantom, a single (anterior-posterior) beam was incorporated into the plans for investigating the influence of the heterogeneities on the transmitted dose. For the breast phantom, an open 6 $\times$ 8 cm^2 (*lateral* $\times$ *sup-inf*) field was sufficient to cover the entire breast with the isocenter located below the breast near the geometric mid-plane of the phantom. This field placement takes full advantage of the curved surface of the breast as well as underlying heterogeneities provided by the lung tissue. Similarly, for the head and neck phantom, the isocenter was placed along the midline (sagittal axis) of the head, below a large air cavity of the mouth. A field size of 10 $\times$ 10 cm^2 was used to provide sufficient coverage of the head without overshooting the edges of the phantom. Dosimetric errors were incorporated into the plans by introducing relative shifts of 0.25 – 1.0 cm between the beam path and phantom geometry.

4.3 Results

4.3.1 Predicting the presence of small inhomogeneities

The Pinnacle^3 dose calculation resulting from the small inhomogeneity inside the large homogeneous phantom is shown in figure 4.3.1. The upper insert in the figure is an expanded view, showing the 0.1 $\times$ 0.1 $\times$ 0.5 cm^3 ROI with a density of air. The lower insert shows a small but perceptible influence on the isodose lines on the central axis due to the presence of the inhomogeneity above.

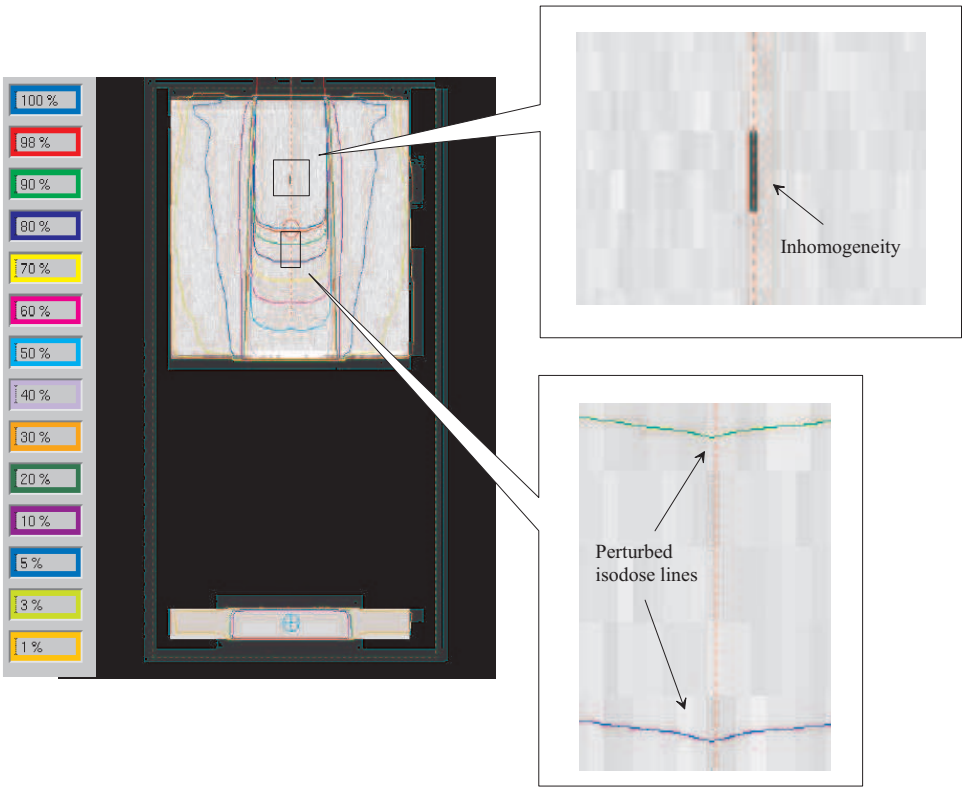

Figure 4.3.1: *The dose distribution calculated by Pinnacle*[3] *for the 0.1 x 0.1 x 0.5 cm inhomogeneity. Insert(upper): a magnified view of the inhomogeneity on the central axis. Insert(lower): a magnified view of the slightly perturbed isodose lines as a result of a small inhomogeneity present above.*

Cross-plane beam profiles extracted at the transmitted dose plane show a dose difference of 0.5 ± 0.02 % [1] (1σ) on the central axis due to the presence of the inhomogeneity (figure 4.3.2 (a)). The dose difference on the central axis increased with the gradual increase in width of the inhomogeneity from 0.1 – 5.0 cm, due to the increase in lateral scatter generated inside the inhomogeneity. The increase in scatter with width also contributed

[1]The dose uncertainty of 0.02 % was estimated by calculating the standard deviation in dose of a 2 × 2 array of pixels centered on the beam axis.

to greater noise in the profiles. Nevertheless, the increase in dose with width leveled off to 2 – 2.5 %, corresponding to a width of about 2 cm at which the scatter contribution from the inhomogeneity reached a maximum (figure 4.3.2 (b)).

Similarly, even for the small range of changes introduced into the height of the inhomogeneity (0.5, 1.0 and 1.5 cm) a similar change in the dose profiles were observed (figure 4.3.2 (c)). It is interesting to note that the slope in dose versus height (figure 4.3.2 (d)) is less than the slope of dose versus width, due to the forward scatter contribution being less than the side scatter. Although not shown in figure 4.3.2 (d), the transmitted dose on the central beam axis is eventually expected to decrease with increasing inhomogeneity height as the primary beam becomes more attenuated.

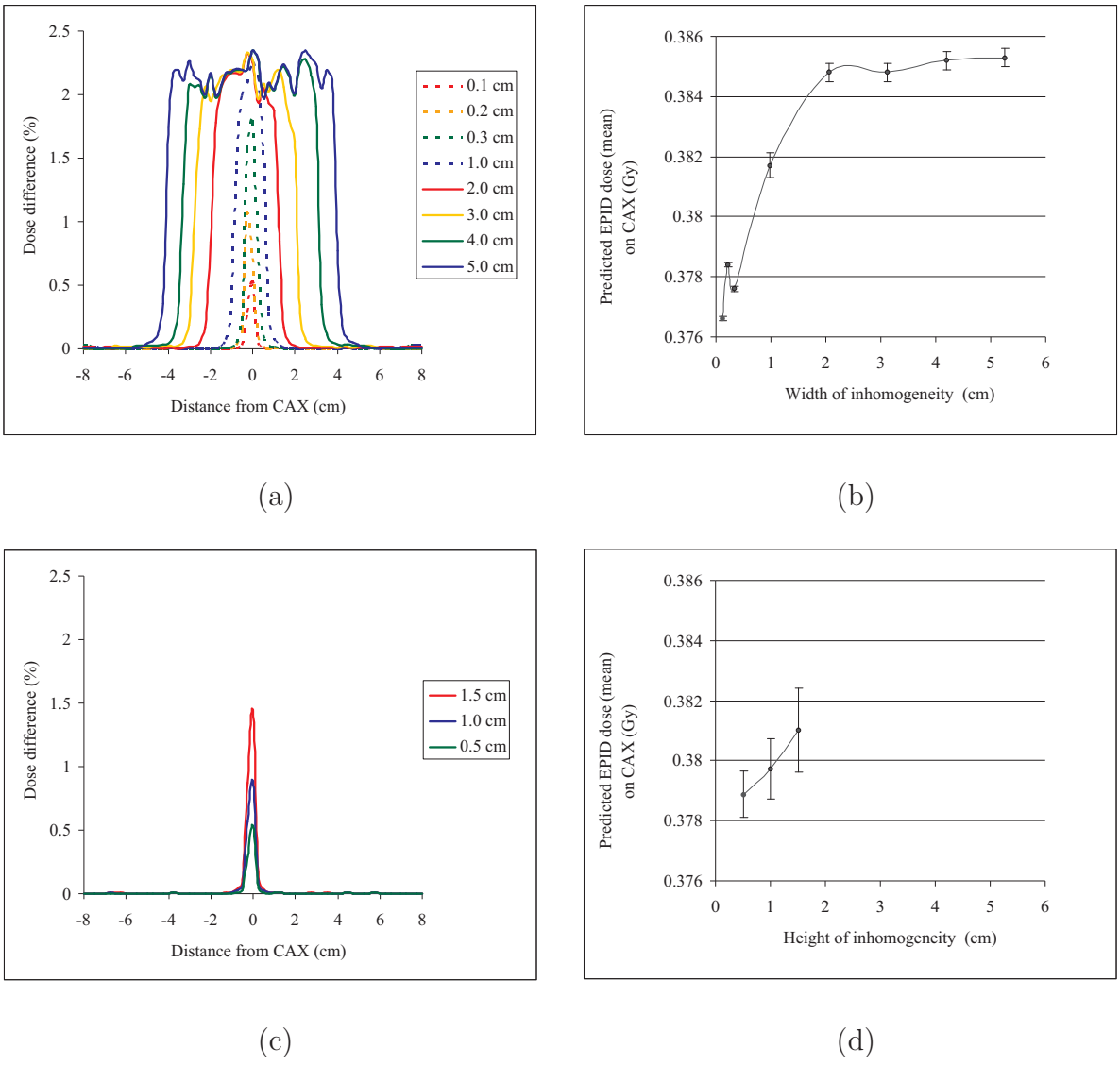

Figure 4.3.2: *(a) Cross-plane beam profiles ((a) and (c)) predicted at the transmitted dose plane for the different sized inhomogeneities and predicted transmitted doses on the central axis as a function of inhomogeneity size ((b) and (d)). NB. Dose differences displayed in each graph represent "reference" plan subtracted from "perturbed" plan, and normalised to the central axis of the reference plan beam profiles.*

4.3.2 Predicting shifts in inhomogeneity position

The Pinnacle^3 dose calculation resulting from the $5 \times 5 \times 5$ cm^3 inhomogeneity introduced on the central axis of the homogeneous phantom is shown in figure 4.3.3 (a). In addition, the dose was calculated on the central axis as the inhomogeneity was shifted laterally from

0.1 – 8.0 cm of the central axis and is recorded in figure 4.3.3(b). This figure illustrates that the minimum shift required to cause a significant change in central axis dose is 2.6 cm, which is equivalent to the Full-Width Half-Maximum (FWHM) of the graph. From a clinical perspective, if transmission or exit dosimetry was performed at a single point such as the central axis, it is possible, for example that the displacement of an air pocket inside the patient would go undetected. This could potentially lead to clinically significant dosimetry errors immediately below the air pocket. This highlights the importance of 2D dosimetry compared with single point measurements. The magnitude of the errors were thus further investigated off-axis by plotting beam profiles at the transmitted dose plane (figure 4.3.4). From figure 4.3.4 (a) it is evident that significant dose differences of more than 2 % occur off-axis for shifts as small as 0.1 cm. The dose differences reached up to 11 % for the largest shift shown in figure 4.3.4(d).

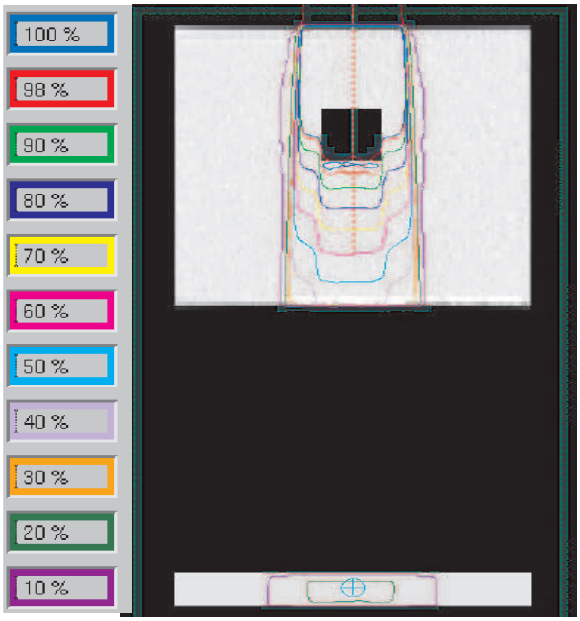

(a)

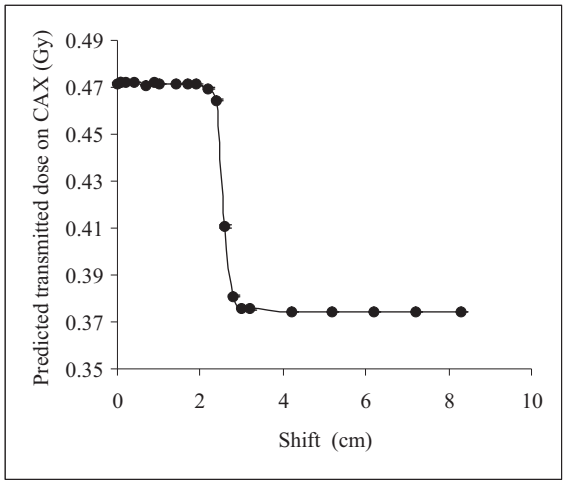

(b)

Figure 4.3.3: *(a) The dose distribution calculated by Pinnacle^3 for the 5 × 5 × 5 cm^3 inhomogeneity. (b) Predicted transmitted dose on the central axis versus displacement in inhomogeneity. NB All plotted points contain error bars but are too small to be visible with the vertical scale.*

Figure 4.3.5(a) are the predicted beam profiles at the transmitted dose plane resulting from the the 2 cm thick, semi-infinite plane of air density ROI displaced at different positions vertically along the central axis. Clearly, there is very little change in transmitted dose, which is to be expected since the beam path is effectively identical in all three scenarios.

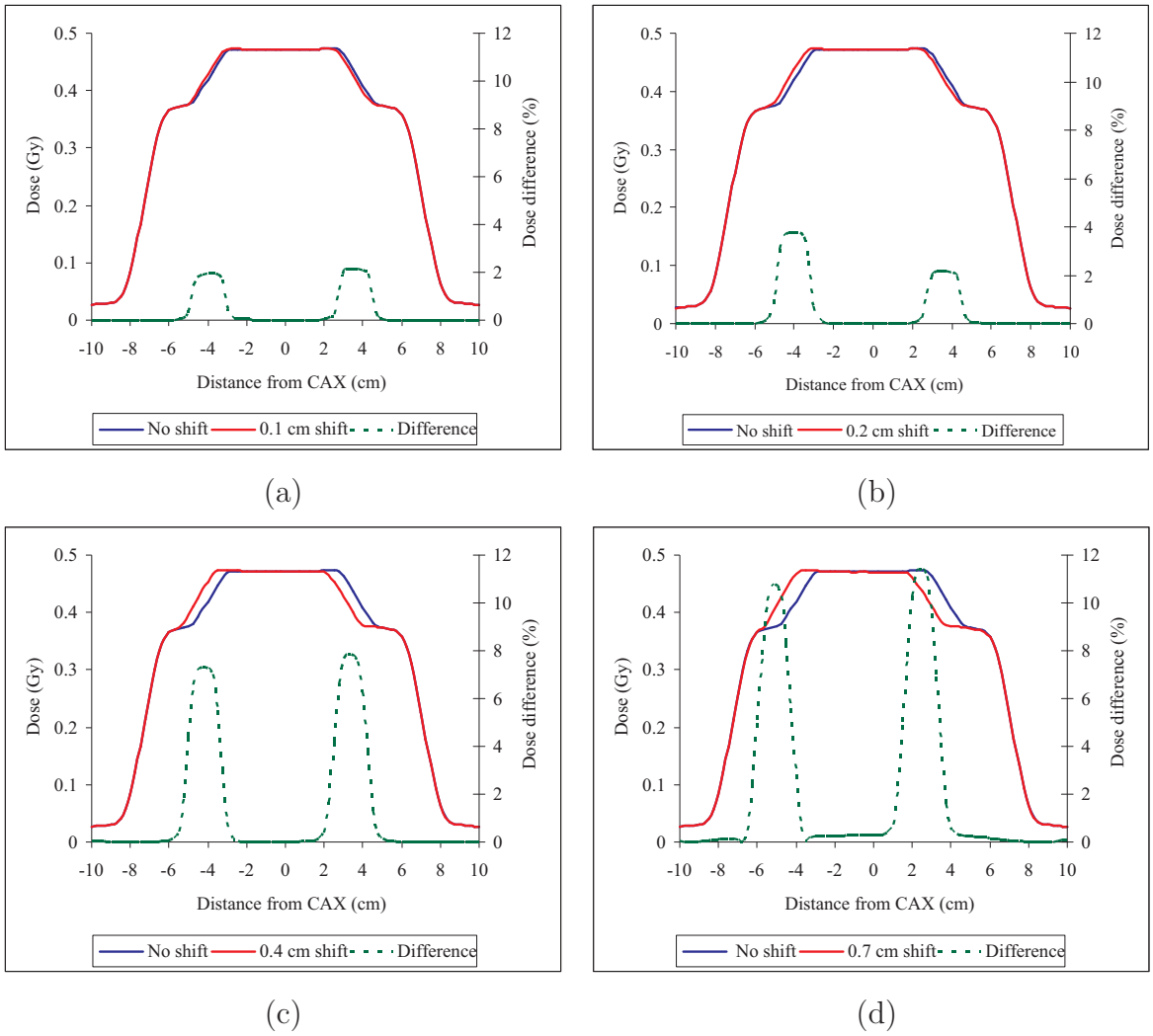

Figure 4.3.4: *Cross-plane beam profiles in the transmitted dose plane resulting from the off-axis inhomogeneity shifts of (a) 0.1 cm, (b) 0.2 cm, (c) 0.4 cm, and (d) 0.7 cm.*

The maximum variations in dose were within 0.5 % and were observed off-axis (see inserts of figure 4.3.5). It is interesting to note in the two inserts, systematic differences in dose depending on the position of the inhomogeneity relative to the central axis. For example, the dose off-axis is slightly greater when the inhomogeneity is located below the central axis compared with when it is above the central axis. This effect may be due to the modelling of the beam spectrum in Pinnacle^3. At larger depths, the spectrum may be different compared to closer to the surface of the phantom where softer x-rays are

still present. This difference may then correspond to the small dose difference observed in the calculation. However, in practice this most likely would not be observed under experimental conditions with an EPID due to the uncertainty and noise in the measured data.

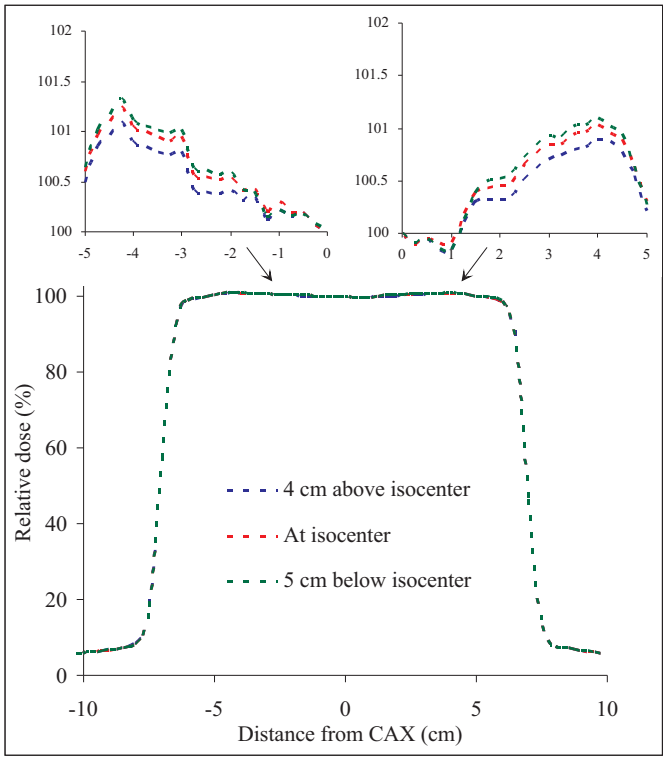

Figure 4.3.5: *Predicted cross-plane beam profiles in the transmitted dose plane resulting from the semi-infinite inhomogeneity at three different depths inside the phantom. The two inserts are magnified views of the beam profiles 5 cm off-axis.*

4.3.3 Predicting changes in transmission due to surface contour

The dosimetric impact due to a relative shift between radiation beam and phantom with a curved surface is expected to be greater than for a phantom with a flat surface due to the variation in tissue thickness perpendicular to the central beam axis. This potentially makes dosimetric errors, and consequently differences in transmitted dose to be more easily identified. A patient's surface contour was initially simulated using two different sized cylindrical phantoms made from tissue equivalent material. A large diameter cylinder was used to simulate a low gradient surface and a smaller diameter cylinder was used to simulate a high gradient surface. In addition, an anthropomorphic pelvis phantom was used to simulate a patient's contour more realistically. The heterogeneities present in the original CT images of the phantom were removed to isolate as best as possible dosimetric effects caused by the surface contours alone. The predicted dose distributions resulting from each of the phantom geometries is shown in figures 4.3.6 and 4.3.7.

In all three phantoms, the doses on the central beam axis in the transmitted dose plane were evaluated as a function of displacement error relative to the central axis. For the two cylinders, the transmitted dose on CAX was found to increase with increasing displacement (figure 4.3.8). As expected, the smaller cylinder produced greater changes in dose on the central axis than the large cylinder for the same sized shifts due to the greater fall off in tissue thickness. In contrast, for the pelvis phantom the variation in dose with shift was not as straightforward. The transmitted dose decreased from 0–1.5 cm shifts before increasing beyond shifts of 1.5 cm. This initial decrease in dose was a result of the small concave region occurring at the the buttocks of the phantom (figure 4.3.7). In the cylindrical phantoms, a 1 cm displacement produced a change in the transmitted dose on the central axis of less than 1 % and less than 2 % for the pelvis phantom (figure 4.3.8). This suggests that 1 cm shifts do not produce significant errors.

However, as mentioned in the previous section recording transmitted dose at a single point can lead to misleading results as indicated in the following beam profiles (figure 4.3.9). The profiles reveal that although dose differences of less than 1 % occur on the central

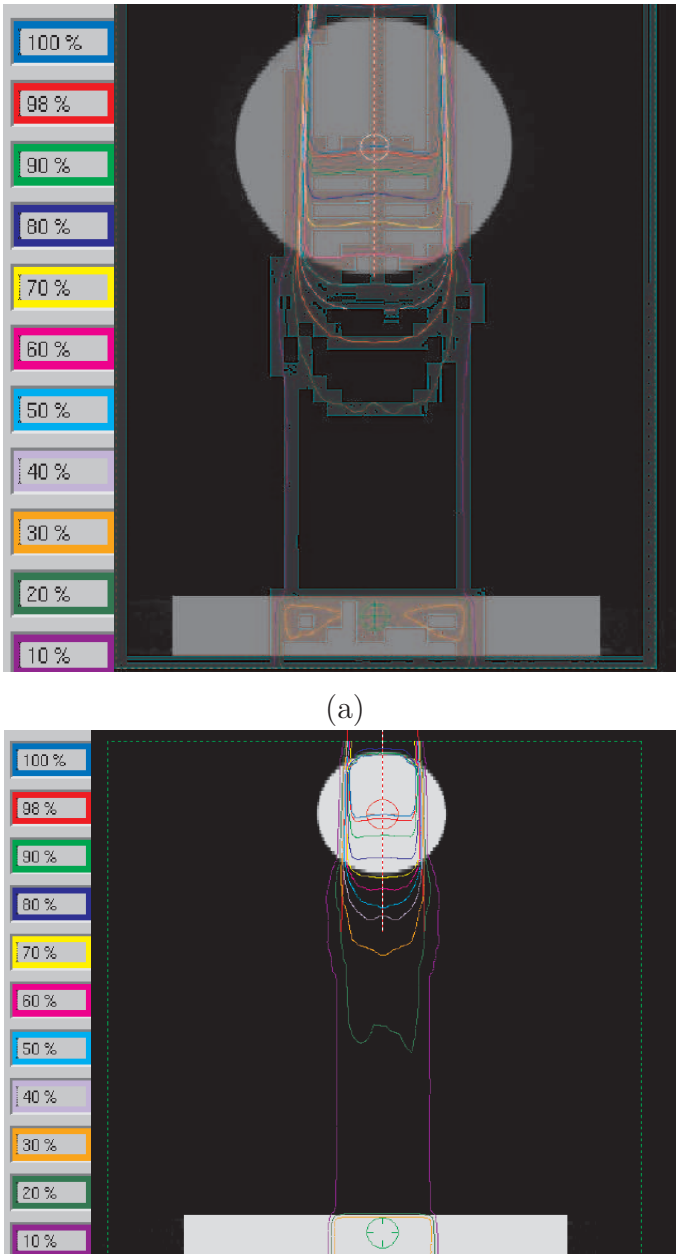

Figure 4.3.6: *Pinnacle*^{3} *isodose distributions calculated for the, (a) large cylinder and (b) Small cylinder.*

axis for the two cylinders, dose differences off-axis of up to 6% and 8 % occur for the large and small cylinders, respectively. Similarly, for the pelvis phantom larger dose differences of up to 3.5 % occur off-axis. In figure 4.3.9, the relative displacement in the cylinders occur to the "left" of the central axis (a "negative" displacement along the x-axis) which

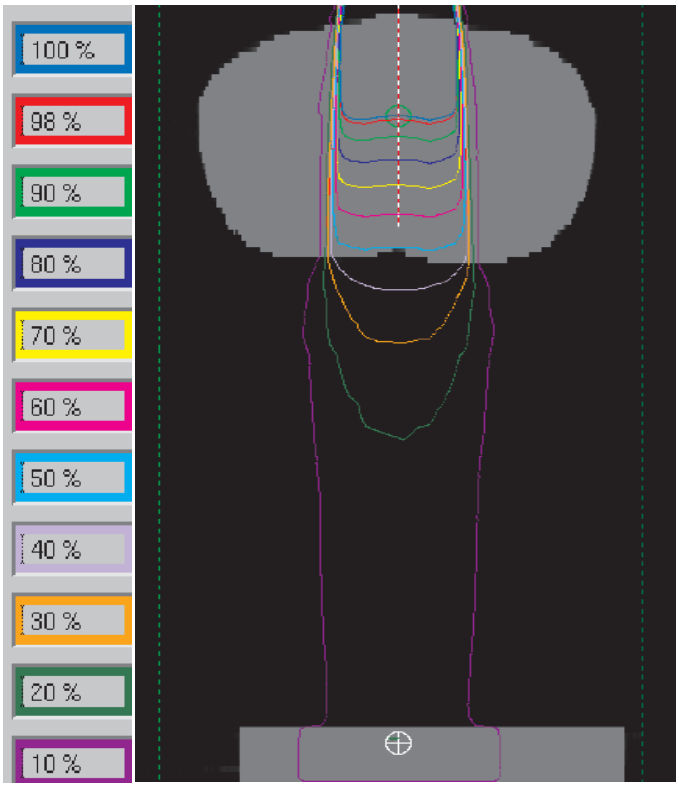

Figure 4.3.7: *Pinnacle^3 isodose distributions calculated for the pelvis phantom.*

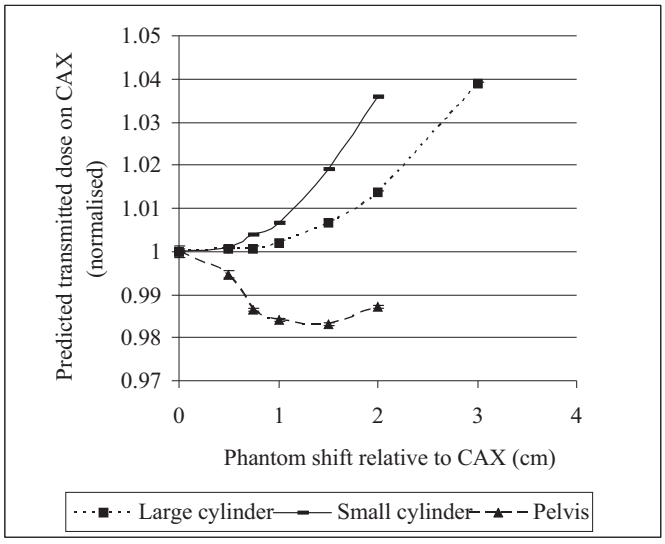

Figure 4.3.8: *Predicted transmitted doses on the central axis for the three homogeneous curved phantoms plotted against relative shift between beam path and phantom geometry. NB All plotted points contain error bars but are too small to be visible with the vertical scale.*

is evident in the distinct horns occurring in the beam profiles (figures 4.3.9 (a)-(c) and (d)-(f)) which become more exaggerated to the "right" of CAX and flatter to the "left" of the central axis. Although, not intuitively obvious from figures 4.3.9 (g)-(i), the relative displacements of the pelvis phantom occur to the "right" of the central axis.

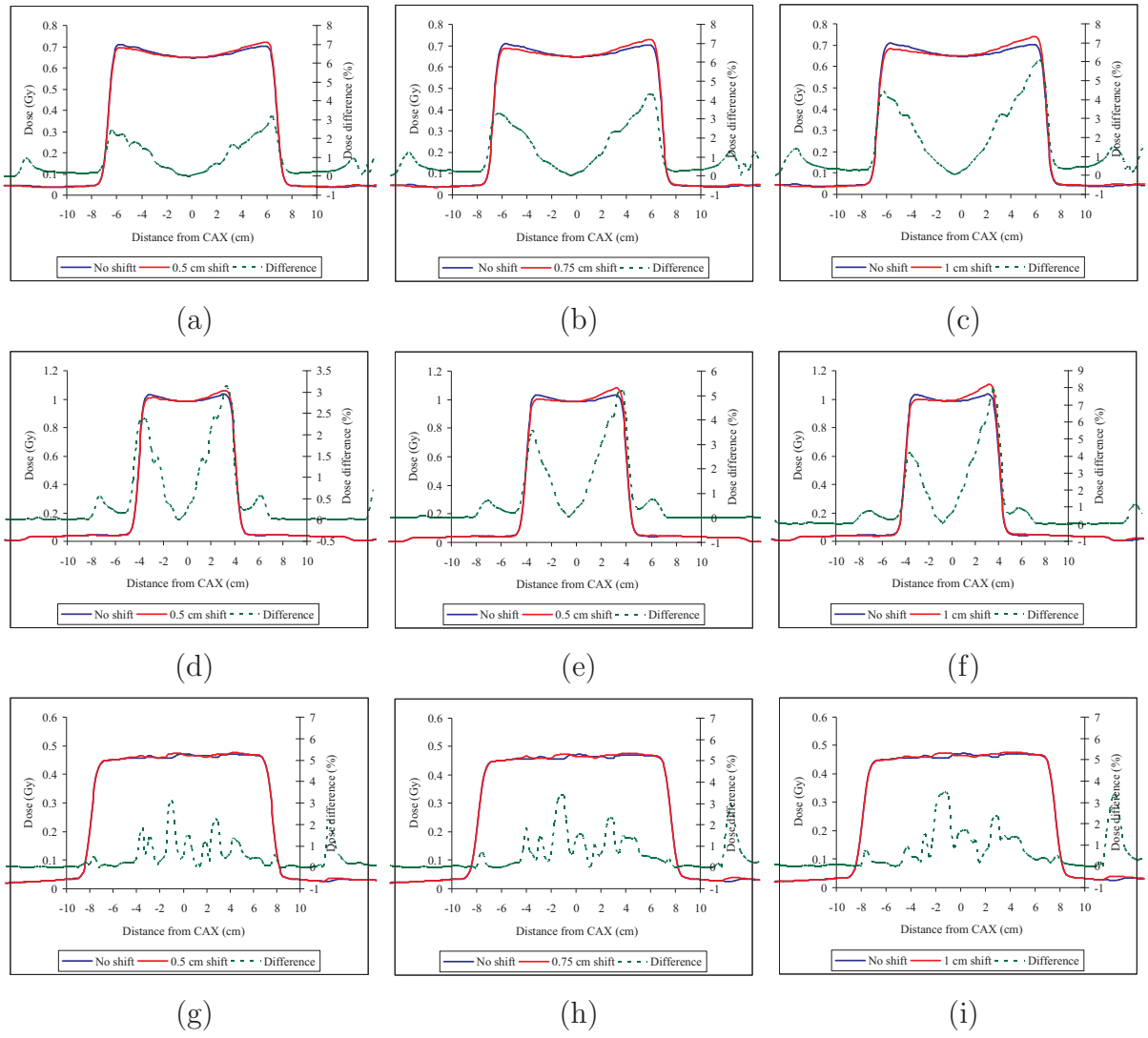

Figure 4.3.9: *Predicted cross-plane beam profiles in the transmitted dose plane resulting from relative beams shifts of 0.5 - 1.0 cm in the large cylinder ((a)–(c)), small cylinder ((d)–(f)), and the pelvic phantom (g)-(i).*

In order to quantify the changes in transmitted dose from a more clinical perspective, the gamma formalism from the previous chapter was used once again. Gamma scores were calculated based on the commonly used 3 %/3 mm gamma criteria [80, 118, 120, 121, 128] to provide an indication of the overall agreement in transmitted dose distributions before and after the relative beam shifts were introduced. Due to the discrete nature of the planning system calculations (2.5 mm grid size), a DTA of 2.5 mm was used instead of 3 mm. In consultation with a visual 2D map of gamma values (where $\gamma \leq 1$ indicates a "pass" and $\gamma > 1$ indicates a "fail") a *gamma score*, defined as the total percentage of data points in agreement was recorded. Although there is no universal consensus on what range of gamma scores constitutes an acceptable dose distribution, a gamma score of 90 % or above has been suggested as a reasonable clinical level of agreement [126, 127] and was adopted here. For the large cylinder, gamma maps (using 3%/ 2.5 mm criteria) resulting from relative displacements between radiation field and phantom geometry are shown in figures 4.3.10(a)–(c).

The grey scale represents regions of agreement (ie gamma values ≤ 1) and the coloured spectrum ranging from blue to red represents mild to strong disagreement, respectively. Based on the clinical gamma criteria, relative shifts of 0.75 –1.0 cm produced gamma scores of 90 % or more. However, by using stricter criteria of 1 %/2.5 mm, gamma scores are significantly reduced to below 90 % for shifts of 0.5 cm (or less). as shown in figures 4.3.10(d)–(f). For the smaller cylinder, using gamma criteria of 3 %/2.5 mm, relative shifts of 0.5 –0.75 cm produced gamma scores of 90 % or more (figures 4.3.11 (a)–(c)). Hence changes in transmitted dose are more sensitive to the same shifts for the smaller cylinder than the larger cylinder, which is to be expected due to the greater surface curvature in the former phantom. However, such shifts are relatively large in magnitude to be producing gamma scores in excess of 90 %. Thus, gamma maps and gamma scores were re-evaluated using tighter criteria of 1%/2.5 mm. This led to significantly reduced gamma scores below 50 %, for shifts of 0.5 cm or less (figures 4.3.11 (d)–(f)). Hence, applying 3 % dose difference gamma criterion to measured transmitted dose maps, would most likely not reveal significant errors in the gamma map analysis. Furthermore, although applying

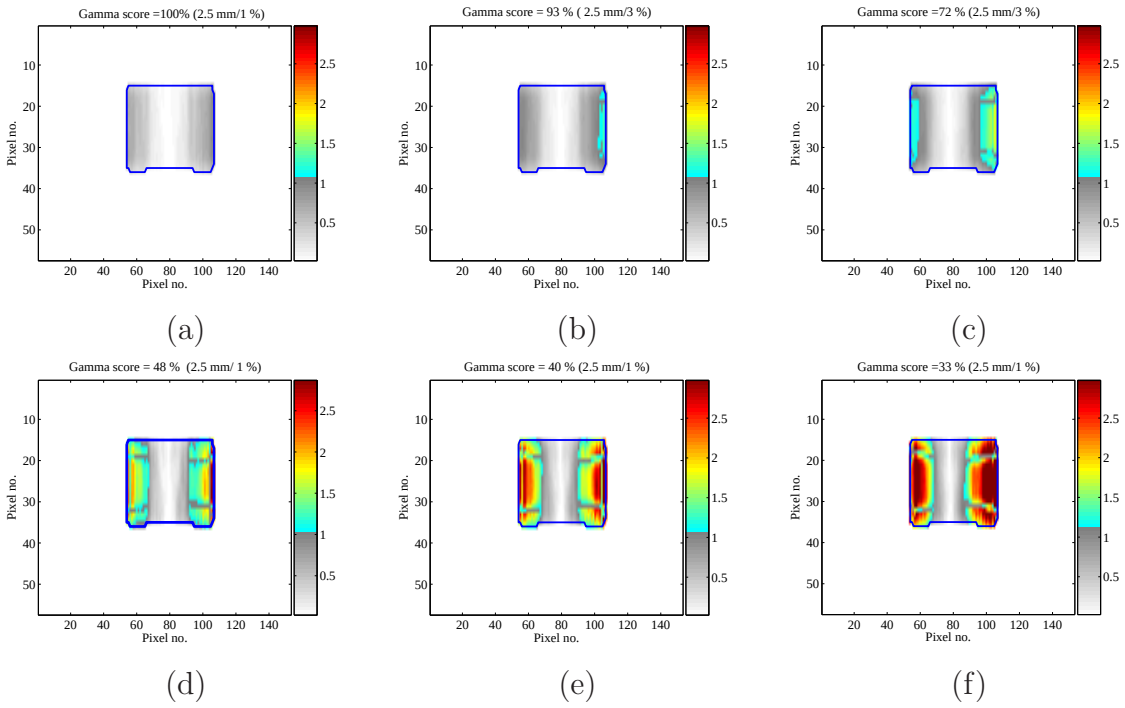

Figure 4.3.10: *Gamma maps and gamma scores calculated within the 50 % isodose lines resulting from relative shifts in the large cylinder. (a), (b) and (c) Relative shifts of 0.5, 0.75 and 1.0 cm, respectively using 3 %/2.5 mm gamma criteria. (d), (e) and (f) Relative shifts of 0.5, 0.75 and 1.0 cm, respectively using 1 %/2.5 mm gamma criteria.*

a tighter dose difference criterion of 1 % would increase the sensitivity of the gamma analysis and hence enhance error detection, in practice, the magnitude of measurement uncertainties may exceed 1 % and thus would mask any dose differences directly related to the displacement errors.

For the pelvis phantom the predicted transmitted dose calculations were significantly less sensitive to displacements. For example, relative shifts of up to 2 cm produced gamma scores above 90 % when adopting 3%/2.5 mm (figures 4.3.12 (a) - (c)), however, adopting the tighter criteria reduced the gamma score considerably below 90 %, for shifts of at least 0.5 cm or more (figures 4.3.12 (d) - (f)). Hence, unless stricter gamma criteria are adopted, changes in transmitted dose may not be very effective in identifying relative shifts between radiation field and patient geometry for regions in the pelvis. However, applying 1 %/ 2.5 mm gamma criteria may be clinically unrealistic compared with 3 %/2.5

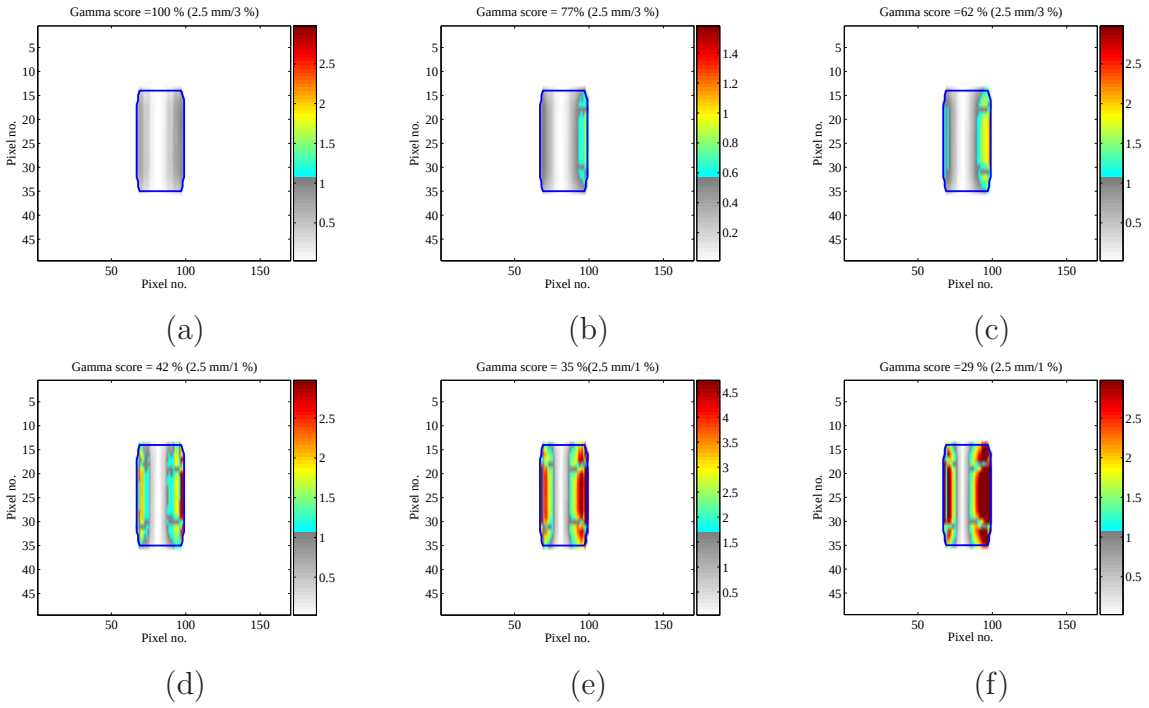

Figure 4.3.11: *Gamma maps and gamma scores calculated within the 50 % isodose lines resulting from relative shifts in the small cylinder. (a), (b) and (c) Relative shifts of 0.5, 0.75 and 1.0 cm, respectively using 3 %/2.5 mm gamma criteria. (d), (e) and (f) Relative shifts of 0.5, 0.75 and 1.0 cm, respectively using 1 %/2.5 mm gamma criteria.*

mm. Hence, the dosimetric changes predicted in the transmitted plane demonstrate that shifts of up to 2 cm may go undetected in the clinic (in regions that are largely flat or homogeneous), unless uncertainties associated with measured transmitted dose maps are less than 1 %.

4.3.4 Predicting changes in transmission in the presence of surface contour and heterogeneities

The impact of relative beam shifts on the transmitted dose was simulated for more realistic patient contours and heterogeneities. An anthropomorphic phantom consisting of a left breast and internal lungs and an anthropomorphic phantom consisting of a head and neck were used to calculate the transmitted dose using a single anterior-posterior beams (figures 4.3.13 (a) and (b)). Anterior-posterior beams were chosen for simplicity and for

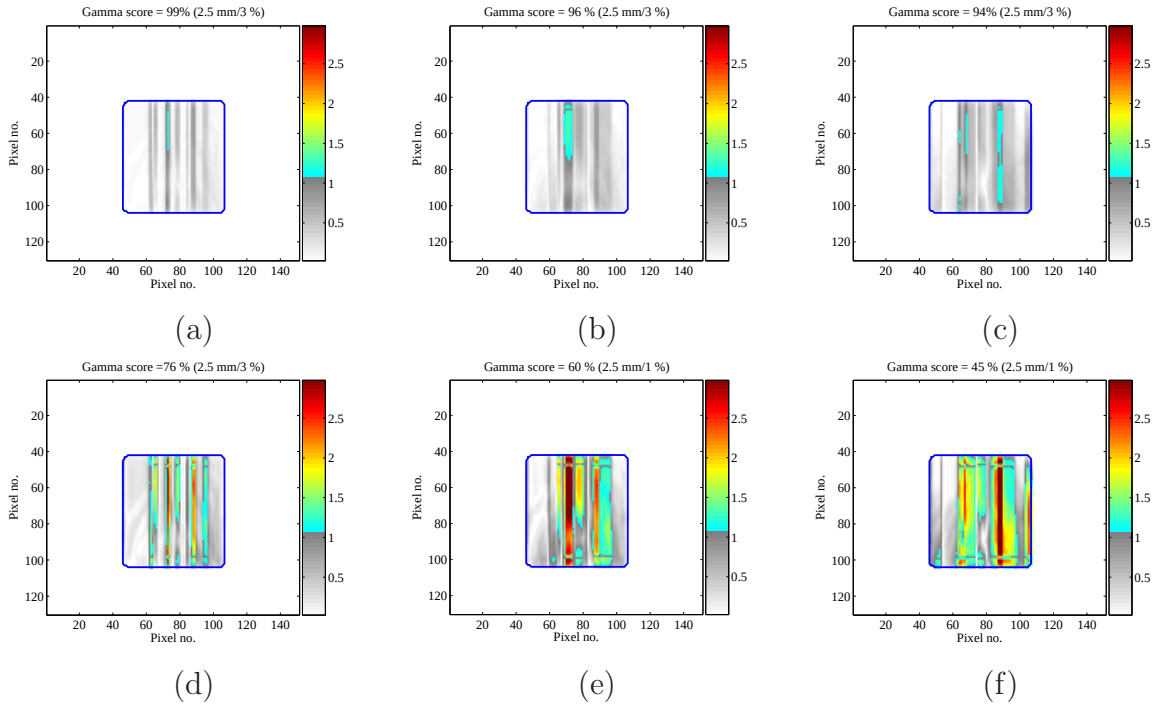

Figure 4.3.12: *Gamma maps and gamma scores calculated within the 50 % isodose lines resulting from relative shifts in the pelvis phantom. (a), (b) and (c) Relative shifts of 0.5, 1.0 cm and 2.0 cm, respectively using 3 %/2.5 mm gamma criteria. (d), (e) and (f) Relative shifts of 0.5, 1.0 and 2.0 cm, respectively using 1 %/2.5 mm gamma criteria.*

comparability with the previous study so that the additional presence of heterogeneities and surface contours on dosimetry errors at the transmitted dose level, can be evaluated. Relative displacements between beam and phantom geometry were simulated by shifting the beam from 0.25 - 1.0 cm, perpendicular to the central beam axis.

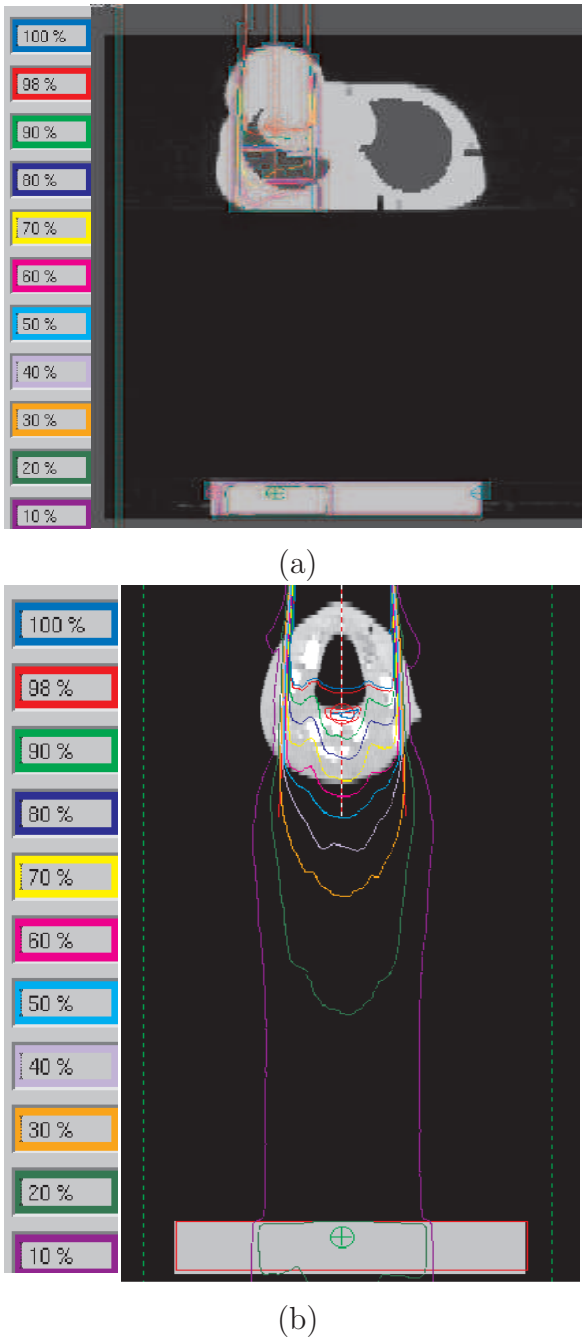

Figure 4.3.13: *(a) Pinnacle^3 isodose distributions calculated for (a) the breast phantom and (b) head and neck phantom.*

The dose on CAX in the transmitted dose plane was recorded as a function of displacement error, followed by a comparison of cross-plane beam profiles and then two-dimensional gamma map analysis. In the breast phantom, the transmitted dose on the central axis

was predicted to be less than 1 % for a 1 cm displacement, in contrast to the more sensitive change in transmitted dose of 2.5 % for the same size displacement in the head and neck phantom (figure 4.3.14).

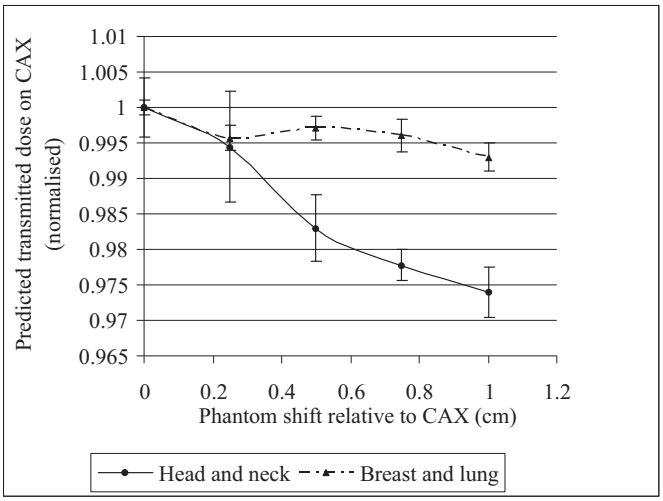

Figure 4.3.14: *Normalised predicted transmitted doses on the central axis for the two anthropomorphic phantoms versus relative phantom shift.*

Beam profiles in the transmitted dose reveal dose differences off-axis of nearly 4 % for displacments as small as 0.25 cm in the breast phantom (figure 4.3.15 (a)) and up to 5.5 % in the head and neck phantom for the same size shift (figure 4.3.15 (d)).

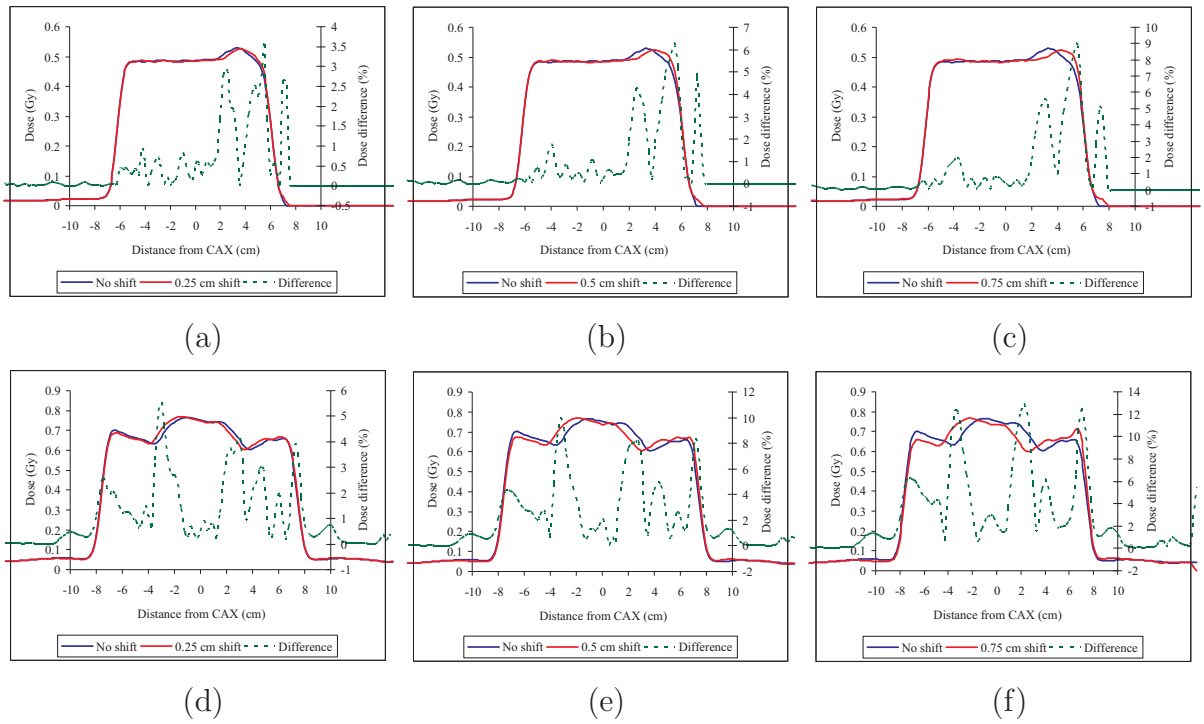

Figure 4.3.15: *Predicted cross-plane beam profiles in the transmitted dose plane for the anthropomorphic phantoms resulting from relative beams shifts of 0.25 - 0.75 cm. (a)-(c) Breast phantom. (d)-(f) Head and neck phantom.*

Two-dimensional gamma analysis of the transmitted dose distributions show that in the breast phantom, displacements in the range 0.25 - 0.50 cm produce gamma scores of 90 % or more when using 3 %/2.5 mm criteria (figures 4.3.16 (a) and(b)). The tighter gamma criteria of 1 %/2.5 mm ensure that shifts down to 0–0.25 cm are detected with gamma scores well below 90 % (figures 4.3.16 (d) and(e)). In the head and neck phantom, changes in transmitted dose distribution are even more sensitive for the same relative shifts. In this case gamma scores were already well below 90 % for shifts of 0–0.25 cm when using both the clinical gamma criteria and the stricter criteria (figure 4.3.17).

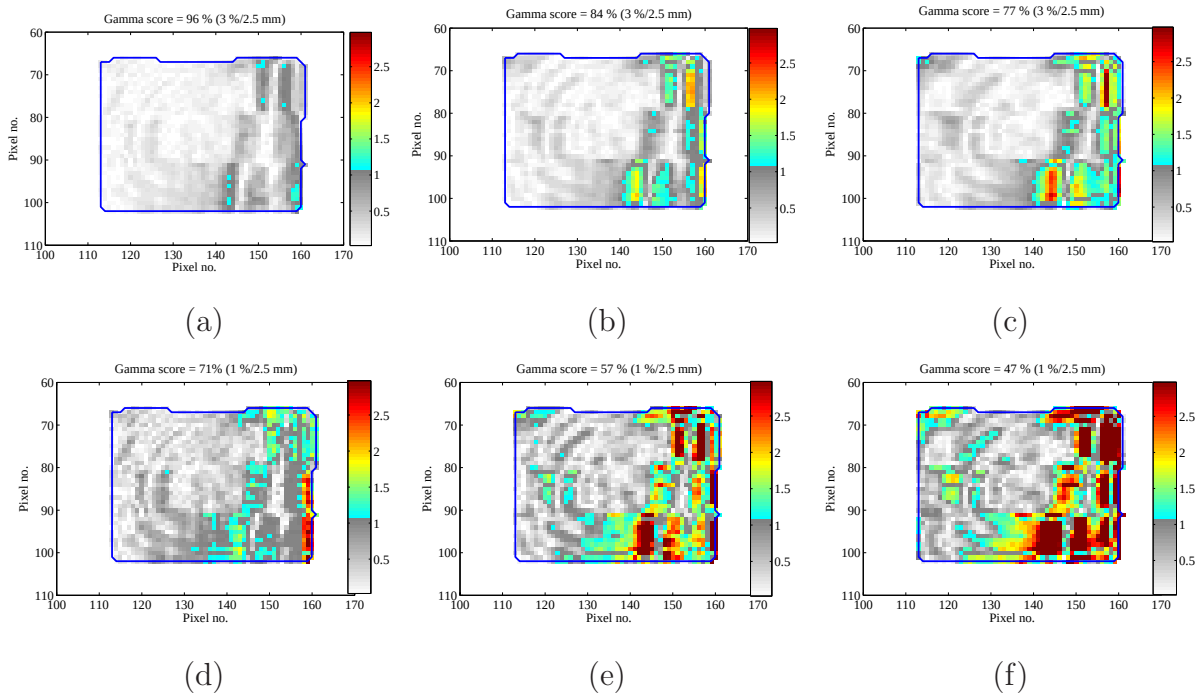

Figure 4.3.16: *Gamma maps and gamma scores calculated within the 50 % isodose lines resulting from relative shifts in the anthropomorphic breast phantom. (a), (b) and (c) Relative shifts of 0.25, 0.5 and 0.75 cm, respectively using 3 %/2.5 mm gamma criteria. (d), (e) and (f) Relative shifts of 0.5, 0.75 and 1.0 cm, respectively using 1 %/2.5 mm gamma criteria.*

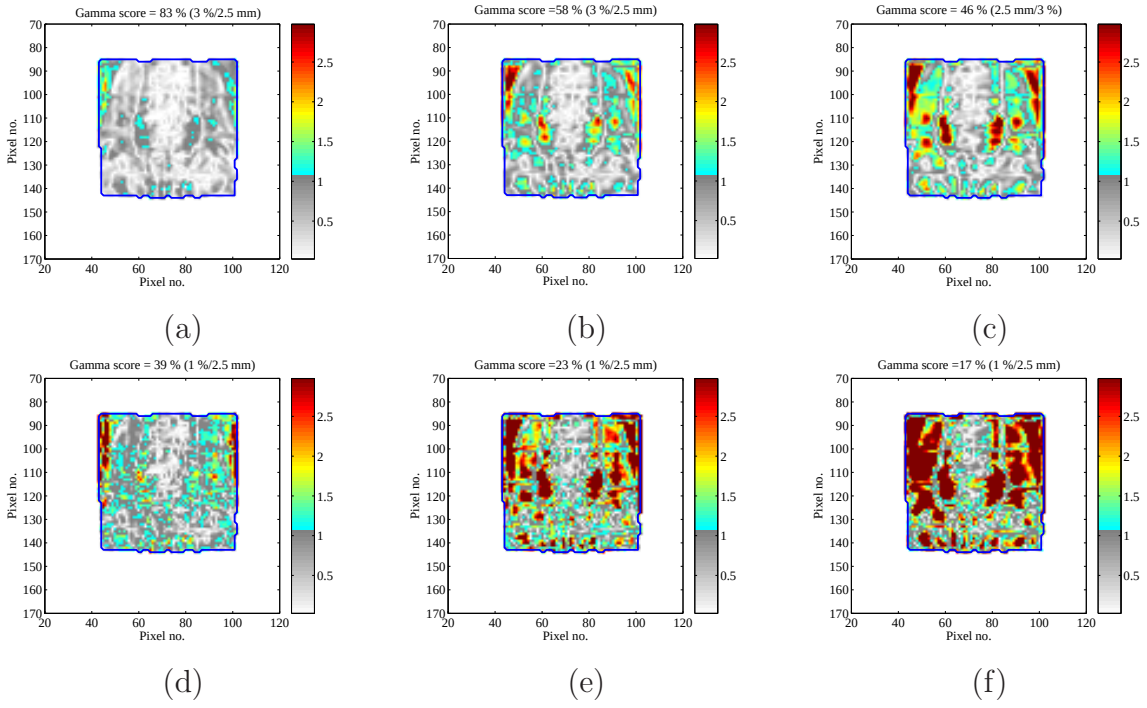

Figure 4.3.17: *Gamma maps and gamma scores calculated within the 50 % isodose lines resulting from relative shifts in the anthropomorphic bhead and neck phantom. (a), (b) and (c) Relative shifts of 0.25, 0.5 and 0.75 cm, respectively using 3 %/2.5 mm gamma criteria. (d), (e) and (f) Relative shifts of 0.5, 0.75 and 1.0 cm, respectively using 1 %/2.5 mm gamma criteria.*

4.3.5 Conclusions

Pinnacle^3 treatment planning system has proven to be a reliable and sensitive tool for predicting changes in transmitted dose under both clinically realistic and exaggerated conditions. For example, in a 30 cm thick slab of water-equivalent material, an inhomogeneity at 9 cm depth with dimensions $0.1 \times 0.1 \times 0.5$ cm^3 was resolved at the transmitted dose plane within the statistical uncertainty of the dose calculations. More realistic sized inhomogeneities such as the simulation of a gas pocket inside the patient (namely, a $5 \times 5 \times 5$ cm^3 region of interest, $\rho = 0$ g/cm^3) caused dose differences off-axis of up to 2 % in transmitted dose when displaced by only 0.1 cm. However, due to the combination of the small dose difference and inhomogeneity displacement, such a shift would most likely go undetected through gamma analysis using clinical criteria of 3 %/2.5 mm. Furthermore, a FWHM in transmitted dose predicted on the central axis versus inhomogeneity shifts

revealed only a significant reduction in signal transmission for 2.6 cm shifts or greater. This indicates the importance of evaluating dosimetry errors throughout the entire radiation field rather than at only a single point such as on the central beam axis, as is often used for exit dosimetry. Pinnacle based calculations predicted no significant changes in transmitted dose for inhomogeneity shifts parallel to the central beam path. Simulating patient surface curvature in combination with realistic relative beam path errors (such as a patient set up errors) using cylindrical phantoms and a pelvic phantom predicted varying degrees of errors at the transmitted dose plane. As expected, the cylinder with the greater radius of curvature had a greater impact on transmitted dose than the the cylinder with the smaller radius of curvature, for identical shifts. However, changes in transmission at treatment sites of a flatter nature such as the pelvis, may not be a sufficient indicator of dosimetry errors resulting from relative shifts in beam path and patient anatomy. In contrast, predicted changes in transmitted dose (by way of introducing errors described above) were more sensitive to the combined heterogeneities and patient contours as simulated by the breast and head and neck heterogeneities. For a clinical of the dosimetry errors in 2D, the commonly used gamma criteria of 3%/2.5 mm may not qualify as being suitable for quantifying relatively significant errors. For example, beam path errors simulated in the pelvis phantom of nearly 1 cm indicated relatively high gamma scores of up 90 % , when using the clinical gamma criteria, compared with using 1%/2.5 mm which produced gamma scores well below 90 % for shifts of 0.5 cm or less. Together with this consideration, uncertainties associated with current measurements of transmitted dose (using film and EPID, for example) would need to be minimised before adopting tighter criteria, or tighter criteria may not be possible, as a result, shifts may not be easily detected.

Chapter 5

An evaluation of transmission dosimetry for a 3D conformal four-field box prostate treatment

5.1 Introduction

Conformal radiotherapy of the prostate forms a large fraction of the treatments in radiotherapy departments due to its prevalence in the male population. From a radiotherapy point-of-view the prostate and its surroundings represents a fairly homogeneous volume surrounded by a relatively flat exterior, the pelvis. This makes it an ideal testing point to determine whether transmission dosimetry is sensitive to differences in dose delivery in such circumstances and is thus the main motivation behind this chapter. This chapter also forms a proof-of-principle approach using a clinical example (four-field box technique) to evaluate transmission dosimetry by simulating a full 3D CRT treatment of the prostate using multiple beams and clinical patient data in the form of CT scans. It is a principal-of-proof study in the sense that it reduces any additional variables associated with measurements of transmitted dose by excluding uncertainties related to (but not limited to) detector calibration, detector noise and random fluctuations in linac out-

put. Although these are important considerations in the overall process of patient dose validation, they are however, independent of the planning system which will be used to evaluate transmission dosimetry and should therefore be treated separately. The modelling approach used in this chapter deals with the investigation of only a few contributing factors at a time, making it easier to analyse the data and to control the transmission dose distinction environment.

5.2 Materials and methods

5.2.1 Expansion of patient CT images

In chapters 3 and 4, limitations of simulating a transmitted dose plane in the planning system (as a result of the limited FOV in the CT images) were overcome by acquiring extended CT scans of various phantoms. However, for patients undergoing a CT scan the above method would not be possible, as a result, in the current chapter this issue was overcome by processing the CT images using in-house software after the patient had undergone the CT scan. Matlab software (version 7.0, The MathWorks, Inc.) containing the image processing tool box was used to import the DICOM patient CT files. A Matlab routine was then written to expand the 512 pixel $\times$ 512 pixel image matrices to 1024 pixel $\times$ 1024 pixels. This effectively surrounded the original CT images with additional air density material so that transmitted dose planes at arbitrary angles and clinically relevant distances from the patient could be modeled in the planning system. A typical CT slice expanded in this fashion is shown in figure 5.2.1. For visual enhancement, the window level in the sample image was exaggerated so that the edges of the original image can be seen. The four dark regions seen in the figure are bore-hole artefacts and were found to have a density close to air. It should be noted that the process of expanding the CT images did not distort or alter in any way the resolution of the original CT images. The expanded image matrices were then written to DICOM files and exported to the treatment planning system.

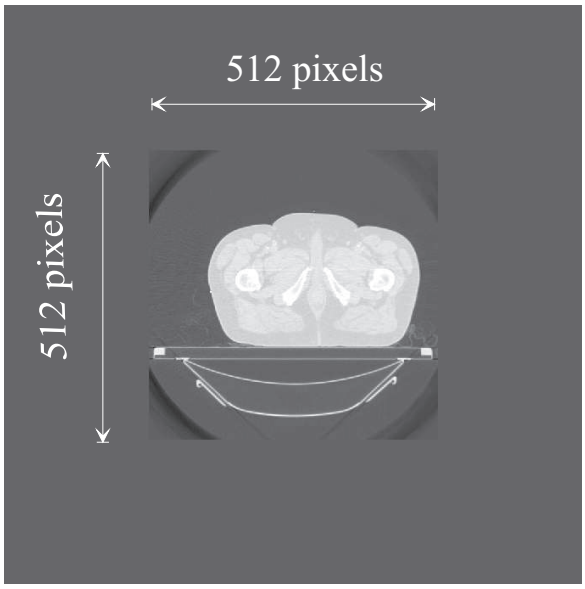

Figure 5.2.1: *An expanded axial CT slice (1024 pixel × 1024 pixel) of a prostate radiotherapy patient.*

5.2.2 Transmitted dose calculations for a four-field box technique

A treatment plan for a conformal prostate treatment based on the patient CT data was created using Pinnacle^3 treatment planning system (version 6.2b, Phillips Medical Systems, Milpitas, CA). A radiation oncologist outlined the Gross Tumour Volume (GTV) for the prostate in accordance to guidelines set out by the Radiation Therapy Oncology Group (RTOG) [129]. The GTV included included the prostate gland plus seminal vesicles. The Planning Target Volume (PTV) was then outlined as the Clinical Target Volume (CTV) + 10 mm with a posterior margin limited to 5 mm, where CTV = GTV. In addition, surrounding critical structures including the bladder, rectum and femoral heads were outlined. Based on the clinical outlines, a radiotherapist adopted a 3D conformal four-field box technique using 23 MV photons [130] and MLCs (Multi-Leaf Collimators). A dose of 2 Gy was prescribed to the isocenter. Four copies of the treatment plan were made so that the transmitted dose distribution could be modeled separately for each of the four beams. This ensured that a given transmitted dose plane did not contain the dose from more than one beam (figure 5.2.2). The transmitted dose was calculated within a 5

$\times$ 32 $\times$ 32 cm^3 Region-Of-Interest (ROI) assigned to a density of 1 g/cm^3 with a surface orthogonal to the central axis of each beam. A thickness of 5 cm was chosen to achieve electronic equilibrium for the 23 MV photon energy that also provided a sufficient amount of backscatter behind d_{max}. The ROIs were created at a Source-to-Surface Distance (SSD) of 145 cm which corresponds to one of the preset EPID positions for the corresponding treatment machine in our department.

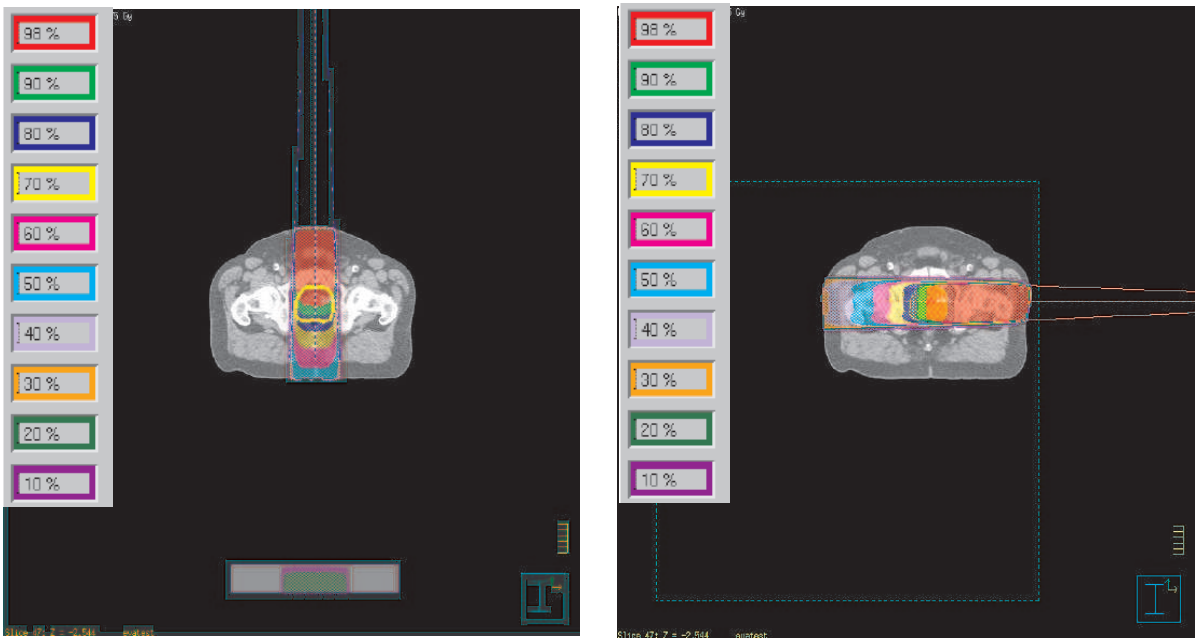

(a) (b)

Figure 5.2.2: *Pinnacle^3 dose distributions for the anterior-posterior beam and (b) left lateral beams.*

All dose calculations were performed using the the collapsed-cone superposition dose engine on a voxel grid of $0.25 \times 0.25 \times 0.25$ cm^3. The file associated with the 3D dose for each beam was located on the planning system and transferred to a separate workstation for additional analysis. The 3D dose array was reconstructed using Matlab and the 2D dose distribution at d_{max} corresponding to the transmitted dose plane was identified as described in chapters 3 and 4. In addition, for image analysis purposes the dose images were cropped at the 20 % isodose lines relative to the maximum dose of each image. The resulting transmitted dose images for each of the four beams are shown in figure 5.2.3.

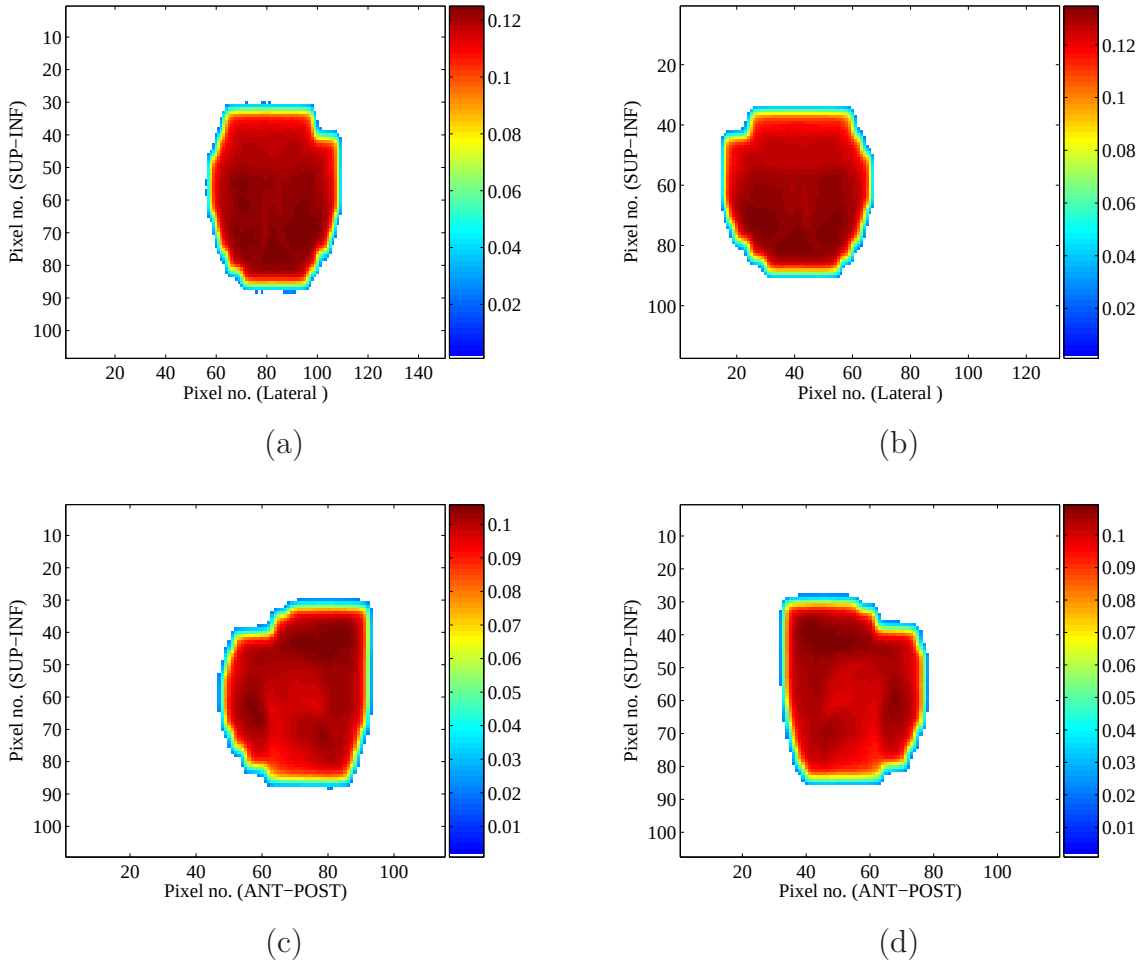

Figure 5.2.3: *Beam's eye view transmitted dose distributions (cropped at 20 % isodose lines) extracted at d_{max} for (a) the anterior-posterior, (b) posterior-anterior beam, (c) Left lateral, and (d) right lateral beams.*

5.2.3 Simulation of dosimetry errors

In order to determine whether transmission dosimetry could in principle be applied in the clinic, dosimetry errors were deliberately introduced into the planning system and any differences at the transmitted dose level were monitored. This is a proof-of-principle study based on a single yet realistic clinical example rather than a cohort study comparing the statistical outcomes of transmitted dose detection for many prostate conformal treatments. Dosimetry errors were simulated as a change in beam path relative to the patient anatomy with the aim of changing the transmitted dose distribution below the patient. A change in beam path can occur due to patient positioning errors, patient motion, internal organ motion and changes and loss or gain in patient weight, for example. However, due to the nature of current planning systems only rigid geometrical transformations such as changes in the position of the radiation field relative to the patient anatomy were simulated. This was achieved by deliberately shifting the isocenter coordinates in each of the four beams along the anterior-posterior, superior-inferior, and left-right lateral axes in increments of 0.5 cm, 1.0 cm and 1.5 cm. Similarly, systematic shifts in the coordinates of the transmitted dose plane (ie ROI) were required in order to simulate the dosimetry errors in the patient anatomy reference frame. (figure 5.2.4). For each combination of beam, direction and magnitude in shift, a separate calculation for transmitted dose was performed.

Shifts of 0.5 cm, 1.0 cm and 1.5 cm were selected to represent typical order of magnitude positioning errors reported in prostate conformal radiotherapy treatments (0.5 cm) [131–133] as well as gross (1.0 cm) and extreme set up errors/shifts (1.5 cm) to determine what ranges can be detected at the transmitted dose level.

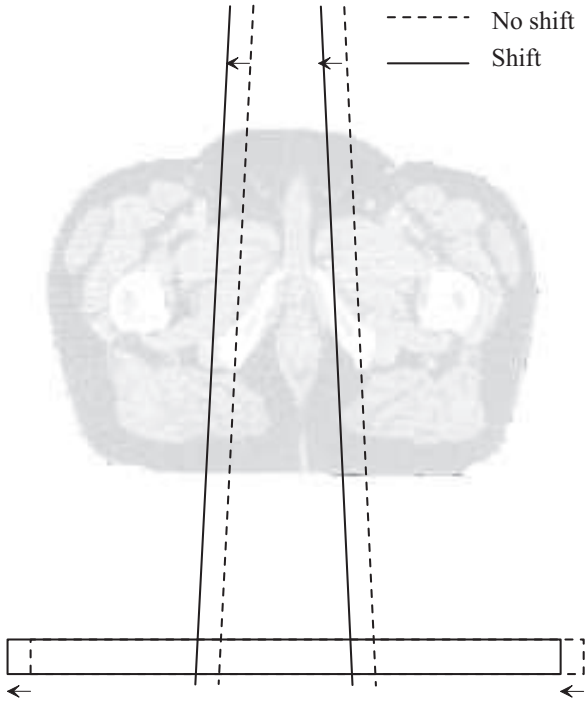

Figure 5.2.4: *Dosimetry errors simulated by shifting the coordinates of the beam and transmitted dose plane in the planning system (shown in the lateral directions only).*

5.2.4 Evaluation of dosimetric errors at the transmitted dose plane

As described in the previous chapter, the gamma function developed by Low *et al* is a useful quantitative and visual tool for comparing two-dimensional dose distributions and was thus employed here. The gamma map provides a visual inspection (ie location and distribution) of dose errors and the gamma score (the number of pixels that pass the specified gamma criteria as a fraction of the total number of pixel values in the dose map) provides a quantitative evaluation of the overall error between the 2D dose distributions. Gamma criteria of 3 %/2.5 mm were incorporated and gamma analysis was restricted to dose maps containing the 20 % isodose lines and higher. This was achieved by applying a 2D mask to the dose map that excludes all dose values less than 20 % of the maximum dose. A 20 % isodose limit was applied as it excludes large areas of low dose/low dose gradient regions outside the radiation field, which would otherwise pass the gamma criteria and give unrealistically high gamma scores [121]. This could then mask important errors

occurring in the dose maps.

5.2.5 Evaluation of dosimetric errors inside the patient

Midplane dose

In order to determine whether the transmitted dose alone is sufficient for detecting dose delivery errors and to investigate whether there is a correlation between the information implied by the calculated transmitted dose and dose at the PTV reference plane, corresponding midplane dose distributions were also extracted and compared for each beam. In this study, the midplane dose was defined as the plane parallel to the transmitted dose plane that intersects the beam's isocenter. However, unlike the transmitted dose plane, the midplane was defined in the reference frame of the patient anatomy, since it is the dose delivered to the target volume that is the object of evaluation (compare with dose-volume histograms). Furthermore, the gamma function was also used for quantifying any differences in dose at the midplane dose level.

Dose-Volume Histograms

Finally, the impact of the dosimetry changes were evaluated from a clinical perspective by comparing Dose-Volume Histograms (DVH) in the target volume as well as those of surrounding critical structures such as the bladder, rectum and femoral heads, before and after introducing the dosimetry errors. This provides an ultimate benchmark for evaluating the efficacy of transmission dosimetry for treatment dose validation.

5.3 Results

5.3.1 Gamma analysis results for anterior and posterior beams

Due to the discrete nature of the planning system dose calculations, gamma analysis for each of the four beams was performed using 3 %/2.5 mm criteria, compared with the

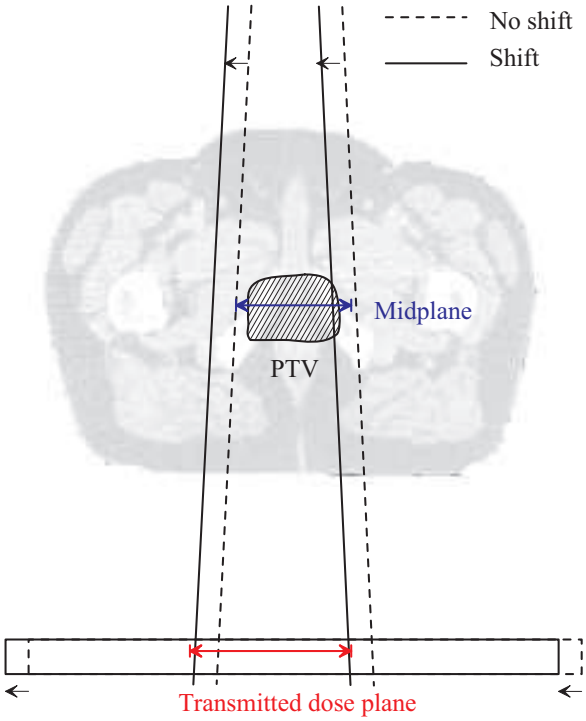

Figure 5.2.5: *A schematic illustrating the locations of the transmitted dose plane and midplane. The midplane is defined relative to patient anatomy, where as the transmitted dose plane is defined relative to the radiation field.*

commonly used 3 %/3 mm combination. For the anterior and posterior beams, the 0.5 cm beam path shifts did not register any regions of fail in the gamma maps, along either the anterior-posterior, superior-inferior or lateral axes. Although, the largest (absolute) dose difference recorded along all three axes was 3 %, the gamma scores indicated 100 % agreement within the 3%/2.5 mm criteria. A typical gamma map for the anterior-posterior beam resulting in a 0.5 cm beam path displacement in right-lateral direction is shown in figure 5.3.1(a). Shades of grey represent regions within 3%/2.5 mm (gamma index ≤ 1) and those that exceed the criteria are shown in colour (gamma index > 1), where blue represents the mildest failing regions and red, excessive failing regions.

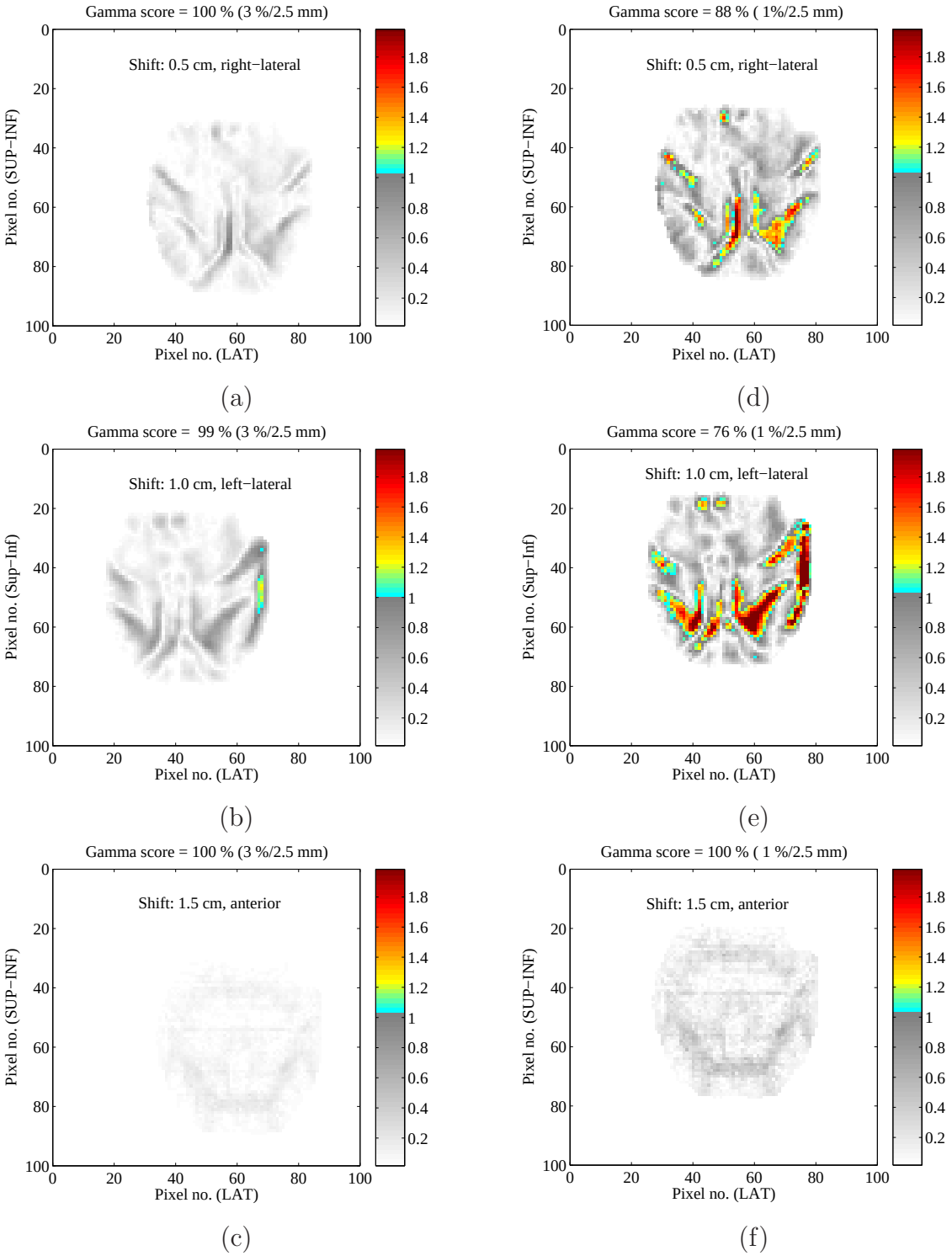

Figure 5.3.1: *Gamma maps (3 %/2.5 mm and 1 %/2.5 mm) resulting from beam path displacements in the anterior-posterior beam. (a) and (d) 0.5 cm, right-lateral, (b) and (e) 1.0 cm, left-lateral, and (c) and (f) 1.5 cm, anterior.*

For the 1.0 cm beam path displacements, regions in gamma maps begin to fail. However, the worse gamma scores recorded were only 90 %, 96 %, and 99 % which occurred for beam path displacements in the inferior, superior and lateral directions (figure 5.3.1(b)), respectively. It is only for beam path shifts of 1.5 cm that gamma scores deteriorated below 90 %. Nevertheless, this only occurred in 2/6 directions (superior and inferior). Thus, based on 3%/2.5 mm gamma criteria, the resulting transmitted dose distribution is relatively insensitive to large changes in radiation beam path through and around the target volume of the prostate patient. To increase the sensitivity of the gamma maps at the transmitted dose level, stricter criteria of 1%/2.5 mm were also used to calculate gamma scores. For the 0.5 cm beam path displacements, this resulted in significantly lower gamma scores of less than 90 % (figure 5.3.1(d)) in 4/6 directions. Similarly, for the 1.0 cm displacements gamma scores were below 76 % (figure 5.3.1(e)) in 4/6 directions. The 1.5 cm beam path displacements produced the lowest gamma scores (below 70 %) in 4/6 directions. Displacements in 2/6 directions (anterior and posterior) consistently produced perfect gamma scores (using either 3%/ 2.5 mm or 1%/2.5 mm) for all shifts up to and including 1.5 cm (figures 5.3.1(c) and (f)). This suggests that the transmitted dose is insensitive to displacements parallel to the central axis of the anterior and posterior beams which is expected since the total effective path length does not change along these axes. A summary of the results is found in table 5.3.1. Gamma scores and dose differences recorded in the transmitted dose plane resulting from the beam displacements are also tabulated for the midplane dose maps. The table immediately shows that gamma scores (3 %/2.5 mm) are consistently more worse in the midplane compared with the transmitted dose plane and that corresponding dose differences resulting are significantly greater at the midplane. In particular, gamma scores in the midplane indicate that the midplane dose maps are sensitive to nearly all beam shifts in the 0.5 –1.5 cm range, whereas the transmitted dose maps are only sensitive to a 1 cm shift in the inferior direction (gamma score = 90 %) and to 1.5 cm shifts along the superior-inferior axis (ie gamma scores $\leq$ 90 %). Also, shifts along the anterior-posterior direction (ie parallel to the central beam axis) did not register a single failure in the gamma map (using either 3 %/2.5 mm or 1

%/2.5 mm criteria) at the transmitted dose plane as opposed to errors recorded in all gamma maps for the midplane dose. A more in depth discussion of gamma maps in the midplane is provided in section 5.3.3.

		Transmitted dose plane			Midplane	
Shift (cm)	Direction	Gamma score (3 %/2.5 mm)	Gamma score (1 %/2.5 mm)	Max/Min dose difference (%)	Gamma score (3 %/2.5 mm)	Max/Min dose difference (%)
0.5 cm	ANT	100	100	1.4/−0.5	96	7.5/−6.1
	POST	100	100	1.4/−0.5	92	4.4/−6.6
	LLAT	100	90	2.5/−2.0	61	50/−50
	RLAT	100	88	1.7/−3.0	61	50/−50
	SUP	100	84	1.6/−2.5	57	36/−43
	INF	100	79	3.0/−1.5	58	41/−36
1.0 cm	ANT	100	100	1.4/−0.2	91	6.1/−3.6
	POST	100	100	1.4/−0.9	81	4.2/−13
	LLAT	99	76	2.7/−3.8	50	76/−74
	RLAT	99	74	2.4/−4.4	50	74/−74
	SUP	96	58	2.0/−4.0	46	60/−71
	INF	90	46	4.8/−1.5	46	70/−61
1.5 cm	ANT	100	100	1.4/−0.3	83	11/−2.9
	POST	100	100	1.4/−0.7	81	3.0/−14
	LLAT	96	69	3.2/−4.7	41	86/−85
	RLAT	96	66	3.2/−5.7	41	85/−85
	SUP	76	23	5.3/−1.6	38	73/−85
	INF	75	26	5.5/−1.6	39	84/−75

Table 5.3.1: *Comparison of gamma scores and maximum (absolute) dose differences between transmitted and midplane dose maps for the anterior-posterior beam.*

5.3.2 Gamma analysis results for left- and right-lateral beams

In contrast to the anterior and posterior beams, simulated 0.5 cm beam path changes in the left- and right lateral beams did register regions of fail in gamma maps for shifts along all three axes (except along the lateral axis, parallel to beam's central axes). However, the worst gamma scores were only 94 and 95 % for displacements in the anterior and posterior directions (figure 5.3.2(a)), respectively. For 1.0 cm changes in beam path, gamma scores deteriorated to below 80 % for shifts along the anterior-posterior axis and also began to fail along the superior-inferior axis but remained above 90 % (figure 5.3.2(b)). For displacements of 1.5 cm only, were gamma scores significantly low (below 60 %) along all 3 axes (except along the lateral axis). By reducing the gamma criteria to 1 %/2.5 mm, gamma maps at the transmitted dose plane became sensitive to beam path changes of 0.5 cm (figure 5.3.2(d)) or greater (figure 5.3.2(e)) along all three axes (except along the lateral axis).The absence of any changes in transmitted dose for displacements along the lateral axis (which yielded perfect gamma scores) also confirms (similar to results for the anterior-posterior beam) that transmitted dose is insensitive to changes in beam path parallel to a beam's central axis (figures 5.3.2(c) and (f)). For the left-and right-lateral beams, midplane dose maps were significantly more sensitive to beam shifts than at the transmitted dose plane for the same beam shifts, as implied by gamma scores (3 %/2.5 mm) shown in table 5.3.2. Based on the gamma scores, midplane dose maps were sensitive (ie produced gamma scores $\leq$ 90 %) to shifts of 0.5 cm or more in all six directions, with the exception of 0.5 cm shifts parallel to the central beam axis (ie the left- and right-lateral directions). This is in contrast to results at the transmitted dose plane in which gamma scores fell below 90 % (3 %/2.5 mm) only for shifts of 1.5 cm in all six directions (except for shifts parallel to the central beam axis). However, its is only by setting gamma criteria to 1 %/2.5 mm for the transmitted dose maps do gamma scores become sensitive to shifts of 0.5 cm or more as predicted by the midplane dose maps.

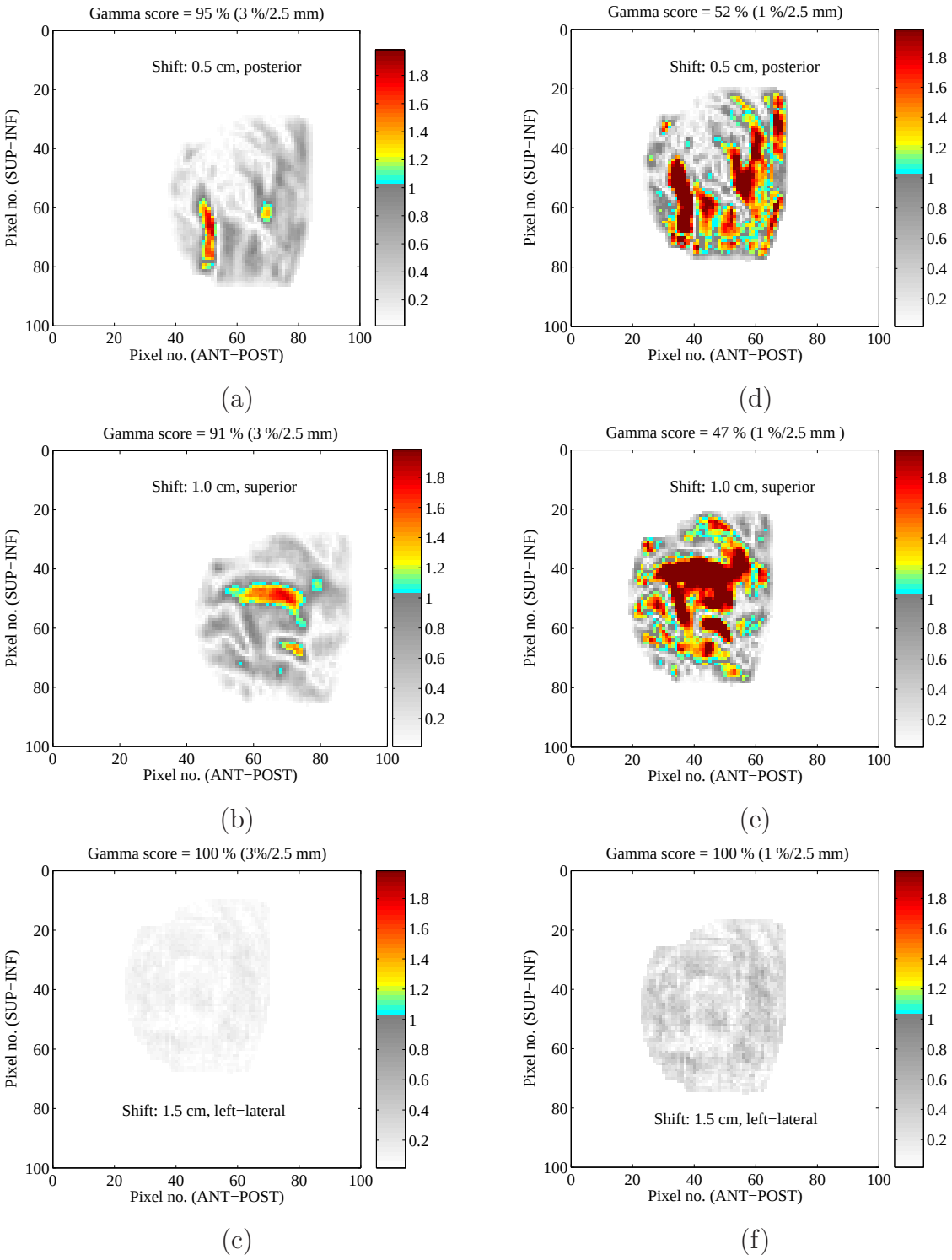

Figure 5.3.2: *Gamma maps (3 %/2.5 mm and 1 %/2.5 mm) resulting from beam path displacements in the left-lateral beam. (a) and (d) 0.5 cm, posterior, (b) and (e) 1.0 cm, superior, and (c) and (f) 1.5 cm, left-lateral.*

In summary, if gamma maps are to be used for quantifying dosimetry errors at the transmitted dose plane, relatively large changes in beam path (in this case up to 1.0 cm in lateral beams and up to 1.5 cm in anterior and posterior beams) may still produce relatively high gamma scores (90 % or greater) and therefore may be considered dosimetrically insignificant, unless stricter gamma criteria are adopted (1%/2.5 mm, for example). In general, transmitted dose is insensitive to beam shifts of 0.5 cm or less and is most sensitive to shifts perpendicular to the central beam axis. Furthermore, in order to determine the origin of a potential dose delivery error[1] via transmission dosimetry, each beam should be evaluated separately and if a single beam fails, then there is a strong indication of a dose delivery error to the patient.

[1] ie any error causing a change in the desired dose distribution inside the patient

		Transmitted dose plane			Midplane	
Shift (cm)	Direction	Gamma score (3 %/2.5 mm)	Gamma score (1 %/2.5 mm)	Max/Min dose difference (%)	Gamma score (3 %/2.5 mm)	Max/Min dose difference (%)
0.5 cm	ANT	94	60	7.5/−4.0	56	58/−54
	POST	95	52	4.3/−6.6	56	54/−58
	LLAT	100	100	0.4/−0.3	94	5.9/−6.5
	RLAT	100	100	0.6/−0.8	94	7.3/−5.5
	SUP	99	79	3.3/−3.6	47	67/−67
	INF	100	80	3.3/−2.9	59	39/−41
1.0 cm	ANT	78	34	10/−6.4	42	78/−74
	POST	71	31	7.1/−8.8	42	75/−78
	LLAT	100	100	0.5/−2.0	89	2.1/−12
	RLAT	100	100	0.4/−0.7	90	10/−2.0
	SUP	91	47	0.7/−5.1	47	67/−67
	INF	95	59	5.5/−4.0	47	65/−67
1.5 cm	ANT	59	21	5.9/−8.2	31	88/−84
	POST	46	19	11/−8.2	33	86/−87
	LLAT	100	100	8.9/−0.4	75	3.1/−13
	RLAT	100	100	0.2/−0.7	83	13/−2.9
	SUP	46	46	6.0/−5.9	39	81/−80
	INF	46	46	6.4/−5.4	40	79/−80

Table 5.3.2: *Comparison of gamma scores and maximum (absolute) dose differences between transmitted and midplane dose maps for the left-lateral beam.*

5.3.3 Gamma analysis results at the patient midplane

Figure 5.3.3 shows typical gamma maps in the midplane of the patient and corresponding gamma maps in the transmitted dose plane. The midplane dose maps clearly indicate large dose differences occurring in and around the PTV due to the geographical misses resulting from the beam displacements. Such differences are not observed in the corresponding transmitted dose maps which indicates that the dosimetric information recorded in the transmitted dose plane is not highly indicative of the dosimetry errors occurring at target volumes inside the patient. For example, in the left-lateral beam (figure 5.3.3(a)), a 0.5 cm change in beam path in the superior direction yield significant dose differences superiorly and inferiorly of the PTV leading to a gamma score below 50 % (3 %/2.5 mm). In the corresponding gamma map for the transmitted dose plane, a near perfect gamma score (99 %) is achieved (figure 5.3.3(b)). For the same beam, a 1.0 cm change in beam path in the posterior direction clearly shows regions in disagreement anteriorly and posteriorly of the PTV in the midplane gamma map, as expected (figure 5.3.3(c)). However, although differences observed in the corresponding transmitted dose plane gamma map do not correlate spatially with those in the midplane, the transmitted gamma map does indicate a significant dosimetry error, with a gamma score as low as 71 % (figure 5.3.3(d)). Finally, in the anterior-posterior beam, a displacement of 1.5 cm in the posterior direction (figure 5.3.3(e)) caused large dose differences around the outline of the PTV due to magnification effects at the midplane, although differences inside the PTV were relatively small (within 3 %). This is clearly not recorded in the gamma map for the corresponding transmitted dose plane which produced a gamma score of 100 % (figure 5.3.3(f)). In the midplane, both in-plane (ie perpendicular shifts) and out-of-plane shifts (ie shifts directly along the central beam axis) produce discrepancies in dose due to a geographic misses at the PTV due to a shift in spatial alignment of the delivered and planned radiation fields, which appear as distinct dose errors especially at the beam penumbra where steep dose gradients exist. In contrast, at the transmitted dose plane, dose errors are only prominent for perpendicular displacements due to the change in the total effective beam path caused

by the proximity of bone (for example, femur) and soft structures in and around the PTV. Shifts directly along the central beam axis result in mostly the same total effective beam path thus causing very little change in the overall transmitted dose.

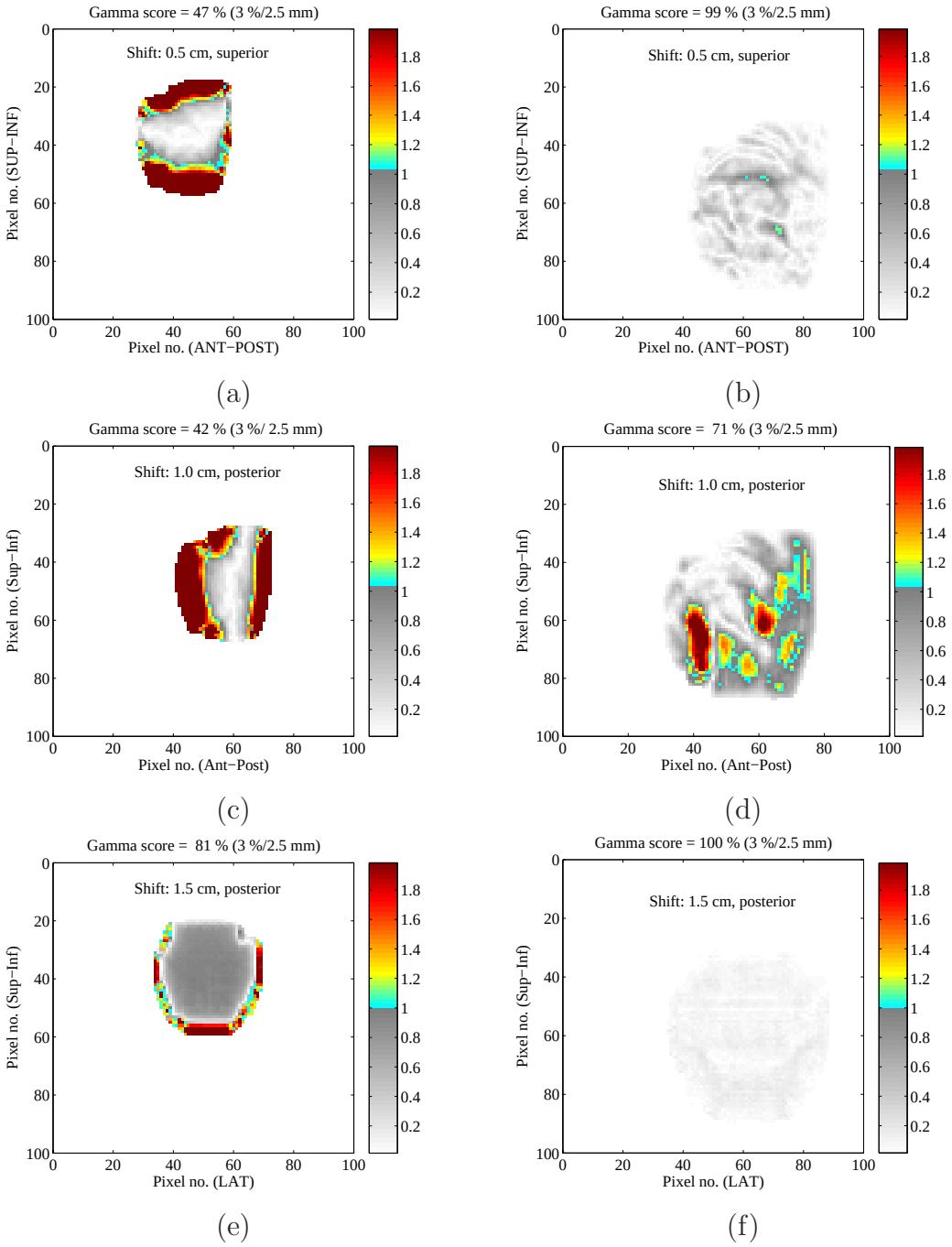

Figure 5.3.3: *Gamma maps calculated using 3 %/2.5 mm in the midplane ((a), (c), (e)) and corresponding gamma maps in the transmitted dose plane ((b), (d), (f)). (a)–(b) left-lateral beam, 0.5 cm shift, superior, (c)–(d) left-lateral beam, 1.0 cm shift, posterior, and (e)–(f) anterior-posterior beam, 1.5 cm shift, posterior.*

5.3.4 DVHs

The clinical impact of the 5, 10 and 15 mm beam shifts on the dose-volume histograms for the PTV and nearby critical structures are plotted in figures 5.3.4–5.3.6. The DVHs represent the dose contribution from all four beams. For simplicity the DVHs were calculated such that the shift between planned and delivered geometry is present in all four beams (eg due to a patient set up error or jaw calibration error) as opposed to an error present in a single beam only which is a less likely scenario. For brevity, results are only shown for beam shifts in the anterior, right-lateral and superior directions. Due to symmetry in the data, results in the remaining three directions are very similar and can be omitted. The greatest change in DVHs occurred for shifts in the anterior and superior directions (5.3.4 and 5.3.6)with little deviation in DVHs (at the critical structures) for shifts in the right-lateral direction (5.3.5). For beam shifts in the anterior direction the minimum dose to the PTV varied by only 2 % for a 0.5 cm shift. However, for shifts of 1 cm and greater, the minimum dose rapidly decreased by up to 36 %. The corresponding dose to the rectum caused improved tissue sparing with a decrease in the mean dose of 9–21 %, for shifts in the range 0.5–1.5 cm. The maximum and mean doses to the bladder and femoral head (left) were less significant with variations in mean dose of 4–10 % for shifts of 0.5–1.5 cm. For shifts in the superior direction, the minimum dose to the PTV decreased by only 4 % due to a 0.5 cm shift but substantially decreased by 20–37 % for shifts of 1.0–1.5 cm. Despite the direction of the beam shift away from the rectal volume, an increase in maximum dose to the rectum was observed but was clinically insignificant (< 0.5 %). This resulted in the average dose to the rectum to increase by only 3-6 % for shifts of 0.5 –1.5 cm. However, shifts as small as 0.5 cm resulted in a increase in average dose to the bladder of 17 % which increased up to 46 % for the largest shift of 1.5 cm. The impact of the superior beam shifts on the femoral head (left) DVH were much less than the bladder, but were clinically significant with an average dose increase of 7–12 % due to the shifts of 0.5 – 1.5 cm. Finally, for shifts along the lateral axis shifts in the right-lateral direction resulted in a significant reduction in dose homogeneity in the PTV

(the minimum dose decreased) but DVHs remained relatively unchanged for all beam shift sizes. For example, shifts of up to 1.5 cm in the right-lateral direction resulted in a variation in average dose to the rectum, bladder and femoral head (left) of only 1, 7, and 0.5 %, respectively. In summary, shifts of 1 cm or greater in all three axes had a clinically significant impact on dose homogeneity in the PTV. Shifts as small as 0.5 cm caused clnically significant variations in DVHs of the critical structures with the greatest variations observed for shifts in the anterior and superior directions. The dose-volume statistics are summarised in tables 5.3.3–5.3.5 for each of the three beam shift directions.

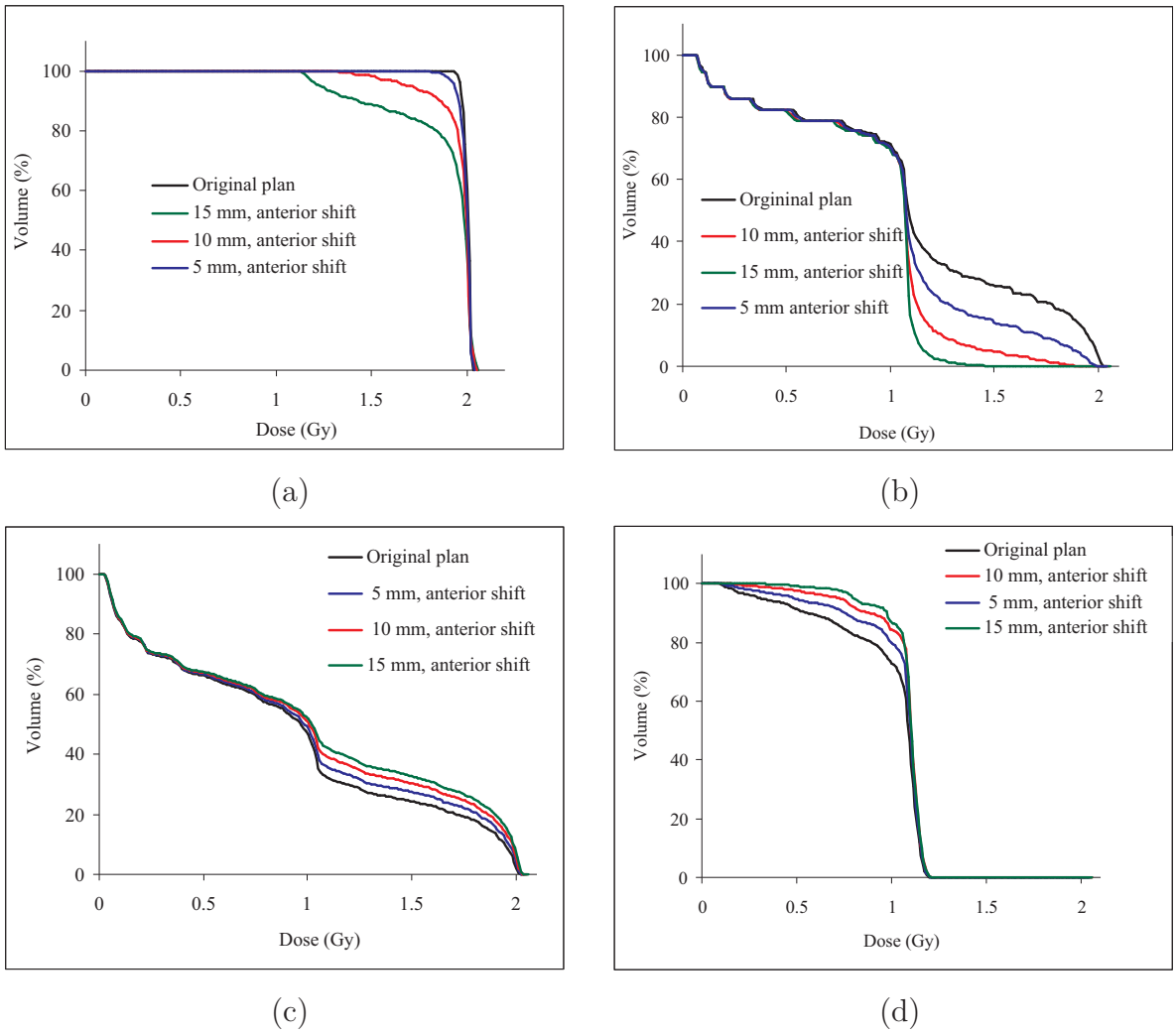

Figure 5.3.4: *Dose-volume histograms evaluated by Pinnacle*^{3} *for beam shifts in the anterior direction. (a) PTV, (b) rectum, (c) bladder, and (d) left femoral head.*

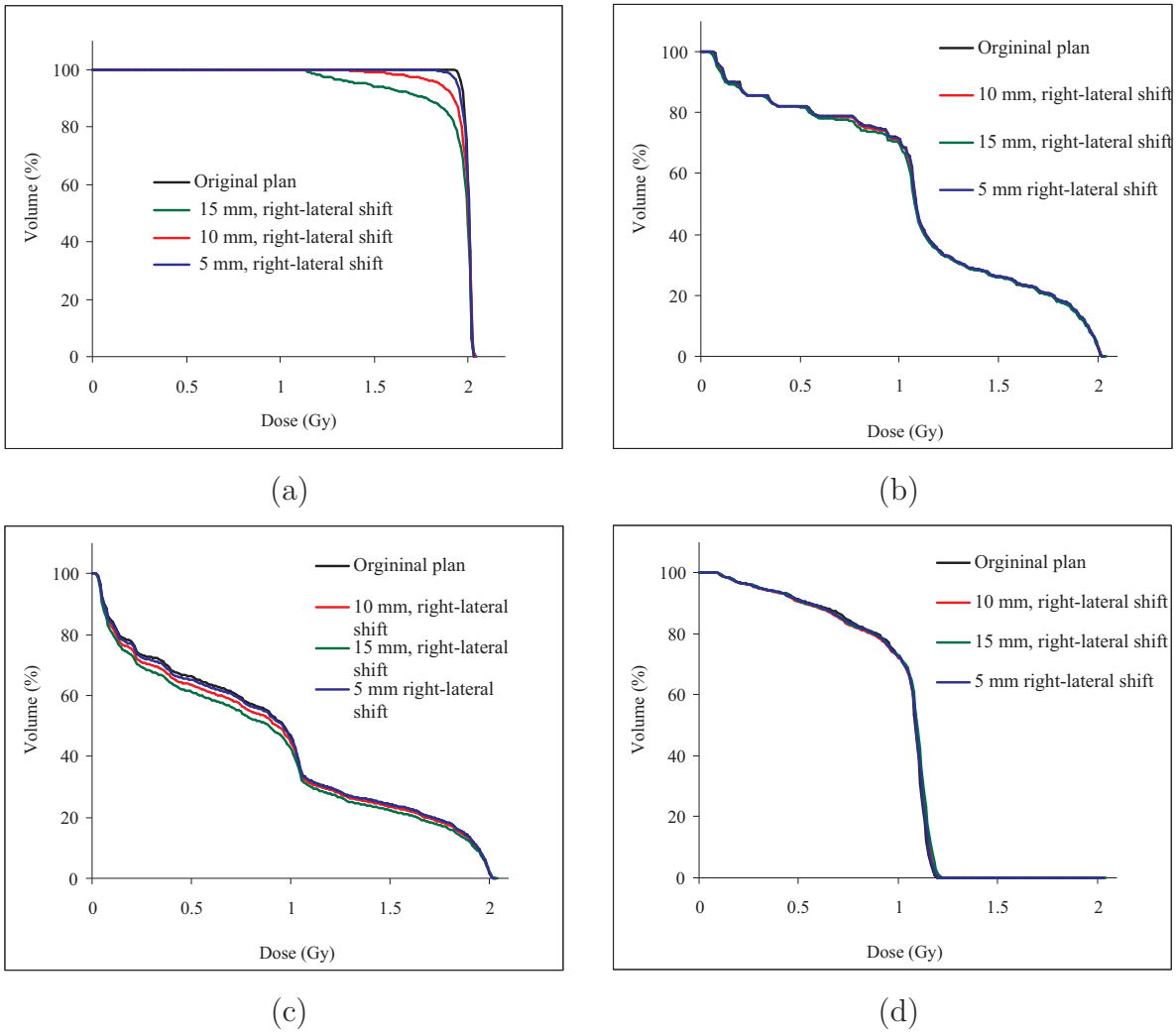

Figure 5.3.5: *Dose-volume histograms evaluated by Pinnacle*^{3} *for beam shifts in the right-lateral direction (a) PTV, (b) rectum, (c) bladder, and (d) left femoral head.*

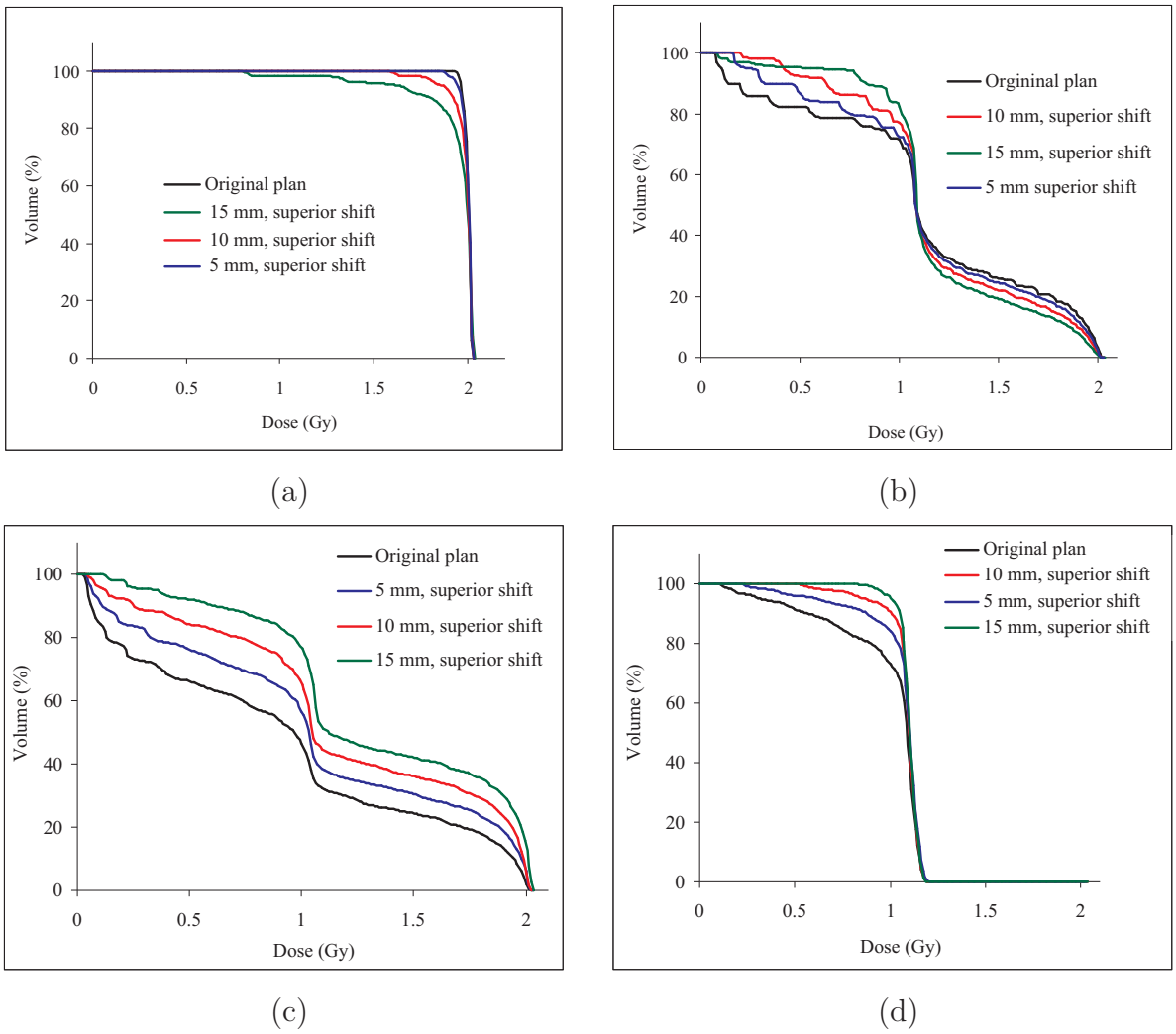

Figure 5.3.6: *Dose-volume histograms evaluated by Pinnacle*^{3} *for beam shifts in the superior direction (a) PTV, (b) rectum, (c) bladder, and (d) left femoral head.*

Volume	Original plan	Anterior shift 0.5 cm	1.0 cm	1.5 cm
PTV				
D_{max} (cGy)	203.3	204.4	205.3	205.8
D_{min} (cGy)	191.0	195.1	122.7	126.1
D_{avg} (cGy)	197.7	200.7	195.4	196.2
Rectum				
D_{max} (cGy)	201.2	198.2	190.8	157.0
D_{avg} (cGy)	110.9	100.7	92.5	88.1
Bladder				
D_{max} (cGy)	201.2	202.3	203.2	203.7
D_{avg} (cGy)	91.1	94.7	98.1	100.8
Femoral head (left)				
D_{max} (cGy)	119.5	120.2	119.7	120.0
D_{avg} (cGy)	97.5	102.0	105.2	107.0

Table 5.3.3: *Clinical dose statistics for the planning target volume and critical structures (single fraction) for beam shifts in the anterior direction.*

5.4 Summary/conclusions

Based on 3%/2.5 mm gamma criteria, the transmitted dose distributions calculated by the planning system was shown to be insensitive to the 0.5 cm simulated beam offsets and were sensitive to displacements as large as 1.0–1.5 cm in only some directions. However, the DVHs (in particular, of the critical structures) resulting from shifts of 0.5 cm or more were found to be clinically unacceptable. This may suggest that transmission dosimetry may not be a reliable surrogate of dosimetry errors related to changes in the beam path for patient treatment sites involving flat body contours and homogeneous density volumes, such as the pelvis in the case of prostate irradiation, for example. Alternatively, basing gamma analysis on stricter criteria (1%/2.5 mm, for example) significantly improves the detectability to changes in transmitted dose and therefore would enable transmission dosimetry to be used under these circumstances. However, measurements of transmitted dose (using EPID and film, for example) are currently limited to 1–2 % accuracy and would most likely not be reliable in detecting differences of the order of 1 %. Furthermore, large

		Right-lateral shift		
Volume	Original plan	0.5 cm	1.0 cm	1.5 cm
PTV				
D_{max} (cGy)	203.3	202.5	202.8	204.3
D_{min} (cGy)	191.0	179.0	124.9	109.8
D_{avg} (cGy)	197.7	199.3	197.3	203.3
Rectum				
D_{max} (cGy)	201.2	201.5	201.7	202.2
D_{avg} (cGy)	110.9	110.0	110.5	109.4
Bladder				
D_{max} (cGy)	201.2	201.5	201.7	202.2
D_{avg} (cGy)	91.1	90.3	88.1	85.0
Femoral head (left)				
D_{max} (cGy)	119.5	120.7	120.8	122.2
D_{avg} (cGy)	97.5	97.4	97.3	98.0

Table 5.3.4: *Clinical dose statistics for the planning target volume and critical structures (single fraction) for beam shifts in the right-lateral direction.*

		Superior shift		
Volume	Original plan	0.5 cm	1.0 cm	1.5 cm
PTV				
D_{max} (cGy)	203.3	203.1	202.3	202.6
D_{min} (cGy)	191.0	182.7	152.2	119.7
D_{avg} (cGy)	197.7	199.3	197.8	193.0
Rectum				
D_{max} (cGy)	201.2	201.0	201.3	201.6
D_{avg} (cGy)	110.9	114.3	117.0	117.4
Bladder				
D_{max} (cGy)	201.2	202.1	202.2	202.6
D_{avg} (cGy)	91.1	106.3	120.8	133.4
Femoral head (left)				
D_{max} (cGy)	119.5	119.4	118.5	118.7
D_{avg} (cGy)	97.5	104.1	107.2	109.2

Table 5.3.5: *Clinical dose statistics for the planning target volume and critical structures (single fraction) for beam shifts in the superior direction.*

differences observed in midplane dose maps that were not recorded in the transmitted dose maps has important implications when performing dosimetric back-projection to a plane (or volume) inside the patient. For example, on a treatment day acquired with no portal images or Cone-Beam CT, a patient positioning error of a prostate conformal radiotherapy treatment may go undetected. Therefore, back-projecting the measured transmitted dose onto the patient using the the original patient CT data would give misleading agreement in expected patient dose distributions. As Cone-Beam CT technology becomes more widely available in radiotherapy departments the potential exists for calculating the transmitted dose on a daily basis for comparison with measured transmitted doses.

Chapter 6

An evaluation of transmission dosimetry for a 3D conformal head and neck treatment

6.1 Introduction

Multi-Leaf Collimators (MLCs) are an important accessory of modern medical linear accelerators for providing conformal beam coverage of tumours and shielding of surrounding healthy tissue structures during radiotherapy. Since MLCs are mechanically driven, separate quality assurance is required compared with conventional beam shaping using customised metal blocks [134–136]. The accuracy in leaf positioning is important in all conformal radiotherapy modalities, especially in IMRT where fields are often composed of many individual subfields. A comparison of MLC controller log files with the prescribed MLC positions may reveal errors in the delivered MLC positions [137–139]. MLC leaf positioning errors may arise from finite precision in the MLC control systems, uncertainty in measurements of leaf positions during MLC calibration [140,141] and also from the effects of gravity. Unless such errors are monitored and controlled they would go unnoticed and could negatively impact on the dose delivered to the patient. An interesting study [142]

showed that signal variations of up to 8 % measured using an ion chamber during IMRT QA were found to be caused by uncertainties in the delivered MLC positions. Studies investigating the sensitivity of 2D transmitted doses (or equivalent 2D intensity maps) to individual MLC leaf errors are small in number [7, 143, 144]. In a study by Fielding *et al*, IMRT fields were delivered to a humanoid phantom and the 2D transmission signal was measured using an EPID. Patient positioning and delivery errors were artificially introduced to determine whether changes could be observed in the EPID images. Using a ratio-of-images technique developed by the authors, delivery errors in the form of 2 mm MLC shifts could be detected. Depuydt *et al* performed EPID dose measurements while simulating a malfunction of an MLC leaf in a delivered IMRT field. Gamma maps were investigated as a potential tool detecting the error in the EPID images. The authors demonstrated that using extremely relaxed gamma criteria (10 %/3 mm) still revealed visually large errors in the gamma maps, although an overall gamma score to quantify the errors in the field was not used in the study.

The aim of this chapter is to determine how sensitive, in theory, 2D transmitted doses are to MLC positioning errors in a head and neck conformal radiotherapy treatment. In particular, what dose differences can be detected at the transmitted dose plane (in the absence of measurements and other uncertainties) for MLC errors in the clinical range of 0–0.5 cm ? Furthermore, gamma map analysis was used to determine the magnitude of gamma scores calculated for shifts in a single leaf position, 5 random leaf positions and an entire bank of leaves, in each of the head and neck fields. Gamma scores of 90 % or lower in the transmitted dose distributions were classified as an indication of a significant delivery error (refer to chapter 3). Midplane dose maps inside the patient were also extracted to determine how well changes in transmitted dose correlate with dose changes at the patient level. Dose-volume histograms were then evaluated to determine the clinical impact of the MLC errors on doses to the target volume and surrounding critical structures.

6.2 Materials and methods

6.2.1 Modification of patient head and neck CT scans

CT scans of a patient previously treated at the Royal Adelaide Hospital with 3D conformal radiotherapy of the head and neck were used in this study. Although the anatomy of the head and neck region is considerably smaller than the pelvis-abdomen region (compared with chapter 5) it was necessary to introduce an additional volume of air surrounding the head and neck scans in order to model the transmitted dose for oblique beam geometries and for extended SSDs to the EPID. The procedure outlined in chapter 5 was adopted for modifying the CT scans used in this study. The original 512 pixels × 512 pixels sized images were padded with 2 matrices of dimensions 428 rows × 1152 columns and 2 matrices of dimensions 512 rows × 320 columns, each with Hounsfield Units = -1000 (corresponding to the density of air in the planning system). The result was an image of dimensions 1368 pixels × 1152 pixels as shown in figure 6.2.1. The modified CT matrices were saved in DICOM format using the Matlab imaging tool box and exported to a Pinnacle^3 computer workstation.

6.2.2 A 3D CRT Head and Neck treatment plan using the modified CT scans

The CT images in Pinnacle^3 were presented to a radiation oncologist and radiotherapist in the department, who agreed to contour the images and design a conformal radiotherapy treatment plan, respectively. The oncologist outlined the target volume and critical structures including the spinal cord, larynx and parotids. The treatment plan consisted of six, monoisocentric fields (left- and right-lateral, left- and right-posterior, anterior-posterior (neck) and anterior-posterior (supraclavicular)) using 6 MV photons with 2 Gy/fraction prescribed to the isocentre in 25 fractions. The 6 MV beam was modeled on a Varian Clinac 21EX linear accelerator equipped with 80-leaf MLCs. All dose calculations were performed using the collapsed-cone convolution dose engine using a dose grid size of 0.25

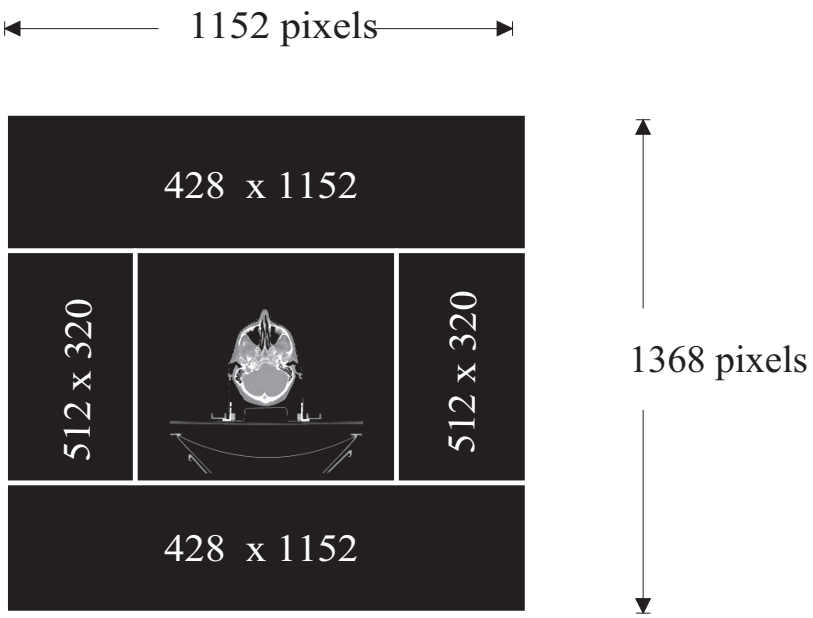

Figure 6.2.1: *A modified CT slice consisting of the original 512 × 512 matrix surrounded by two pairs of matrices of dimensions 428 × 1152 and 512 × 320.*

$\times$ 0.25 $\times$ 0.25 cm^3.

6.2.3 Simulation of the 2D transmitted dose

Once the treatment plan was completed, a copy of the plan was saved and duplicated 6 times so that the transmitted dose could be calculated individually for each of the 6 fields. This was achieved by removing all but one of the 6 beams in each plan. The Region Of Interest (ROI) tool available in Pinnacle^3 was used to create a "virtual" EPID for calculating the transmitted dose. The virtual EPID was constructed from a 32 $\times$ 5 cm^2 rectangle created in the axial plane of a given CT slice and assigned a density of 1 g/cm^3. The rectangle was then automatically pasted to multiple CT slices to form a 32 $\times$ 5 $\times$ 32 cm^3 water-equivalent volume. For each beam, the distance from the beam to d_{max} = 1.5 cm inside the virtual EPID was defined at 145 cm SSD, corresponding to one of the standard distances of the Varian EPID used in the department. For the two oblique beams, the coordinates of the virtual EPID were derived using trigonometry based on

the known beam angles, the isocenter-to-virtual EPID distance (defined above) and the dimensions of the virtual EPID. Upon creating the virtual EPIDs at oblique angles, step artifacts at the edges were observed due to the finite rectilinear grid used by the planning system. Such artifacts have been reported in the literature involving MC simulations of transmitted dose in oblique rectangular slabs created on a Cartesian grid [95]. In the current study, the height and length of the steps ranged from 0.089–0.17 cm and was not expected to introduce significant artifacts in the calculated isodose lines since the largest step size was smaller than the dose grid size (0.25 cm). However, a dose calculation in one of the oblique beams revealed significant undulations in the isodose lines (of the order of 30 %) at the entrance surface of the virtual EPID (figure 6.2.2). This is most likely a result of interpolation in the dose grid across the discrete steps in the CT data. Such artifacts were considered to be irrelevant in this study as they did not occur below the surface of the virtual EPID itself (including at d_{max}).

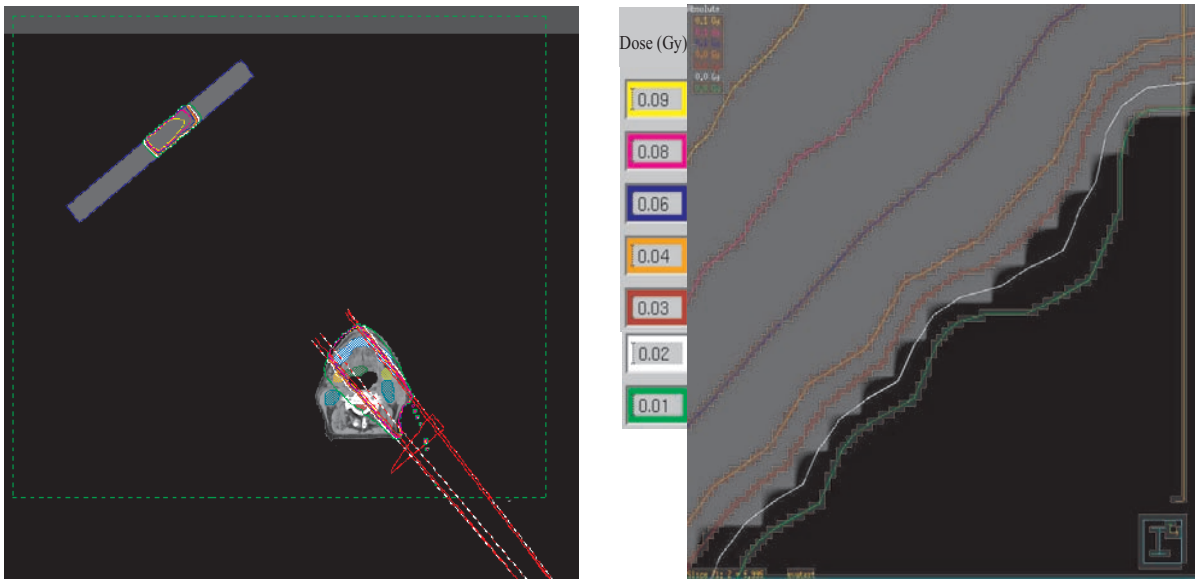

(a) (b)

Figure 6.2.2: *(a) Simulation of transmitted dose in a water-equivalent medium for one of the oblique beams, and (b) close up of the surface of the transmitted dose medium showing artifacts in the isodose lines. The artifacts are only present at the surface of the virtual EPID.*

In each plan the dose distribution was calculated using the collapsed-cone convolution dose engine on a 0.25 cm x 0.25 cm x 0.25 cm dose grid. The dose matrix file corresponding to each beam was extracted using the procedure described in chapter 3. However, for the oblique beams, an additional step was required to be able to extract the transmitted dose in a rectilinearly defined plane. The 3D dose array reconstructed in Matlab was rotated about the isocenter (in the axial plane) so that the transmitted dose calculated in the plane of the virtual EPID was aligned in rows and columns. This allowed for the transmitted dose distribution at d_{max} to be extracted as a single 2D matrix. The new coordinates of d_{max} in the rotated array were then derived using the following transformation equation:

$$\begin{pmatrix} x' \\ y' \\ z' \end{pmatrix} = \begin{pmatrix} cos\theta & sin\theta & 0 \\ -sin\theta & cos\theta & 0 \\ 0 & 0 & 1 \end{pmatrix} \begin{pmatrix} x \\ y \\ z \end{pmatrix}, \tag{6.2.1}$$

where x, y and z are the co-ordinates of d_{max} in the 3D dose matrix (before the matrix transformation) and x', y' and z' are the co-ordinates of d_{max} in the dose matrix following the 3D matrix rotation by the angle, θ. A diagram indicating the geometry of the 3D matrix rotation is shown in figure 6.2.3.

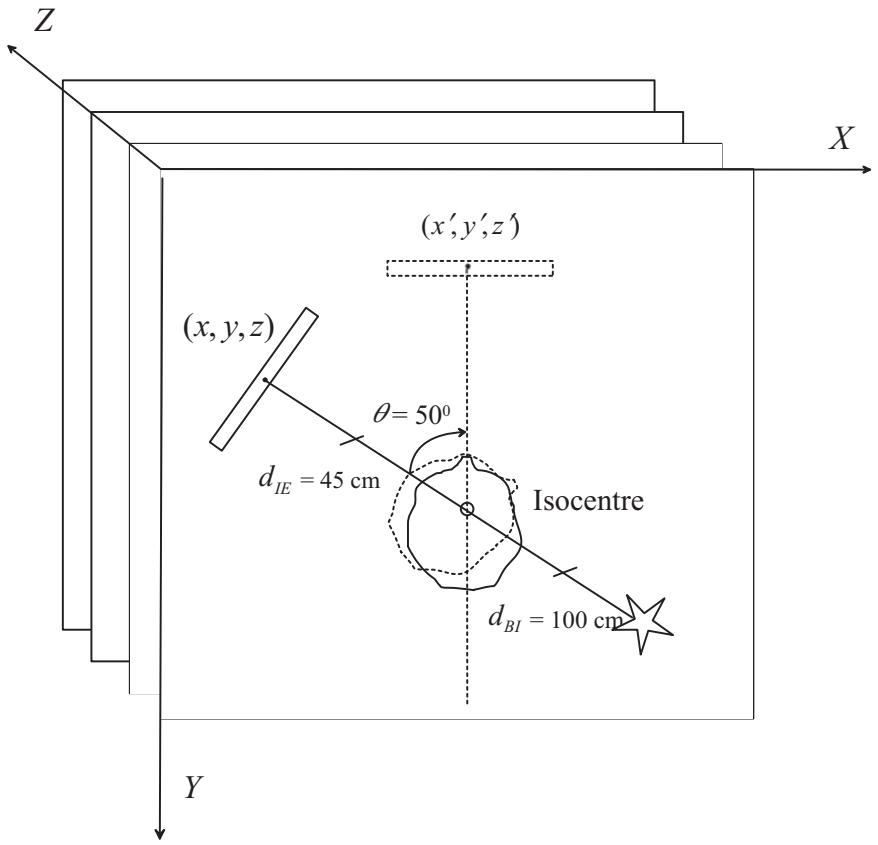

Figure 6.2.3: *The co-ordinate system in Matlab used to derive the coordinates of d_{max} in the virtual EPID following the 3D matrix rotation. The dose matrix for the right-posterior oblique beam is shown. The beam focus-to-isocentre distance is denoted by d_{BI}, and the isocentre-to-EPID distance (defined at d_{max}, not at the surface) is denoted by d_{IE}.*

Since this step involved additional image processing (compared with orthogonal beams), the isodose lines calculated inside the virtual EPID were compared before and after rotating the 3D dose array (figure 6.2.4). No significant differences in the isodose lines were observed and in particular, the dose at d_{max} before and after the rotation differed by only 0.2 %.

Finally, the extracted transmitted dose maps were cropped at 5 % isodose lines relative to the local maximum dose. This was performed for two reasons. Firstly, to incorporate gamma analysis within the radiation field, by excluding dose regions outside the radiation field. This would otherwise produce misleadingly high gamma scores as a result of the

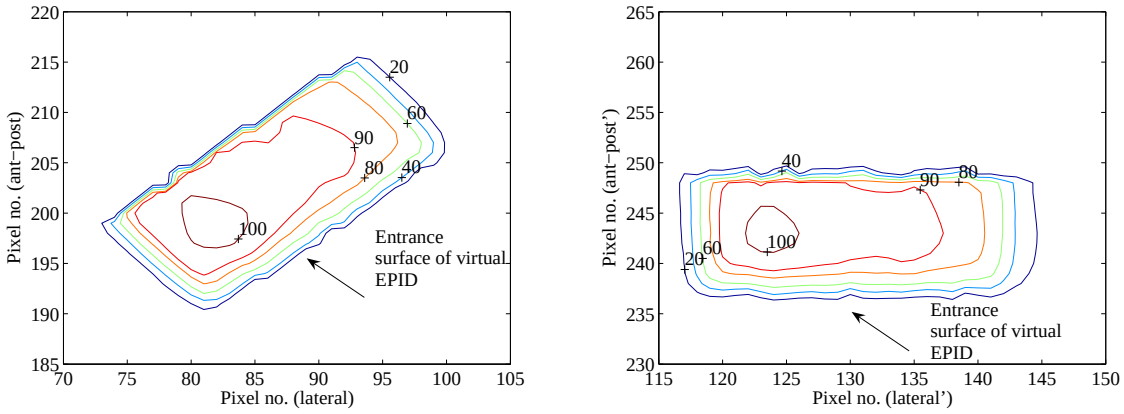

(a) (b)

Figure 6.2.4: *(a) An axial view through the transmitted dose medium before rotation and (b) after rotation. A direct comparison of isodose lines (20 %, 40 %, 60 %, 80 %, 90 %, and 100 % - relative to d_{max}) revealed no significant changes in dose after rotating the 3D dose array.*

majority of EPID dose regions in agreement outside the the radiation field[1]. Secondly, 5 % isodose lines provide an additional margin for detecting possible MLC errors (discussed in the following section) in the radiation field. The final Beam's Eye View (BEV) dose maps extracted at d_{max} in the virtual EPIDs for each of the six beams are shown in figure 6.2.5.

[1]The EPID area itself is much larger than the radiation field size.

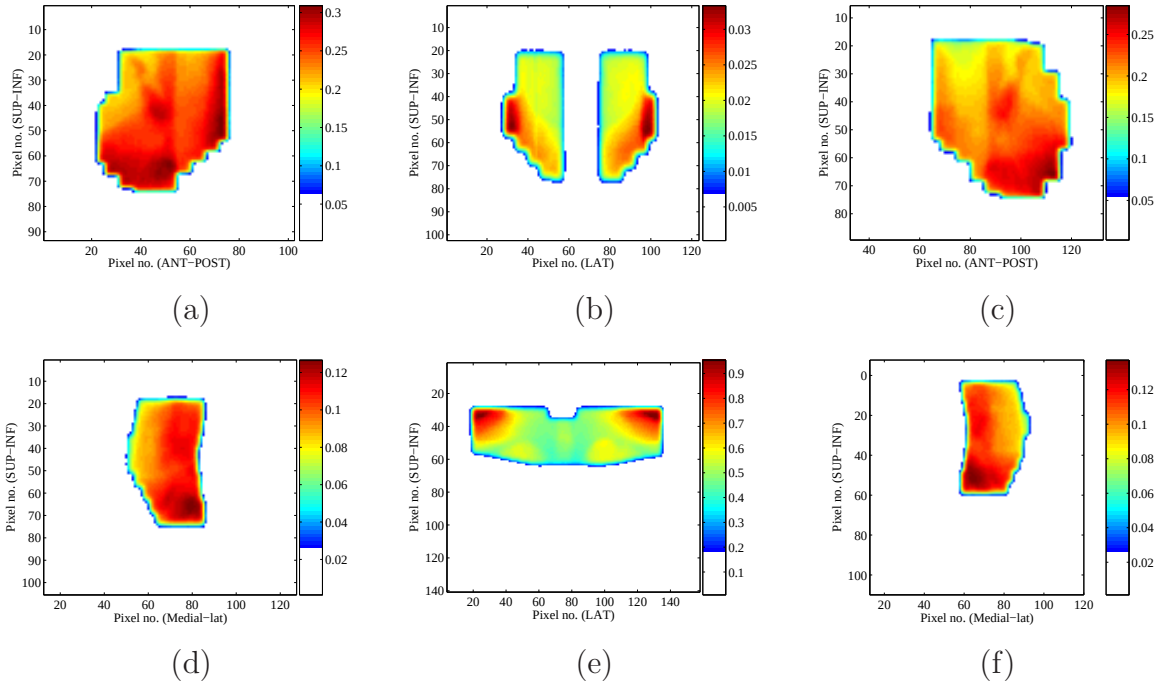

Figure 6.2.5: *Calculated transmitted dose maps (at d_{max} = 1.5 cm in the plane of the virtual EPID) cropped at the 5 % isodose lines. (a) Left-lateral beam, (b) anterior beam (neck), (c) right-lateral beam, (d) left posterior-oblique beam, (e) anterior beam (supraclavicular), and (f) right posterior-oblique beam.*

6.2.4 Simulation of MLC errors in the head and neck treatment plan

Minimum detectable MLC shifts

Beam delivery errors were simulated by shifting a single leaf by 0.01 cm, 0.02 cm, 0.05 cm, 0.10 cm, 0.25 cm and 0.5 cm at five arbitrary locations in each of the six fields. Dose difference maps at the calculated transmitted dose plane were recorded to determine the size of the dose variations as a function of leaf shift size. Dose difference maps were defined as:

$$\Delta D(i,j) = \frac{D_{leaf}(i,j) - D_{orig}(i,j)}{D_{orig,max}} \times 100\%, \tag{6.2.2}$$

where $D_{leaf}(i,j)$ and $D_{orig}(i,j)$ are 2D dose matrices corresponding to plans with and without the introduced leaf errors, respectively, and $D_{orig,max}$ is the maximum dose in

$D_{orig}(i, j)$. In addition, gamma analysis using 3%/2.5 mm criteria was used to record gamma scores for each MLC error introduced into each field.

Efficacy of gamma evaluation for detecting MLC errors

The gamma formalism as discussed in chapter 3 was assessed for error detection in MLC beam deliveries. Errors in the form of a single leaf, 5 leaves and an entire bank of leaves shifted from 0–0.5 cm in each field, were simulated to determine at what point gamma maps reflect a clinically significant error in beam delivery. Gamma scores of 90 % or less were considered to be an indication of a relevant delivery error [126, 127].

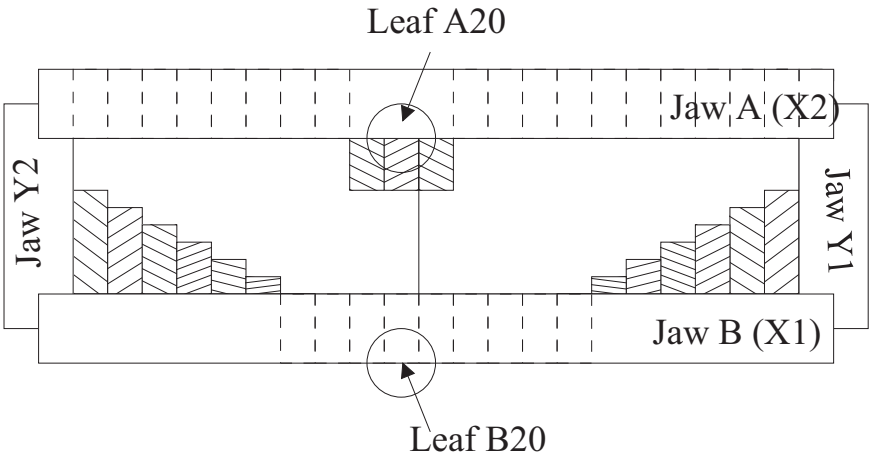

Figure 6.2.6: *The anterior-posterior (supraclavicular) field. The locations of leaves A20 and B20 are circled. (Note that leaf B20 is hidden behind jaw B).*

Impact of dose grid size on the predicted transmitted dose

All treatment planning dose calculations in this study were performed using a dose grid size of 0.25 × 0.25 × 0.25 cm^3, as is routinely used by planners in this department. However, due to the size of the calculation grid compared with the size of the smallest leaf shifts that were simulated (0.01 cm at the isocenter[2]), dose calculations were repeated for grid sizes ranging from 0.1 × 0.1 cm^2 to 0.4 × 0.4 cm^2 at the virtual EPID, to determine

[2]Corresponding to manufacturer's stated accuracy in leaf positioning.

whether a dose grid size of 0.25×0.25 cm^2 or larger is sufficient for detecting the simulated MLC leaf errors. The anterior-posterior (supraclavicular) field was chosen for this study and beam delivery errors involving two MLC leaves located at different distances from the jaw were simulated (figure 6.2.6). Leaf "A20" located 1.07 cm in front of jaw "A" and leaf "B20" located 0.02 cm behind jaw "B" were each shifted to and from their original positions from 0–0.3 cm, in 0.01 cm increments. Dose difference in the plane of the virtual EPID as a function of leaf displacement for the two leaves were recorded; firstly using a dose calculation grid size of 0.25×0.25 cm^2, followed by 0.10×0.10 cm^2, 0.15 cm $\times$ 0.15 cm^2, and 0.4×0.4 cm^2.

Midplane dose

In order for transmission dosimetry to be applicable as an independent and stand-alone tool for patient *in vivo* dosimetry, the dosimetric information contained within transmitted dose maps should correlate with the dose inside the patient. This was investigated by recording any dose differences at the midplane of the patient PTV as a function of leaf displacements, and compared with any dose differences at the transmitted dose level. Correlations between differences at the transmitted dose plane and patient midplane PTV have been investigated by some authors involving prostate cancer patient studies [145]. A good correlation was found on a beam-by-beam basis for a large group of patients. For the anterior-posterior (supraclavicular) field chosen, the midplane is defined as the plane intersecting the isocenter, parallel to the transmitted dose plane as shown in figure 6.2.7.

Dose-volume histograms

Dose-Volume Histograms (DVHs) were used to assess the clinical impact of the MLC errors on the dose delivered to the patient. DVHs in the original head and neck plan containing all six beams were extracted for the Planning Target Volume (PTV), spinal cord, larynx and the left and right parotids. MLC leaf errors involving a single leaf, five leaves and a complete bank of leaves were firstly introduced separately into each of the six fields and the 3D dose was calculated in each case. This simulates a possible random error

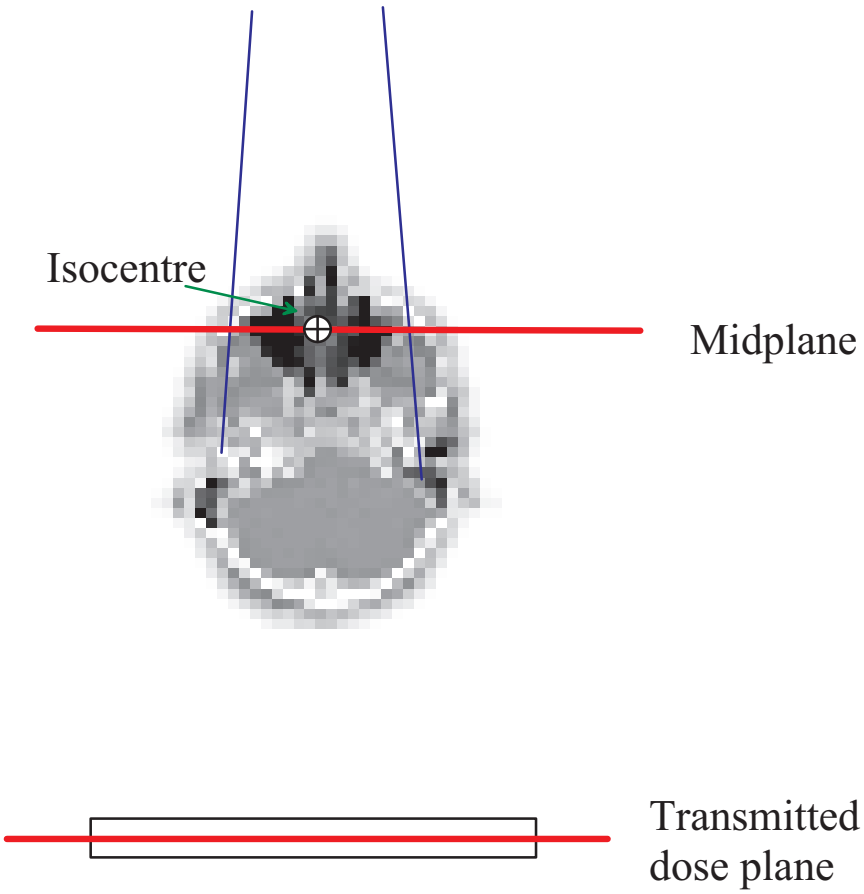

Figure 6.2.7: *(a)Location of the midplane relative to the transmitted dose plane for the anterior-posterior (supraclavicular) beam.*

occurring in either of the six fields. A systematic error was then simulated by replicating the same MLC errors throughout all six fields. The single leaf, five leaves and bank of leaves were each simulated within the clinical range 0–0.5 cm for two different shift sizes (0.25 cm and 0.5 cm). The minimum dose, maximum dose and average dose delivered to the outlined volumes were recorded and compared with values recorded in the original treatment plan.

6.3 Results

Minimum detectable MLC shifts

Figures 6.3.1 (a)–(d) are difference maps plotted in the transmitted dose plane for the anterior-posterior field (neck) resulting from leaf shifts of 0.01 cm, 0.02 cm, 0.05 cm and 0.1 cm at five different positions. The radiation field (defined by the 5 % isodose lines) is represented by the blue contour overlaid on each figure. In the colour map alongside each figure, the blue end of the spectrum represents negative dose differences (ie a decrease in dose relative to the original planned dose, corresponding to a leaf shift towards the center of the field) and the red end of the spectrum represents positive dose differences (ie an increase in dose relative to the original planned dose, corresponding to a leaf shift away from the center of the field). Figure 6.3.1 (a) shows that at five different leaf locations only one leaf shift (0.01 cm) registered a dose difference (+7 %).

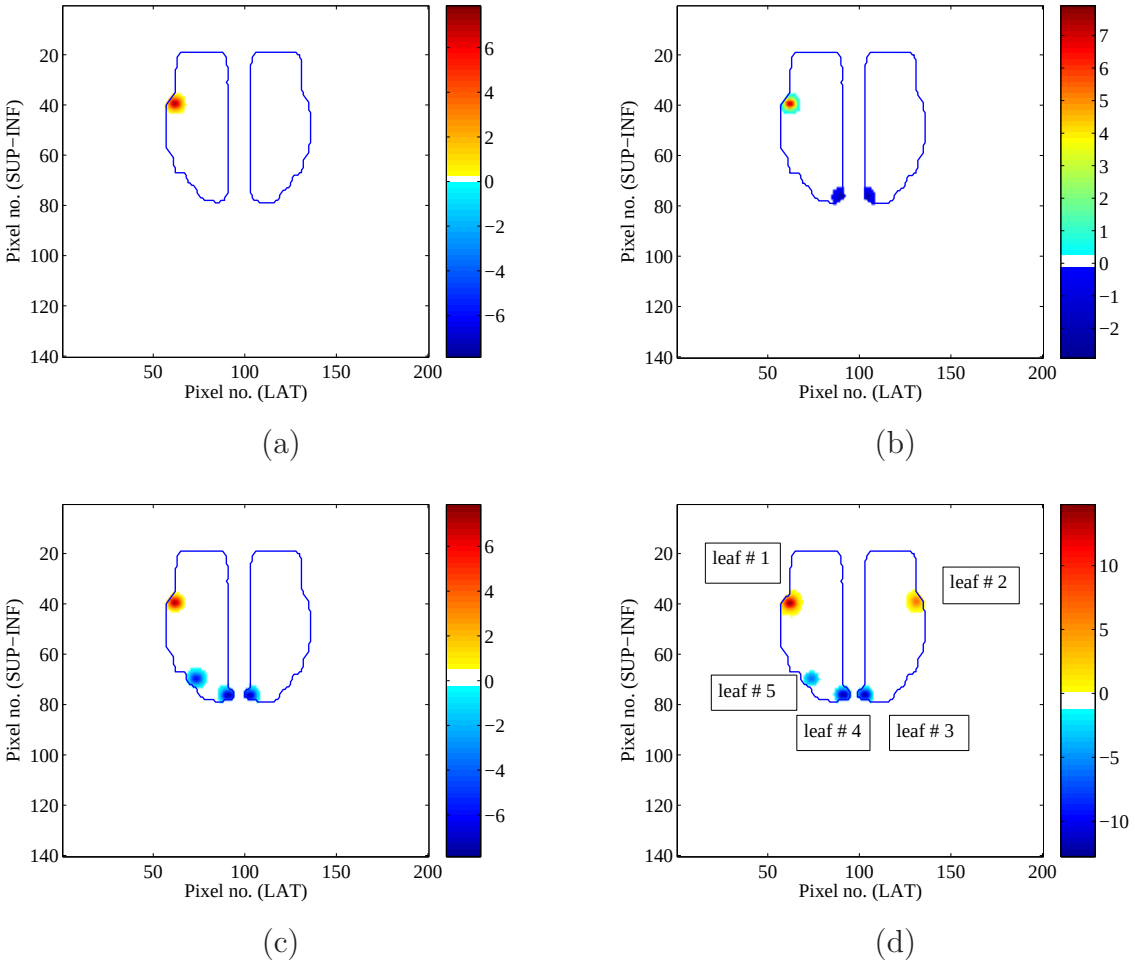

Figure 6.3.1: *Difference maps in the transmitted dose plane resulting from five leaves (leaf # 1- leaf# 5) shifted by (a) 0.01 cm, (b) 0.02 cm, (c) 0.05 cm, and (d) 0.1 cm.*

For a shift size of 0.02 cm in the same five leaf positions, an additional two leaves were detected producing dose differences both within −3 %. A shift size of 0.05 cm resulted in a single additional leaf error of −5.9 %. Finally, all 5 leaf shifts were detected for a shift size of 0.1 cm. Dose differences resulting from the 0.1 cm shifts were +14 %, +6.6 %, −12 %, −12 % and −5.9 %, for leaf numbers 1, 2, 3, 4 and 5, respectively (figure 6.3.1(d)). For leaf shifts of 0.25 cm and 0.5 cm (figures not shown), all five leaves were detected in this manner. It was found that in all six fields, all five randomly chosen leaves that were shifted by 0.1 cm or more caused a detectable dose difference at the transmitted dose plane. The results (number of leaves detected) for the five leaves shifted by 0–0.5 cm in

each field is summarised in table 6.3.1.

Table 6.3.1: *The number of leaves detected at the transmitted dose plane resulting from the MLC displacement errors simulated in each of the six beams.*

	Leaf shift					
Beam	0.01 cm	0.02 cm	0.05 cm	0.10 cm	0.25 cm	0.50 cm
L-LAT	0/5	0/5	4/5	5/5	5/5	5/5
R-LAT	0/5	0/5	0/5	5/5	5/5	5/5
AP(neck)	1/5	3/5	4/5	5/5	5/5	5/5
AP(sclav)	0/5	1/5	4/5	5/5	5/5	5/5
L-POST OBL	2/5	2/5	5/5	5/5	5/5	5/5
R-POST OBL	1/5	3/5	4/5	5/5	5/5	5/5

Efficacy of gamma evaluation for detecting MLC errors

Table 6.3.2 is a summary of the gamma map maps analysed for MLC shifts of 0–0.5 cm introduced into each of the head and neck fields. Gamma scores were recorded to give a quantitative indication of the MLC errors at the transmitted dose level. Perfect gamma scores (100 %) were obtained for all leaf shifts in the range 0–0.1 cm and hence were not recorded in table 6.3.2. Significant gamma scores of 90 % or less only occurred for leaf shifts (0.25 cm or greater) involving five leaves or more. Furthermore, the table indicates that errors involving a smaller number of leaves (ie five) shifted by a greater amount (ie 0.5 cm) can potentially have the same overall impact as errors involving a larger number of leaves (ie a bank of leaves) but shifted by a smaller amount (ie 0.25 cm). For example, similar gamma scores of less than 90 % occurred for both the 5 leaf/ 0.5 cm shift combination and the leaf bank/0.25 cm shift combination. This is also shown in figure 6.3.2 which illustrates that the relative proportion of regions exceeding the 3%/2.5 mm criteria are similar in the two cases. Table 6.3.2 also shows that gamma scores for the oblique beams were slightly worse (for the same leaf shifts) than the other fields. This is most likely due to the slightly smaller field size which effectively increases the proportion of regions exceeding 3%/2.5 mm relative to the radiation field size, hence reducing the

Table 6.3.2: *Gamma scores calculated with 3%/2.5 mm criteria for 0.25 cm and 0.50 cm leaf shifts introduced into each of the six fields.*

	One leaf		Five leaves		Bank of leaves	
Beam	0.25 cm	0.5 cm	0.25 cm	0.5 cm	0.25 cm	0.5 cm
L-LAT	99 %	98 %	95 %	94 %	90 %	88 %
R-LAT	99 %	98 %	95 %	94 %	97 %	94 %
AP(neck)	99 %	99 %	93 %	91 %	89 %	86 %
AP(sclav)	99 %	99 %	95 %	93 %	87 %	85 %
L-POST OBL	98 %	97 %	90 %	86 %	88 %	87 %
R-POST OBL	98 %	97 %	90 %	88 %	86 %	82 %

overall gamma score. This enforces the need to crop dose distributions tightly to the radiation field, in order for gamma scores to be used as a sensitive, quantitative measure of MLC delivery errors.

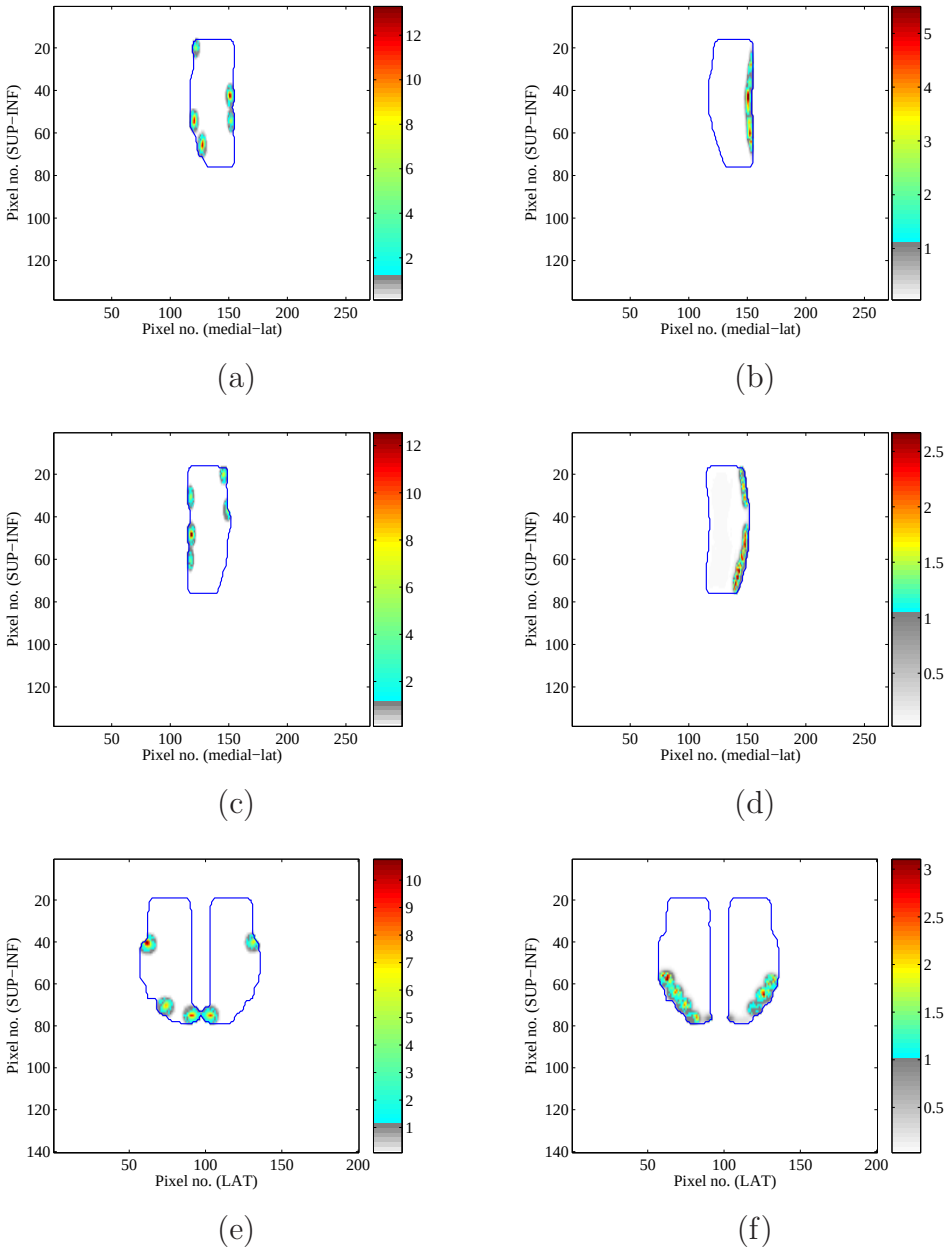

Figure 6.3.2: *Comparison of gamma maps (3 %/2.5 mm) for two different combinations of shift size and number of leaves shifted. (a) Five leaves/0.5 cm shift in the L-OBL beam, (b) bank of leaves/0.25 cm shift in the L-OBL beam, (c) five leaves/0.5 cm shift in the R-OBL beam, (d) bank of leaves/0.25 cm shift in the R-OBL beam, (e) five leaves/0.5 cm shift in the AP(neck) beam, and (f) bank of leaves/0.25 cm shift in the AP(neck) beam.*

Impact of dose grid size on the predicted transmitted dose

For the anterior-posterior field (supraclavicular), the maximum and minimum variations in transmitted dose at leaf positions A20 and B20, as a function of leaf displacement are

shown in figure 6.3.3. Leaf displacements away from the centre of the field (relative to their original positions) are shown along the negative, horizontal axis and correspond to an increase in transmitted dose (refer to equation 6.2.2). Similarly, leaf shifts toward the centre of the field are shown along the positive, horizontal axis and correspond to a decrease in transmitted dose. Increasing the leaf shift size in leaf A20 (in both directions) cause dose variations to increase by up to 21 %. The dose increases in a step-wise manner rather than linearly due to the discrete sampling size of the dose calculations.

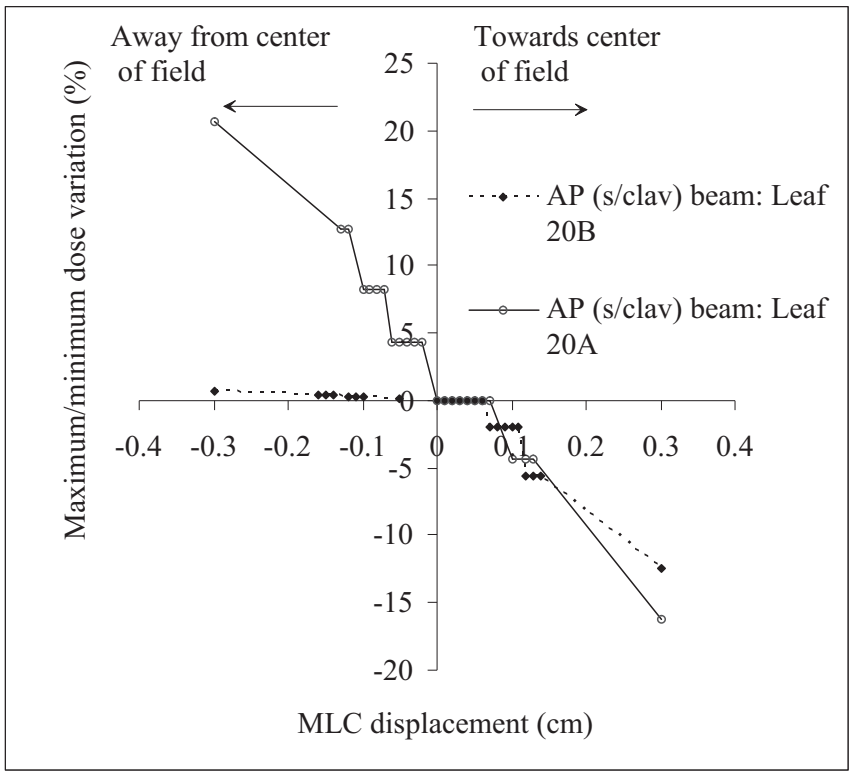

Figure 6.3.3: *The variation in transmitted dose as a function of leaf displacement for two different leaf positions (leaf 20A and 20B).*

This was also observed for leaf shifts involving leaf B20. Figure 6.3.3 also demonstrates that at leaf A20, shifts of up to 0.07 cm along the positive axis produced no dose variation, compared with -8 % for the same shift size in the opposite direction. Shifts in leaf B20 caused slightly smaller dose variations of up to 12 %, corresponding to a leaf

shift of 0.3 cm relative to its original location. Despite the initial location of leaf B20 underneath jaw B, shifts of up to 0.3 cm further underneath the jaw caused a small dose variation of 0.6 %. This non-zero signal variation is most likely due to small doses from the beam penumbra extending beyond the edge of the jaw as well as, possible differences in scattered dose contribution from the nearby jaw with increasing distance.

The stepped variations in dose with leaf displacement, observed in both leaf A20 and B20, prompted further investigation into the size of the dose grid. Calculations were thus repeated using the following range of dose grid sizes: 0.1×0.1 cm^2, 0.15×0.15 cm^2, 0.25×0.25 cm^2, and 0.4×0.4 cm^2. The results for the four different grid size calculations for leaf A20 are shown in figure 6.3.4. The superimposed curves show that dose differences due to MLC shifts using a grid size of 0.4×0.4 cm^2 can disagree by up to 4 %, compared with using a grid size of 0.15×0.15 cm^2. Thus, the particular grid size defined in Pinnacle^3 may impact on the accuracy of the predicted transmitted doses compared with measured transmitted doses. Since most 2D detectors (EPID and film, for example) have a spatial resolution of 0.1 cm or better, using a calculation grid size of 0.1 cm or smaller would be optimal. However, the version of the planning system used in this study allows a minimum grid size of 0.1×0.1 cm^2. Furthermore, this can only be achieved if the grid size perpendicular to this plane is 0.5 cm or greater. Attempting to calculate the dose using a finer dose grid produces memory allocation errors by the planning system. Similarly, calculations on a dose grid size of 0.15×0.15 cm^2 may only be carried out with a minimum dose grid size of 0.25 cm along the remaining axis. Thus, using a smaller grid size in the plane of the virtual EPID means a trade off in the dose resolution perpendicular to this plane. Hence, using an overall dose grid size of $0.15 \times 0.15 \times 0.25$ cm^3 may be more optimal than using an overall grid size of $0.10 \times 0.10 \times 0.5$ cm^3. This is evident in figure 6.3.4, in which one would expect greater discrepancies in predicted dose differences between 0.4×0.4 cm^2 and 0.1×0.1 cm^2 compared with 0.4×0.4 cm^2 and 0.15×0.15 cm^2, for example. In general, the discrepancy in dose variations using 0.4×0.4 cm^2 and 0.15×0.15 cm^2 grid sizes is greater than that of using 0.4×0.4

cm^2 and 0.10 × 0.10 cm^2 grid sizes. This is most likely due to the lower grid resolution perpendicular to virtual plane, in the latter grid size (0.5 cm) compared with the former grid size (0.25 cm).

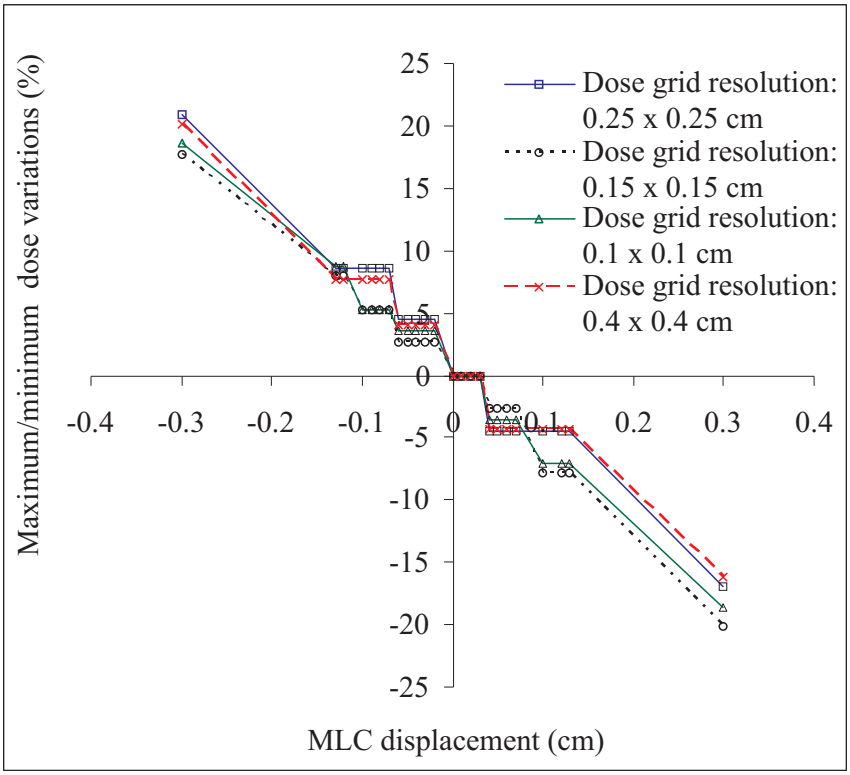

Figure 6.3.4: *Variation in transmitted dose as a function of leaf displacement for different dose grid sizes.*

Finally, figure 6.3.4 demonstrates that using a larger dose grid size tends to overestimate the dose difference resulting from MLC shifts along the negative axis, and underestimate the dose difference resulting from MLC shifts along the positive axis. This is mainly a consequence of dose interpolation by the planning system between discrete voxels. Large voxel sizes lead to either an under- or overestimation in dose compared with a smaller voxel size. This is illustrated in figures 6.3.5 and 6.3.6. Figure 6.3.5 indicates the in-plane beam profiles extracted from the anterior-posterior (supraclavicular) field at the transmitted dose plane for a typical MLC error. Figure 6.3.6 indicates the progressive deterioration in the estimated beam profiles with increasing voxel size.

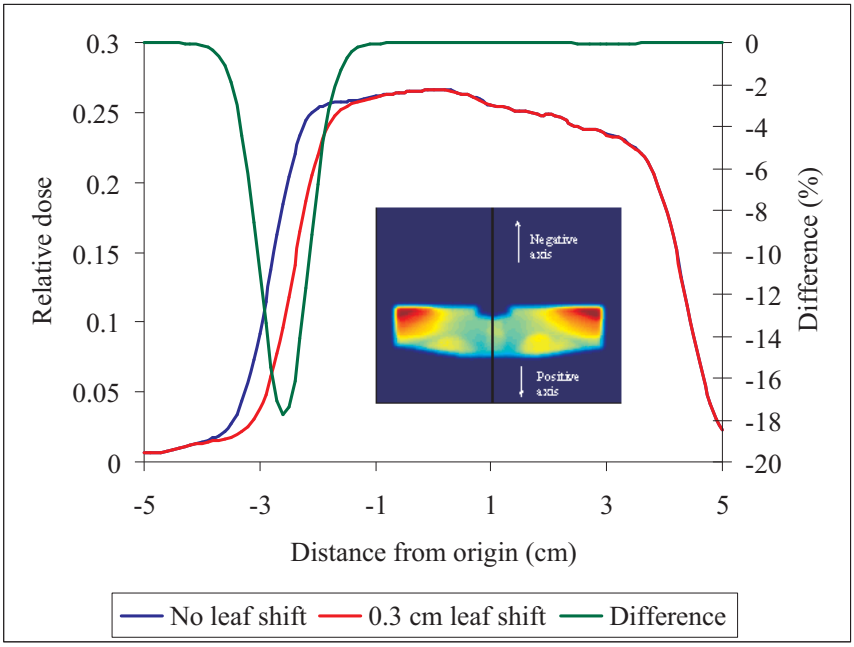

Figure 6.3.5: *Typical beam profiles (calculated using a 0.1 × 0.1 cm^2 grid size) intersecting at leaf A20 for a 0.3 cm leaf shift in leaf A20.*

Midplane dose

In addition to dose differences recorded in the transmitted dose plane, dose differences in the midplane for the anterior-posterior (supraclavicular) field for shifts at leaves 20A and 20 B were also recorded. Dose variations in the transmitted dose plane versus leaf displacement correlated well with variations in the midplane (figure 6.3.7). In figure 6.3.7(a), absolute differences predicted in the midplane were within ±3% of absolute differences predicted in the transmitted dose plane for leaf shifts of ±0.3 cm. Also, for leaf displacements of 0–0.07 cm along the positive axis, both planes recorded no dose differences. Similarly, in figure 6.3.7(b), differences recorded in the midplane agreed within 2 % with differences in the transmitted dose plane for leaf shifts of ±0.3 cm. This demonstrates that on a beam-by-beam basis, dose differences at the transmitted level caused by MLC errors are potentially a good surrogate for dose differences occurring inside the patient. Although a beam-by-beam analysis can not predict the cumulative effect of dosimetry errors inside the patient from combining all six beams, it does allow

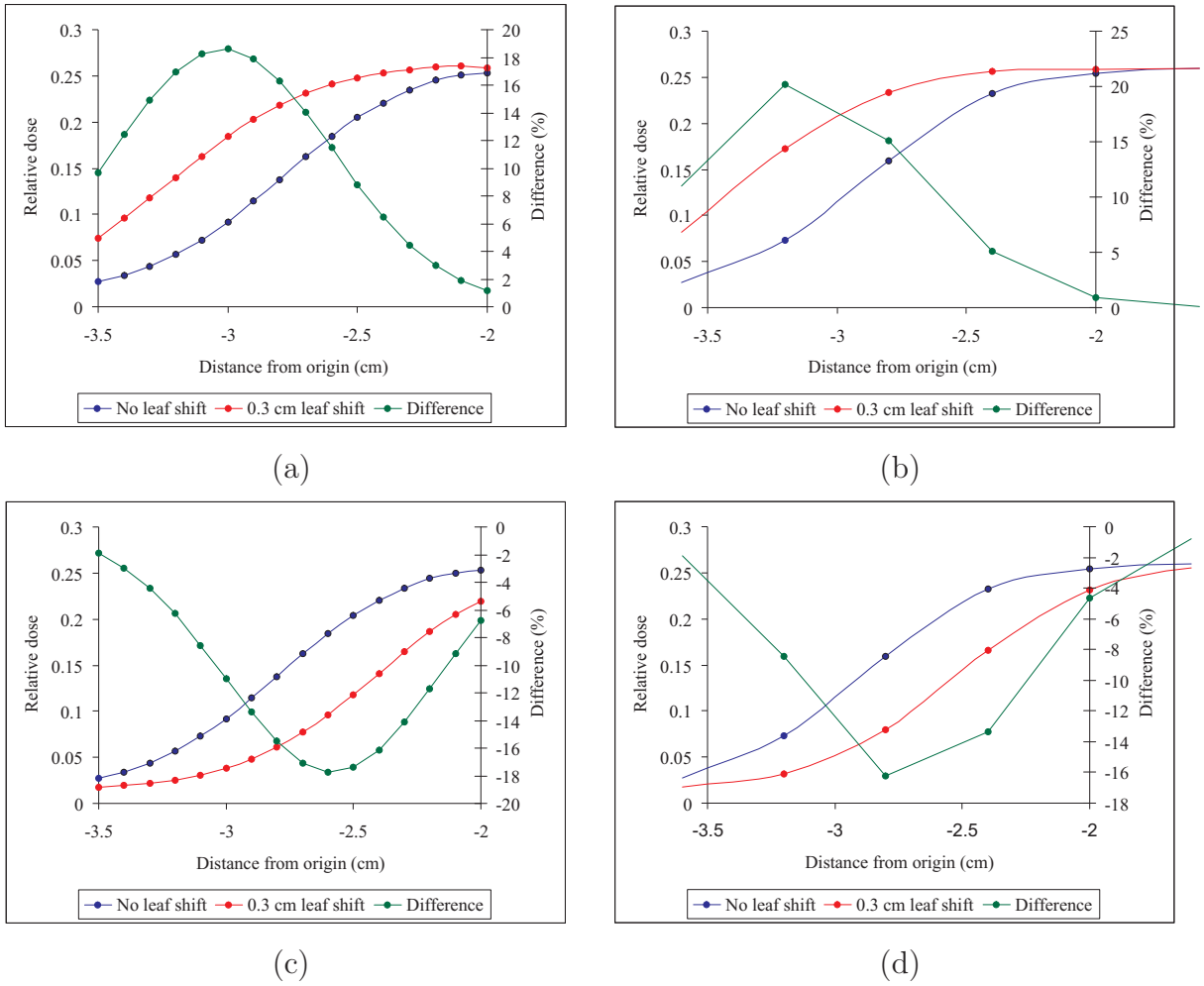

Figure 6.3.6: *Magnified views of beam profiles (with and without an MLC shift) at the plane of the virtual EPID for the anterior-posterior (supraclavicular) field. Dose difference profiles are superimposed. (a) Leaf A20 shifted by 0.3 cm shift along the negative axis using a 0.1 × 0.1 cm^2 calculation grid size, and (b) leaf A20 shifted by 0.3 cm shift along the positive axis using a 0.4 × 0.4 cm^2 calculation grid size.*

the source of the beam delivery errors to be isolated in individual beams.

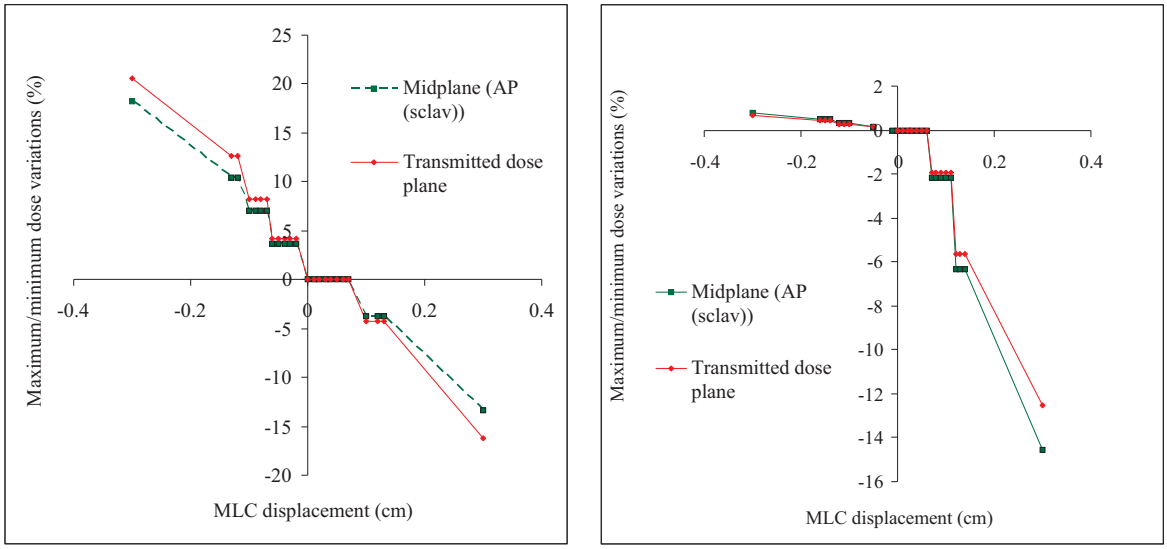

Figure 6.3.7: *Comparison of dose variations in the transmitted dose plane and midplane at two different leaf locations in the anterior-posterior (supraclavicular) field.(a) Leaf 20A and (b) leaf 20B.*

Dose-volume histograms

In general, the greatest changes in DVHs were caused by MLC leaf errors systematically present in all six beams, compared with MLC errors present in individual beams. This is shown in figures 6.3.8 and 6.3.9, and 6.3.10 and 6.3.11. In particular, the average dose to the larynx varied by $-$ 7.7 %, caused by the 0.25 cm shift in 5 leaves, compared with -4.1 % variation in dose to the larynx for an entire leaf bank shift (ten leaves) of 0.5 cm. This suggests that a larger shift (0.5 cm) in a larger number of leaves (ten) does not necessarily produce the largest dose variation. That is, dose variations depend on both the number and location of the leaves with respect to the tissue volume. The maximum dose received by the spinal cord was 185.6 cGy (+5.5 %) due to a 0.5 cm shift in five leaves, occurring in all six beams. However, the same size shift but in an entire leaf bank resulted in a similar dose maximum of 184.4 cGy (+4.8 %). The minimum dose to the PTV decreased by $-$ 6.8 % due to a 0.25 cm shift in a leaf bank in all six beams. For MLC errors introduced separately in each beam the delivered maximum dose (D_{max}),

minimum dose (D_{min}) and average dose (D_{avg}) varied by less than $\pm 5\%$ in all cases. For example, D_{max} to the spinal increased by +4.7 % due to 0.5 cm leaf shift in a leaf bank of the left-oblique posterior beam. For the same beam, a 0.25 cm shift in a leaf bank caused a reduction in D_{min} of -3.6 %. In the anterior-posterior (supraclavicular) field, D_{avg} to the larynx decreased by -4.9 % due to a 0.5 cm shift in five leaves. In the left-lateral beam, the worse dose variation also occurred in the larynx, in which D_{avg} decreased by -4.2 % due to 0.5 cm shift in a leaf bank. A summary of the DVH statistics for each outlined structure is recorded in tables 6.3.3–6.3.7. Due to symmetry in the results, errors simulated individually in each of the six beams are displayed for the left-oblique posterior, anterior-posterior (supraclavicular), left-lateral, and anterior-posterior (neck) beams only. Results for MLC errors simulated in all six beams are presented in full in table 6.3.7.

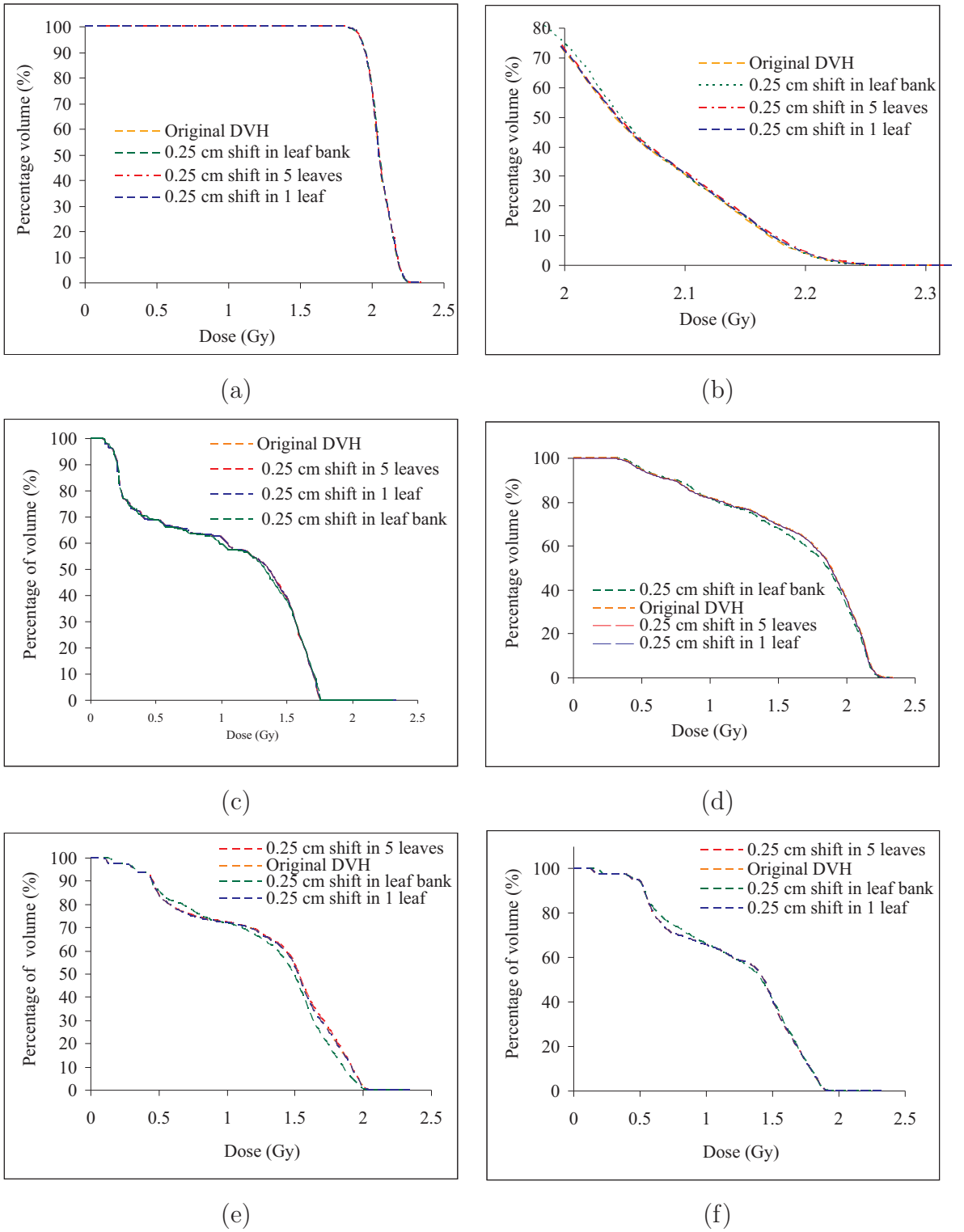

Figure 6.3.8: *Original DVHs and DVHs due to MLC errors present in the left-posterior oblique beam. (a) PTV, (b) a zoom in of PTV, (c) spinal cord, (d), larynx, (e) left parotid, and (f) right parotid.*

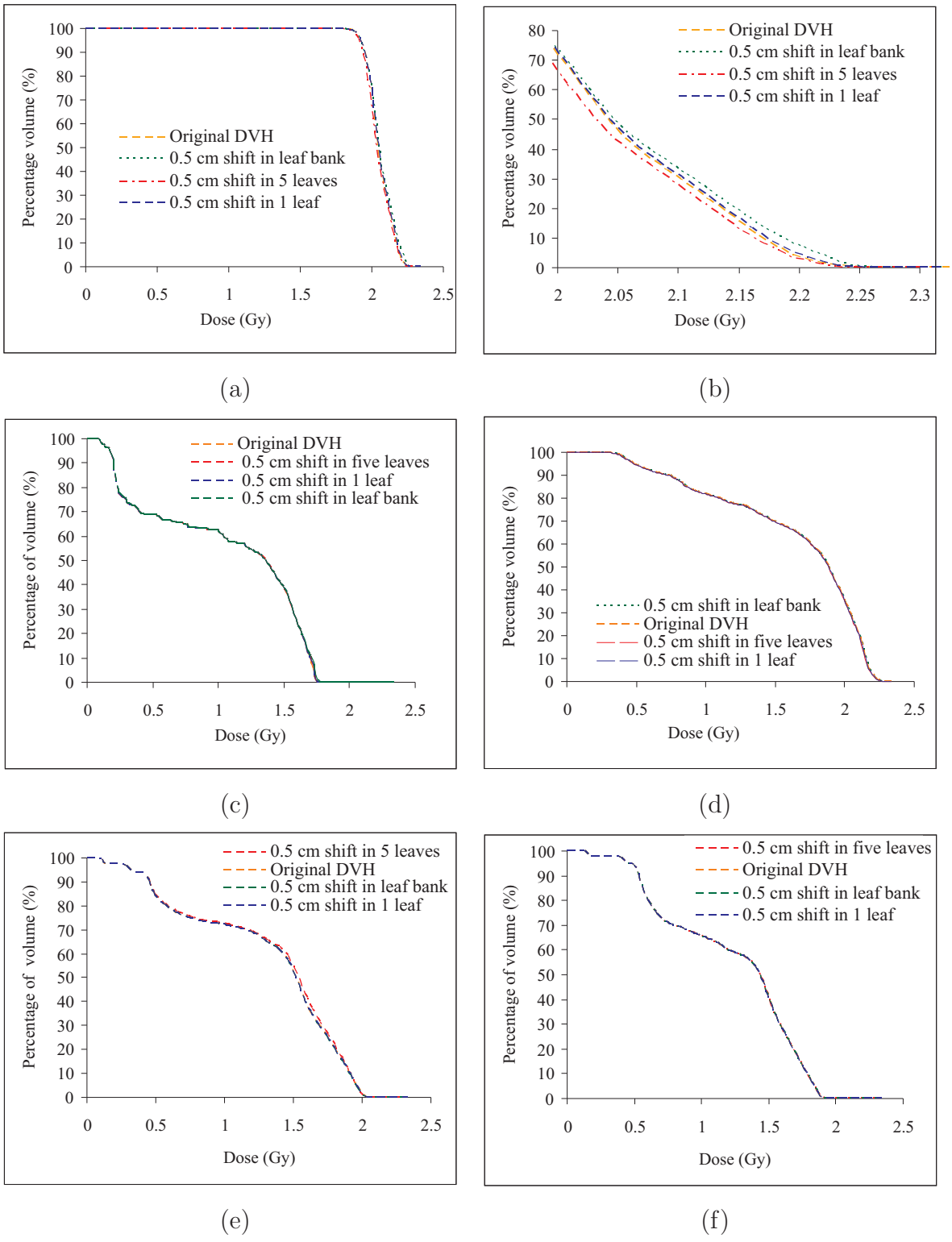

Figure 6.3.9: *Original DVHs and DVHs due to MLC errors present in the left-posterior oblique beam. (a) PTV, (b) a zoom in of PTV, (c) spinal cord, (d), larynx, (e) left parotid, and (f) right parotid.*

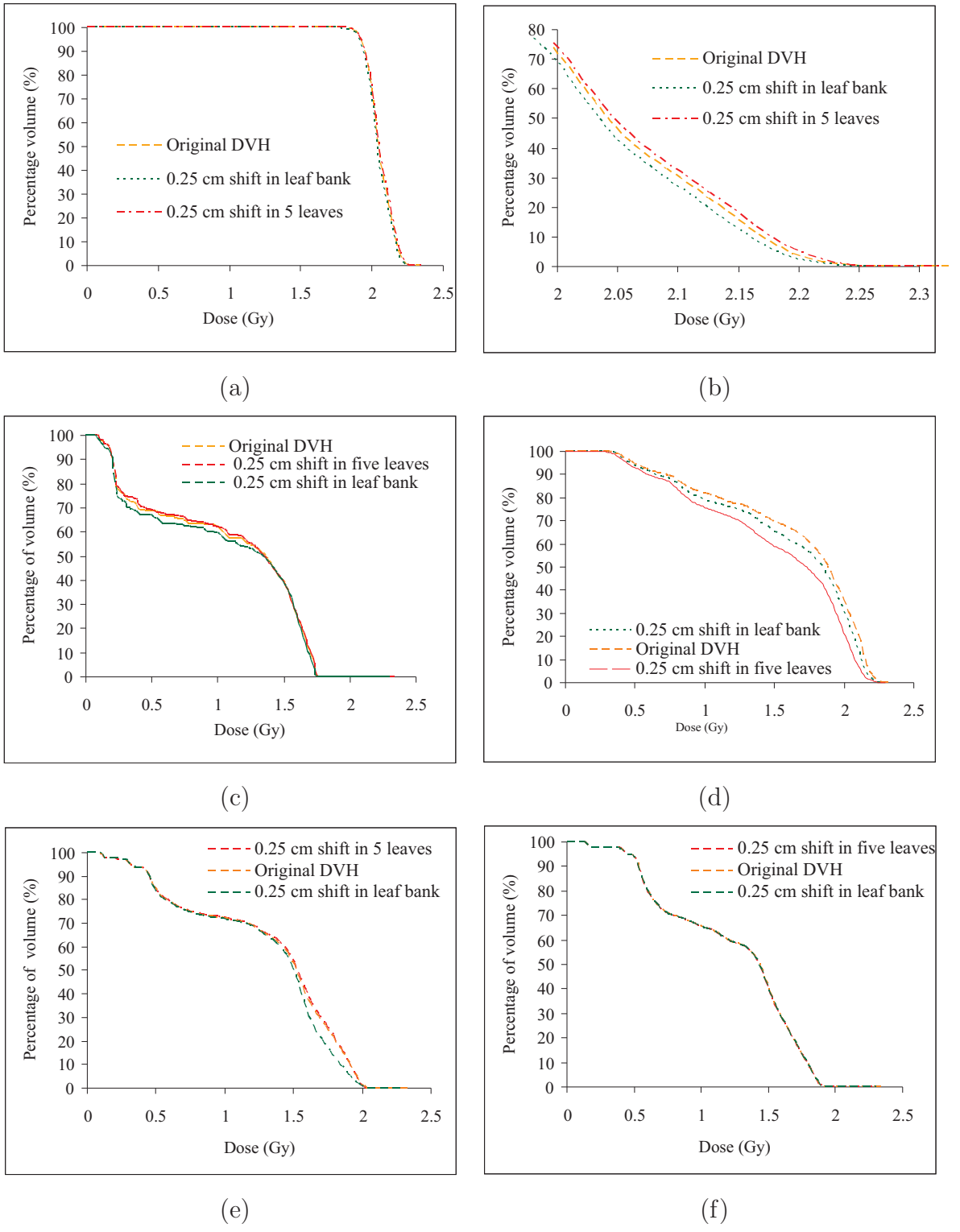

Figure 6.3.10: *Original DVHs and DVHs due to MLC errors present in all beams. (a) PTV, (b) a zoom in of PTV, (c) spinal cord, (d), larynx, (e) left parotid, and (f) right parotid.*

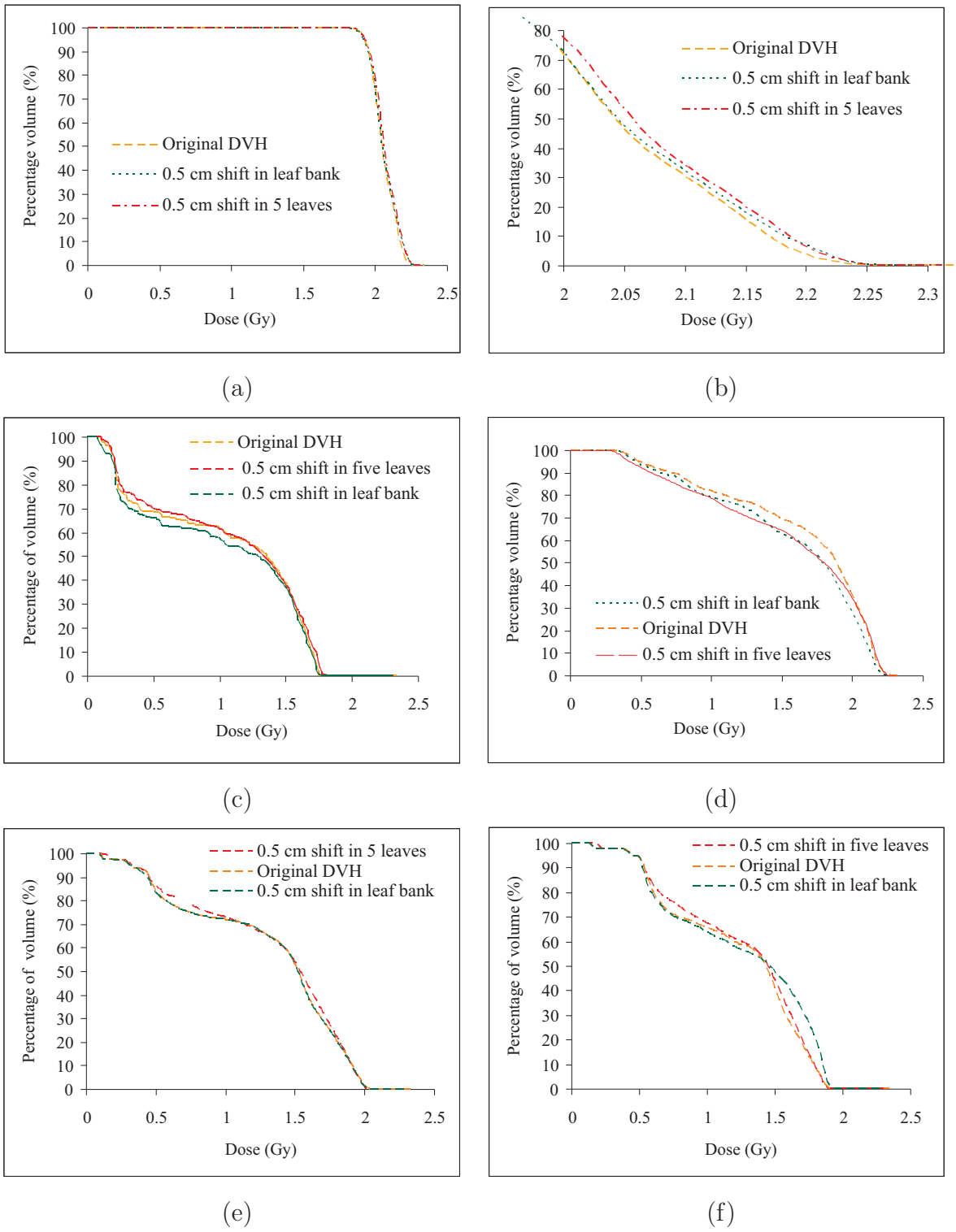

Figure 6.3.11: *Original DVHs and DVHs due to MLC errors present in all beams. (a) PTV, (b) a zoom in of PTV, (c) spinal cord, (d), larynx, (e) left parotid, and (f) right parotid.*

Volume	Original plan	0.25 cm shift			0.5 cm shift		
		1 leaf	5 leaves	leaf bank	1 leaf	5 leaves	leaf bank
PTV							
D_{max}	228.3 cGy	226.7 cGy	226.7 cGy	228.0 cGy	226.7 cGy	228.3 cGy	227.9 cGy
D_{min}	173.9 cGy	170.0 cGy	171.5 cGy	167.6 cGy	170.3 cGy	174.0 cGy	170.3 cGy
D_{avg}	205.6 cGy	204.7 cGy	204.8 cGy	205.5 cGy	204.8 cGy	206.0 cGy	205.3 cGy
Spinal cord							
D_{max}	176.0 cGy	175.0 cGy	175.0 cGy	176.0 cGy	177.4 cGy	177.1 cGy	184.4 cGy
D_{avg}	104.7 cGy	104.7 cGy	104.7 cGy	104.7 cGy	104.7 cGy	104.8 cGy	105.0 cGy
Larynx							
D_{max}	226.4 cGy	231.4 cGy	231.4 cGy	226.3 cGy	231.4 cGy	226.4 cGy	231.4 cGy
D_{avg}	162.9 cGy	164.2 cGy	164.2 cGy	162.5 cGy	164.2 cGy	162.8 cGy	164.3 cGy
Left parotid							
D_{max}	204.4 cGy	204.3 cGy	204.4 cGy	203.5 cGy	204.4 cGy	204.4 cGy	203.2 cGy
D_{avg}	131.9 cGy	130.5 cGy	131.4 cGy	128.7 cGy	130.5 cGy	133.8 cGy	130.5 cGy
Right parotid							
D_{max}	193.9 cGy	191.4 cGy	191.5 cGy	193.8 cGy	191.4 cGy	193.9 cGy	191.5 cGy
D_{avg}	123.0 cGy	121.4 cGy	121.4 cGy	123.0 cGy	121.4 cGy	123.1 cGy	121.4 cGy

Table 6.3.3: *D_{max}, D_{min} and D_{avg} DVH statistics recorded in the original plan and for plans simulated with MLC errors in the left-posterior oblique beam.*

Volume	Original plan	0.25 cm shift			0.5 cm shift		
		1 leaf	5 leaves	leaf bank	1 leaf	5 leaves	leaf bank
PTV							
D_{max}	228.3 cGy	226.6 cGy	227.7 cGy	227.7 cGy	226.6 cGy	227.7 cGy	226.7 cGy
D_{min}	173.9 cGy	170.3 cGy	171.4 cGy	171.4 cGy	170.3 cGy	171.3 cGy	170.3 cGy
D_{avg}	205.6 cGy	204.6 cGy	204.6 cGy	204.5 cGy	204.6 cGy	204.5 cGy	204.5 cGy
Spinal cord							
D_{max}	176.0 cGy	175.0 cGy	174.9 cGy	173.7 cGy	175.0 cGy	174.9 cGy	173.8 cGy
D_{avg}	104.7 cGy	105.1 cGy	104.3 cGy	103.5 cGy	105.6 cGy	102.9 cGy	102.0 cGy
Larynx							
D_{max}	226.4 cGy	231.3 cGy	231.2 cGy	231.2 cGy	231.3 cGy	231.2 cGy	231.4 cGy
D_{avg}	162.9 cGy	166.7 cGy	162.0 cGy	164.1 cGy	169.3 cGy	154.9 cGy	164.3 cGy
Left parotid							
D_{max}	204.4 cGy	204.3 cGy	204.2 cGy	204.2 cGy	204.3 cGy	204.2 cGy	204.4 cGy
D_{avg}	131.9 cGy	130.5 cGy	130.6 cGy	130.5 cGy	130.5 cGy	130.6 cGy	130.5 cGy
Right parotid							
D_{max}	193.9 cGy	191.4 cGy	191.3 cGy	191.3 cGy	191.4 cGy	191.3 cGy	191.4 cGy
D_{avg}	123.0 cGy	121.4 cGy	121.4 cGy	121.4 cGy	121.4 cGy	121.4 cGy	121.4 cGy

Table 6.3.4: *D_{max}, D_{min} and D_{avg} DVH statistics recorded in the original plan and for plans simulated with MLC errors in the anterior-posterior (supraclavicular) beam.*

Volume	Original plan	0.25 cm shift			0.5 cm shift		
		1 leaf	5 leaves	leaf bank	1 leaf	5 leaves	leaf bank
PTV							
D_{max}	228.3 cGy	226.6 cGy	226.6 cGy	227.3 cGy	227.8 cGy	227.8 cGy	226.9 cGy
D_{min}	173.9 cGy	170.3 cGy	170.3 cGy	170.5 cGy	170.2 cGy	170.3 cGy	171.4 cGy
D_{avg}	205.6 cGy	204.6 cGy	204.6 cGy	204.5 cGy	204.6 cGy	204.6 cGy	204.4 cGy
Spinal cord							
D_{max}	176.0 cGy	175.0 cGy	175.0 cGy	174.0 cGy	175.0 cGy	175.0 cGy	173.7 cGy
D_{avg}	104.7 cGy	105.7 cGy	105.7 cGy	103.5 cGy	106.6 cGy	106.7 cGy	102.3 cGy
Larynx							
D_{max}	226.4 cGy	231.3 cGy	231.3 cGy	225.0 cGy	231.3 cGy	231.3 cGy	224.6 cGy
D_{avg}	162.9 cGy	164.2 cGy	164.8 cGy	160.4 cGy	164.2 cGy	165.5 cGy	156.0 cGy
Left parotid							
D_{max}	204.4 cGy	204.3 cGy	204.3 cGy	204.1 cGy	204.3 cGy	204.3 cGy	203.8 cGy
D_{avg}	131.9 cGy	130.5 cGy	130.6 cGy	130.6 cGy	130.5 cGy	130.6 cGy	130.5 cGy
Right parotid							
D_{max}	193.9 cGy	191.4 cGy	191.4 cGy	191.4 cGy	191.4 cGy	191.4 cGy	191.0 cGy
D_{avg}	123.0 cGy	121.4 cGy	121.4 cGy	121.4 cGy	121.4 cGy	121.4 cGy	121.3 cGy

Table 6.3.5: *D_{max}, D_{min} and D_{avg} DVH statistics recorded in the original plan and for plans simulated with MLC errors in the left-lateral beam.*

		0.25 cm shift			0.5 cm shift		
Volume	Original plan	1 leaf	5 leaves	leaf bank	1 leaf	5 leaves	leaf bank
PTV							
D_{max}	228.3 cGy	226.6 cGy	226.6 cGy	226.9 cGy	226.7 cGy	226.7 cGy	226.9 cGy
D_{min}	173.9 cGy	170.3 cGy	170.3 cGy	170.5 cGy	170.3 cGy	170.3 cGy	170.5 cGy
D_{avg}	205.6 cGy	204.6 cGy	204.5 cGy	204.6 cGy	204.5 cGy	204.5 cGy	204.6 cGy
Spinal cord							
D_{max}	176.0 cGy	175.0 cGy	175.0 cGy	174.0 cGy	175.0 cGy	175.0 cGy	174.0 cGy
D_{avg}	104.7 cGy	104.7 cGy	104.7 cGy	104.7 cGy	104.7 cGy	104.8 cGy	104.7 cGy
Larynx							
D_{max}	226.4 cGy	231.3 cGy	231.3 cGy	231.6 cGy	231.4 cGy	231.4 cGy	231.6 cGy
D_{avg}	162.9 cGy	164.3 cGy	164.4 cGy	164.2 cGy	164.4 cGy	164.7 cGy	164.3 cGy
Left parotid							
D_{max}	204.4 cGy	204.3 cGy	203.2 cGy	204.6 cGy	204.4 cGy	200.8 cGy	204.6 cGy
D_{avg}	131.9 cGy	130.5 cGy	130.4 cGy	130.5 cGy	130.4 cGy	130.4 cGy	130.5 cGy
Right parotid							
D_{max}	193.9 cGy	191.4 cGy	190.2 cGy	191.6 cGy	191.4 cGy	190.3 cGy	191.7 cGy
D_{avg}	123.0 cGy	121.4 cGy	121.3 cGy	121.4 cGy	121.4 cGy	121.3 cGy	121.4 cGy

Table 6.3.6: *D_{max}, D_{min} and D_{avg} DVH statistics recorded in the original plan and for plans simulated with MLC errors in the anterior-posterior (neck) beam.*

		0.25 cm shift			0.5 cm shift	
Volume	Original plan	1 leaf	5 leaves	leaf bank	1 leaf	5 leaves	leaf bank
PTV							
D_{max}	228.3 cGy		227.8 cGy	227.0 cGy		228.6 cGy	227.8 cGy
D_{min}	173.9 cGy		171.5 cGy	162.1 cGy		173.6 cGy	170.0 cGy
D_{avg}	205.6 cGy		205.1 cGy	203.7 cGy		206.5 cGy	205.0 cGy
Spinal cord							
D_{max}	176.0 cGy		177.3 cGy	176.3 cGy		185.6 cGy	184.4 cGy
D_{avg}	104.7 cGy		105.8 cGy	103.0 cGy		107.2 cGy	105.0 cGy
Larynx							
D_{max}	226.4 cGy		225.3 cGy	227.4 cGy		226.6 cGy	225.5 cGy
D_{avg}	162.9 cGy		150.4 cGy	159.8 cGy		156.8 cGy	156.2 cGy
Left parotid							
D_{max}	204.4 cGy		202.2 cGy	205.3 cGy		201.9 cGy	203.5 cGy
D_{avg}	131.9 cGy		131.2 cGy	129.1 cGy		133.5 cGy	130.0 cGy
Right parotid							
D_{max}	193.9 cGy		191.8 cGy	193.8 cGy		190.8 cGy	193.1 cGy
D_{avg}	123.0 cGy		121.3 cGy	123.1 cGy		125.1 cGy	124.8 cGy

Table 6.3.7: *D_{max}, D_{min} and D_{avg} DVH statistics recorded in the original plan and for plans simulated with MLC errors in all six beams.*

6.4 Summary and conclusions

Calculating the transmitted dose inside a virtual EPID at oblique planes, using a TPS based on a rectilinear co-ordinate system is reliable, provided the dose is extracted below the surface of the virtual EPID. Due to discrete steps present at the surface of the virtual EPID, isodose line artifacts of up to 30 % were present at the surface but were found to be negligible (< 0.5 %) at d_{max} inside the virtual EPID. Simulating MLC delivery errors in a conformal radiotherapy head and neck treatment demonstrates that leaf shifts as small as 0.01 cm can theoretically be detected, which corresponds to a dose difference of 7 % at the virtual EPID. However, since this error could not be reproduced at all leaf positions in a given field, it was not considered to be a reliable measure of the minimum detectable MLC leaf shift. Instead it was found that MLC shifts as small as 0.1 cm could be detected for any given group of leaves (for at least 5 randomly chosen leaf positions) in any given field. In an empirical study, Mohammadi and Bezak evaluated the efficacy of SLIC-EPID transmission dose measurements in detecting MLC shifts in the range of 0.01–0.2 cm for various IMRT field segments (6 MV photons) incident on different anatomical sites of an anthropomorphic phantom [143]. The authors found that for a particular head and neck IMRT field segment, the minimum MLC shift that could be detected was 0.02 cm, which translated into a difference in transmitted dose of 5 %. This is comparable to the planning system calculations which predicted a dose difference of a similar magnitude (7 %) due to a 0.01 cm MLC shift in one of the conformal head and neck fields. Although the setup of two studies were not identical in setup (for example, the SLIC-EPID dose measurements were performed at 140 cm SSD, compared with the planning system simulations at 145 cm SSD), the planning system dose calculations performed under clinically realistic conditions do show some promise in modelling transmitted dose differences due to small MLC errors.

In the current study, gamma map analysis using 3 %/2.5 mm criteria is sensitive to MLC leaf errors in the clinical range (0–0.5 cm) provided that errors occur in at least five leaves. In particular, a possible leaf calibration error of 0.25 cm or more in an entire leaf bank may produce gamma scores of 90 % or lower. Varying the size of the calculation dose grid

caused discrepancies in predicted dose differences caused by MLC shifts of 0–0.5 cm of up to 4 %. This would have implications in the accuracy of predicted transmitted doses compared with transmitted dose measurements. The optimal voxel size is a function of both the pixel size in the plane of the virtual EPID as well as the resolution in pixels perpendicular to this plane and is governed by the maximum memory allocation of the dose matrix in the planning system. In this study, the optimal grid resolution was 0.15 $\times$ 0.15 $\times$ 0.25 cm^3. A coarser dose grid tended to slightly over-estimate dose differences caused by leaf displacements towards the near jaw, compared with a finer dose grid. However, for leaf displacements away from the near jaw, a coarser dose grid tended to slightly underestimate the dose relative a finer dose grid. Dose differences predicted at the transmitted dose plane correlated well with differences in the midplane caused by corresponding MLC leaf shifts. The magnitude of the errors were consistently over-estimated (by up to 3 %) at the transmitted dose plane relative to the errors at the midplane. In principle, this implies that MLC shift resulting in a dosimetry error in the midplane will therefore be detected at the transmitted dose plane. Dose-volume histogram studies revealed that the change in D_{avg} and D_{max} at the head and neck PTV caused by the simulated MLC leaf errors were negligible (< 1 %). However, a 0.25 cm error in a leaf bank in all six beams caused D_{max} to decrease by 6.8 %. The organ at risk most effected by the MLC shifts was the larynx. MLC errors present in a single field resulted in variations in D_{max}, D_{min}, or D_{avg} of within $\pm$5%. In contrast, MLC errors present in all six beams resulted in D_{avg} inside the larynx to decrease by up to 7.7 %.

Chapter 7

An evaluation of transmission dosimetry for a 3D conformal opposing tangential breast treatment

7.1 Introduction

The treatment of breast cancer presents a significant challenge in the practice of radiotherapy due to the complex geometry of the breast and the proximity of sensitive normal tissues such as the lungs and heart (in the case of the ipsilateral breast). In terms of cosmetic outcomes for the patient, dose homogeneity plays an important role in radiotherapy treatments [146–148]. However, the varying thickness along a given part of the breast makes it difficult to deliver a homogeneous dose distribution throughout the target volume, prompting the use of techniques such as opposing tangential beams [149, 150], IMRT [151–153], breast tissue compensation [154–156] and non-coplanar techniques [157, 158]. In addition to the above challenges is the spatial uncertainty in the target volume due to patient setup errors and respiratory motion [159–161]. Patient breathing is of particular concern for

breast treatments due to the resulting motion of the breast caused by excursions of the chest wall. This has prompted the development of breathing control, voluntary breath-hold, deep inspiration breath-hold, and respiratory gating techniques to account for or limit the effects of breathing motion on the delivered dose [162–165].

Due to the limited number of published studies in the literature reporting on the efficacy of *in vivo* dosimetry (especially, 2D and 3D based techniques) in breast radiotherapy treatments, the following investigation was pursued. A conformal radiotherapy breast plan (mono-isocentric) was used in this study to simulate delivery errors related to respiratory motion and shifts in the position of the treatment beams relative to patient geometry. An advantage of performing a theoretical study of transmitted dose variations is the absence of any experimental uncertainties associated with EPID dose measurements such as detector noise, dose calibration errors and random variations in linac output which may mask true dose delivery errors and otherwise make the evaluation of transmission dosimetry more complex. However, the accuracy in the dose algorithm of the treatment planning system is also important and any limitations in the calculations should be taken into account. Respiratory motion was simulated by introducing specific shifts in beam position using an "Anatomy Reference Frame" model adopted by George *et al* [166]. The beam shifts used in the current study were chosen from a typical range of breathing excursions reported for conformal breast radiotherapy treatments [159,166–168]. In addition to uncertainties in the position of the breast relative to the radiation field due to respiratory motion, uncertainties in patient positioning errors also exist. Thus, breathing simulations were combined with simulations of patient set up errors. The sensitivity of the transmitted dose calculations were then determined by comparing the doses calculated in the original and perturbed plans using the gamma formalism described in chapter 3.

7.2 Materials and Methods

Patient CT data

In order to simulate the measured transmitted dose distribution resulting from the shape and composition of the breast and surrounding tissue, a treatment plan based on patient CT data was used in this study. The patient was previously treated at the Royal Adelaide Hospital for breast conservative conformal radiotherapy using a conventional wedged parallel opposed tangents technique. To perform transmitted dose calculations beyond the limiting CT field of view, the volume of air surrounding the original CT images was extended as performed in previous chapters. A radiotherapist and radiation oncologist agreed to create a replica of the original patient plan based on the enlarged CT data set. Planning was performed using the Pinnacle^3 treatment planning system. The oncologist prescribed a baseline for the location and angle of the tangent beams and outlined the whole ipsilateral breast, heart and both lungs. A pair of opposing wedged, monoisocentric, conformal photon beams of 6 MV energy were inserted by the radiotherapist and 2 Gy/fraction in 25 fractions were prescribed to a point near the surface of the apex of the breast (figure 7.2.1).

7.2.1 Construction of the *virtual* EPID

Once the treatment plan was complete the presence of the couch in the CT scans was removed using the density override ($\rho = 1.0$ g/cm^3) option in Pinnacle^3. This eliminated any influence of couch transmission on the computed transmitted dose distributions following breathing simulations incorporated in the next section. The treatment plan was duplicated into in order to introduce the dosimetry errors. Furthermore, in a given plan, one of the beams was removed so that the transmitted dose could be calculated separately for each of the tangent beams. A "virtual" EPID volume ($32 \times 32 \times 3.5$ cm^3 and assigned a density of $\rho = 1.0$ g/cm^3) was created for each beam using the Pinnacle^3 Region Of Interest (ROI) tool. Due to the oblique beam angle of the beams, the co-ordinates of the virtual EPID were explicitly derived using trigonometry combined with the known

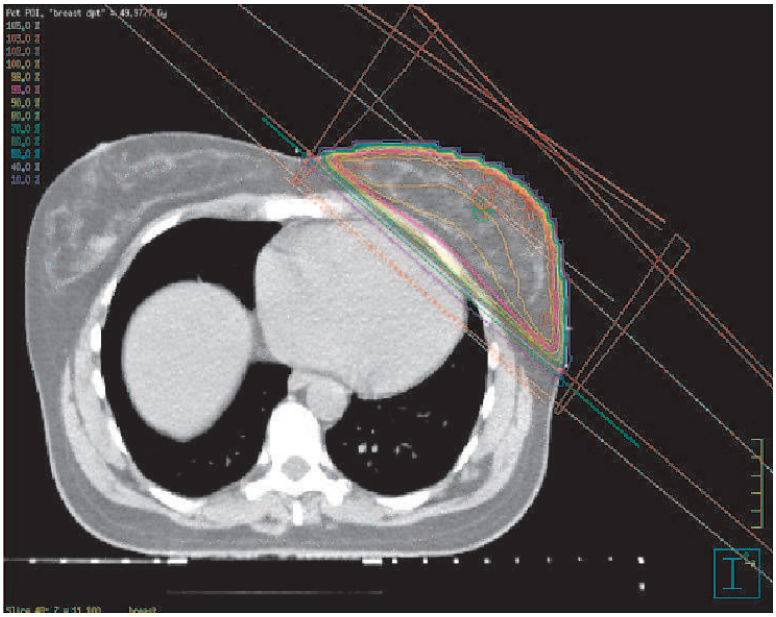

Figure 7.2.1: *A wedged parallel opposed breast plan created in Pinnacle*^{3} *used to simulate patient breathing.*

angle of the beam and the distance from the beam focus to the virtual EPID. The beam focus to virtual EPID distance (1.5 cm below the surface) was defined to be 145 cm, as used in the previous two chapters. All dose calculations were performed using the convolution/superposition dose engine with a calculation grid size of 0.25 cm in all three directions.

As observed in the previous chapter, there are stepped edges in CT density at the surface of the virtual EPID (0.7– 2 mm), due to the way oblique edges are represented in a rectilinear CT data set. Nevertheless, the steps were not expected to have an impact on the calculated isodose lines inside the virtual EPID since they are smaller than the dose grid size used. Beam profiles of calculated dose within the virtual EPID as shown in figure 7.2.2 confirm this. Large undulations in dose (of the order of 38 %) were only observed at the air-EPID interface due to interpolation within the 0.25 cm dose grid across alternating regions of CT density.

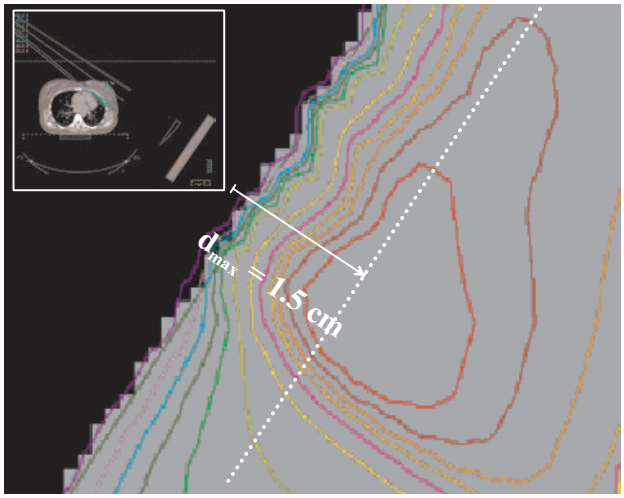

(a)

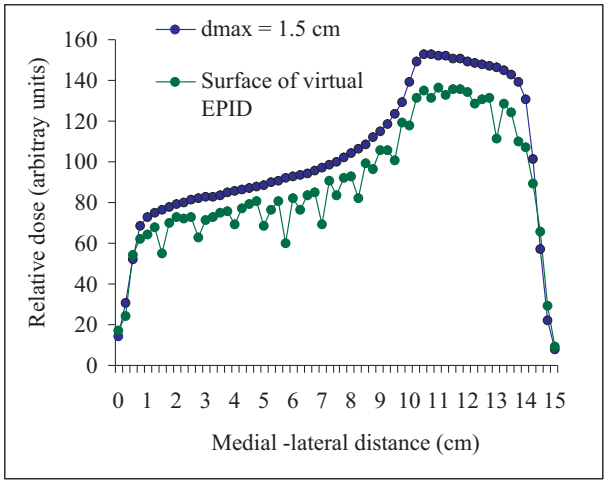

(b)

Figure 7.2.2: *(a)An axial slice through the virtual EPID (water-equivalent) displaying the isodose lines calculated by Pinnacle*^{3}*, (b) beam profiles predicted by the Pinnacle*^{3} *treatment planning system through an axial cross-section of the virtual EPID. Dose artifacts are clearly present at the surface of the virtual EPID but not at* d_{max}.

7.2.2 Dose extraction at the virtual EPID

The two-dimensional dose distribution corresponding to d_{max} = 1.5 cm below the surface of the virtual EPID in Pinnacle^3 was identified and extracted using Matlab in the same manner as described in previous chapters. In addition, due to the oblique orientation of the virtual EPID, a 3D matrix rotation (about the axial axis) was performed on the extracted 3D dose array so that the dose could be easily extracted. The new co-ordinates for extracting the dose plane at d_{max} were then derived using the transformation matrix equation (6.2.1) defined in chapter 6. A comparison of the isodose lines inside the virtual EPID before and after the matrix rotation was made to ensure that no image processing artifacts were introduced. A direct comparison of isodose lines ranging from 10–100 % revealed near identical dose distributions with the the dose at d_{max} after rotation differing by only 0.3 % compared with the original dose distribution 7.2.3. The final extracted dose distribution for the tangent beams are shown in figure 7.2.4.

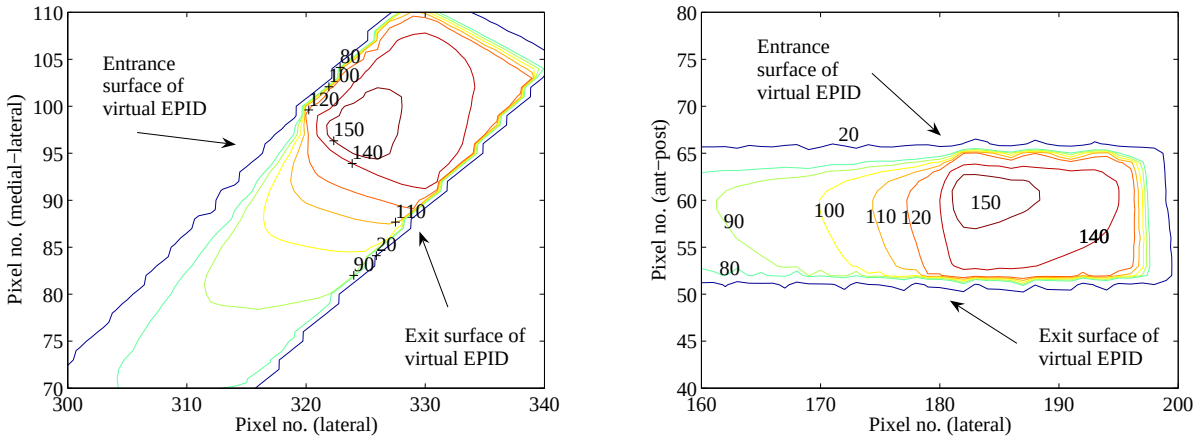

(a) (b)

Figure 7.2.3: *Calculated isodose lines through the cross section of the virtual EPID. (a) Before matrix rotation and (b) after matrix rotation. The rotation had minimal effect on the isodose lines (0.3 % at d_{max}).*

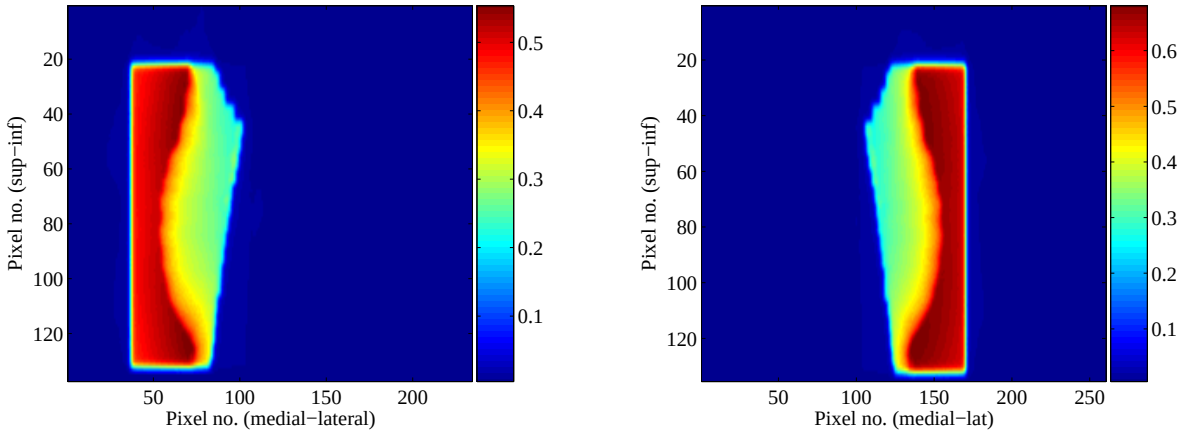

Figure 7.2.4: *Two-dimensional computed transmitted dose distributions at d_{max} for (a) lateral tangent, and (b) medial lateral beam.*

7.2.3 Simulation of respiratory motion

Respiratory motion in breast radiotherapy patients is known to cause movements in the breast of 0–11 mm in anterior and posterior directions, relative to the radiation field [159,166–168]. In this chapter, breathing was simulated by displacing the isocenter of the tangent beams relative to the CT data. Furthermore, the virtual EPID was shifted in an equivalent manner so that breathing motion appeared in the reference frame of the CT data. Shifting the position of the isocentre and virtual EPID was necessary since the CT data itself is fixed within the planning system. This model assumes that breathing motion occurs in the anterior-posterior and lateral directions only and that there is no deformation in the patient [166, 169]. Although breathing is expected to cause tissue deformation at the lungs, the resulting change in dosimetry to the lung may be ignored. The change in lung density as a result of breathing has been estimated in the literature [161] to be less than 10 %, which translates into a dosimetric change of 0.5 % inside the lungs. In the current study, patient breathing was simulated in both inhale and exhale directions and for simplicity were assumed to be equal in magnitude. Shifts in the isocentre of 2 mm and 11 mm in the anterior-posterior and lateral directions were used to model shallow

and deep breathing, respectively (figure 7.2.5).

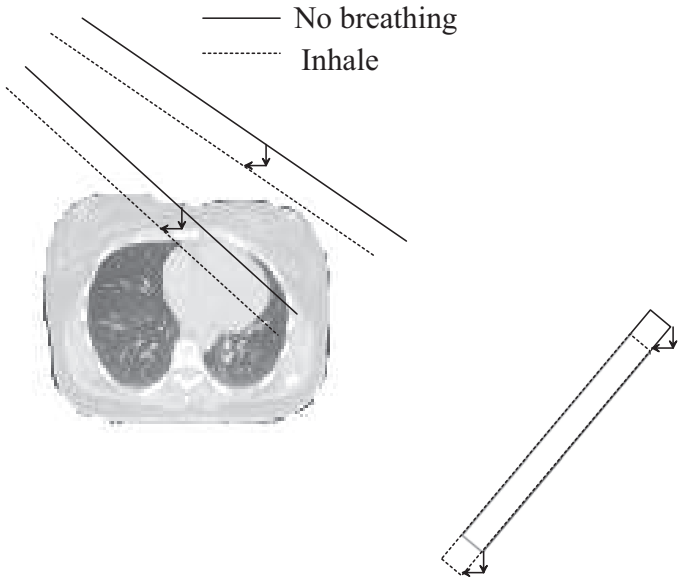

(a)

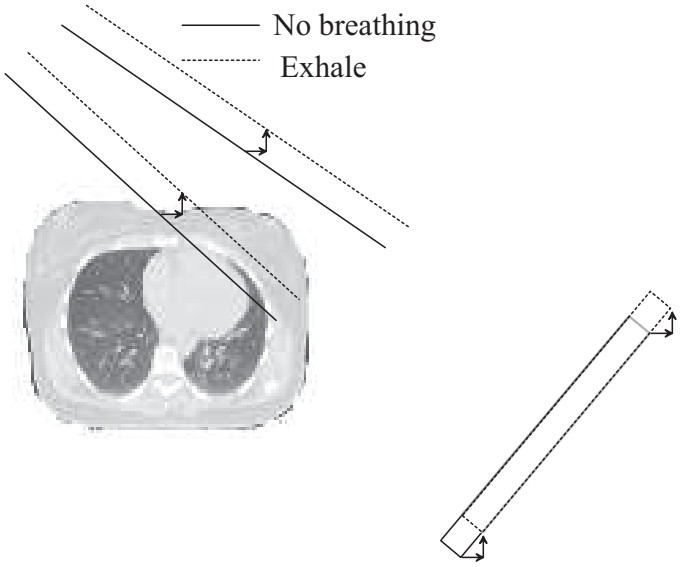

(b)

Figure 7.2.5: *Respiratory motion simulated in the anatomy frame of reference, in which the beam and virtual EPID move relative to the fixed anatomy. (a) Inhale breathing and (b) exhale breathing.*

In breast radiotherapy the treatment fields are aligned to the breast itself and hence any set up errors will aslo combine with respiratory motion. Hence, in this study, breathing motion was combined with possible set up errors. A situation involving a 0 mm (ie no set up error) and a 2.5 mm error were considered in both directions of the superior-inferior axes. Set up errors were not repeated along the other axes (ie lateral and anterior-posterior directions) to avoid cancellation with the beam shifts used to simulate breathing. The magnitude of the breathing and set up error combinations are summarised in table 7.2.1. For each table entry, the transmitted dose distribution at the virtual EPID was computed and compared with dose distributions in the unperturbed plans.

lateral/medial lateral beams									
Shallow breathing (mm)				Deep breathing (mm)				Setup error (mm)	
Inhale		Exhale		Inhale		Exhale			
POST	R-LAT	ANT	L-LAT	POST	R-LAT	ANT	L-LAT	SUP	INF
2	2	2	2	11	11	11	11	0.0	0.0
2	2	2	2	11	11	11	11	2.5	2.5

Table 7.2.1: *Magnitude and direction of beam shifts used to simulate the breathing and setup errors.*

7.2.4 Two-dimensional gamma analysis

Gamma analysis based on the original formalism of [118] was investigated as a potential error detection tool for quantifying any dosimetry errors (at the transmitted dose level) caused by the simulated breathing motion and setup errors. In addition, gamma maps were enhanced by incorporating a *sign matrix* into the original gamma function [125] to distinguish between positive and negative dose differences. For example a gamma index of "+ 1" would indicate a positive dose difference and a gamma index of "- 1" would indicate a negative dose difference. Criteria of 3 %/2.5 mm, commonly used in the the clinic [80, 118, 120, 121] were adopted to determine the overall significance of the

errors in terms of gamma scores. A gamma score of 90 % or less was considered as an indication of a significant delivery error. More relaxed gamma criteria of 5 %/2.5 mm were also adopted to take into account possible limitations in the accuracy of the planning system dose calculations or uncertainties associated with measurements, if a comparison was to be made. In order for gamma scores to correlate as closely as possible with the spatial occurrence (or density) of the errors within the radiation field, gamma analysis was confined to the radiation field defined by the 20 % isodose lines. Furthermore, the portion of radiation field overshooting the breast was also omitted in the gamma analysis as it unnecessarily contributes to higher gamma scores. This was achieved by defining the 20 % isodose lines at the midplane inside the CT data and projecting this field at d_{max} inside the virtual EPID. Similar gamma analysis was performed for midplane dose distributions.

7.2.5 Dose-Volume Histograms

Dose Volume Histograms (DVHs) in both the target volume and organs at risk were used as a benchmark for comparing the plans with and without the simulated delivery errors. Since the total dose delivered to the target volume consists of the dose delivered separately from the two beams, it is possible that the dose may be deposited at different points in the patient's breathing cycle. For example, the patient may inhale for one of the beam deliveries and exhale for the other, or vice-versa. In addition, the patient may also inhale during the delivery of both beams or exhale during the delivery of both beams. Since, the latter two cases would most likely produce the greatest dose variations, DVHs for these two scenarios were recorded. Statistics parameters such as the minimum, maximum and average dose delivered to the outlined structures were also recorded for a quantitative comparison of the planned and delivered dose distributions.

7.3 Results

7.3.1 Two-dimensional gamma analysis

Gamma maps resulting from the comparison of transmitted dose distributions calculated in the original plan and those simulating breathing are shown in figure 7.3.1. The colour legend next to each figure represents gamma values. Regions within 3 %/2.5 mm are represented in grey scale and regions exceeding these criteria are shown in colour. The red end of the scale are represented by negative gamma values ($<$ -1) and indicate an increase in the transmitted dose, where as the blue end of the scale are represented by positive gamma values ($>$ + 1) and indicate a decrease in the transmitted dose. The transmitted dose is very sensitive to the shallow simulations, which correspond to beam shifts as small as 2 mm along the anterior-posterior and lateral axes. Gamma scores were calculated to be lower than 70 %, with gamma values exceeding $\pm$1 indicating dose differences in excess of $\pm$3 %. In particular, 2 mm breast excursions due to inhale, caused "cold" spots ($>$ 3 %) along the anterior edge of the breast, where as for the same excursion in the exhale direction, "hot" spots along the anterior edge of the breast were observed. This can be explained in terms of the effective beam path through different sections of the breast. For example, breathing in the inhale direction corresponds to the thicker part of the breast moving closer to the radiation field, resulting in greater attenuation at the breast and thus a reduction in transmission measured at the virtual EPID, as observed in figure 7.3.1(a). Conversely, breathing in the exhale direction the thinner part of the breast becomes more exposed resulting in less attenuation at the breast and thus an increase in transmission measured at the virtual EPID (figure 7.3.1(b)).

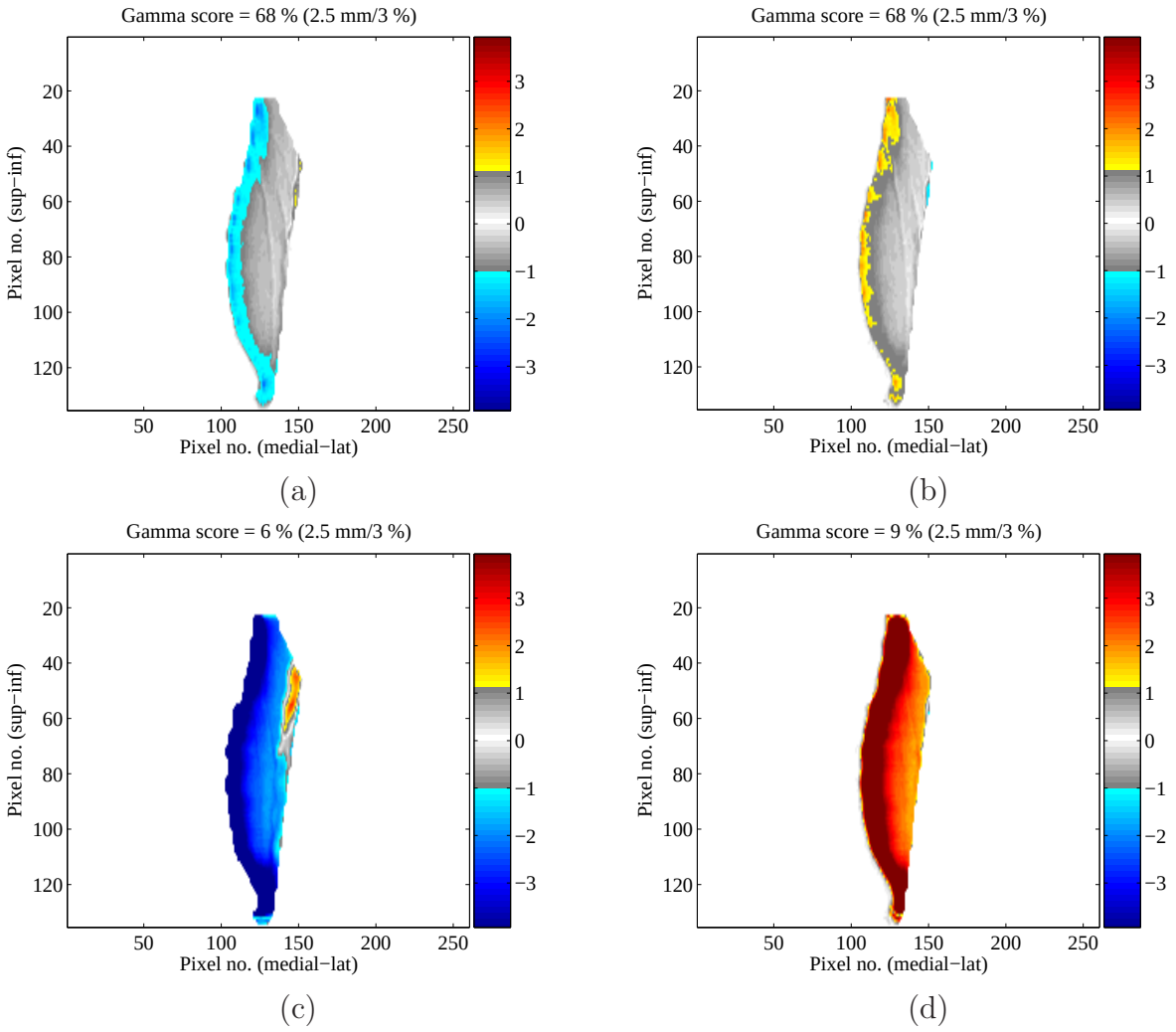

Figure 7.3.1: *Gamma maps (for the lateral beam) resulting from (a) Breathing inhale of 2 mm, (b) breathing exhale of 2 mm, (c) breathing inhale of 11 mm, and (d) breathing exhale of 11 mm.*

Simulations of deep breathing resulted in the poorest gamma results, with gamma scores less than 10 % (figures 7.3.1(c)-(d)). Furthermore, gamma values of up to ±4 occurring towards the anterior edge of the breast, indicate dose differences substantially greater than ±3 %. A geometric miss can clearly be seen in figure 7.3.1(c) in which a localised hot spot is present near the chest wall. This may be due to the presence of lung and and bony rib structures which can be seen in the CT scans. Figure 7.3.2 are gamma maps calculated for breathing simulations combined with 2.5 mm setup errors in both directions of the superior-inferior axis.

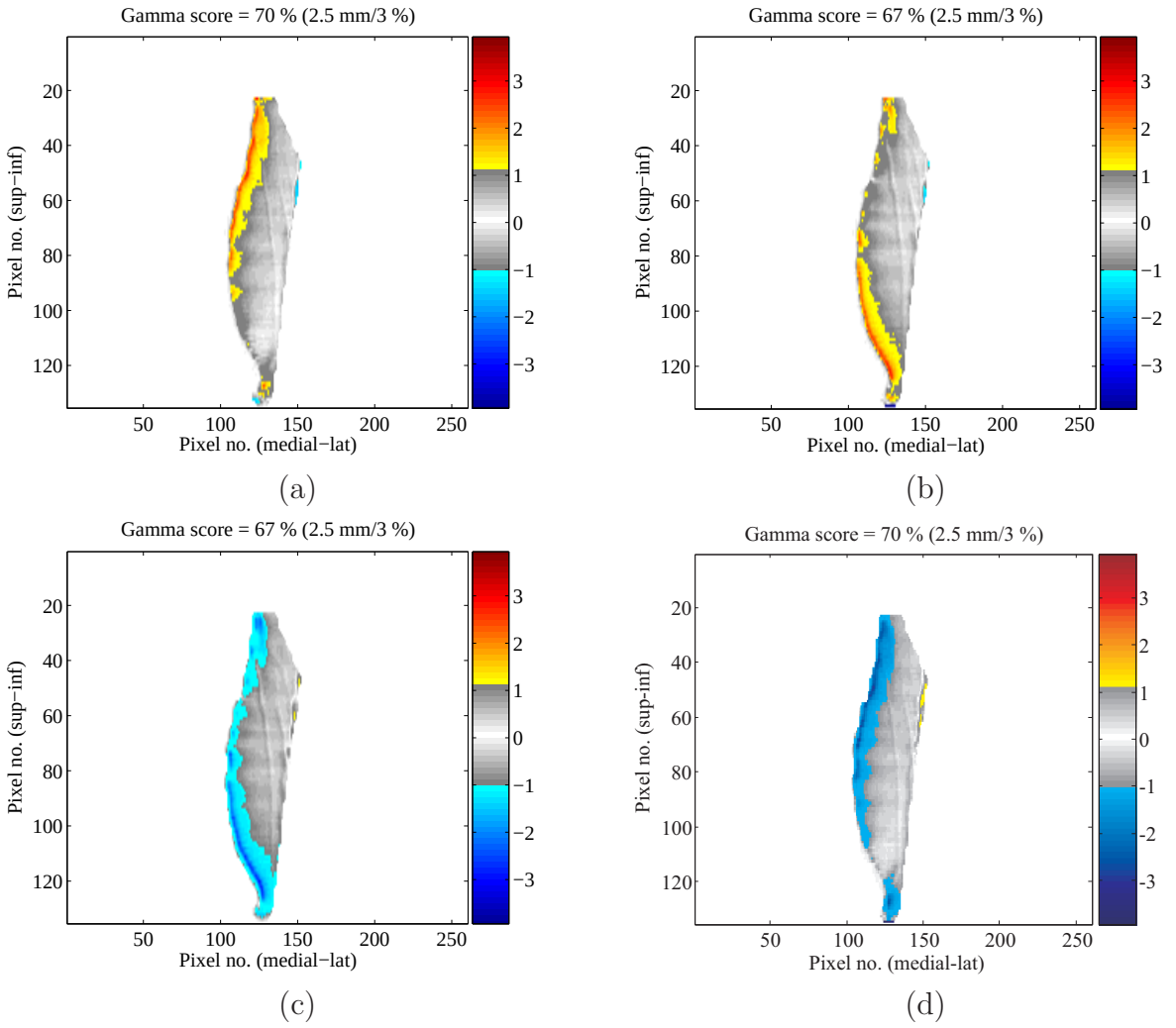

Figure 7.3.2: *Gamma maps (for the lateral beam) resulting from (a) Breathing exhale of 2 mm combined with 2.5 mm beam shift (superior), (b) Breathing exhale of 2 mm combined with 2.5 mm beam shift (inferior), (c) Breathing inhale of 2 mm combined with 2.5 mm beam shift (superior), and (d) Breathing inhale of 2 mm combined with 2.5 mm beam shift (inferior).*

Gamma scores are nearly identical to the previous scenario with no set up errors present. However, the distribution of the errors are noticeably different with the presence of set up errors. For example, shallow breathing in the exhale direction combined with a 2.5 mm set up error in the inferior direction (ie beam shift along the superior axis) resulted in an increased proportion of hot spots toward the superior edge of the breast. Similarly, breathing combined with a setup error in the opposite direction caused an increase proportion of hot spots toward the inferior edge of the breast. The increase in the density

of hot spots is a consequence of the breast being thinner at the superior and inferior edges compared with the middle of the breast. For set up errors combined in the inhale direction, the cold spots resulting from the breathing, are reduced (ie become 'warmer') in either the superior or inferior direction for the same reasons described above. Once again, overall gamma scores were nearly identical with or without the presence of the set up errors, however the distribution of the dosimetry errors is not the same. This implies that gamma scores should always be accompanied with a 2D gamma map to enhance the interpretation of any dosimetry errors identified at the transmitted dose level.

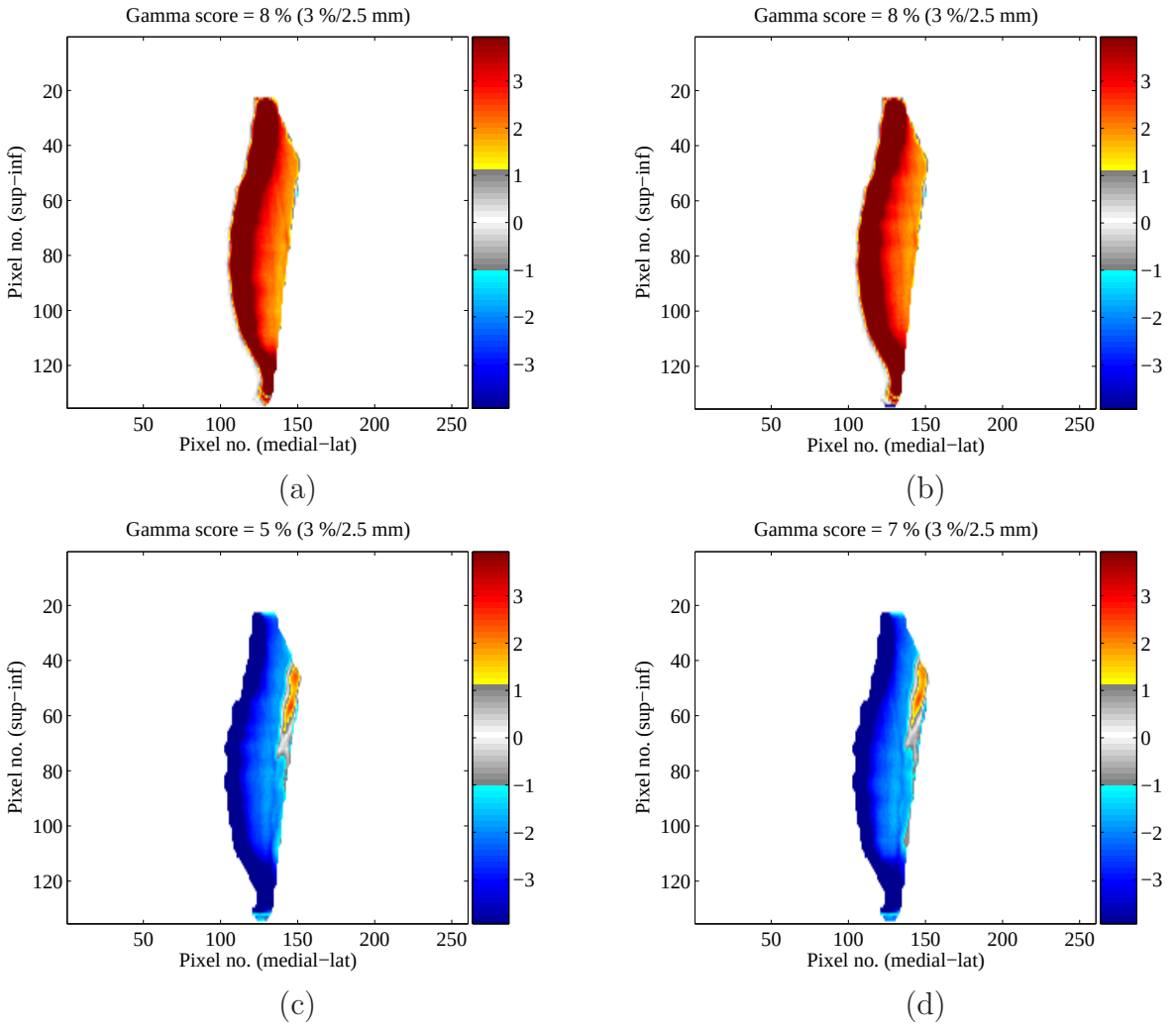

Figure 7.3.3: *Gamma maps (for the lateral beam) resulting from (a) Breathing exhale of 11 mm combined with 2.5 mm beam shift (superior), (b) Breathing exhale of 11 mm combined with 2.5 mm beam shift (inferior), (c) Breathing inhale of 11 mm combined with 2.5 mm beam shift (superior), and (d) Breathing inhale of 11 mm combined with 2.5 mm beam shift (inferior).*

Setup errors combined with the deep breathing simulations resulted in the largest dose discrepancies and therefore the poorest gamma scores (< 10 %). Due to the magnitude of the breast excursions (11 mm) compared with the magnitude of the setup errors (2 mm), dose differences due to the set up errors alone were dominated by the breathing errors, resulting in very little change to the gamma map distributions seen in figures 7.3.3(c)-(d). Gamma scores calculated using 5 %/2.5 mm to account for inaccuracies in the Pinnacle^3 dose algorithm or potential measurement uncertainties, produced higher gamma scores

	Shallow breathing		Deep breathing		Setup error (mm)	
	Inhale	Exhale	Inhale	Exhale	Direction	
Gamma criteria	Gamma scores (%)				Superior	Inferior
3 %/2.5 mm	68	68	6.0	9.0	0.0	0.0
	67	67	5.0	8.0	0.0	2.5
	71	67	7.0	8.0	2.5	0.0
5 %/2.5 mm	83	83	13	11	0.0	0.0
	82	82	12	11	0.0	2.5
	84	82	13	10	2.5	0.0
10 %/2.5 mm	96	96	59	46	0.0	0.0
	95	95	58	47	0.0	2.5
	95	95	59	46	2.5	0.0

Table 7.3.1: *Gamma scores calculated using clinical gamma criteria (3 %/2.5 mm) and less strict criteria of 5 %/2.5 mm and 10 %/2.5 mm for the combined breathing and set up errors in the lateral beam.*

but were significantly below the 90 % level for acceptable gamma scores. Gamma scores exceeding 90 % were attained by setting exaggerated criteria of 10%/2.5 mm, but only for the shallow breathing simulations(with or without the set up errors). The results are summarised in table 7.3.1.

Gamma maps: Midplane versus transmitted dose plane

A direct comparison of gamma map distributions at the transmitted dose plane and midplane resulting from the simulated breathing is shown in figure 7.3.4. The localisation of dose errors along the lateral edge of the breast is apparent in both the midplane and transmitted dose planes indicating a fairly good correlation. Furthermore, gamma scores calculated for the two planes are all below 90 % and similar in magnitude. For example, the simulated breathing in the inhale direction yielded gamma scores of 68 % and 73 % for the transmitted dose plane and midplane, respectively. Similarly, the simulated breathing in the exhale direction yielded gamma scores of 70 % and 65 % for the transmitted dose plane and midplane, respectively. However, the gamma score calculated for the transmitted dose map (83 %) is quite larger than that of the midplane dose map (68 %) for the simulation of breathing combined with the setup error (figures 7.3.4(e)–(f)). However, the 83 % gamma score differs from the other gamma scores (68–70 %) which is not clear at present but may be a coincidental result of the convolution of the two simulated errors. The sign of the dose errors at the transmitted dose plane are also reversed compared with the midplane. For example, in the midplane positive dose differences occur for the breathing in the inhale direction as this corresponds to a beam shift (medial-lateral direction) towards the chest wall, resulting in an increase in dose along the edge of the chest wall. A corresponding decrease in dose (negative dose difference) is expected to occur at the opposite edge of the field (ie near the surface of the breast), however, due to the finite pixel size of 2.5 mm in the image, the 2 mm beam shift used to simulate the breathing, most likely could not be resolved.

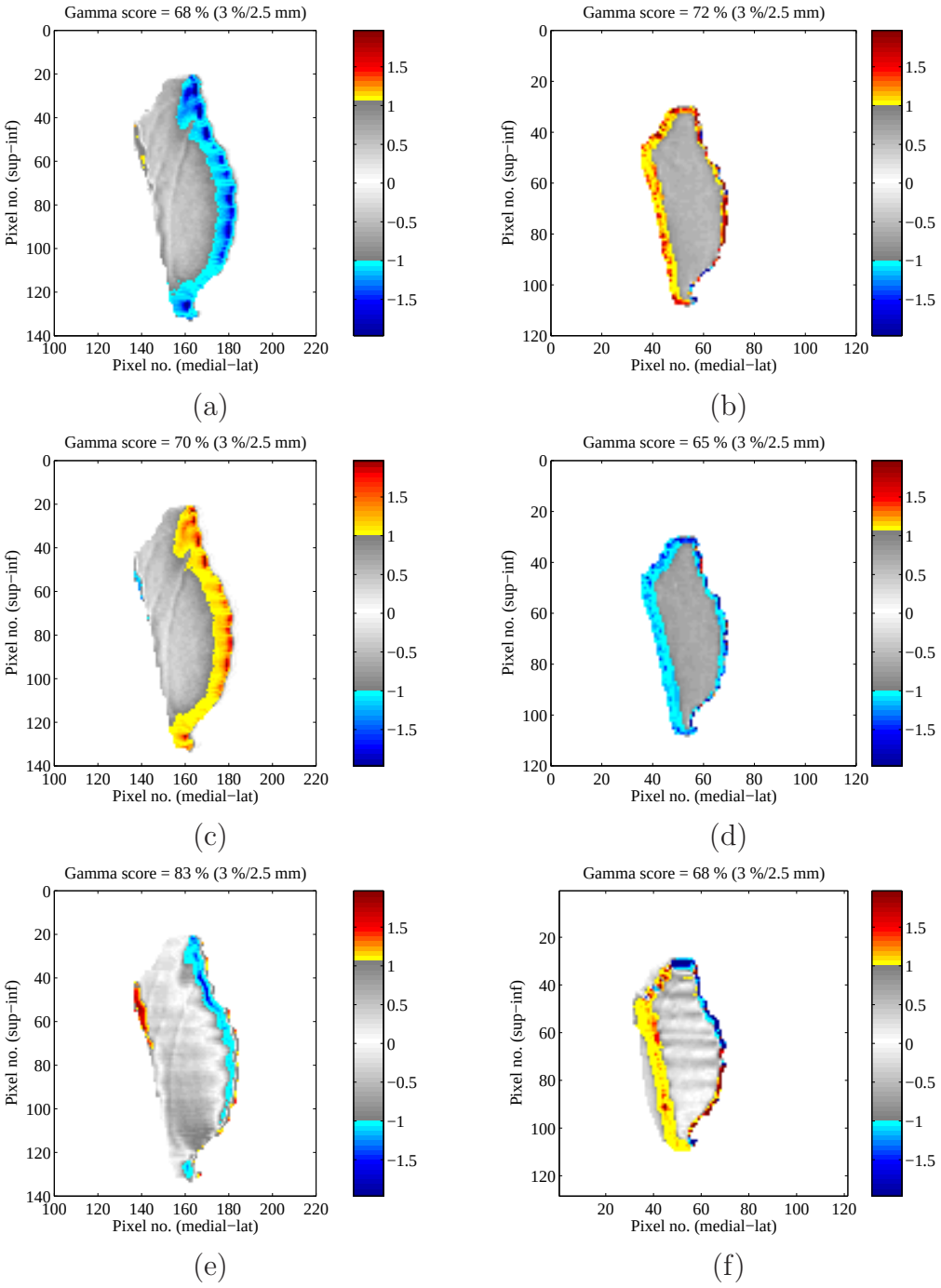

Figure 7.3.4: *A comparison of gamma maps (3 %/2.5 mm) for the medial tangent beam in the midplane and transmitted dose planes resulting from breathing simulations. (a)–(b) Shallow breathing in the inhale direction, (c)–(d) shallow breathing in the exhale direction, (e)–(f) shallow breathing in the inhale direction combined with a 2.5 mm setup error in the superior direction (ie beam shift in the inferior direction).*

7.3.2 Dose volume histograms

The effects of the magnitude and direction of the respiratory motion on the PTV, lung and heart DVHs are shown in figure 7.3.5. For simplicity and for purposes of emphasising the potential magnitude of dosimetry errors caused by breathing, planning was simulated with breathing combined in the same direction for both beams. For example, DVHs were not evaluated for an inhale excursion in one beam and an exhale excursion in the opposing beam. The curve labelled "original plan" refers to the ideal case of no breathing and indicates optimum beam coverage. Breathing simulated at the exhale phase caused the delivered dose heterogeneity to increase, whereas inhale breathing resulted in a decrease in the dose heterogeneity. The reduced dose heterogeneity to the breast, however compromised the dose distribution resulting at the critical organs. For example, the maximum dose to the lungs increased by 5 % for shallow breathing and up to 16 % for deep breathing. Similarly, the maximum dose to the lungs increased by 6 % and 18 % for shallow and deep breathing, respectively. In contrast, breathing in the exhale direction did not cause a change in the maximum dose to the PTV but caused the mean dose to decrease by 4 %, for shallow breathing. For deep breathing (in the same direction), however, the maximum dose to the breast increased by up to 8 %, but overall, the average dose decreased by 16 % (see figure 7.3.5(a)). The maximum dose to the lung and heart, resulting from shallow breathing (exhale) were reduced by 6 % and 18 %, respectively. Deep breathing in the same direction produced the greatest variations in dose to the critical organs, in which the maximum dose to the lung decreased from 180 cGy to 20 cGy, and the maximum dose to the heart decreased from 176 cGy to 15 cGy. A summary of the DVH statistics is given in table 7.3.2.

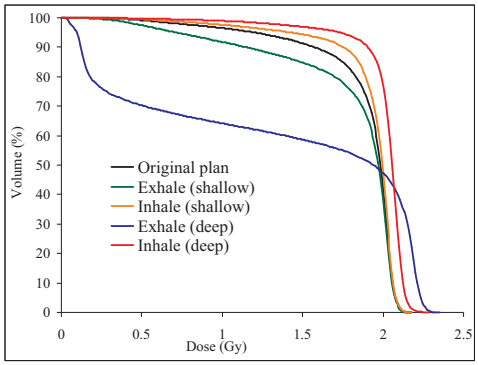

(a)

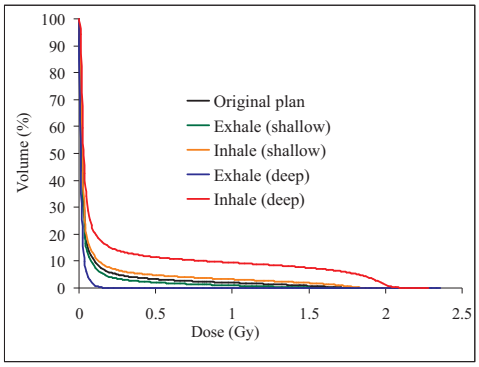

(b)

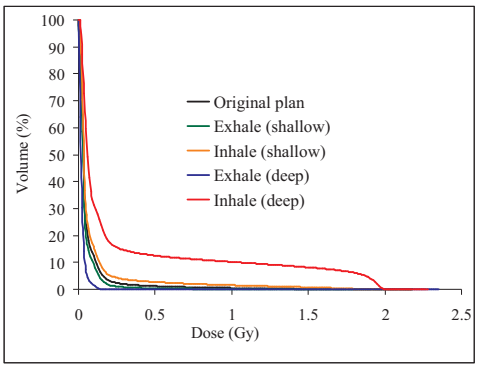

(c)

Figure 7.3.5: *Dose-volume histograms resulting from simulated breathing excursions combined in the same direction in both beams. (a) Planning Target Volume (ipsilateral breast), (b) ipsilateral lung, and (c) heart.*

Volume	Original plan	Inhale		Exhale	
		Shallow	Deep	Shallow	Deep
PTV (ipsilateral breast)					
D_{max} (cGy)	217	216	228	217	235
D_{avg} (cGy)	187	191	153	179	157
Ipsilateral lung					
D_{max} (cGy)	185	195	214	174	157
D_{avg} (cGy)	6.45	8.96	21.6	4.50	1.07
Heart					
D_{max} (cGy)	176	187	208	148	15.4
D_{avg} (cGy)	5.12	7.55	25.4	3.7	1.53

Table 7.3.2: *Clinical dose statistics for the planning target volume and critical structures (single fraction) for simulated breathing. NB. breathing excursions are combined in the same direction in both beams.*

7.3.3 Summary and conclusions

The possibility of detecting discrepancies between planned and delivered dose distributions caused by patient breathing was investigated by comparing the calculated transmitted dose with and without breathing as simulated using the Pinnacle^3 treatment planning system. A clinical, 3D breast conformal radiotherapy plan incorporating a parallel opposed tangents technique was used in the study. Shallow and deep breathing was simulated by displacing the isocenter of the two tangents perpendicular to their central axes (in both directions) by 2 mm and 11 mm, respectively. The effectiveness of gamma maps for error detection at the transmitted dose plane was examined by calculating 2D gamma map distributions and their corresponding gamma scores for the commonly used 3%/2.5 mm criteria as well as more relaxed gamma criteria of 5 %/2.5 mm and 10 %/2.5 mm. The calculated transmitted dose distributions were found to be sensitive to both the 2 mm and 11 mm beam shifts used to simulate the breathing. Discrepancies exceeding 3%/2.5 mm criteria occurred along the anterior edge of the breast producing gamma scores less than 70 %. Adopting less strict gamma criteria of 5 %/2.5 mm to account for possible limitations in the accuracy of the dose algorithm yielded gamma scores of less than 85

%, which still suggest significant regions in error. Only by setting the gamma criteria to extremely loose values (10 %/2.5 mm) did gamma scores attain acceptable values of 95 % or better. The deep breathing simulations (11 mm) suggest very large geographic misses with nearly the entire gamma map area exceeding the 3 %/2.5 mm criteria. Setting the gamma criteria to 5 %/2.5 mm did not significantly improve the gamma scores which were calculated to be 10 % or higher. Furthermore, using extremely loose criteria of 10 %/2.5 mm yielded significantly low gamma scores of less than 60 %. Combining the breathing simulations with set up errors of 2.5 mm along the superior-inferior axis contributed to errors at the transmitted dose plane by altering the spatial distribution of the errors (in the superior and inferior direction) caused by the breathing simulations alone. Nevertheless, the addition of the setup errors to the breathing simulations produced nearly identical gamma scores compared to the scenario with only breathing simulations. This demonstrates that gamma scores alone are not sufficient for quantifying dose discrepancies at the transmitted dose level and should thus be accompanied with a 2D visual gamma distribution.

Chapter 8

Conclusions

8.1 Major conclusions of this thesis

The Pinnacle^3 treatment planning system can be used for predicting *absolute* two-dimensional transmitted dose distributions in a water-equivalent, virtual EPID. In particular, for flat, homogeneous (water-equivalent) phantoms irradiated by 6 MV photons in a 10 $\times$ 10 cm^2 field, an accuracy of 3.7 %/3.8 mm in transmitted dose calculations can be achieved relative to an appropriately calibrated two-dimensional dosimeter. Such accuracy is in agreement with results published in the literature, in particular the work of McNutt *et al* [70]. Similar agreement between Pinnacle^3 based calculations and transmitted dose measurements under inhomogeneous conditions may also be achieved as published in work stemming from this thesis [170].

In addition to its primary function as a planning system, Pinnacle^3 is a useful tool for predicting the transmitted dose as well as evaluating the efficacy of transmission dosimetry as an *in vivo dosimetry technique*, by simulating dosimetry errors such as beam path changes, MLC errors or respiratory motion encountered in clinical treatments. A prerequisite for modelling the transmitted dose (especially for oblique beam geometries) requires the expansion of the original CT data beyond the CT field-of-view in order to be able to perform calculations at the extended distances used by most EPIDs in the clinic.

The inherent noise (defined by the standard deviation) of the transmitted dose calculations (homogeneous conditions) on the central beam axis was within 0.1 % compared with 0.8 % as measured by the SLIC-EPID. The transmitted dose calculations were sensitive to (homogeneous) phantom thickness changes of ± 1 mm. Furthermore, the planning system can calculate dose changes caused by the presence of inhomogeneities as small as 0.1×0.1 cm $\times$ 0.5 cm^3 and homogeneity shifts orthogonal to the central axis of 0.1 cm or more. The effect of introducing a shift in beam path of up to 0.5 cm in curved homogeneous phantoms were not detected by the planning system dose calculations. However, for anthropomorphic phantoms, shifts in beam path of at least 0.25 cm can be detected.

Based on the two-dimensional gamma analysis (3%/3.5 mm) of transmitted dose, the simulation of beam path errors in a 3D conformal four-field box prostate treatment suggest that shifts of 0.5 cm along either the three orthogonal axes would most likely go undetected in the clinic based on transmission dose measurements. Furthermore shifts of up to 1.0 cm may only go detected for some shifts only. Provided that measurement uncertainty of transmission doses is less than 1 %, (hence allowing stricter gamma criteria (1 %/2.5 mm) to be adopted), shifts of at least 0.5 cm are potentially detectable. A disadvantage of transmission dosimetry (for largely flat, homogeneous regions) is that shifts parallel to the central beam axis (ie orthogonal to the transmission plane) are not detectable, even for shifts of 1.5 cm or more. The simulation in the planning system suggests that for treatment errors caused by patient misalignment, dose differences at the transmission plane are not an accurate representation of the dose differences occurring at the midplane of the PTV.

In theory, individual MLC shifts as small as 0.01 cm may potentially be detected in the presence of heterogeneities (such as a head and neck conformal treatment) via transmission dosimetry, provided that little or no additional uncertainties relating to changes in beam transmission are present. This result is comparable to the minimum shift in MLC

position 0.02 cm detected via transmission dose measurements (in the presence of heterogeneities) with a SLIC-EPID [143]. The impact of MLC errors on the two-dimensional dose distribution most likely becomes significant for shifts of 0.5 cm or greater when the number of shifts involved exceeds 5. However, it is possible for shifts as small as 0.25 cm to have a significant impact on the transmitted dose distribution, if an entire bank of leaves are involved (for example, due to an MLC calibration error). In a head and neck conformal treatment, this may produce clinically observable differences in DVHs, especially in critical structures such as the larynx, for example. Dose differences on the central axis at the transmission plane correlated well with differences in the midplane of the PTV.

The demonstrated sensitivity of the transmitted dose calculations to simulations of both small (2 mm) and large (11 mm) excursions in the breast in and out of the field, suggest the potential for using transmission dosimetry in detecting respiratory motion for conformal tangential beam deliveries. The majority of the errors occurred along the superior-inferior edge of the breast. Furthermore, combining the small breathing simulations with 2.5 mm setup errors in both superior and inferior directions resulted in additional observable changes in the 2D gamma map distributions, although little change in the total gamma score was generally observed. Gamma distributions in the transmission plane were found to be reasonably indicative of those in the midplane showing similar gamma scores close to 70 % (3%/2.5 mm) in both cases. The shallow and deep breathing simulations showed significant deviations in DVHs at the PTV, and only significant deviations in critical structure (ipsilateral lung and heart) for the deep breathing simulation.

8.2 Future directions

In principle, the method of expanding the CT data for enabling the transmitted dose to be calculated at arbitrary SSDs could be applied to any planning system, provided that the modified CT data still conforms to the DICOM standard accepted by the planning system. In fact, expanded CT images were successfully imported into the XiO treatment

planning system (CMS, St Loius, USA). However, the planning system could not cope with performing a dose calculation due to the substantial increase in memory usage of the image file.

A potential avenue of future research may be to extract the 3D entrance fluence file from Pinnacle^3 and modify it at the virtual EPID plane to further improve the transmitted dose calculations. Once modified, the fluence file can be re-entered into the planning system to calculate an improved dose distribution. Furthermore, for EPID detectors that are non water-equivalent, such as a-Si based EPIDs, the fluence in the planning system could be adjusted (by applying empirically derived 2D kernels, for example) to match the dose response of the EPID.

There is also scope for predicting transmitted dose distributions with greater precision using Monte Carlo simulations for benchmarking against the treatment planning system and in-house algorithms. Although, some work has already been performed on comparing the dose response of certain EPID designs relative to the dose response of water-equivalent models of the EPID [94] more studies could provide valuable information for possibly improving portal dose prediction algorithms.

Predicting the transmitted dose based on Cone-Beam CT data acquired at treatment should ideally be performed in the future as the technology becomes more readily available. This would improve the effectiveness and reliability of both the "forward" prediction and"back-projection" *in vivo* dosimetry techniques.

Finally, if portal dose prediction is to be implemented in the clinic for in vivo dosimetry, setting appropriate gamma criteria for different treatment modalities (such as 3D CRT and IMRT) as well as the different treatment sites within each modality, will need to be investigated further. Currently there are no universally accepted guidelines for gamma criteria, although 3 %/3 mm appears to be the most commonly used in the clinic. Furthermore, questions like: "for a given set of gamma criteria, what size gamma scores

constitute an acceptable agreement between the predicted and calculated dose maps?", should also be addressed.

Appendix A

Appendix

A.1 Expansion of the original patient CT images

The following Matlab code imports patient CT images and modifies each image to include a larger region of air surrounding the original CT images. The modified images are then re-exported in DICOM format to the planning system.

```
% Locate CT files
FilePath = ('C:\dicom\*.dcm');
% Open multiple CT files
[dFILENAME, dPATHNAME] = uigetfile(FilePath, 'File Open','MultiSelect', 'on');
sz = size(dFILENAME);
%For each *.dcm file surround the original image matrix with 4 separate
%matrices to form a 1152 x 1368 matrix
for i = 1:sz(2);
S{i} = [dPATHNAME dFILENAME{i}];
X{i} = dicomread(S{i});
[X_row{i} X_col{i}] = size(X{i});
Xmodified{i} = X{i}(1:320,:);
% create matrix 320 x 512 with entries = -1000 (HU)
```

```
Xmodified{i}(X{i}(1:320,:) == X{i}(1:320,:)) = -1000;
% perform matrix concatenation
X_concat{i} = [Xmodified{i};X{i};Xmodified{i}];
sz_2 = size(X_concat{i});
Ymodified{i} = X_concat{i}(:,1:428);
% create matrix 512 x 428 with entries = -1000 (HU)
Ymodified{i}(X_concat{i}(:,1:428) == X_concat{i}(:,1:428)) = -1000;
% perform matrix concatenation
Y_concat{i} = [Ymodified{i},X_concat{i},Ymodified{i}];
figure; imshow(Y_concat{i},[])
S_2{i} = ['C:\dicom\' dFILENAME{i}];
%write expanded CT data to DICOM file
dicomwrite(Y_concat{i},S_2{i},'ObjectType','CT Image Storage')
 end
```

A.2 3D dose reconstruction of dose file from Pinnacle[3]

The following Matlab code was used to extract the binary dose file from Pinncale[3] and to reconstruct the 3D dose information.

```
 %Locate the Pinnacle binary file (eg "*.004") corresponding
to the 3D dose matrix
 FilePath = ('C:\MATLAB701\work\Input data\Pinnacle\Patient_10297\*.*');
 [dFILENAME, dPATHNAME] = uigetfile(FilePath, 'File Open');
 filename = [dPATHNAME dFILENAME];
 %Define the matrix dimensions given by the dimensions of the Pinnacle dose
 %grid
 LAT = input('Please enter the dimensions of the dose matrix
along the lateral axis');
```

```
 AP = input('Please enter the dimensions of the dose matrix
along the anterior-posterior axis');
 SI = input('Please enter the dimensions of the dose matrix
along the superior-inferior axis');
 %Defines a "ZERO" matrix of dimensions [LAT] x [AP] x [SI] for reading in
 %the Pinnacle dose matrix.
 z =zeros(LAT,AP,SI);
 %Open the binary dose file for read only & perform a byte swap (UNIX -->
 %Windows)
 fd = fopen(filename,'r','b');
 %Define length of binary string
 N_pixel = (LAT)*(AP)*(SI);
 %Read in data as a 1xN_pixel array (string) in floating point, big endian
 %format
 x = fread(fd,[1,N_pixel],'float32');
 fclose(fd);
 for AP_i = 1:AP;
     for LAT_i = 1:LAT;
         for    SI_i  = 1:SI;
             y = (SI_i-1)*AP*LAT+(AP_i -1)*(LAT) + (LAT_i) ;
              z(LAT_i,AP_i,SI_i) = x(y);
          end
     end
 end
```

A.3 Masking of transmitted dose images

The following Matlab code was used to mask out dose values outside a specified isodose line (eg 20 % isodose line) to be used in conjunction with gamma analysis for calculating gamma scores, within the specified region of interest bounded by the isodose line.

```
%Define the mask function with input matrix A and isodose cut-off (eg "iso"
%= 20 %)
function [A_mask,BW,b] = mask(A,iso);
% Define the dimensions of the dose matrix
sz_A = size(A);
%Normalise maximum dose value to 100 % isodose line
A_max = max(max(A));
A_norm = A/A_max;
A_iso = (iso/100);
%Define all dose values less than "iso" % to have a dose value of zero.
A_norm(A_norm<A_iso) =0;
% Convert dose image into binary image with values > 20 %, eg ==1,
% remaining values ==0.
BW = im2bw(A_norm,A_iso);
[row,col] = find(BW ==1);
colm = min(col);
rowm = min(find(BW(:,colm)>0));
%Convolve 2D mask image to original dose matrix
A_mask = A.*BW;

%Find co-ordinates of mask outline defined by, eg the 20 %, isodose line.
boundarym = bwtraceboundary(BW,[rowm,colm],'N');
BW_filled = imfill(BW,'holes');
boundaries = bwboundaries(BW_filled);
```

```
sz_b = size(boundaries);

%plot eg boundary of eg 20 % isodose line.
for k= 1:sz_b(1);
    b{k} = boundaries{k};
    roi_handler = plot(b{k}(:,2),b{k}(:,1),'b','LineWidth',1);
end
```

A.4 Gamma function

The following Matlab code (the gamma component, of which was written by M. Mohammadi) is based on Low *et al's* gamma formalism [118]. In addition, masking of the transmitted dose images was incorporated into the original code for calculating gamma scores within a region of interest bounded by a specified isodose line.

```
clear all; % Clear all previously defined variables
close all; % Close all previous figures
clc; % Clear command window
warning('off','MATLAB:divideByZero')
%Retrieve measured/original TPS transmitted dose file (*.mat)
FilePath_a = ('C:\MATLAB701\work\Output data\Pinnacle\Patient_10297\*.mat');
[dFILENAME_a, dPATHNAME_a] = uigetfile(FilePath_a, 'File Open');
filename_a = [dPATHNAME_a dFILENAME_a];
%Retrieve calculated/TPS transmitted dose file
(containing error, eg beam shift) (*.mat)
FilePath_b = ('C:\MATLAB701\work\Output data\Pinnacle\Patient_10297\*.mat');
%EPID_patient_9377_L_Oblique_ten_leaf_5mm_BEAM.mat');   %%%% Choose 'Resized' folde
[dFILENAME_b, dPATHNAME_b] = uigetfile(FilePath_b, 'File Open');
filename_b = [dPATHNAME_b dFILENAME_b];
A = load(filename_a); % A => measured/original dose plane file
```

```
B = load(filename_b); % B => calculated/dose plane file (containing error)
%Open either a transmitted or midplane dose file (axial or coronal)
A=A(1).M_BEV;  %E_BEV;      %M_BEV_c  %M_BEV %Ax
B=B(1).M_BEV;  %E_BEV;      %M_BEV_c %M_BEV  % Ax
%Apply image mask to dose plane (eg bounded by 20 % isodose line)
[A_mask,BW_A,a] = mask(A,20);
[B_mask,BW_B,b] = mask(B,20);
bw = BW_A;
%-----------------------------------------------------------------------
%The following block of code was originally written by M. Mohammad
DTA= input('Please enter the desired DTA');
DDFF= input('Please enter the desired dose tolerance');
RI=A; % Define as 'reference' image (in gamma map terminology)
%Define normalisation point for dose difference component in
gamma map analysis
RI_max = double(max(max(RI)));
EI=B;
SZ=size(EI);
Field=DTA;
rng =DTA +1;
FRT=zeros(SZ(1),SZ(2));
FF =zeros(SZ(1),SZ(2));
H=DTA^2;
for i=1:SZ(1);
      for j=1:SZ(2);
          k1=i-Field;
          k2=i+Field;
          l1=j-Field;
          l2=j+Field;
```

```
            if k1<=0, k1=i; end
            if k2>SZ(1); k2=SZ(1); end
            if l1<=0, l1=j; end
            if l2>SZ(2); l2=SZ(2); end
            EI1=EI(k1:k2,l1:l2);
            c=k2-k1+1;
            d=l2-l1+1;
            G=zeros(c,d);
                  for k=1:c
                      for l=1:d
                          RI1=RI(i,j);
                          v=i-(k-rng);
                          w=j-(l-rng);
                          DTA(k,l)=((((i-v)^2)+((j-w)^2))/(H));
                          if sqrt(DTA(k,l))<=0.001;
                          DTAA(k,l)=0;
                          elseif sqrt(DTA(k,l))>=0.5 & sqrt(DTA(k,l))<1;
                          DTAA(k,l)=0.5;
                          else sqrt(DTA(k,l))>=1;
                          DTAA(k,l)=1; end
                          SDTAA=DTAA.^2;
                          DD(k,l)=((((double(RI1)-double(EI1(k,l)))
/(RI_max*(DDFF*0.01))))^2);  % (double(M(75,52))
                          G(k,l)= sqrt(SDTAA(k,l)+DD(k,l));
                      end
                  end
                  G;
                  SM(i,j) = sign(double(EI(i,j)) - double(RI(i,j)));
% "Sign" matrix for gamma
```

```
                FRT(i,j)=SM(i,j)* min(min(G));
        end
  end
 FRT;
 gamma_function=FRT;
 gamma_function(find(gamma_function<=1 & gamma_function>=-1 ))=1;
 gamma_function(find(gamma_function>1))=0;
 gamma_function(find(gamma_function<-1))=0;
 imagesize = size(FRT);
 %----------------------------------------------------------------
 rs = reshape(FRT,imagesize(1)*imagesize(2),1);
 % Calculate gamma score within masked dose image only
 N_pass =sum(sum(gamma_function.*bw > 0));
 Total_N_points_in_mask =sum(sum(bw))
 Area_mask =bwarea(bw)
 Perc_points_pass = 100*N_pass/Total_N_points_in_mask
 A_msk_cord = find(bw > 0);
 FRT_mask = rs(A_msk_cord);
 % Plot 2D gamma map (masked)
 figure;
 imagesc(FRT.*bw)
 daspect([1 1 1])
 colormap(jet)
 hold on;
 xlabel('Pixel no. (medial-lat)','FontName','Times New Roman','FontSize',14);
 ylabel('Pixel no. (sup-inf)','FontName','Times New Roman','FontSize',14);
 colorbar('FontName','Times New Roman','FontSize',14);
 title(['Gamma score = ',int2str(Perc_points_pass), ' % (3 %/2.5 mm)'],
'FontName','Times New Roman','FontSize',14)
```

```
 %Superimpose boundary of 20 % isodose line on gamma map
 sz_b = size(b);
 for k= 1:sz_b(2);
     roi_handler = plot(b{k}(:,2),b{k}(:,1),'b','LineWidth',1);
 end
 hold off;
%Plot 2D dose difference map
 DD_map = -(100*(A - B)/RI_max);
 figure; imagesc(DD_map.*bw)
 title('Percentage dose difference map')
 colorbar
 ylabel('pixel no. (AP)')
 xlabel('pixel no. (SI)')
 %Define in-plane and cross-plane profiles, and gamma profiles and output
to Excel spreadsheets
 a = a{1};
 a_r = a(:,1); % rows of line a
0 a_c = a(:,2); % columns of line a
 %%%%% central co-ords of masked matrices
 maxc =max(a(:,2)), minc = min(a(:,2));
 maxr =max(a(:,1)),minr = min(a(:,1));
 centr = round((maxr +minr)/2);
 centc = round((maxc +minc)/2);
 %%%%%%%%%%% Line profiles %%%%%%%
 row_sz = size(a(:,1));
 col_sz = size(a(:,2)); %si = col
 r_ax =((minr:maxr)-centr)*0.25;
 c_ax =((minc:maxc) -centc)*0.25;
 c_ax = c_ax';
```

```
A_row = A(minr:maxr,centc);  %% Ie rows are in plane profiles
A_col = A(centr,minc:maxc);  %% Ie columns are cross plane profiles
B_row = B(minr:maxr,centc);
B_col = B(centr,minc:maxc);
DD_row =DD_map(minr:maxr,centc);
DD_col =DD_map(centr,minc:maxc);
FRT_row =FRT(minr:maxr,centc);
FRT_col =FRT(centr,minc:maxc);
T_row = [r_ax',A_row,B_row,DD_row,FRT_row];
T_col = [c_ax,A_col',B_col',DD_col',FRT_col'];
xlswrite2(T_row);
xlswrite2(T_col);
```

Bibliography

[1] D. Huyskens, J. V. Dam, and A. Dutreix, "Midplane dose determination using in vivo dose measurements in combination with portal imaging.," *Phys Med Biol*, vol. 39, no. 7, pp. 1089–101, 1994.

[2] S. Broggi, C. Fiorino, and R. Calandrino, "A simple and robust method for in vivo midline dose map estimations using diodes and portal detectors.," *Radiother Oncol*, vol. 58, no. 2, pp. 169–78, 2001.

[3] R. Boellaard, M. van Herk, and B. J. Mijnheer, "A convolution model to convert transmission dose images to exit dose distributions.," *Med Phys*, vol. 24, no. 2, pp. 189–99, 1997.

[4] P. Metcalfe, T. Kron, and P. Hoban, *The Physics of Radiotherapy X-Rays from Linear Accelerators*. Medical Physics Publishing, Madison, WI, 2004.

[5] K. L. Pasma, B. J. Heijmen, M. Kroonwijk, and A. G. Visser, "Portal dose image (PDI) prediction for dosimetric treatment verification in radiotherapy. I. An algorithm for open beams.," *Med Phys*, vol. 25, no. 6, pp. 830–40, 1998.

[6] M. Mohammadi, *EPID Dosimetry in Intensity Modulated Radiation Therapy Applications*. PhD thesis, School of Chemistry and Physics, University of Adelaide, 2006.

[7] T. Depuydt, A. V. Esch, and D. P. Huyskens, "A quantitative evaluation of IMRT dose distributions: refinement and clinical assessment of the gamma evaluation.," *Radiother Oncol*, vol. 62, no. 3, pp. 309–19, 2002.

[8] "Determination of absorbed dose in a patient irradiated by beams of X or gamma rays in radiotherapy procedures," ICRU Report 24, International Commission on Radiation Units and Measurements (ICRU), 1976.

[9] G. J. Kutcher, L. Coia, M. Gillin, W. F. Hanson, S. Leibel, R. J. Morton, J. R. Palta, J. A. Purdy, L. E. Reinstein, and G. K. Svensson, "Comprehensive QA for radiation oncology: report of AAPM Radiation Therapy Committee Task Group 40.," *Med Phys*, vol. 21, no. 4, pp. 581–618, 1994.

[10] "Procedures in external radiation therapy dosimetry with electron and photon beams with maximum energies between 1 and 50 MeV. Recommendations by the Nordic Association of Clinical Physics (NACP).," *Acta Radiol Oncol*, vol. 19, no. 1, pp. 55–79, 1980.

[11] "Developing standards for radiation treatment services in australia," tech. rep., Tripartite Committee: RANZCR Faculty of Radiation Oncology, Australian Institute of Radiography, and the Australasian College of Physical Scientists and Engineers in Medicine., November 2005.

[12] E. B. Podgorsak, ed., *Review of Radiation Oncology Physics: A Handbook for Teachers and Students*. Education Report Series, International Atomic Energy Agency, Vienna, Austria, November 2004.

[13] G. Leunens, J. V. Dam, A. Dutreix, and E. van der Schueren, "Quality assurance in radiotherapy by in vivo dosimetry. 1. Entrance dose measurements, a reliable procedure.," *Radiother Oncol*, vol. 17, no. 2, pp. 141–51, 1990.

[14] B. Nilsson, B. I. Ruden, and B. Sorcini, "Characteristics of silicon diodes as patient dosemeters in external radiation therapy.," *Radiother Oncol*, vol. 11, no. 3, pp. 279–88, 1988.

[15] C. Fiorino, D. Corletto, P. Mangili, S. Broggi, A. Bonini, G. M. Cattaneo, R. Parisi, A. Rosso, P. Signorotto, E. Villa, and R. Calandrino, "Quality assurance by systematic in vivo dosimetry: results on a large cohort of patients.," *Radiother Oncol*, vol. 56, no. 1, pp. 85–95, 2000.

[16] A. Rizzotti, C. Compri, and G. F. Garusi, "Dose evaluation to patients irradiated by ^{60}Co beams, by means of direct measurement on the incident and on the exit surfaces.," *Radiother Oncol*, vol. 3, no. 3, pp. 279–83, 1985.

[17] G. Leunens, J. V. Dam, A. Dutreix, and E. van der Schueren, "Quality assurance in radiotherapy by in vivo dosimetry. 2. Determination of the target absorbed dose.," *Radiother Oncol*, vol. 19, no. 1, pp. 73–87, 1990.

[18] J. A. Terrón, F. Sánchez-Doblado, R. Arráns, B. Sánchez-Nieto, and L. Errazquin, "Midline dose algorithm for *in vivo* dosimetry.," *Med Dosim*, vol. 19, no. 4, pp. 263–7, 1994.

[19] M. Cohen, D. E. A. Jones, and D. Greene, "Central axis depth dose data for use in radiotherapy.," *Br J Radiol*, vol. Suppl 11:, p. 59, 1972.

[20] M. Essers, J. H. Lanson, and B. J. Mijnheer, "In vivo dosimetry during conformal therapy of prostatic cancer.," *Radiother Oncol*, vol. 29, no. 2, pp. 271–9, 1993.

[21] S. Heukelom, J. H. Lanson, and B. J. Mijnheer, "In vivo dosimetry during pelvic treatment.," *Radiother Oncol*, vol. 25, no. 2, pp. 111–20, 1992.

[22] R. Boellaard, M. Essers, M. van Herk, and B. J. Mijnheer, "New method to obtain the midplane dose using portal in vivo dosimetry.," *Int J Radiat Oncol Biol Phys*, vol. 41, no. 2, pp. 465–74, 1998.

[23] J. V. Dam, C.Vaerman, N. Blanckaert, G. Leunens, A. Dutriex, and E. van der Schueren, "Are port films reliable for in vivo exit dose measurements?," *Radiother. Oncol.*, vol. 45, pp. 67–72, 1992.

[24] M. Ebert and T. Kron, "Portal films for relative exit dose determinations.," *Australas Phys Eng Sci Med*, vol. 17, no. 2, pp. 71–8, 1994.

[25] C. Fiorino, A. del Vecchio, G. M. Cattaneo, M. Fusca, B. Longobardi, P. Signorotto, and R. Calandrino, "Exit dose measurements by portal film dosimetry.," *Radiother Oncol*, vol. 29, no. 3, pp. 336–40, 1993.

[26] S. Broggi, C. Fiorino, and R. Calandrino, "In vivo estimation of midline dose maps by transit dosimetry in head and neck radiotherapy.," *Br J Radiol*, vol. 75, no. 900, pp. 974–81, 2002.

[27] R. Bogaerts, D. Huyskens, C. Weltens, and A. Dutreix, "Variation of relative transit dose profiles with patient-detector distance.," *Radiother Oncol*, vol. 54, no. 1, pp. 29–37, 2000.

[28] C. Weltens, D. Huyskens, A. Dutreix, and E. van der Schueren, "Assessment of dose inhomogeneities in clinical practice by film dosimetry.," *Radiother Oncol*, vol. 49, no. 3, pp. 287–94, 1998.

[29] M. Takai and M. Kaneko, "Dosimetric verification using a fluoroscopic portal imaging device. (Abstract)," *Med Biol Eng Comput.*, vol. 29 (suppl.), p. 860, 1991.

[30] M. C. Kirby and P. Williams, "Measurement possibilities using using an electronic portal imaging device," *Radiother. Oncol.*, vol. 29, pp. 237–243, 1993.

[31] J. Leong, "Use of digital fluoroscopy as an on-line verification device in radiation therapy.," *Phys Med Biol*, vol. 31, no. 9, pp. 985–92, 1986.

[32] H. Meertens, M. van Herk, and J. Weeda, "A liquid ionisation detector for digital radiography of therapeutic megavoltage photon beams.," *Phys Med Biol*, vol. 30, no. 4, pp. 313–21, 1985.

[33] E. J. Morton, W. Swindell, D. G. Lewis, and P. M. Evans, "A linear array, scintillation crystal-photodiode detector for megavoltage imaging.," *Med Phys*, vol. 18, no. 4, pp. 681–91, 1991.

[34] A. G. Visser, H. Huizenga, V. G. Althof, and B. N. Swanenburg, "Performance of a prototype fluoroscopic radiotherapy imaging system.," *Int J Radiat Oncol Biol Phys*, vol. 18, no. 1, pp. 43–50, 1990.

[35] L. E. Antonuk, J. Boudry, W. Huang, D. L. McShan, E. J. Morton, J. Yorkston, M. J. Longo, and R. A. Street, "Demonstration of megavoltage and diagnostic x-ray imaging with hydrogenated amorphous silicon arrays.," *Med Phys*, vol. 19, no. 6, pp. 1455–66, 1992.

[36] B. J. Heijmen, K. L. Pasma, M. Kroonwijk, V. G. Althof, J. C. de Boer, A. G. Visser, and H. Huizenga, "Portal dose measurement in radiotherapy using an electronic portal imaging device (EPID).," *Phys Med Biol*, vol. 40, no. 11, pp. 1943–55, 1995.

[37] M. Essers, B. R. Hoogervorst, M. van Herk, H. Lanson, and B. J. Mijnheer, "Dosimetric characteristics of a liquid-filled electronic portal imaging device.," *Int J Radiat Oncol Biol Phys*, vol. 33, no. 5, pp. 1265–72, 1995.

[38] Y. Zhu, X. Q. Jiang, and J. V. Dyk, "Portal dosimetry using a liquid ion chamber matrix: dose response studies.," *Med Phys*, vol. 22, no. 7, pp. 1101–6, 1995.

[39] H. Parsaei, E. el Khatib, and R. Rajapakshe, "The use of an electronic portal imaging system to measure portal dose and portal dose profiles.," *Med Phys*, vol. 25, no. 10, pp. 1903–9, 1998.

[40] L. N. McDermott, R. J. Louwe, J. J. Sonke, M. B. van Herk, and B. J. Mijnheer, "Dose-response and ghosting effects of an amorphous silicon electronic portal imaging device," *Med Phys*, vol. 31, no. 2, pp. 285–95., 2004.

[41] Y. El-Mohri, L. E. Antonuk, J. Yorkston, K. W. Jee, M. Maolinbay, K. L. Lam, and J. H. Siewerdsen, "Relative dosimetry using active matrix flat-panel imager (AMFPI) technology.," *Med Phys*, vol. 26, no. 8, pp. 1530–41, 1999.

[42] P. B. Greer and C. C. Popescu, "Dosimetric properties of an amorphous silicon electronic portal imaging device for verification of dynamic intensity modulated radiation therapy.," *Med Phys*, vol. 30, no. 7, pp. 1618–27, 2003.

[43] L. E. Antonuk, "Electronic portal imaging devices: a review and historical perspective of contemporary technologies and research.," *Phys Med Biol*, vol. 47, no. 6, pp. R31–65, 2002.

[44] A. L. Boyer, L. Antonuk, A. Fenster, M. V. Herk, H. Meertens, P. Munro, L. E. Reinstein, and J. Wong, "A review of electronic portal imaging devices (EPIDs).," *Med Phys*, vol. 19, no. 1, pp. 1–16, 1992.

[45] K. A. Langmack, "Portal imaging," *Br J Radiol*, vol. 74, no. 885, pp. 789–804., 2001.

[46] P. Munro, "Portal Imaging Technology: Past, Present, and Future.," *Semin Radiat Oncol*, vol. 5, no. 2, pp. 115–133, 1995.

[47] M. G. Herman, J. M. Balter, D. A. Jaffray, K. P. McGee, P. Munro, S. Shalev, M. V. Herk, and J. W. Wong, "Clinical use of electronic portal imaging: report of AAPM Radiation Therapy Committee Task Group 58.," *Med Phys*, vol. 28, no. 5, pp. 712–37, 2001.

[48] M. C. Kirby and P. Williams, "The use of an electronic portal imaging device for exit dosimetry and quality control measurements," *Int. J. Radiat. Oncol. Biol. Phys.*, vol. 31, pp. 593–603, 1994.

[49] R. Boellaard, M. van Herk, H. Uiterwaal, and B. Mijnheer, "Two-dimensional exit dosimetry using a liquid-filled electronic portal imaging device and a convolution model.," *Radiother Oncol*, vol. 44, no. 2, pp. 149–57, 1997.

[50] R. Boellaard, M. van Herk, H. Uiterwaal, and B. Mijnheer, "First clinical tests using a liquid-filled electronic portal imaging device and a convolution model for the verification of the midplane dose.," *Radiother Oncol*, vol. 47, no. 3, pp. 303–12, 1998.

[51] M. Wendling, R. J. Louwe, L. N. McDermott, J. J. Sonke, M. van Herk, and B. J. Mijnheer, "Accurate two-dimensional imrt verification using a back-projection epid dosimetry method," *Med Phys*, vol. 33, no. 2, pp. 259–73., 2006. Journal Article.

[52] R. J. W. Louwe, E. M. F. Damen, M. van Herk, A. W. H. Minken, O. Torzsok, and B. J. Mijnheer, "Three-dimensional dose reconstruction of breast cancer treatment using portal imaging.," *Med Phys*, vol. 30, no. 9, pp. 2376–89, 2003.

[53] R. J. W. Louwe, M. Wendling, M. B. van Herk, and B. J. Mijnheer, "Three-dimensional heart dose reconstruction to estimate normal tissue complication probability after breast irradiation using portal dosimetry.," *Med Phys*, vol. 34, no. 4, pp. 1354–63, 2007.

[54] R. Bogaerts, A. V. Esch, R. Reymen, and D. Huyskens, "A method to estimate the transit dose on the beam axis for verification of dose delivery with portal images.," *Radiother Oncol*, vol. 54, no. 1, pp. 39–46, 2000.

[55] W. Swindell and P. M. Evans, "Scattered radiation in portal images: a Monte Carlo simulation and a simple physical model.," *Med Phys*, vol. 23, no. 1, pp. 63–73, 1996.

[56] V. N. Hansen, W. Swindell, and P. M. Evans, "Extraction of primary signal from EPIDs using only forward convolution.," *Med Phys*, vol. 24, no. 9, pp. 1477–84, 1997.

[57] L. Spies, M. Partridge, B. A. Groh, and T. Bortfeld, "An iterative algorithm for reconstructing incident beam distributions from transmission measurements using electronic portal imaging.," *Phys Med Biol*, vol. 46, no. 8, pp. N203–11, 2001.

[58] T. R. McNutt, T. R. Mackie, P. Reckwerdt, and B. R. Paliwal, "Modeling dose distributions from portal dose images using the convolution/superposition method.," *Med Phys*, vol. 23, no. 8, pp. 1381–92, 1996.

[59] T. R. McNutt, T. R. Mackie, and B. R. Paliwal, "Analysis and convergence of the iterative convolution/superposition dose reconstruction technique for multiple treatment beams and tomotherapy.," *Med Phys*, vol. 24, no. 9, pp. 1465–76, 1997.

[60] L. Spies and T. Bortfeld, "Analytical scatter kernels for portal imaging at 6 MV.," *Med Phys*, vol. 28, no. 4, pp. 553–9, 2001.

[61] L. Spies, P. M. Evans, M. Partridge, V. N. Hansen, and T. Bortfeld, "Direct measurement and analytical modeling of scatter in portal imaging.," *Med Phys*, vol. 27, no. 3, pp. 462–71, 2000.

[62] B. M. McCurdy and S. Pistorius, "Photon scatter in portal images: physical characteristics of pencil beam kernels generated using the EGS Monte Carlo code.," *Med Phys*, vol. 27, no. 2, pp. 312–20, 2000.

[63] B. M. McCurdy and S. Pistorius, "Photon scatter in portal images: accuracy of a fluence based pencil beam superposition algorithm.," *Med Phys*, vol. 27, no. 5, pp. 913–22, 2000.

[64] B. M. McCurdy and S. Pistorius, "A two-step algorithm for predicting portal dose images in arbitrary detectors.," *Med Phys*, vol. 27, no. 9, pp. 2109–16, 2000.

[65] J. W. Wong, E. D. Slessinger, R. E. Hermes, C. J. Offutt, T. Roy, and M. W. Vannier, "Portal dose images. i: Quantitative treatment plan verification," *Int J Radiat Oncol Biol Phys*, vol. 18, no. 6, pp. 1455–63., 1990. Journal Article.

[66] Proceedings of the 8th International Conference on the use of Computers in Radiation Therapy, *The Delta-Volume Method for 3-Dimensional photon dose calculations*, (Toronto and Canada.), Silver Spring, Maryland: Computer Society Press, IEEE, 1984.

[67] X. Ying, L. Y. Geer, and J. W. Wong, "Portal dose images II : Patient dose estimation," *Int. J. Radiat. Oncol. Biol. Phys.*, vol. 18, pp. 1465–1475, 1990.

[68] M. R. Sontag and J. R. Cunningham, "The equivalent tissue-air ratio method for making absorbed dose calculations in a heterogeneous medium.," *Radiology*, vol. 129, no. 3, pp. 787–94, 1978.

[69] M. K. Woo and J. R. Cunningham, "The validity of the density scaling method in primary electron transport for photon and electron beams.," *Med Phys*, vol. 17, no. 2, pp. 187–94, 1990.

[70] T. R. McNutt, T. R. Mackie, P. Reckwerdt, N. Papanikolaou, and B. R. Paliwal, "Calculation of portal dose using the convolution/superposition method.," *Med Phys*, vol. 23, no. 4, pp. 527–35, 1996.

[71] N. Papanikolaou, *Clinical Photon Beam Treatment Planning Using Convolution and Superposition.* PhD thesis, The University of Wisconsin - Madison., 1994.

[72] T. R. Mackie, A. F. Bielajew, D. W. Rogers, and J. J. Battista, "Generation of photon energy deposition kernels using the EGS Monte Carlo code.," *Phys Med Biol*, vol. 33, no. 1, pp. 1–20, 1988.

[73] R. Bracewell, *The Fourier Transform and its applications.* McGraw-Hill, New York, 1965.

[74] A. Boyer and E. Mok, "A photon dose distribution model employing convolution calculations.," *Med Phys*, vol. 12, no. 2, pp. 169–77, 1985.

[75] T. R. Mackie, J. W. Scrimger, and J. J. Battista, "A convolution method of calculating dose for 15-mv x rays," *Med Phys*, vol. 12, no. 2, pp. 188–96., 1985.

[76] J. E. O'Connor, "The variation of scattered x-rays with density in an irradiated body.," *Phys Med Biol*, vol. 1, no. 4, pp. 352–69, 1957.

[77] K. L. Pasma, S. C. Vieira, and B. J. M. Heijmen, "Portal dose image prediction for dosimetric treatment verification in radiotherapy. II. An algorithm for wedged beams.," *Med Phys*, vol. 29, no. 6, pp. 925–31, 2002.

[78] P. Storchi and E. Woudstra, "Calculation models for determining the absorbed dose in water phantoms in off-axis planes of rectangular fields of open and wedged photon beams.," *Phys Med Biol*, vol. 40, no. 4, pp. 511–27, 1995.

[79] P. Storchi and E. Woudstra, "Calculation of the absorbed dose distribution due to irregularly shaped photon beams using pencil beam kernels derived form basic beam data.," *Phys Med Biol*, vol. 41, no. 4, pp. 637–56, 1996.

[80] A. V. Esch, T. Depuydt, and D. P. Huyskens, "The use of an aSi-based EPID for routine absolute dosimetric pre-treatment verification of dynamic IMRT fields.," *Radiother Oncol*, vol. 71, no. 2, pp. 223–34, 2004.

[81] W. J. C. van Elmpt, S. M. J. J. G. Nijsten, B. J. Mijnheer, and A. W. H. Minken, "Experimental verification of a portal dose prediction model.," *Med Phys*, vol. 32, no. 9, pp. 2805–18, 2005.

[82] R. Mohan, C. Chui, and L. Lidofsky, "Energy and angular distributions of photons from medical linear accelerators.," *Med Phys*, vol. 12, no. 5, pp. 592–7, 1985.

[83] J. Deng, S. B. Jiang, A. Kapur, J. Li, T. Pawlicki, and C. M. Ma, "Photon beam characterization and modelling for Monte Carlo treatment planning.," *Phys Med Biol*, vol. 45, no. 2, pp. 411–27, 2000.

[84] R. L. Siddon, "Fast calculation of the exact radiological path for a three-dimensional CT array.," *Med Phys*, vol. 12, no. 2, pp. 252–5, 1985.

[85] N. Nelson, H. Hirayama, and D. Rogers, *The EGS4 Code System*. National Technical Information Service, Springfield, VA, 1985.

[86] A. Bielajew and D. Rogers, "PRESTA–The Parameter Reduced Electron-Step Transport Algorithm for Electron Monte Carlo Transport," Tech. Rep. PIRS-0042, National Research Council of Canada, 1987.

[87] B. M. McCurdy, K. Luchka, and S. Pistorius, "Dosimetric investigation and portal dose image prediction using an amorphous silicon electronic portal imaging device.," *Med Phys*, vol. 28, no. 6, pp. 911–24, 2001.

[88] A. Ahnesjö, L. Weber, A. Murman, M. Saxner, I. Thorslund, and E. Traneus, "Beam modeling and verification of a photon beam multisource model.," *Med Phys*, vol. 32, no. 6, pp. 1722–37, 2005.

[89] C. V. Dahlgren, A. Ahnesjö, A. Montelius, and G. Rikner, "Portal dose image verification: formalism and application of the collapsed cone superposition method.," *Phys Med Biol*, vol. 47, no. 24, pp. 4371–87, 2002.

[90] A. Ahnesjö and M. M. Aspradakis, "Dose calculations for external photon beams in radiotherapy.," *Phys Med Biol*, vol. 44, no. 11, pp. R99–155, 1999.

[91] P. Keall and P. Hoban, "Accounting for primary electron scatter in x-ray beam convolution calculations.," *Med Phys*, vol. 22, no. 9, pp. 1413–8, 1995.

[92] C. V. Dahlgren, K. Eilertsen, T. D. Jorgensen, and A. Ahnesjö, "Portal dose image verification: the collapsed cone superposition method applied with different electronic portal imaging devices.," *Phys Med Biol*, vol. 51, no. 2, pp. 335–49, 2006.

[93] J. V. Siebers, J. O. Kim, L. Ko, P. J. Keall, and R. Mohan, "Monte Carlo computation of dosimetric amorphous silicon electronic portal images.," *Med Phys*, vol. 31, no. 7, pp. 2135–46, 2004.

[94] H. Keller, M. Fix, and P. Ruegsegger, "Calibration of a portal imaging device for high-precision dosimetry: a Monte Carlo study.," *Med Phys*, vol. 25, no. 10, pp. 1891–902, 1998.

[95] P. W. Chin, E. Spezi, and D. G. Lewis, "Monte Carlo simulation of portal dosimetry on a rectilinear voxel geometry: a variable gantry angle solution.," *Phys Med Biol*, vol. 48, no. 16, pp. N231–8, 2003.

[96] Proc. 7th Int. Workshop on Electronic Portal Imaging, *A Monte Carlo simulation of an amorphous silicon flat panel imager for portal dose prediction*, (Vancouver, Canada), 2002.

[97] Proc. 9th Int. Workshop on Electronic Portal Imaging, *Fast Monte Carlo based computation of a-si dose images for IMRT treatment fields*, (Melbourne, Australia), 2006.

[98] L. Parent, A. L. Fielding, D. R. Dance, J. Seco, and P. M. Evans, "Amorphous silicon EPID calibration for dosimetric applications: comparison of a method based on Monte Carlo prediction of response with existing techniques.," *Phys Med Biol*, vol. 52, no. 12, pp. 3351–68, 2007.

[99] L. Parent, J. Seco, P. M. Evans, A. Fielding, and D. R. Dance, "Monte Carlo modelling of a-Si EPID response: the effect of spectral variations with field size and position.," *Med Phys*, vol. 33, no. 12, pp. 4527–40, 2006.

[100] F. F. Yin, M. C. Schell, and P. Rubin, "Input/output characteristics of a matrix ion-chamber electronic portal imaging device.," *Med Phys*, vol. 21, no. 9, pp. 1447–54, 1994.

[101] M. van Herk and H. Meertens, "A matrix ionisation chamber imaging device for on-line patient setup verification during radiotherapy.," *Radiother Oncol*, vol. 11, no. 4, pp. 369–78, 1988.

[102] M. Mohammadi and E. Bezak, "Two-dimensional transmitted dose measurements using a scanning liquid ionization chamber EPID.," *Phys Med Biol*, vol. 51, no. 11, pp. 2971–85, 2006.

[103] M. van Herk, "Physical aspects of a liquid-filled ionization chamber with pulsed polarizing voltage.," *Med Phys*, vol. 18, no. 4, pp. 692–702, 1991.

[104] R. Boellaard, M. van Herk, and B. J. Mijnheer, "The dose response relationship of a liquid-filled electronic portal imaging device.," *Med Phys*, vol. 23, no. 9, pp. 1601–11, 1996.

[105] A. V. Esch, B. Vanstraelen, J. Verstraete, G. Kutcher, and D. Huyskens, "Pre-treatment dosimetric verification by means of a liquid-filled electronic portal imaging device during dynamic delivery of intensity modulated treatment fields.," *Radiother Oncol*, vol. 60, no. 2, pp. 181–90, 2001.

[106] M. Essers, R. Boellard, M. van Herk, H. Lanson, and B. Mijnheer, "Transmission dosimetry with a liquid-filled electronic portal imaging device," *Int. J. Radiat. Oncol. Biol. Phys.*, vol. 34, pp. 931–941, 1996.

[107] M. Mohammadi, E. Bezak, and P. Reich, "The use of extended dose range film for dosimetric calibration of a scanning liquid-filled ionization chamber electronic portal imaging device.," *J Appl Clin Med Phys*, vol. 8, no. 1, pp. 69–84, 2007.

[108] V. N. Hansen, P. M. Evans, and W. Swindell, "The application of transit dosimetry to precision radiotherapy.," *Med Phys*, vol. 23, no. 5, pp. 713–21, 1996.

[109] E. C. McCullough and A. M. Krueger, "Performance evaluation of computerized treatment planning systems for radiotherapy: external photon beams.," *Int J Radiat Oncol Biol Phys*, vol. 6, no. 11, pp. 1599–605, 1980.

[110] H. Dahlin, I. L. Lamm, T. Landberg, S. Levernes, and N. Ulso, "User requirements on CT-based computed dose planning systems in radiation therapy.," *Acta Radiol Oncol*, vol. 22, no. 5, pp. 397–415, 1983.

[111] "Use of computers in external beam radiotherapy procedures with high-energy photons and electrons," ICRU Report 42, International Commission on Radiation Units and Measurements (ICRU), 1987.

[112] J. V. Dyk, R. B. Barnett, J. E. Cygler, and P. C. Shragge, "Commissioning and quality assurance of treatment planning computers.," *Int J Radiat Oncol Biol Phys*, vol. 26, no. 2, pp. 261–73, 1993.

[113] J. Venselaar, H. Welleweerd, and B. Mijnheer, "Tolerances for the accuracy of photon beam dose calculations of treatment planning systems.," *Radiother Oncol*, vol. 60, no. 2, pp. 191–201, 2001.

[114] K. R. Hogstrom, M. D. Mills, J. A. Meyer, J. R. Palta, D. E. Mellenberg, R. T. Meoz, and R. S. Fields, "Dosimetric evaluation of a pencil-beam algorithm for electrons employing a two-dimensional heterogeneity correction.," *Int J Radiat Oncol Biol Phys*, vol. 10, no. 4, pp. 561–9, 1984.

[115] A. S. Shiu, S. Tung, K. R. Hogstrom, J. W. Wong, R. L. Gerber, W. B. Harms, J. A. Purdy, R. K. T. Haken, D. L. McShan, and B. A. Fraass, "Verification data for electron beam dose algorithms.," *Med Phys*, vol. 19, no. 3, pp. 623–36, 1992.

[116] A. Cheng, W. B. S. Harms, R. L. Gerber, J. W. Wong, and J. A. Purdy, "Systematic verification of a three-dimensional electron beam dose calculation algorithm.," *Med Phys*, vol. 23, no. 5, pp. 685–93, 1996.

[117] W. B. S. Harms, D. A. Low, J. W. Wong, and J. A. Purdy, "A software tool for the quantitative evaluation of 3D dose calculation algorithms.," *Med Phys*, vol. 25, no. 10, pp. 1830–6, 1998.

[118] D. A. Low, W. B. Harms, S. Mutic, and J. A. Purdy, "A technique for the quantitative evaluation of dose distributions.," *Med Phys*, vol. 25, no. 5, pp. 656–61, 1998.

[119] D. A. Low and J. F. Dempsey, "Evaluation of the gamma dose distribution comparison method.," *Med Phys*, vol. 30, no. 9, pp. 2455–64, 2003.

[120] N. Agazaryan, T. D. Solberg, and J. J. DeMarco, "Patient specific quality assurance for the delivery of intensity modulated radiotherapy.," *J Appl Clin Med Phys*, vol. 4, no. 1, pp. 40–50, 2003.

[121] L. N. McDermott, M. Wendling, B. van Asselen, J. Stroom, J. J. Sonke, M. van Herk, and B. J. Mijnheer, "Clinical experience with EPID dosimetry for prostate IMRT pre-treatment dose verification.," *Med Phys*, vol. 33, no. 10, pp. 3921–30, 2006.

[122] E. De Martin, C. Fiorino, S. Broggi, B. Longobardi, A. Pierelli, L. Perna, G. M. Cattaneo, and R. Calandrino, "Agreement criteria between expected and measured field fluences in imrt of head and neck cancer: the importance and use of the gamma histograms statistical analysis," *Radiother Oncol*, vol. 85, no. 3, pp. 399–406, 2007.

[123] N. L. Childress, R. A. White, C. Bloch, M. Salehpour, L. Dong, and I. Rosen, "Retrospective analysis of 2d patient-specific imrt verifications," *Med Phys*, vol. 32, no. 4, pp. 838–50, 2005.

[124] A. Bakai, M. Alber, and F. Nusslin, "A revision of the gamma-evaluation concept for the comparison of dose distributions.," *Phys Med Biol*, vol. 48, no. 21, pp. 3543–53, 2003.

[125] M. Mohammadi, E. Bezak, and P. Reich, "Comparison of two-dimensional transmitted dose maps: evaluation of existing algorithms," *Australas. Phys. Eng. Sci. Med.*, vol. 29, no. 2, pp. 179–187, 2006.

[126] A. van Esch and D. Huyskens, "The asi-based EPID for routine absolute dosimetric pre-treatment verification of dynamic imrt fields," in *Proceedings of Engineering and Physical Sciences in Medicine*, (Geelong, Australia), p. 240, 2004.

[127] A. van Esch. Private communication, 2004.

[128] G. Liu, W. Fernando, M. Grace, and K. Rykers, "An IMRT dose distribution study using commercial verification software.," *Australas Phys Eng Sci Med*, vol. 27, no. 3, pp. 129–35, 2004.

[129] J. Michalski, J. Purdy, D. W. Bruner, and M. Amin, *A Phase III Randomised study of high dose 3D-CRT/IMRT versus standard dose 3D-CRT/IMRT in patients treated for localised prostate cancer*. Radiation Therapy Oncology Group RTOG 0126, 2006.

[130] "Central axis depth dose data for use in radiotherapy," British Journal of Radiology, supplement 17, The British Institute of Radiology, London, United Kingdom, 1983.

[131] J. Booth, *Modelling the impact of treatment uncertainties in radiotherapy*. PhD thesis, School of Chemistry and Physics, University of Adelaide, 2002.

[132] J. T. Booth and S. F. Zavgorodni, "Set-up error & organ motion uncertainty: a review.," *Australas Phys Eng Sci Med*, vol. 22, no. 2, pp. 29–47, 1999.

[133] P. B. Greer, C. C. Jose, and J. H. Matthews, "Set-up variation of patients treated with radiotherapy to the prostate measured with an electronic portal imaging device.," *Australas Radiol*, vol. 42, no. 3, pp. 207–12, 1998.

[134] M. Pasquino, V. C. Borca, P. Catuzzo, F. Ozzello, and S. Tofani, "Transmission, penumbra and leaf positional accuracy in commissioning and quality assurance program of a multileaf collimator for step-and-shoot imrt treatments," *Tumori*, vol. 92, no. 6, pp. 511–6, 2006.

[135] A. K. Bhardwaj, T. S. Kehwar, S. K. Chakarvarti, A. S. Oinam, and S. C. Sharma, "Dosimetric and qualitative analysis of kinetic properties of millennium 80 multileaf collimator system for dynamic intensity modulated radiotherapy treatments," *J Cancer Res Ther*, vol. 3, no. 1, pp. 23–8, 2007.

[136] A. Boyer, P. Biggs, J. Galvin, E. Klein, T. LoSasso, D. Low, K. Mah, and C. Yu., "Basic applications of multileaf collimators," AAPM report no. 72, Report of Task Group No. 50, Radiation Therapy Committee, July July 2001.

[137] A. M. Stell, J. G. Li, O. A. Zeidan, and J. F. Dempsey, "An extensive log-file analysis of step-and-shoot intensity modulated radiation therapy segment delivery errors," *Med Phys*, vol. 31, no. 6, pp. 1593–602., 2004.

[138] O. A. Zeidan, J. G. Li, M. Ranade, A. M. Stell, and J. F. Dempsey, "Verification of step-and-shoot IMRT delivery using a fast video-based electronic portal imaging device.," *Med Phys*, vol. 31, no. 3, pp. 463–76, 2004.

[139] D. W. Litzenberg, J. M. Moran, and B. A. Fraass, "Verification of dynamic and segmental IMRT delivery by dynamic log file analysis.," *J Appl Clin Med Phys*, vol. 3, no. 2, pp. 63–72, 2002.

[140] L. Parent, J. Seco, P. M. Evans, D. R. Dance, and A. Fielding, "Evaluation of two methods of predicting MLC leaf positions using EPID measurements," *Med Phys*, vol. 33, no. 9, pp. 3174–82., 2006.

[141] G. J. Budgell, J. H. Mott, P. C. Williams, and K. J. Brown, "Requirements for leaf position accuracy for dynamic multileaf collimation," *Phys Med Biol*, vol. 45, no. 5, pp. 1211–27., 2000.

[142] M. K. Woo and A. Nico, "Impact of multileaf collimator leaf positioning accuracy on intensity modulation radiation therapy quality assurance ion chamber measurements.," *Med Phys*, vol. 32, no. 5, pp. 1440–5, 2005.

[143] M. Mohammadi and E. Bezak, "Evaluation of MLC leaf positioning using a scanning liquid ionization chamber EPID.," *Phys Med Biol*, vol. 52, no. 1, pp. N21–33, 2007.

[144] A. L. Fielding, P. M. Evans, and C. H. Clark, "Verification of patient position and delivery of imrt by electronic portal imaging," *Radiother Oncol*, vol. 73, no. 3, pp. 339–47, 2004.

[145] K. L. Pasma, M. Kroonwijk, S. Quint, A. G. Visser, and B. J. Heijmen, "Transit dosimetry with an electronic portal imaging device (epid) for 115 prostate cancer patients," *Int J Radiat Oncol Biol Phys*, vol. 45, no. 5, pp. 1297–303., 1999.

[146] D. E. Wazer, T. DiPetrillo, R. Schmidt-Ullrich, L. Weld, T. J. Smith, D. J. Marchant, and N. J. Robert, "Factors influencing cosmetic outcome and complication risk after conservative surgery and radiotherapy for early-stage breast carcinoma.," *J Clin Oncol*, vol. 10, no. 3, pp. 356–63, 1992.

[147] C. L. Ikner, R. Russo, M. B. Podgorsak, G. M. Proulx, and R. J. Lee, "Comparison of the homogeneity of breast dose distributions with and without the medial wedge.," *Med Dosim*, vol. 23, no. 2, pp. 89–94, 1998.

[148] A. M. Moody, W. P. Mayles, J. M. Bliss, R. P. A'Hern, J. R. Owen, J. Regan, B. Broad, and J. R. Yarnold, "The influence of breast size on late radiation effects and association with radiotherapy dose inhomogeneity.," *Radiother Oncol*, vol. 33, no. 2, pp. 106–12, 1994.

[149] E. E. Klein, M. Taylor, M. Michaletz-Lorenz, D. Zoeller, and W. Umfleet, "A mono isocentric technique for breast and regional nodal therapy using dual asymmetric jaws.," *Int J Radiat Oncol Biol Phys*, vol. 28, no. 3, pp. 753–60, 1994.

[150] U. F. Rosenow, E. S. Valentine, and L. W. Davis, "A technique for treating local breast cancer using a single set-up point and asymmetric collimation.," *Int J Radiat Oncol Biol Phys*, vol. 19, no. 1, pp. 183–8, 1990.

[151] Y. Abo-Madyan, M. Polednik, A. Rahn, F. Schneider, B. Dobler, F. Wenz, and F. Lohr, "Improving dose homogeneity in large breasts by IMRT: efficacy and dosimetric accuracy of different techniques.," *Strahlenther Onkol*, vol. 184, no. 2, pp. 86–92, 2008.

[152] L. L. Kestin, M. B. Sharpe, R. C. Frazier, F. A. Vicini, D. Yan, R. C. Matter, A. A. Martinez, and J. W. Wong, "Intensity modulation to improve dose uniformity with tangential breast radiotherapy: initial clinical experience.," *Int J Radiat Oncol Biol Phys*, vol. 48, no. 5, pp. 1559–68, 2000.

[153] L. Hong, M. Hunt, C. Chui, S. Spirou, K. Forster, H. Lee, J. Yahalom, G. J. Kutcher, and B. McCormick, "Intensity-modulated tangential beam irradiation of the intact breast.," *Int J Radiat Oncol Biol Phys*, vol. 44, no. 5, pp. 1155–64, 1999.

[154] W. P. Mayles, J. R. Yarnold, and S. Webb, "Improved dose homogeneity in the breast using tissue compensators.," *Radiother Oncol*, vol. 22, no. 4, pp. 248–51, 1991.

[155] R. Valdagni, M. Ciocca, L. Busana, A. Modugno, and C. Italia, "Beam modifying devices in the treatment of early breast cancer: 3-D stepped compensating technique.," *Radiother Oncol*, vol. 23, no. 3, pp. 192–5, 1992.

[156] A. L. Boyer, "Compensating filters for high energy x rays.," *Med Phys*, vol. 9, no. 3, pp. 429–33, 1982.

[157] A. Fogliata, A. Clivio, G. Nicolini, E. Vanetti, and L. Cozzi, "A treatment planning study using non-coplanar static fields and coplanar arcs for whole breast radiotherapy of patients with concave geometry.," *Radiother Oncol*, vol. 85, no. 3, pp. 346–54, 2007.

[158] G. Nicolini, A. Fogliata, and L. Cozzi, "Critical appraisal of a non-coplanar technique for radiotherapy of breast minimising lung involvement.," *Radiother Oncol*, vol. 76, no. 3, pp. 319–25, 2005.

[159] R. C. Frazier, F. A. Vicini, M. B. Sharpe, D. Yan, J. Fayad, K. L. Baglan, L. L. Kestin, V. M. Remouchamps, A. A. Martinez, and J. W. Wong, "Impact of breathing motion on whole breast radiotherapy: a dosimetric analysis using active breathing control," *Int J Radiat Oncol Biol Phys*, vol. 58, no. 4, pp. 1041–7, 2004.

[160] G. Baroni, C. Garibaldi, M. Scabini, M. Riboldi, G. Catalano, G. Tosi, R. Orecchia, and A. Pedotti, "Dosimetric effects within target and organs at risk of interfractional patient mispositioning in left breast cancer radiotherapy.," *Int J Radiat Oncol Biol Phys*, vol. 59, no. 3, pp. 861–71, 2004.

[161] P. Mavroidis, S. Axelsson, S. Hyodynmaa, J. Rajala, M. A. Pitkanen, B. K. Lind, and A. Brahme, "Effects of positioning uncertainty and breathing on dose delivery and radiation pneumonitis prediction in breast cancer," *Acta Oncol*, vol. 41, no. 5, pp. 471–85, 2002.

[162] K. E. Sixel, M. C. Aznar, and Y. C. Ung, "Deep inspiration breath hold to reduce irradiated heart volume in breast cancer patients.," *Int J Radiat Oncol Biol Phys*, vol. 49, no. 1, pp. 199–204, 2001.

[163] A. N. Pedersen, S. Korreman, H. Nystrom, and L. Specht, "Breathing adapted radiotherapy of breast cancer: reduction of cardiac and pulmonary doses using voluntary inspiration breath-hold.," *Radiother Oncol*, vol. 72, no. 1, pp. 53–60, 2004.

[164] V. M. Remouchamps, F. A. Vicini, M. B. Sharpe, L. L. Kestin, A. A. Martinez, and J. W. Wong, "Significant reductions in heart and lung doses using deep inspiration breath hold with active breathing control and intensity-modulated radiation therapy for patients treated with locoregional breast irradiation.," *Int J Radiat Oncol Biol Phys*, vol. 55, no. 2, pp. 392–406, 2003.

[165] P. Giraud, F. Reboul, S. Clippe, R. Garcia, C. Carrie, F. Campana, B. Dubray, J. C. Rosenwald, and J. M. Cosset, "Respiration-gated radiotherapy: current techniques and potential benefits," *Cancer Radiother*, vol. 7 Suppl 1, pp. 15s–25s, 2003.

[166] R. George, P. J. Keall, V. R. Kini, S. S. Vedam, J. V. Siebers, Q. Wu, M. H. Lauterbach, D. W. Arthur, and R. Mohan, "Quantifying the effect of intrafraction motion during breast imrt planning and dose delivery," *Med Phys*, vol. 30, no. 4, pp. 552–62, 2003.

[167] C. L. Hector, S. Webb, and P. M. Evans, "The dosimetric consequences of inter-fractional patient movement on conventional and intensity-modulated breast radiotherapy treatments," *Radiother Oncol*, vol. 54, no. 1, pp. 57–64, 2000.

[168] M. G. Saliou, P. Giraud, L. Simon, N. Fournier-Bidoz, A. Fourquet, R. Dendale, J. C. Rosenwald, and J. M. Cosset, "Radiotherapy for breast cancer: respiratory and set-up uncertainties," *Cancer Radiother*, vol. 9, no. 6-7, pp. 414–21, 2005.

[169] H. D. Kubo and B. C. Hill, "Respiration gated radiotherapy treatment: a technical study," *Phys Med Biol*, vol. 41, no. 1, pp. 83–91, 1996.

[170] M. Mohammadi, E. Bezak, and P. Reich, "Verification of dose delivery for a prostate sIMRT treatment using a SLIC-EPID," *Applied Radiation and Isotopes.*, 2008.